The Expected Angular Resolution of the JEM-EUSO Mission

Dissertation
der Mathematisch-Naturwissenschaftlichen Fakultät
der Eberhard Karls Universität
zur Erlangung des Grades eines
Doktors der Naturwissenschaften
(Dr. rer. nat.)

vorgelegt von Dipl. Phys. Thomas Mernik
aus Hamburg

Tübingen
2014

Tag der mündlichen Qualifikation: 17.Oktober 2014
Dekan: Prof. Dr. Wolfgang Rosenstiel
1. Berichterstatter: Prof. Dott. Andrea Santangelo
2. Berichterstatter: Prof. Dr. Josef Jochum

Thesis advisor: Andrea Santangelo Thomas Mernik

The Expected Angular Resolution of the JEM-EUSO Mission

Abstract

The *Extreme Universe Space Observatory on board the Japanese Experiment Module* (JEM-EUSO) is a next generation observatory for the observation of ultra high energy cosmic rays (UHECR). It is being designed to be mounted on the International Space Station (ISS). From here it will monitor the earth's atmosphere in the ultraviolet range for extended air showers (EAS). These are induced by UHECR striking nitrogen molecules when entering the atmosphere. JEM-EUSO will detect particles with energies from 10^{19} eV on up to the decade of 10^{20} eV. These particles have an unknown origin. Due to the large target volume monitored, JEM-EUSO will be able to record hundreds of events exceeding energies of $7 \cdot 10^{19}$ eV. Therefore, it is the key instrument to improve the statistics in the high energy part of the cosmic ray spectrum, where the flux of events is extremely low, by one order of magnitude. Orbiting the earth at an altitude of about 400 km JEM-EUSO will provide an all sky coverage. The high exposure in combination with a sufficient spatial resolution will enable the identification of the sources of UHECR. During the development of the mission, the JEM-EUSO Collaboration is conducting a number of pathfinder missions to demonstrate the feasibility of the envisaged experiment. Among them is the EUSO-Balloon, a downscaled version of the JEM-EUSO instrument using the same components like optics and electronics. From summer 2014 on, it will conduct a number of stratospheric flights to measure the UV background and laser generated, artificial EAS.

ESAF, the *EUSO Simulation and Analysis Framework* is a software package to simulate space borne UHECR missions. Within a full end-to-end approach, it is capable to take into account all physical processes occurring, when an UHECR hits the atmosphere. From the generated data, we can reconstruct the properties of the UHECR primary — its energy, incoming direction and the type of particle it was. We use ESAF to simulate the JEM-EUSO instrument and its pathfinders.

In the scope of this dissertation, we evaluate the expected angular reconstruction performance of the planned JEM-EUSO mission. We can confirm that the instrument meets the scientific requirements. Apart from the baseline instrument, a possible advanced configuration is subject to study. From our findings we can conclude an even improved performance for this instrument. A special emphasis is given to the question how atmospheric scattering affects the fluorescence light signal. We analyze the relevance of this issue and quantify to which extent it affects the angular resolution. Further investigations deal with a possible tilting of the telescope from its nadir position for an increased exposure. We analyse how the reconstruction performance changes in dependence of the tilting angle and find that for high tilting angles the instrument looses its angular resolution capabilities.

Betreuer: Andrea Santangelo Thomas Mernik

The Expected Angular Resolution of the JEM-EUSO Mission

ZUSAMMENFASSUNG

Das *Extreme Universe Space Observatory on board the Japanese Experiment Module* (JEM-EUSO) ist ein neuartiges Weltraumteleskop zur Beobachtung kosmischer Strahlung. Noch in dieser Dekade wird es von der internationalen Raumstation (ISS) aus, im ultravioletten Bereich, Luftschauer (EAS) in der Erdatmosphäre beobachten, welche von ultrahochenergetischen kosmischen Strahlen (UHECR) erzeugt werden. EAS sind Lawinen von Sekundärteilchen, die entstehen wenn UHECR mit Stickstoffmolekülen kollidieren. JEM-EUSO wird UHECR mit Energien ab 10^{19} eV bis über 10^{20} eV hinaus beobachten. Die Größe des beobachteten Targetvolumens ermöglicht JEM-EUSO hunderte von Ereignissen mit Energien über $7 \cdot 10^{19}$ eV zu messen und die Statistiken im höchstenergetischen Teil der Spektrums der kosmischen Strahlen um eine Größenordnung zu erhöhen, da der Teilchenfluss in diesem Bereich des Spektrums extrem klein ist. JEM-EUSO ist geeignet die bislang unbekannte Herkunft dieser Teilchen zu bestimmen. Vom Orbit der ISS aus, lässt sich der gesamte Himmel gleichmäßig abdecken. Im Laufe des Mission führt die JEM-EUSO Collaboration einige Pathfinder-Experimente durch, um die Durchführbarkeit des geplanten Konzepts zu demonstrieren. Der EUSO-Ballon ist eine verkleinerte Variante von JEM-EUSO, mit der gleichen Optik und Elektronik.

ESAF, das *EUSO Simulation and Analysis Framework* ist ein Software Paket, um weltraumgestützte UHECR Missionen zu simulieren. Es berücksichtigt dabei alle relevanten physikalischen Prozesse die auftreten wenn ein UHECR in die Atmosphäre eindringt. Aus den generierten Daten können die Eigenschaften des ursprünglichen UHECR rekonstruiert werden - seine Energie, Ankunftsrichtung und die Art des Teilchens. Wir benutzen ESAF um das JEM-EUSO Teleskop und seine Pathfinder zu simulieren.

Betreuer: Andrea Santangelo Thomas Mernik

Im Rahmen dieser Dissertation evaluieren wir die zu erwartende Winkelauflösung der geplanten JEM-EUSO Mission und können bestätigen, dass sie den wissenschaftlichen Anforderungen genügt. Neben dem Standardinstrument untersuchen wir auch eine potentielle verbesserte Variante des Teleskops. Diese *advanced option* zeigt eine deutlich verbesserte Leistung im Vergleich zum Standardinstrument. Ein besonderer Fokus ist den Auswirkungen der Streueffekte von Fluoreszenzlicht in der Atmosphäre auf die Winkelauflösung gewidmet. Wir zeigen, dass dieser Effekt signifikante Auswikungen auf das Signal hat und quantifizieren die dadurch entstehende Verschlechterung der Auflösung. In einer weiteren Studie bestimmen wir, wie sich ein mögliches Kippen des Teleskops aus seiner Lotrechten, welches einer Erhöhung der Exposure dient, auf die Winkelrekonstruktion auswirkt. Wir stellen fest, dass große Kippwinkel zu einer starken Einschränkung der Leistungsfähigkeit des Teleskops führen.

Contents

Listing of figures

Acknowledgements

THE WORK PRESENTED IN THIS DISSERTATION is the outcome of a collective work in the context of the JEM-EUSO collaboration. Without the support of my group in the Institute for Astronomy and Astrophysics at the Universität Tübingen and the simulation task force of the JEM-EUSO collaboration this work would not have been possible. Hence, I wish to thank my dearest colleagues for their support, their contributions and the cheering up.

I wish to express my deepest ans sincere gratitude to my supervisor Andrea Santangelo whose patience and appreciative attitude enabled me to steer into the right direction. Being part of his group for six years allowed me to gain a deep understanding, not only of astroparticle physics but of science in a broader perspective.

Travelling to the many meetings and conferences has been a vital part of this work. I deeply appreciate the generous grants provided by the ESA Topical Team Activities funds, the DAAD travel grants, the Kepler Graduiertenkolleg funds and the Freunde der Universität Tübingen travel support.

I would like to thank the RICC, the RIKEN Integrated Cluster of Clusters in Saitama, Japan, for an allocation of extensive computing resources. Furthermore, I would like to thank the ESAF developers for making the ESAF software package available to the JEM-EUSO collaboration.

I wish to express my greatest appreciations to my loved ones and friends for morally supporting me during the time of research and writing this dissertation.

DANKE SEHR!

The shortest distance between two points is often unbearable.

Charles Bukowski

1

Introduction

Every second of time, each square metre on top of our atmosphere is bombarded with charged particles coming from all directions of the sky. Their nature is manifold. Even though the majority of these particles are protons and helium nuclei, also heavier nuclei up to iron can be found together with electrons and a small fraction of antimatter. Their energy ranges over more than 13 orders of magnitude, starting at about 10^8 eV up to more than 10^{20} eV. We call them cosmic rays.

The origin of cosmic rays depends on their energy. While the less energetic ones, up to some Gev, are ejected from solar flares into space [104], the higher energetic particles up to 10^{18} eV are referred to as the *galactic component*. They originate from sources inside our galaxy. Basic ingredients for their acceleration are strong irregular magnetic fields and traversing shock fronts — a combination found in supernova remnants. Supernova remnants are regarded as the most likely source for particles with energies up to 10^{15} eV. For higher energies the source of these particles is unclear. There have been attempts to explain their existence. However, up to the present no widely accepted explanation exists. From 10^{18} eV on, cosmic rays are believed to originate from outside the galaxy [269]. Particles exceeding this energy are referred to as ultra high energy cosmic rays (UHECR). As potential sources active galactic nuclei (AGN) or clusters of galaxies are under discussion, yet without any conclusive evidence. Due to the strong suppression of the cosmic ray flux in this energy range, only a small number of events has been measured so far. This makes the discovery of sources a challenging task. Due to the shielding effect of the atmosphere, cosmic rays do not reach the surface of the earth. For direct measurement, the detector has to be either mounted on a balloon or space craft. In the high energy regime, the flux of incoming particles becomes extremely low. For instance, at 10^{20} eV, only one particle per square kilometre per millennium reaches the earth. Thus, a direct detection is impossible, since it would require an enormously outstretched detector. Hence, an indirect observation technique is used. When penetrating the atmosphere, cosmic rays interact with the nitrogen and oxygen molecules and create avalanches of secondary particles — extended air showers (EAS). Decay products of these showers reach the ground and can be detected by scintillation detectors or Cherenkov water tanks. Another detection technique is the observation of the EAS with UV telescopes. From the direction and intensity of the EAS, we can reconstruct the properties of the primary UHECR. The scarcity of events in the high energy region exceeding $\sim 5 \cdot 10^{19}$ eV is the main motivation for a novel approach. The potential for ground based telescopes are regarded as rather limited due to spatial and monetary constraints. Thus, a space borne instrument will be the key to identify the sources. This new generation of UHECR detectors will monitor a large fraction of the earth's atmosphere to use it as a huge target volume. This will enable us to record a meaningful number of UHECR in a reasonable amount of time.

The *Extreme Universe Space Observatory on board the Japanese Experiment Module* (JEM-EUSO) is such a next generation UHECR observatory. It has been developed to be mounted on the Japanese module of the International Space Station (ISS) before 2020 [251]. JEM-EUSO is a 2.5 metre UV telescope that uses the fluorescence technique to observe EAS generated by UHECR from an altitude of about 400 km. Its lower energy threshold at 10^{19} eV allows for cross-calibration with the large ground based observatories. Due to its large aperture of $5 \cdot 10^5$ km^2 sr [257], JEM-EUSO will improve the statistics in the ultra high energy part of the cosmic ray spectrum by one order of magnitude. With this new detector important questions in the field of UHECR science can be successfully addressed. Among them are urgent topics such as the identification of the sources and the composition of the cosmic ray flux at highest energies. In the proposed lifetime of the mission of 3 + 2 years, JEM-EUSO will measure about 1000 UHECR events $> 10^{20}$ eV [94] and will therefore be the gate opener to astroparticle astronomy.

Since no detector of such a design has been launched into space so far, the JEM-EUSO collaboration has decided to prove the feasibility of this mission in advance by developing two pathfinders: Telescope Array EUSO (TA-EUSO) and the JEM-EUSO Balloon. These are downscaled versions of the originally envisaged detector. Both feature a system of Fresnel lenses and the same kind of electronics, JEM-EUSO will be equipped with. TA-EUSO has been deployed inside the grounds of the Telescope Array (TA) site in the desert of Utah, USA. TA is a large cosmic ray detector which is already taking data. Even though TA-EUSO monitors a far smaller fraction of the sky than TA, the aim is to measure a small number of events for cross calibration of the detectors. The main purpose of the pathfinders however, is to demonstrate the technological readiness potential. The JEM-EUSO balloon is essentially the same instrument as TA-EUSO. Though, this instrument is an atmospheric balloon payload and will conduct several flights at altitudes of about 40 km from this year on. This will enable the JEM-EUSO collaboration to test the detector under quasi space conditions and to conduct background studies.

During the construction of the mission, extensive simulation work is required to estimate the expected performance of the instrument, to check its different components and to verify their capabilities. ESAF - the *EUSO Simulation and Analysis Framework* is a software designed to simulate space based UHECR detectors. With this software we simulate the JEM-EUSO mission and its pathfinders.

In the scope of this dissertation, we describe the evolution of the field of cosmic ray science during the past 100 years. Summarizing the current status in the field we motivate the space approach and discuss its potentials and challenges. We present the JEM-EUSO mission, the scientific objectives and the technology of the instrument and its pathfinders. Using the ESAF package, we evaluate the expected angular resolution of the instruments. We study the performance of the standard JEM-EUSO telescope as well as potential alternative detectors. The aim is to characterize the conditions under which the optimum performance can be reached and whether these estimates are sufficient to comply with the scientific requirements of the mission. A special emphasis is given to the question how the scattering of fluorescence light photons in the atmosphere affects the observation of the air showers. Another objective aims at quantifying the impact of a possible tilting of the instrument on the angular resolution.

We, on the other hand, must take for granted that the things that exist by nature are, either all or some of them, in motion.

Aristotle

2

Cosmic Rays

ALMOST EXACTLY A CENTURY AGO, Victor Hess[1] conducted his first experiments to measure electric discharges induced by ionizing radiation. During a number of balloon flights he measured the time it took for the electrometers to loose charge. It was well known at that time that electrometers discharge due to the ionizing radiation, produced in the decay of radioactive isotopes which naturally exists in the soil. Therefore, he expected the discharge time to become longer the more the electrometer would be carried away from ground. This assumption proved to be true for the first 1000 m of ascent: the dose of radiation became gradually lower. Afterwards however, the discharge time started to decrease again. Thus, the radiation levels were rising again. From these findings he concluded the presence of another source of radioactivity - the sky. He called this new form of radiation *Höhenstrahlung*, a term which is still used in aviation. This was the hour of birth of cosmic ray science.

In 2012, a similar expedition was conducted. This time the balloon gondola was

---

[1] Victor Franz Hess, ⋆24 June 1883 Schloss Waldstein, Austria †17 December 1964 Mount Vernon, New York, USA; Nobel Prize in Physics in 1936

Figure 2.0.1: Victor F. Hess, centre, departing from Vienna about 1911, was awarded the Nobel Prize in Physics in 1936. Pic. taken from [73].

equipped with self-made astro muon detectors, a commercial Geiger counter and a self-made electroscope very similar to the one Victor Hess had been using. This balloon flight went up to an altitude of 6000 m a.s.l. [25]. The results were remarkably comparable to those obtained by Hess, one century before (Fig. 2.0.2).

Already one year earlier than Hess, Domenico Pacini[2] (Fig. 2.0.3) came to the same conclusion after conducting several measurements with electroscopes on land at sea level, on a boat ashore and under water with a diving apparatus. From the decreasing radiation under water he concluded that at least a part of the radiation has to come from the sky [202]. As shown by Giglietto in 2011, Pacini performed his measurements in parallel or earlier to the ones of Hess [114]. He was certainly the first to realize that the earth itself cannot be the only source of radioactivity. Although, his experiments did not exclude the atmosphere as a possible source [88].

Werner Kolhörster[3] (Fig. 2.0.3b) conducted further balloon flights even reaching altitudes such as 10000 m a.s.l., using the newly invented Geiger-Müller counters. More-

---

[2] Domenico Pacini, ⋆February 20 1878, Marino, Italy †Rome, May 23 1934

[3] Werner Kolhörster, ⋆December 28 1887, Schwiebus (Swiebodzin), Brandenburg Province of Prussia †August 5 1946, Munich, Germany

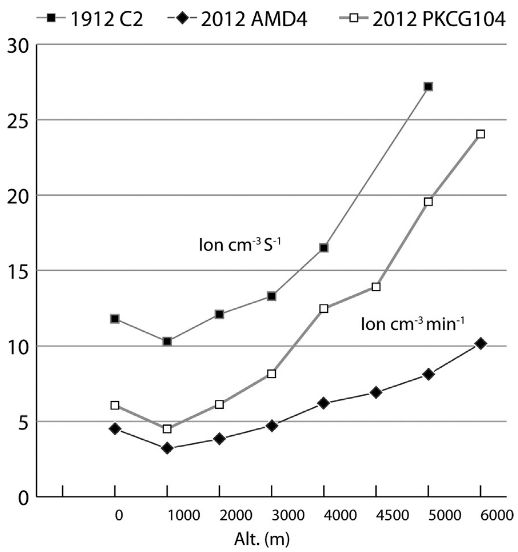

Figure 2.0.2: Comparison of the data recorded by Hess in 1912 and the VHANESSA flight in 2012. Pic. taken from [25].

over, together with Bruno Rossi[4] he used the coincidence technique [135, 277] by comparing the signals of several detectors that where arranged in an array . The coincidence technique for an array of detectors lead to the discovery of extended air showers (EAS). In the 1930s, Pierre Auger[5] used an array of ground detectors that were displaced by 300 m. Auger identified the coinciding events he detected as secondary particles being part of nucleonic cascades of cosmic origin [26].

In the 1930s and 1940s an amazing progress in the cosmic ray field was made. Due to new inventions, such as the bubble chamber, and new theories in a relatively short amount of time new particles were discovered and many of the underlying processes in air shower development identified [see 220, for instance].

In the 1960s, new experiments lead to the discovery of particles with energies exceeding 10^{20} eV at the Volcano Ranch experiment by using a network of scintillation counters [169]. In 1991, an event exceeding even $3 \cdot 10^{20}$ eV has been observed by the Fly's Eye experiment. This event is still referred to as the *Oh-My-God particle*, since nobody had believed in the existence of such a particle before [95]. Between the 1990s and today a number of ever growing cosmic ray experiments has been conducted. The Akeno Giant Air Shower Array (AGASA) [85] in Japan e.g. was using 111 scintillation detectors and 27 muon detectors distributed over an area of about 100 km^2 to measure

---

[4] Bruno Benedetto Rossi, ⋆April 13 1905, Venice, Italy †November 21 1993, Cambridge, Massachusetts, USA

[5] Pierre Victor Auger, ⋆May 14 1899, Paris, France †December 25 1993, Paris, France

Figure 2.0.3: Left: Domenico Pacini. Taken from [114]. Right: Kolhörster and Auger at Jungfraujoch, Switzerland. Taken from [135].

a large collection of data in the UHE regime of cosmic rays. Results contradictory to data from other experiments lead to the development of even larger arrays sometimes using different detection techniques at the same time for improved results.

In this century of cosmic ray science, magnificent discoveries have been made. These major achievements were partly possible due to new technological developments leading to detector designs. Additionally, it is the development of new interaction models, acceleration and propagation mechanisms that contributes to our nowadays understanding. It is the joint effort of both, experimental physicists and theoreticians that could reveal many answers to the question of the nature of cosmic radiation [197]. The following sections give an overview about the current status of the field. First of all, we describe the properties of cosmic rays, their spectrum and composition. Focusing on UHECR, we present the current ideas of how they are created and propagated to earth. We briefly introduce the principles of their detection and we summarize the recent developments and highlight the open questions.

2.1 UHECR

Cosmic rays are essentially charged particles, i.e. protons, electrons, nuclei and positrons. Although, neutral particles as neutrons, neutrinos and gammas are sometimes included as well, when referring to cosmic rays in a broader sense [186]. For that matter it is important to distinguish between the primary radiation, produced at some acceleration site or resulting from a decay and the secondary radiation arriving to earth after traversing the ISM. The first comprises of positively charged protons or heavier nuclei. The latter includes neutral particles, among them neutrinos and photons, as well as some antimatter or decay products from the spallation of nuclei. Secondary radiation is produced due to interaction of the primaries with matter, fields and photons of the ISM. The term *ultra high energy cosmic rays* (UHECR) refers to particles exceeding the energy of 10^{18} eV. Particles beyond 10^{20} eV are called *extremely high energy cosmic rays* (EHECR).

2.1.1 Spectrum

The spectrum of cosmic rays extends over many orders of magnitude in energy and flux. The energy of cosmic rays ranges from 10^9 eV up to at least some 10^{20} eV, with a steeply and monotonously decreasing flux [106]. Their energy distribution is highly non-thermal, i.e. it can be described by a steep broken power law spectrum E^{-a}. The proportionality of $a \sim -3$ suddenly changes slightly in some regions of the otherwise almost featureless spectrum (Fig. 2.1.1).

In the low energy range at about 10^{11} eV the flux is of the order of $10^{12} m^{-2} s^{-1} sr^{-1}$. In this energy region the flux is time-dependent since most of the particles are ejected in solar flares. The exponent of the spectrum in this range is between 2.5 to 2.7 [172]. (For comparison: the largest man-made accelerator ever built, the LHC[6] at CERN[7] reaches energies of the order of TeV [255].) The first remarkable feature is the so called *knee* at E $\sim 5 \cdot 10^{15}$ eV. From here on, the flux steepens with an $a \sim 3.1$. Data recorded by the KASKADE experiment actually revealed the existence of a number of knee-like structures in the region 4 - $5.7 \cdot 10^{15}$ eV [128]. An inefficient confinement of the particles in the galaxy is discussed as the mechanism behind [40]. This is supported by the KASKADE findings that the individual knees are shifted towards higher energies with an increasing atomic number of the primaries. A steepening feature at 80 - 90 PeV has been identified with a flux suppression of the heavy mass component by the KASKADE-Grande array [105, 128]. Already in this energy range, the flux is too low for a direct detection of CR.

At $5 \cdot 10^{17}$ eV there is a small characteristic - the *second knee*. The gradient again becomes slightly steeper. The reasons for this occurrence are unclear. Perhaps some

---

[6] LHC: Large Hadron Collider

[7] CERN: Conseil Européen pour la Recherche Nucléaire

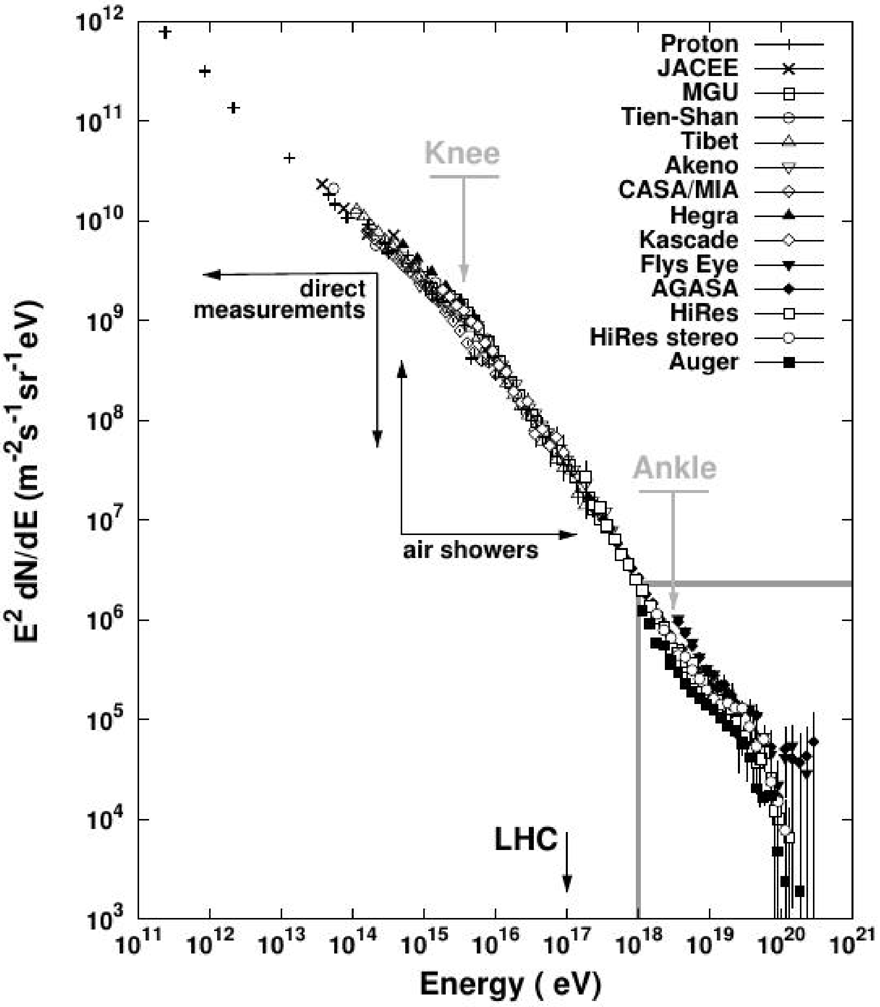

Figure 2.1.1: The cosmic ray spectrum ranges over nine orders of magnitude in energy and flux. This is the differential energy spectrum showing data collected in various cosmic ray experiments using a variety of different detection techniques. It features a steep broken power law, starting at 10^{11} eV with a high flux of $10^{12} m^{-2} s^{-1} sr^{-1}$. The flux decreases with a gradient of 2.7 until 10^{15} eV the so called *knee*, where the gradient becomes steeper (about 3). A second remarkable feature appears at $\sim 3 \cdot 10^{18}$ eV, where the gradient becomes lower, again. This feature is called the *ankle*. As indicated, at about 10^{14} eV, the flux is to low for any direct measurement. Above this energy, cosmic rays are detected indirectly by the observation of extended air showers which are created when they interact with oxygen or nitrogen molecules while traversing the earth's atmosphere. Taken from [165].

component of CRs from here on originates from extra-galactic sources [43, 112].

The second important feature is the *ankle* at $3 \cdot 10^{18}$ eV (Fig. 2.1.2). Here, the gradient of the flux recovers a little and we can observe a clear flattening of the spectrum for energies $\geq 5 \cdot 10^{18}$ eV. However, due to the low flux, only one particle per square kilometre and century arrives to the earth. These extremely low statistics make the detection of CR in this range utterly challenging. The origin of the ankle is under discussion. A common interpretation is the transition from a galactic to an extra-galactic component [46], since the galactic magnetic field is not sufficiently strong to confine particles of this energy [18, 112] (Chap. 2.5.3). Immediately after the ankle, a weak dip appears in the differential spectrum. This has been identified with energy losses due to pair production [19, 46].

At $5 \cdot 10^{19} eV$ one can clearly see a cut-off that has been linked to the GZK-effect (Chap. 2.5). At this energy, the flux drops to 1 particle per square kilometre per millennium. However, this is not the end of the spectrum. Today we know that even if the flux becomes extremely low, there are still events to be found for energies exceeding 10^{20} eV. These confirmed EHECR events have been measured by different experiments. The Pierre Auger Collaboration has claimed the measurement of more than 77 events above $5 \cdot 10^{19}$ eV[8] alone [177]. Furthermore, data from other experiments like AGASA and HiRes/TA [48] have clearly shown that the depression at $5 \cdot 10^{19}$ eV is not the end of the spectrum.

2.1.2 COMPOSITION

Ever since the discovery of the latitude effect and the East-West effect it was evident that the predominant components of cosmic rays were positively charged [240]. On top of the atmosphere, approximately 85 % of the particles are protons, 12 % are ionized helium and heavier nuclei (~ 1 %). The remaining 2 % are electrons. The fraction of antimatter is comparatively low. Positrons make up a few percent and anti-protons contribute only a few 10^{-4} [60]. This estimate has recently been confirmed in the energy range of 0.5 to 350 GeV by the AMS[9] experiment [10]. From the knee on, the fraction of heavy elements increases continuously with the energy up to about 10^{17} eV.

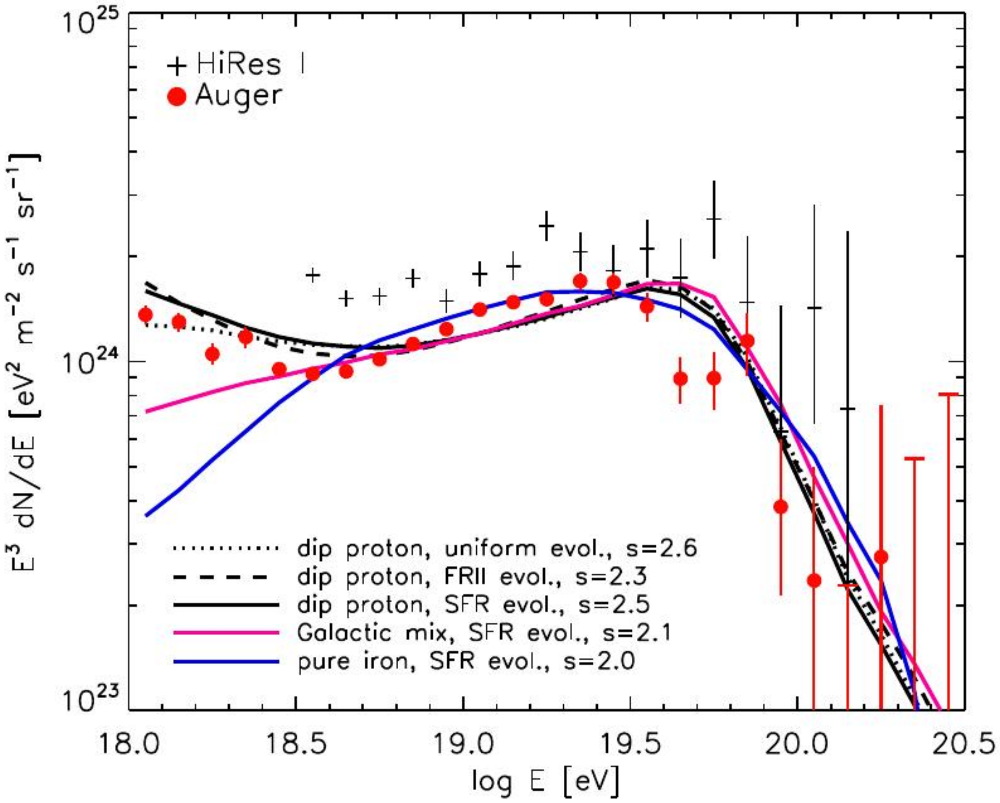

Figure 2.1.2: Energy spectrum of UHECRs multiplied by E^3. The five lines correspond to different models describing the transition from galactic to extragalactic origin of UHECR, different chemical compositions and spectral indices. The data points come from HiRES I and Auger measurements. Taken from [156, and references therein].

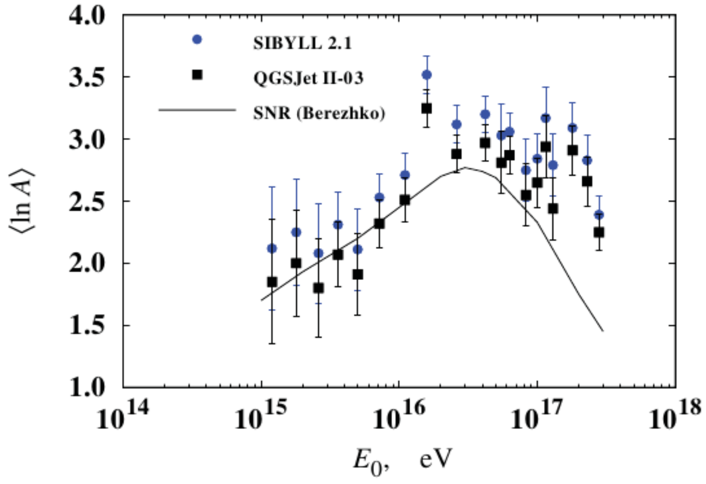

Figure 2.1.3: Mean natural logarithm of the CR atomic number $< lnA >$ plotted against logarithm of the CR energy. The data is derived from the small Cherenkov setup which is part of the Yakutsk array. Identification of A due to slant depth X_{max} of the EAS in atmosphere. Data points in blue: mass composition estimated according to SIBYLL2.1 model, black squares according to the QGSJet II-03 model, respectively. The solid line represents the prediction of the composition expected from supernova remnants (SNR). Taken from[155].

Afterwards it turns to elements with lower masses again [155] (Fig. 2.1.3).

For the trans-GZK-events there is no conclusive evidence about the particle type. From the energy range of 10^{15} eV on, the determination of the chemical composition of the primary cosmic ray becomes a difficult task since the air shower observation techniques do not directly allow to infer this information. The observation of EAS with multiple cores suggest that the primaries in the high energy regime are at least not exclusively protons [172]. One way to indirectly determine the number of charged nucleons in the primary is by means of its slant depth X_{max} which is correlated to the cross-section of the particle. I.e., the same air shower would be created by a proton at a given energy or an iron nucleus with a Lorentz factor 56 less than the proton, only at a higher altitude. Thus, on average proton showers develop lower in the atmosphere. Moreover, they have higher fluctuations $\sigma(X_{max})$. (For the definition of X_{max}, see Chap. 2.6.1)

Unfortunately, using $\langle X_{max} \rangle$ and $\sigma(\langle X_{max} \rangle)$ as indicators yield conflicting results for different experiments. The HiRes and TA composition measurements are in very good agreement to each other [30, 253]. These two experiments in the northern hemisphere

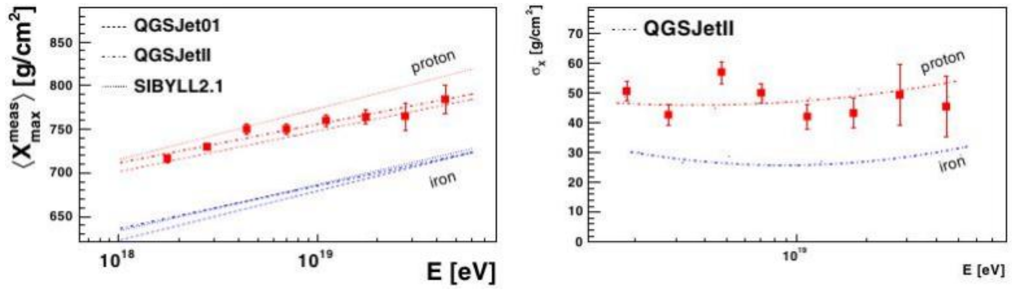

(a) UHECR composition measured by HiRes [30]

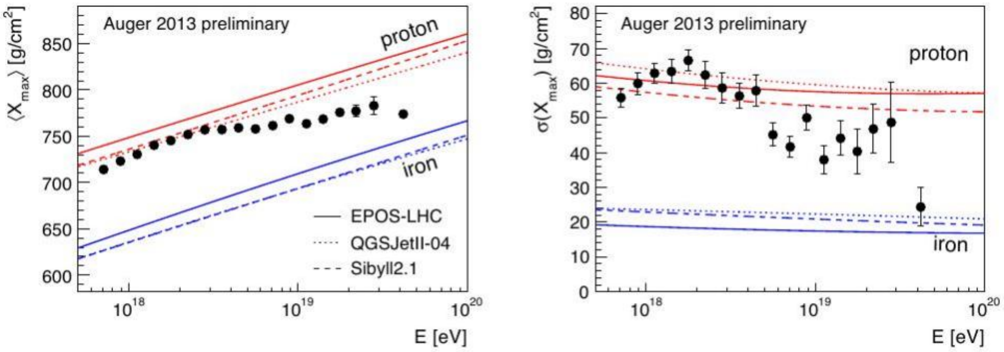

(b) UHECR composition measured by PAO [166]

Figure 2.1.4: Measured X_{max} (left) and RMS(X_{max}) (right) for different experiments (top: HiRes, bottom: PAO). The red areas indicate MC predictions from different hadronic interaction models for protons, the blue area for iron nuclei, respectively.

favour a pure proton flux. However, the data of the PAO clearly shows a transition towards heavier elements in this energy range [166] (Fig. 2.1.4). It is important to point out that the total number of collected events by the PAO exceeds those of TA clearly (up to the factor of 10, depending on cuts and comparability due to different setups.) [30].

Thus, even though there are strong hints that UHECR beyond 10^{19} eV are not purely protons. Nonetheless, the confirmation by a second independent experiment is still pending. Perhaps a few years more of PAO operation can substantiate this claim.

2.1.3 Anisotropy

The question whether or not discrete sources of UHECR exist is among the most interesting and challenging. Anisotropy patterns can be the ultimate tool to identify poten-

---

[8] status 2012

[9] AMS: Alpha Magnetic Spectrometer

tial sources. However, as described in Chap. 2.5.3, magnetic fields play an important role in the propagation of UHECR. Therefore, even if there were discrete sources, the trajectories of UHECR could be distorted in such a way that the crucial information about the direction of the origin might got lost. This depends, of course strongly on the energy of the particle as well as on the charge. The more elementary charges it carries, the more it gets deflected by the fields. Thus, the anisotropy question is closely connected to the composition of the flux at the highest energies.

First correlations of clusters of UHECR events with local scale structures or BL Lac objects have already been suggested in the 1990s [156, and references therein]. The latest claim about the isotropy distribution was announced by the PAO [213] in 2007 (Fig. 2.1.5). It was also maintained three years later in 2010, using an even larger amount of data [4, 188].

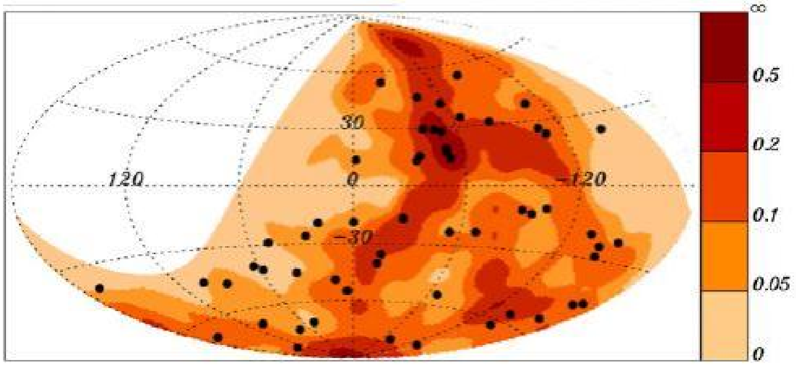

Figure 2.1.5: Projection of the sky in galactic coordinates. AGNs within 200 Mpc smoothed with an angular scale $\sigma = 5°$. Arrival directions of the CRs with energy E $\geq$55 EeV detected with the PAO in black dots . Taken from[4].

This was contradicted by measurements of the HiRes experiment in 2008. The HiRes Collaboration analysed their own data set using similar methods as the PAO Collaboration with theirs. Neither could there be found any correlation with nearby AGNs, nor a significance in clustering of large scale anisotropies at all [132] (Fig. 2.1.6). The HiRes findings gained even more substance when in 2011, after 40 month of additional data taking, the conclusions were still the same [5]. Of course, on should keep in mind that HiRes is taking data mostly in the northern hemisphere, whereas the PAO exposure peaks in the southern. Moreover, the statistics of PAO are considerably larger compared to HiRes.

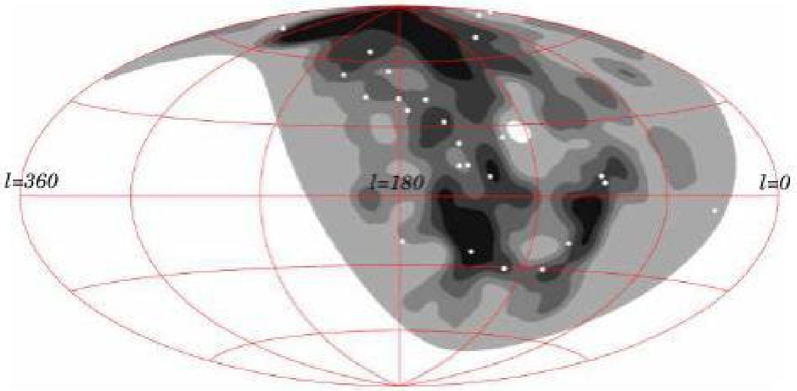

Figure 2.1.6: The sky map in galactic coordinates of the expected flux at energy threshold 57 EeV with the Telescope Array events superimposed (white dots). The smearing angle is 6°. The white region indicates no exposure. Taken from[5].

2.2 PRODUCTION

The spectrum and composition of cosmic rays we observe, impose certain requirements on the sources. A meaningful source model should reproduce the power-law shape of the spectrum. Moreover, the chemical composition at the creation site should be comparable to the abundances in the CR flux we measure. Above all should it be able to account for the highest energies observed. Of course, the sources alone can not account for all of the spectral features. Some of them are certainly the effects of the propagation, i.e. interaction with the ISM on the way to earth. Others are certainly induced by the fact that there is not a single species of astrophysical objects responsible for the production of the entire spectrum. Most likely a mixture of galactic and extra-galactic objects determine the shape of the different energy parts of the spectrum [159]. The miracle of particles with energies beyond 10^{20} eV, has lead to the formulation of a diversity of theories to explain their existence. They can roughly be divided into two families of theories - the *bottom-up* scenario and the *top-down* scenario.

2.2.1 BOTTOM-UP SCENARIOS

In general, a variety of different scenarios is plausible to transfer energy from a macroscopic environment to particles. Under consideration are magnetic or electric acceleration, as well as magnetohydrodynamical scenarios. However, due to the abundance of ionised plasma in cosmic environments, electric fields will hardly persist for a sufficient amount of time. Furthermore, simple static magnetic fields can be excluded for the reason that field strength and extension required to produce the highest CR energies would surmount those of any astrophysical object we could imagine by far. It is in fact most likely that the accelerator has a strong magnetic field, yet in an environment that is characterized by strong magnetohydrodynamical turbulences and shock fronts. This scenario allows to confine the particles inside the accelerating region for a sufficient amount of time to gain high energies. Of course, magnetic field strength and spatial dimension would still be major ingredients to reach the maximum energies we observe. A simple rule of thumb calculation to estimate the maximum achievable energy in such a scenario is expressed by

$$E_{max} = \beta Ze \left(\frac{B}{1\mu G}\right)\left(\frac{R}{1kpc}\right) EeV \tag{2.1}$$

here β denotes the shock front velocity traversing the region of size R with a magnetic field B. The Hillas plot maps candidate sites for sources of UHECR in the parameter space of expansion and magnetic field strength [134] (Fig. 2.2.1). The Hillas criterion imposes such strong constraints on the potential sources that most of the known astrophysical objects are effectively excluded [143].

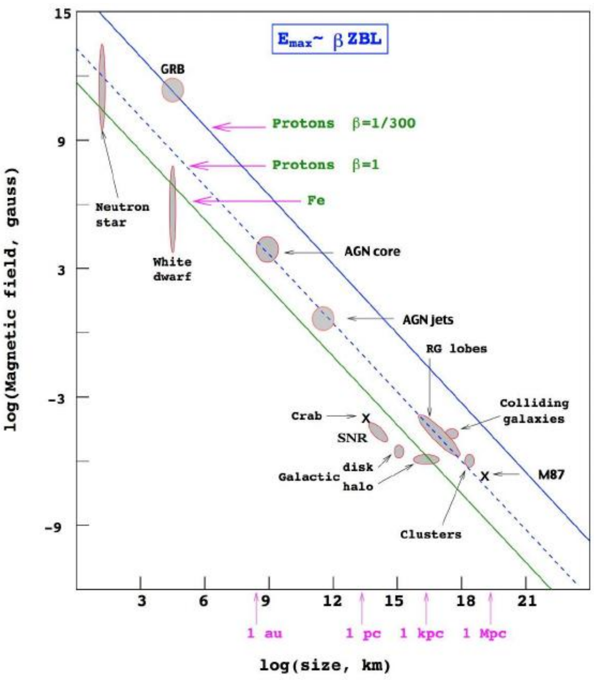

Figure 2.2.1: Hillas plot of potential acceleration sites for UHECR depending on extension and magnetic field strength. [165]

The idea of a statistical process in which a particle encounters multiple interaction with an accelerating medium has firstly been proposed by Enrico Fermi[10]. In the 1970s the idea of shock front acceleration has been developed by a number of groups [34, 35, 65, 158]. It is referred to as the *first order Fermi mechanism*.

In the following derivation, taken from [221, p. 51 - 56], the idea is that a supersonic shock front passes through a medium which contains a magnetic field that is turbulent and highly irregular. Such a scenario can be found in the expanding shell of supernova remnants or in the jets of AGNs. By passing through the medium, the shock accelerates a small part of the gas particles to high energies. It travels with a velocity U dividing the medium into an un-shocked upstream region (ρ_1, v_1, P_1) and a shocked downstream region (ρ_2, v_2, P_2). In this simple approximation, we assume the medium to be an ideal gas with a ratio of specific heats $\Gamma = 5/3$ and neglect radiative losses. We consider the scenario in the limiting case of a shock with a high Mach number $\mathcal{M}_1 \gg 1$ so

$$\frac{v_2}{v_1} = \frac{1}{4} \tag{2.2}$$

applies. Moreover, we demand a conservation of mass flux across the discontinuity

$$\mathcal{F}_{mass} = \rho_1 v_1 = \rho_2 v_2. \tag{2.3}$$

Thus, we get

$$\frac{\rho_2}{\rho_1} = 4. \tag{2.4}$$

And so the velocity of the gas flowing into the shock is $v_1 = U$. When it flows out of the shock $v_2 = U/4$. For the rest frame of the upstream region the downstream region approaches with a speed $v \equiv |v_2 - v_1| = 3U/4$ (Fig. 2.2.2). When a relativistic particle with momentum $p_x = E/c$ dives from the upstream region into the downstream region, it interacts with irregularities of the magnetic field in the downstream region and gains energy

$$E' = E + p_x v. \tag{2.5}$$

For a non-relativistic shock $(\gamma \approx 1)$, we get

$$\frac{\Delta E}{E} = \frac{v}{c}, \quad \text{with} \quad \Delta E = E' - E. \tag{2.6}$$

---

[10] Enrico Fermi, ⋆29 September 1901, Rome, Italy †28 November 1954, Chicago, Illinois, United States; Nobel Prize in Physics in 1938

Now, we look at the same process from the reference frame of the downstream region. The upstream gas flows into the shock at a speed of $v \equiv |v_1 - v_2| = 3U/4$. Thus, the energy gain is the same for a relativistic particle, independent from which side of the shock it traverses the front. Due to the irregularities of the magnetic fields in the vicinity of the shock front. The particle loses its original direction while crossing the front. There is a certain probability that soon after the crossing, it again dives into the other region. The increase in energy is proportional to v/c. This is the reason why it is called the first order Fermi mechanism.

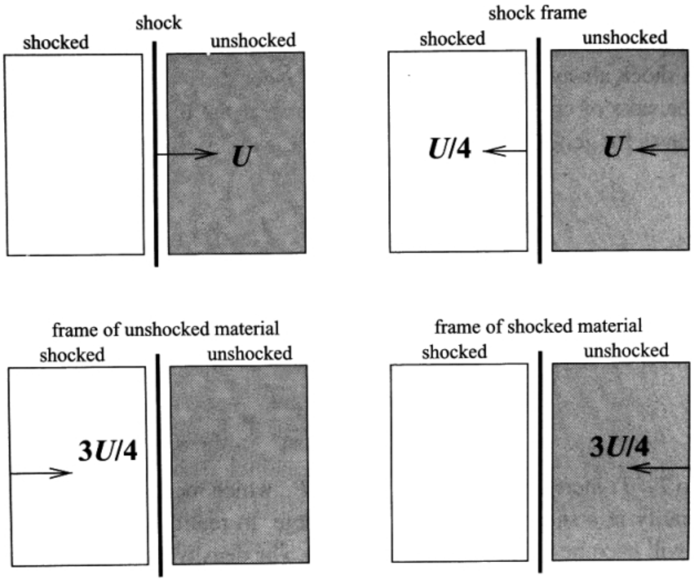

Figure 2.2.2: The dynamics of a particle in the vicinity of a strong shock wave. Upstream- and downstream regions are characterized by variables of state p, T and ρ. Particle flux seen from the reference frame co-moving with the shock front. Taken from [221].

To determine the shape of the resulting energy spectrum, we have to consider how often a particle can traverse the shock front. Each crossing yields an energy gain of a factor $\beta = 1 + v/c$. When a particle with an initial energy E_0 crosses the front j times, it will acquire a total energy of $E = E_0\beta^j$. For one particle, the probability to remain in the region may be $\mathcal{P}$. Thus, after j crossings $N = N_0\mathcal{P}^j$ out of N_0 particles remain in the region. We eliminate j

$$\frac{\log\left(\frac{N}{N_0}\right)}{\log\left(\frac{E}{E_0}\right)} = \frac{\log\mathcal{P}}{\log\beta} \tag{2.7}$$

and get

$$\frac{N}{N_0} = \left(\frac{E}{E_0}\right)^{\log \mathcal{P}/\log\beta}. \tag{2.8}$$

The differential form is

$$n(E) \propto E^{(\log\mathcal{P}/\log\beta)-1} \propto E^{-k} dE, \tag{2.9}$$

defining the power law index as $k = 1 - (\log\mathcal{P}/\log\beta)$. The shape of the emerging spectrum is *non-thermal.*

Now, we want to calculate the probability $\mathcal{P}$. From geometrical considerations we find that the number of particle that cross the shock per area and time, i.e. the flux is $\mathcal{F} = nc/4$, with n being the number density of particles. [see 221, p.54 for details] The advection speed of the particles in the downstream region is $U/4$. Thus, the amount of particles advected outside the accelerator is $(nU/4)/(nc/4) = U/c$. Since $U \ll c$, we can approximate

$$\log\mathcal{P} = \log\left(1 - \frac{U}{c}\right) \approx -\frac{U}{c}. \tag{2.10}$$

For the estimation of β, we consider particles crossing the front with an incident angle θ, gaining an energy

$$\frac{\Delta E}{E} = \frac{v}{c}\cos\theta. \tag{2.11}$$

The amount of penetrating particles between $[\theta, \theta + d\theta]$ is $\propto \sin\theta$. The rate of particles reaching the shock front is $\propto \cos\theta$, since it is proportional to their velocity component parallel to the normal of the shock front. Now, we normalize the energy gain per crossing:

$$\left\langle\frac{\Delta E}{E}\right\rangle = \frac{v}{c}\int_0^{\pi/2} 2\cos^2\theta\sin\theta d\theta = \frac{2}{3}\frac{v}{c}. \tag{2.12}$$

For one round trip, we get

$$\beta = \frac{E}{E_0} = 1 + \frac{4}{3}\frac{v}{c} \tag{2.13}$$

and with $v = 3U/4$

$$\log\beta = \log\left(1 + \frac{U}{c}\right) \approx \frac{U}{c}. \tag{2.14}$$

We obtain a power law index

$$k = 1 - \frac{\log\mathcal{P}}{\log\beta} \approx 2. \tag{2.15}$$

The form of the spectrum appears as $n(E)dE \propto E^{-2}dE$. This is in fact relatively close to what we observe. The index depends on the assumptions we made during the derivation. Thus, depending on the astrophysical model behind, other indices could be obtained.

A whole family of magnetohydrodynamical models has emerged since the first formulation of the Fermi acceleration model. Many of them are far more sophisticated. However, the underlying statistical principles can be regarded as loosely related. We briefly introduce the most prominent models, developed in the recent years.

THE DIP-MODEL, formulated by Aloisio, Berezinsky, Gazizov et al. [19, 46], states an almost pure proton injection spectrum for energies higher than $\sim 10^{18}$ eV [22]. For the lower energies, the composition is believed to be exclusively iron nuclei [43]. The ankle appears in the spectrum as a feature of the pair-production dip. The ingredients are:

- A pure proton composition injected at the acceleration site for extragalactic EHECR;
- The power law index at the source is assumed to be $\gamma_g = 2.7$ [19, 46];
- The transition from the heavy, galactic to the light, extra-galactic component begins at the second knee ($\sim 10^{17}$ eV) [18] and ends at the beginning of the dip ($\sim 10^{18}$ eV) [43];
- The dip between 10^{18} and $5 \cdot 10^{19}$ eV is a signature of pair production losses. This cannot happen, if either the spectral index $\gamma < 2.4$ or a heavy nuclei fraction larger than 15 % is injected at 10^{18} eV [17];
- The cut-off is a feature of the GZK-effect (due to the CMB) [15].

The dip model is favoured by the measured spectra taken by the HiRes and TA experiments — both in the northern hemisphere. The mass composition analysis of the UHE flux of both data sets show indications of a proton dominated spectrum. The total flux predicted by the model shows a very good agreement with the all particle spectrum of many experiments [18], including the KASCADE-Grande measurements [173]. Nevertheless, the PAO mass composition measurements strongly contradict the claims of this model. The PAO data show a clear transition to a heavier component than protons. The reason why the observations differ from other experiments is still subject to discussion.

THE MIXED COMPOSITION MODEL, developed by Allard, Parizot and Olinto [13–15, 89] is based on the following assumptions:

- A flat injection spectrum $\gamma \approx 2.2$ - 2.3 [15] (2.3 is a necessary condition for holistic models in which the same type of source accelerates cosmic rays to all energies);
- A chemical composition at UHE with similar abundances as for lower energy galactic CR (proton dominated with a substantial fraction of heavier nuclei $>$ 30 %) [15];
- A maximum possible energy for protons $E^p_{max} = 10^{20.5}$ eV [15];
- A rigidity dependent acceleration mechanism $E^A_{max} = Z \cdot E^p_{max}$ [15];
- At the ankle (E $< 10^{19}$ eV) a substantial fraction of extra-galactic UHE nuclei in the flux (mixed composition) [17];
- The transition from a galactic to an extragalactic component is expected at $E_{tr} > 3 \cdot 10^{18}$ eV [17];
- The ankle is not explained as a pair production dip but by means of a transition feature [15];
- Extragalactic component are nuclei of various types, transition occurs from iron to lighter nuclei of mixed composition [43];
- Protons dominate the spectrum only for the highest energies E $> 10^{19}$ eV [17], [22];
- The cut-off appears due to nuclear disintegration (by IR, optical, UV photons) [15].

The model nicely reproduces the PAO spectrum. Moreover, it is well in accordance with the PAO mass composition measurements. Although, it contradicts the data of HiRes/TA. According to [17], the model critically depends on the composition at the source, due to many parameters to fit the data. Basic differences to the dip model are the point of transition to extragalactic CR and the composition in energy range 10^{18} – 10^{19} eV.

The Disappointing Model has been developed by Aloisio and Berezinsky, especially to explain the data measured by the PAO [20, 21]. It acknowledges the fact that the mass composition is becoming steadily heavier with increasing energy from 3 EeV to 35 EeV. Basic assumptions of this model are:

- A proton-dominated mass composition at energies between 1 to 3 EeV (This component is thought to be of extragalactic origin. The proton prevalence vanishes for higher energies);
- A substantial ratio of heavier nuclei in the spectrum already at $E > 4 \cdot 10^{18}$ eV [18];
- A flat injection spectrum with $\gamma_g = 2.0$ [18];
- A maximum acceleration energy for protons of E^p_{max} 4-10 EeV [18];
- A rigidity dependent acceleration mechanism $E^A_{max} = Z\, E^p_{max}$ (Z denotes the atomic charge number of the nucleus A. Thus, the mass composition rises with energy) [22];
- The highest energy in the spectrum, reached by iron, does not exceed 100-300 EeV [20];
- A mixed composition at the sources consisting of protons, helium- and iron-nuclei [18];
- The transition from galactic to extragalactic origin is placed at energies around 10^{18} eV [18];
- The observed cut-off is a feature of photo disintegration [21].

The mixed composition has been introduced to match the PAO observations. In this model, the average energy per nucleon is less than 2-4 EeV, therefore certain consequences arise [21]:

1. No pion photo-production on CMB photons;
2. There is no GZK cut-off in the spectrum;
3. No production of cosmogenic neutrinos due to interaction with the CMB;

4. The flux of cosmogenic neutrinos due to the interaction of UHECR with EBL photons is too low to be observed in current experiments (insufficient exposure);

5. Since the charged nuclei are strongly affected by magnetic fields, no correlation with nearby sources is possible.

The model reproduces the PAO data but the total flux does not seem to be in perfect agreement with observations in particular at energies around the transition region with HiRes [18]. Due to the severe consequences of this model for future observations Aloisio and Berezinzky have called it the *disappointing model*. Uncertainties in the model come mostly from the estimate of E^p_{max}. Both the disappointing and the mixed composition model assume homogeneously distributed sources and neglect their cosmological evolution.

2.2.2 POTENTIAL SOURCES

Several proposals for potential acceleration sites for UHECR have been made. The persisting problem is to identify a region in the cosmos, where the conditions in terms of magnetic field strength and extension are met in order to fulfil the scenario described in the Hillas plot (see Fig. 2.2.1) for a sufficient amount of time. There are only a few systems we know of, having an ample potential for this. The most reasonable candidates are briefly introduced in the following.

ACTIVE GALACTIC NUCLEI (AGN) is a unified classification scheme for a wide range of objects such as radio loud, radio quiet, Seyfert 1 and Seyfert 2 galaxies, radio quiet quasars and blazars [186]. Common for all of them is a strong, non-thermal emission from the core of the host galaxy. The different objects are categorised by phenomenological considerations instead of the physical nature of the sources[233] (Fig. 2.2.3).

At the centre of an AGN is a rotating super massive black hole which is accompanied by an accretion disc. This system is surrounded by a dusty torus of gas. From the centre region, a jet of plasma is ejected along the spin axis of the BH. The entire object is surrounded by clouds of gas. (See Fig. 2.2.4) Depending on the viewing angle towards this object different emission regions come into the observers line of sight. Thus, the

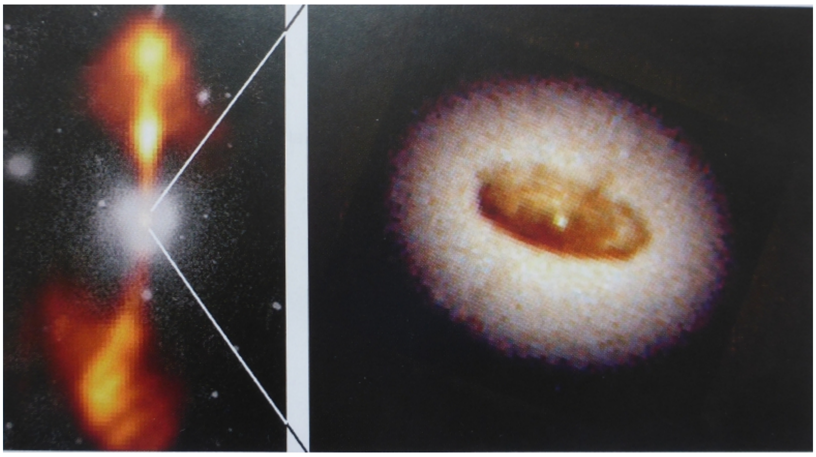

Figure 2.2.3: The elliptical galaxy NGC 4261 (left: picture from ground telescopes, width ~ 88,000 light years) and the close-up of the core (right: picture from the Hubble Space Telescope (HST), width ~ 400 light years) Taken from [233, p. 210].

phenomenology of such an object depends mainly on the orientation of the torus and the jet relative to the observer.

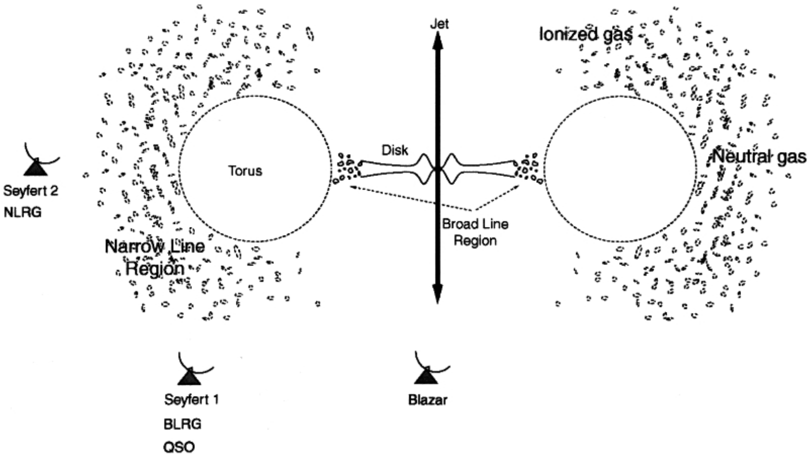

Figure 2.2.4: Sketch of the unified classification scheme of AGNs. Basic components are shown and the different viewing angles under which the various sources appear. Taken from [233, p. 209].

Jets can occur during the accretion of matter from a disc onto a large compact object. A collimated outflow of photons, electrons and positrons is then ejected orthogonal to the plane of the accretion disc and along the rotational axis of the central object. Jets of AGNs are ejected with extreme velocities, having Lorentz factors up to 30 [221, p. 311].

Little is known about the actual consistence of jets. Hypothetically, they consist of an electrically neutral mixture of electrons, positrons, protons and photons. Recently a study of one particular black hole with jets has given strong indications for the presence of a baryonic component [267]. A large fraction of observed AGNs have one or two jets. It is not entirely clear if the scenario of only one jet really exists. This could merely be to the fact that the jet ejected into the direction of the observer appears much brighter than it actually is, due to relativistic Doppler boosting. The same argument might lead to a vanishing opposite jet when the Doppler effect weakens its radiation. This effect can account for a factor 100 in the perception of the brightness [233, p. 212]. Jets of AGNs reach out as far as several hundred or even hundreds of thousands of parsec into the cosmos [269, p. 446]. When jets strike interstellar matter, turbulent shock fronts are created that are moving with the jet at high speeds while slowing it down until it slowly dies out. The jet eventually terminates in huge lobes visible in the radio range. This is a prominent feature for quasars and radio galaxies. Comparable jets can form on smaller scales, in the vicinity of neutron stars or stellar mass black holes, e.g..

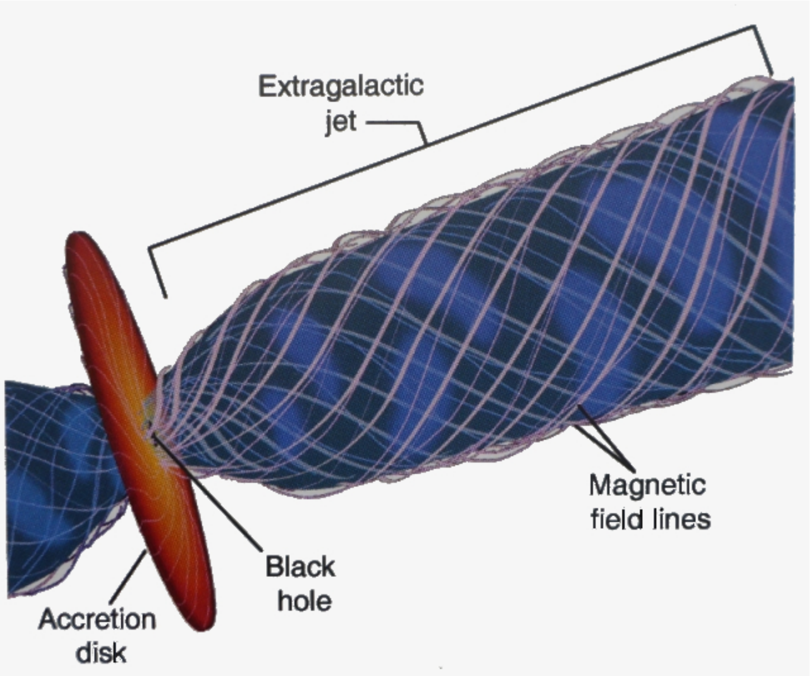

Figure 2.2.5: Illustration of the relativistic jet model. Taken from [233, p. 212].

The creating mechanism of the jet still remains unclear. There is a common agreement that it is somehow powered by accretion and the spinning black hole. Two different kinds of explanations are delivered. Penrose claims that a frame dragging effect spirals up the magnetic field lines. This leads to an extraction of particles and momentum [204]. Blandford and Znajek argue that "energy and angular momentum can be extracted from a rotating black hole by a purely electromagnetic mechanism" [66]. Jets of black holes are identified as sites where the Fermi mechanism could occur [92]. Especially blazars are believed to be candidates [216]. The acceleration of UHECR is thought to happen either inside the jets nearby the central engine (BH) or at the termination, where the jet strikes the ISM.

Gamma-ray bursts (GRBs) are flashes of γ-rays of extreme luminosity and a duration of approximately seconds to a few minutes. It is a non-repeating phenomenon and isotropically distributed in the sky. Due to the very short duration and the unpredictable occurrence, it was impossible from the first accidental discovery by military satellites in the 1960s till the late 1990s to determine their origin. GRBs are followed by an afterglow in the other wavelengths for some hours. By taking advantage of this effect, the satellite BeppoSAX[11] had been able to determine the cosmological origin of GRBs [269].

Light curves of GRBs have a large variety in their temporal structure. Some are single peaked, others show multiple peaks or even a complex and chaotic behaviour. Nevertheless, we can roughly distinguish between two kinds of γ-ray bursts. Short GRBs have a duration of usually below 2 seconds. They account for about one third of all events. The long events usually have a duration of approximately 10 to 20 seconds.

The extremely luminous γ-fluxes during such an event make GRBs the brightest events in the universe since the Big Bang. If they were emitting isotropically, they would have an average energy output of $\sim 10^{53} - 10^{55}$ erg. That corresponds to approximately one solar rest mass — unleashed in a few seconds. Moreover, the luminosity is far above the Eddington limit[12] of $L_{Ed} \approx 10^{38}(M/M_{Sun})$ erg s^{-1}. Hence, there are strong hints that this emission must be anisotropic, supposedly beamed in a cone with an opening angle of a few degrees. Though the amount of energy still would make up $\sim 10^{51}$ erg. This is comparable to a supernova explosion.

---

[11] BeppoSAX: 1996-2002

[12] At the Eddington limit, radiation pressure exceeds gravity. Therefore a system exceeding this limit cannot be stable.

One popular scenario for the creation of GRBs is the so called *fireball model.* It states that the release of this amount of energy is due to an effect caused by dissipation of the kinetic energy when highly relativistically ejected plasma, e.g. in form of a jet strikes the ISM. These jets are required to have a high Lorentz factor of perhaps 100 [186]. Although the initial causation of these events is not fully understood, a widely accepted theory links the physical engine behind to the mergers of two neutron stars[269]. However, large variety of theories have been established until today. Many of them could not be excluded by the observations made so far [186].

Supernova Remnants are the remains of a supernova explosion. It consists of the ejected material of the progenitor star and expands in a shock wave into the interstellar medium. Supernovae are phenomenologically categorized in different branches. Type I do not show any hydrogen lines in their spectrum, whereas type II SN do. [233, p. 48]

SN type II and SN type I b, c are explosions at the final stages of massive (m$\geq 8 \cdot m_{Sun}$) stars. They are core collapse SN. In the lifetime of massive stars, first the hydrogen supply is burned into helium and at a later stage, helium and heavier elements are fused up to iron. Iron is the most stable element in the periodic table. From here on, no more energy can be gained by nuclear fusion. The star collapses under its own gravity. During a the collapse a rebound occurs. A shock front heats up the material of the outer shells and ejects it. After the explosion, a neutron star or black hole remains at the centre of the expanding shell. [233, p. 48]

SN Ia, are thought to be the explosion of a white dwarf star binary system. During its lifetime, the white dwarf slowly captures matter from the larger companion. When the accumulated mass reaches the Chandrasekhar limit [13] of 1.44 solar masses, a thermonuclear explosion, due to the ignition of carbon, is triggered and the system explodes [180]. There are no remains of the white dwarf left. SN I act as *standard candles* in cosmological distance determination, since their conditions are always highly similar and thus their luminosity is about the same order of magnitude [233, p. 49]. It is however, still unclear, whether this scenario can account for type Ia supernovae, since here no hydrogen is detected. The low mass companion in such binary system does contain hydrogen. This brings the so called double-degenerate binaries into focus. They consist of two white dwarf stars orbiting each other. Unfortunately, the occurrence of such kind of system is not enough to statistically explain the amount of SN type Ia.

---

[13] Chandrasekhar limit: is the theoretical upper boundary for the mass of a white dwarf.

They could only account for about one tenth [180, p. 407].

The initial expansion velocities of SN are of the order of 10^4 km s^{-1} into the ISM [269, p. 358]. During the expansion the shock-front sweeps up material of the ISM. Gradual decelerations of the expanding shell begins, once its density clearly exceeds the density of the ISM [241, p. 61]. After 200 years with a radius of about 2 pc, the expanding shell becomes gradually slower with velocities of approximately 100 km s^{-1} and radii up to 30 pc. The shells eventually dissolves with a diameter of about 100 pc, when the speed is about the speed of the movements of the surrounding ISM of 10 km s^{-1}. The total lifetime of a remnant is approximately 10^6 years. The collision of the expanding hull with the ISM generates high temperatures. Thus, the thermal radiation is mainly emitted in the X-ray range, but also in radio and optical wavelengths [269, p. 358]. (See Fig. 2.2.6)

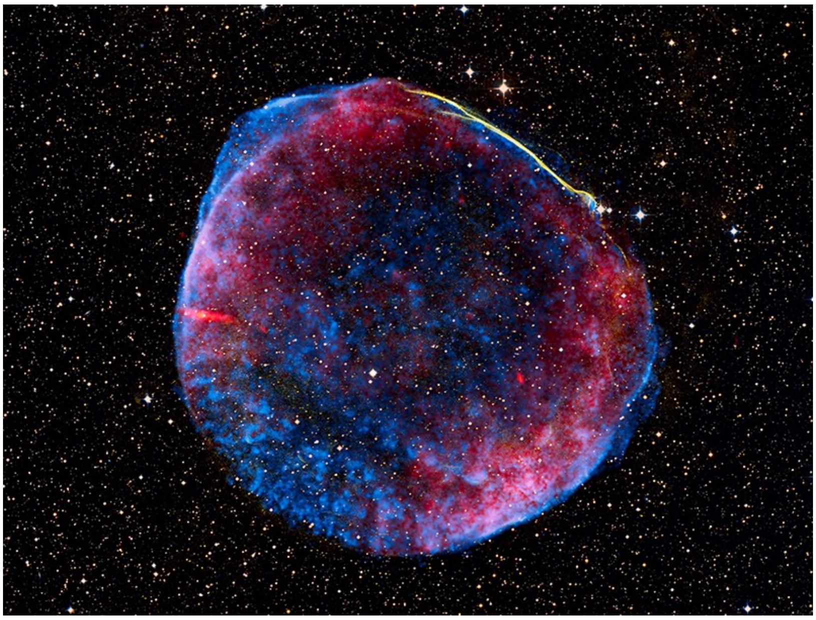

Figure 2.2.6: Supernova Remnant SN 1006. The expanding shell emits across the electromagnetic spectrum. Composite view of X-ray data in blue, optical data in yellow, and radio image data in red. The remnant has a diameter of about 60 light years and is likely to represent the remains of a type Ia event. Taken from [168].

A few younger SNR, have a central pulsar - a remain of the exploding progenitor star. The quickly rotating neutron-star is responsible for most of the radiation emitted by the entire SNR. These remnants are called *Pulsar Wind Nebulae* (PWN).

SNRs are attractive candidates for potential acceleration sites of cosmic rays. When the expansion of the shell slows down, a part of its kinetic energy is transferred to cosmic rays [241]. They bear important ingredients. A sufficient lifetime, strong magnetic fields and turbulent shock fronts. However, it is widely agreed that SNR are only capable of accelerating UHECR up to maximum energies of about 10^{15} eV. Nevertheless, SNR are considered as the most attractive candidate for the acceleration of galactic cosmic rays. “If only 5 % to 10 % of the kinetic energy of supernova remnants is converted to accelerated cosmic rays this would provide the energy of all galactic cosmic rays.” [165, and references therein].

Neutron Stars and Magnetars are compact objects with diameters of about 10 km. Their mass is of the order of 1.4 to 3.2 solar masses. Generally, compact objects of less than 1.44 solar masses are white dwarfs. Objects heavier than 2-3 solar masses could become quark stars or black holes. Further collapse to a black hole is prevented because of quantum degeneracy pressure due to the Pauli exclusion principle[14]. The average density of a NS can be estimated as roughly $3.7 \cdot 10^{17}$ to $5.9 \cdot 10^{17}$ kg/m^3. However, at the surface the density is less and increases below the crust, where it can even exceed the density of atomic nuclei. Little is know about the state of the matter in the interior of the neutron star (NS). Possibilities of a liquid core of super fluid quark matter are discussed. The surface temperature of NS is of the order of $6 \cdot 10^5$ K. Their magnetic field can reach up to 10^8 Tesla. [221, p. 185]

NS are formed during the collapse of a star formed in a supernova type I b, c or type II event. Because of the conservation of its angular momentum in the collapse, where the radius of the star shrinks from thousands of kilometres to a small fraction, the resulting NS rotates extremely fast. The rotation periods lie between milliseconds to a few ten seconds. [221, p. 164] Quickly rotating NS can emit electromagnetic radiation on form of collimated jets along the spin axis. They appear as quasars. The same arguments as for the spin period applies to the magnetic field lines. If the progenitor star had had a magnetic field of the order of 10^{-4} Tesla, during the collapse, the field lines are compressed in such a way that the resulting NS would have a field strength of approximately 10^6 Tesla. [269, p. 274]

Magnetars are distinguished from ordinary neutron stars by even stronger magnetic fields and slower rotations. The rotation period of a magnetar is about several seconds. Their magnetic field strength is considerably larger and reaches 10^{11} Tesla [269, p. 279].

---

[14] Pauli exclusion principle: no two fermions can occupy the same quantum state in the same location simultaneously

It causes very strong and characteristic bursts of X-rays and γ-rays. However, the strong field decays after approximately 10,000 years. Therefore, its activity and the intense X-ray emission vanishes.

The genesis of a magnetar basically takes place in analogy other NS. Although, in this particular case, a magnetohydrodynamical effect occurs. When rotation, magnetic field and temperature of the proto-neutron-star stage are within the right ranges, a massive dynamo mechanism could convert the energy from the heat and rotation into an even stronger magnetic field. Prerequisite for this special type of NS is therefore a rapid rotation of the core of the progenitor star. [214]

The question on the origin of cosmic rays is now one century old. For most parts of the spectrum, convincing explanations have been widely agreed upon. Nevertheless, the higher the energy gets, the more mysterious potential sources become. From theoretical considerations we can estimate what it takes to speed up the particles to the energies we measure. But finding an object that could account for magnetic fields of the order we need, plus sufficient extension and lifetime is a puzzling task. From the experimental point of view, tracking down the sources of particles with energies up to 10^{20} eV is afflicted with high uncertainties. Below this energy the particle's trajectory is strongly affected by galactic and intergalactic magnetic fields in a way that its arrival direction does not point back to the emitter. Despite of that, we can still search for *smoking guns* by means of secondary effects such as γ-ray detection. While interacting with interstellar material, UHE protons produce neutral pions. These pions decay into gamma rays. By searching for the characteristic neutral pion decay signature we can therefore test the hypothesis of high energy proton acceleration in SNRs [6]. This has proven to be successful. However, these tests only confirm acceleration up to some hundred Gev [91].

Active galactic nuclei and gamma ray bursts are perhaps the most attractive candidates [41]. In principle, GRBs have the potential to act as acceleration sites, even up to the highest energies observed so far. Problematic however is the scarcity of events within the GZK radius [91, and references therein]. A more fruitful candidate are AGNs and especially jets of AGNs. Within jets of AGNs, multiple shock fronts are traversing each other and provide a perfect scenario for drift acceleration of UHECR. They remain the most popular candidates for good reason. However, still the question of E_{max} is an open issue.

2.2.3 Top-Down Scenarios

Top-down model is a common name for theories with the approach to explain UHECR by means of a decay of even more energetic entities (X-particles). This approach was mainly but not only inspired to account for the data measured by the AGASA (Akeno Giant Air Shower Array) experiment. These results show a remarkably strong trans-GZK flux, significantly higher than what would have been expected from theoretical predictions. Moreover, those events could not be correlated to any nearby source. They appeared to be rather isotropically distributed on large scales, even though some doublets and one triplet had been identified [178, 252]. Today, the shape of the UHECR spectrum is far less disputed than at the time of the HiRes/AGASA debate. However, still nearly all bottom-up scenarios as shown above, have either intricacies to account for the measured maximum energies or yield unsatisfactory predictions of the fluxes or spectra [45]. The top-down scenario elegantly avoids the acceleration issue. It can roughly be subdivided into two kinds of theories, the decay of super-heavy dark matter (SHDM) or topological defects (TD). The notion of topological defects draw further motivation from predictions of the Grand Unified Theories (GUT). The SHDM scenario is further motivated by dark matter search, since is would be an attractive candidate. Both ideas require physics beyond the standard model (SM) of particle physics.

Topological Defects (TDs) are meta-stable configurations of matter beyond the SM of particle physics. They are are non-trivial configurations of the classical fields. Many GUTs allow topological defects to have been formed during the symmetry breaking phase in the early universe. There could exist

- magnetic monopoles (0-dimensional, have magnetic charge, either north or south and large gravitational fields [27]),
- cosmic strings (one-dimensional lines with length of cosmological distances),
- domain walls (two-dimensional fabrics, dividing the universe into discrete cells),
- TDs with higher dimensions,
- or configurations consisting of more complex hybrids such as cosmic necklaces (systems of monopoles connected to two strings each) [44]

The X-particles needed to explain UHECR are the super-heavy gauge bosons of the underlying spontaneously broken gauge theory with masses of the GUT-scale ($m_X \approx 10^{25}$

eV). Even though X-particles would have a very short lifetime, trapped within TDs they were prevented from decaying. When TDs collapse or annihilate, X-particles are released and decay [164]. A very appealing candidate for the production of UHECR are cosmic necklaces and magnetic monopole-antimonopole pairs. Berezinsky has identified them "as most plausible sources, which can provide the observed flux and spectrum" [40]. The GZK-feature should however be less pronounced than in the bottom-up approach due to the dominance of photons [140].

Super-Heavy Dark Matter (SHDM) are hypothetical particles that might have been produced shortly after the Big Bang. Cosmic rays of the highest energies we observe can be understood as a decay product of even more energetic particles with energies exceeding 10^{21} eV. In order to observe the decay products now, these relic particles are required to have lifetimes comparable to the age of the universe [164, p. 286]. They are regarded as a part of the predicted cold dark matter component and as such expected to enrich gravitationally in the galactic halo. This lies well within the GZK horizon. Therefore, neither would we expect to observe a cut-off, nor should we observe a clear galactic isotropy. Furthermore, according to the decay models, the composition would strongly favour neutrinos and photons over nuclei [140].

Since the heyday of top-down theories a reasonable amount of data has been taken by the current UHECR experiments. It is clear that the shape of the AGASA spectrum for the highest energies cannot be maintained any longer. Therefore, strong constraints apply on the top-down models, rejecting most of them. The same argument applies to the composition at the end of the spectrum. Even though, it is not clear whether protons or heavier elements dominate, certainly no photons or neutrinos are detected in an abundance to account for the top-down scenario. Additionally, no topological defect has been observed so far. As Olinto remarks in [197]:

> "Top-down models may still contribute at some level, but are not the dominant source of UHECRs"

Especially due to the data collected by the Pierre Auger Observatory, SHDM theories can be excluded because of the missing photonic component. The same applies to TD models, at least for the regime below 10^{20}eV. Some TD models might still contribute above this energy. The vital test to discriminate the remaining top-down scenarios from the bottom-up is going to be conducted by means of UHE neutrino search [236].

2.3 UHE-Neutrinos

In order to satisfy the laws of conservation of energy and momentum for the beta decay, Pauli[15] postulated a missing, neutral, third particle in 1930. Later it was named neutrino (small neutron) by Fermi. However, it took until 1956 to verify the existence of the neutrino experimentally.

In the scope of cosmic ray research, UHE neutrinos play an important role to discriminate UHECR production theories. In 1969, Beresinsky and Zatsepin first proposed the existence of UHE-ν soon after the prediction of the GZK cut-off for protons [39]. By using the observed flux of UHECR on earth, reliable estimations of the cosmogenic neutrino fluxes according to the different bottom-up models can be numerically computed. (See Fig. 2.3.1) Models for these flux calculations are based on basically three major factors. First, the observed UHECR flux is a vital parameter. Second, assumptions on the cosmological evolution of the sources have an impact on the estimates. Third, the maximum energy of acceleration of the source E_{source}^{max} imposes a strong limit [42]. A major factor, introducing uncertainties in the predictions of neutrino fluxes, is the current uncertainty about the UHECR composition for the high energy end of the spectrum. If these events are protons, a lower limit is imposed on the cosmogenic neutrino flux. The upper limit of the UHE-ν energy is imposed by the maximum achievable energy of the bottom-up source $\mathrm{E}_{source}^{max} \approx 10^{21} - 10^{22}$ eV. E_ν cannot exceed the maximum energy $\mathrm{E}_{source}^{max}$. Upper limits for the expected ν-flux were first proposed by Waxman and Bahcall in 1999 [272]. Only two years later, Mannheim placed a new upper limit using more sophisticated calculations [176].

In both scenarios, bottom-up and top-down, UHECR neutrinos with $E_\nu > 10^{17}$eV are produced. In the bottom-up case, cosmogenic neutrinos are produced due to interaction of UHECR with the cosmic microwave background (CMB). In the top-down case UHECR neutrinos are naturally created as decay products of the X-particles. For the top-down scenarios, the maximum E_ν lies some orders of magnitude higher. Therefore, E_ν^{max} serves as a signature to discriminate these two scenarios from another [42].

In general, neutrinos are perfect messengers, since their trajectories are not disturbed by galactic and extra-galactic magnetic fields. So neutrinos could pinpoint the direction of their production site. However, neutrinos with $E_\nu > 10^{12} - 10^{13}$ eV will interact with

---

[15] Wolfgang Ernst Pauli, ⋆25 April 1900 in Vienna, Austria, †15 December 1958 in Zürich, Switzerland; Nobel Prize in Physics in 1945

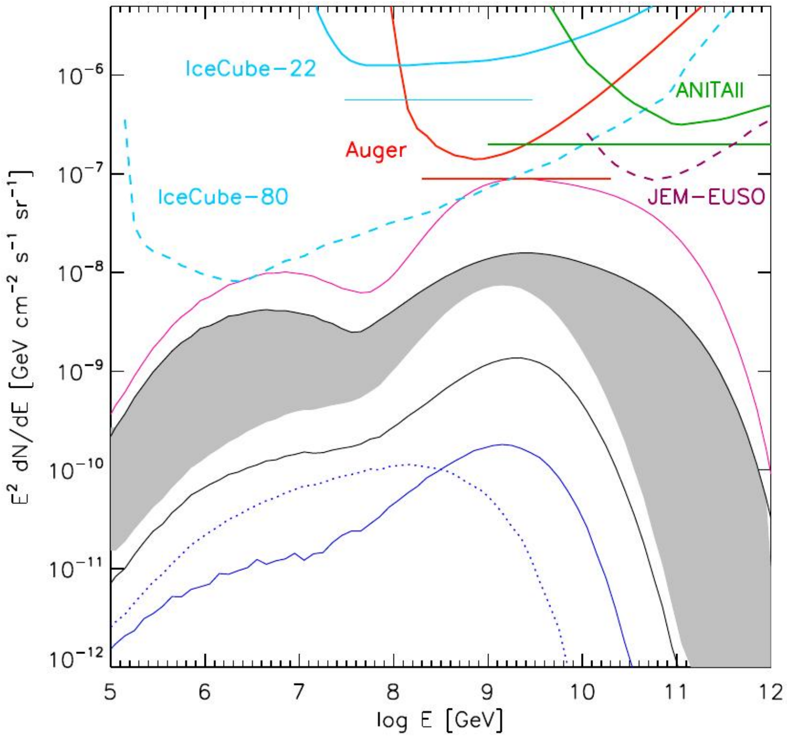

Figure 2.3.1: Cosmogenic neutrino flux for all flavours, for different UHECR parameters compared to instrument sensitivities. Pink solid line corresponds to a strong source evolution case with a pure proton composition, dip transition model, and $E_{max} = 3$ ZeV. Blue lines correspond to uniform source evolution with: iron rich (30%) composition and $E_{Z,max} < Z$ 10 EeV (dotted line) and pure iron injection and $E_{Z,max} = Z$ 100 EeV (solid). Grey shaded range brackets dip and ankle transition models, with evolution of star formation history for $z < 4$, pure proton and mixed 'Galactic' compositions, and large proton $E_{max}(> 100$ EeV)). Including the uniform source evolution would broaden the shaded area down to the black solid line. Current experimental limits (solid lines) assume 90% confidence level and full mixing neutrino oscillation. The differential limit and the integral flux limit on a pure E^{-2} spectrum (straight line) are presented for IceCube 22 lines (pale blue), ANITA-II (green) and Auger South (red). For future instruments, we present the projected instrument sensitivities (dashed lines) for IceCube 80 lines (pale blue), and for JEM-EUSO (purple). Plot and caption taken from [156, 165].

the CMB relic photons. First they create electron positron pairs via pair production. Then, the high-energy electrons up-scatter the γs of the CMB or radio background due to inverse Compton scattering. This triggers electromagnetic cascades. Therefore, the ν horizon is effectively limited to some Mpc for 100 TeV ν. [156, and references therein] Nevertheless, for energies above 10^{18} eV, the universe becomes ν-transparent, opening the possibilities for UHE-ν-astronomy. Unfortunately, due to the very low cross-sections of neutrinos, detection on earth is a difficult task. Several experiments have been taken data for many years. A more comprehensive description, summarizing the most important of them can be found in [64]. Important and very large ν experiments are IceCube and ANTARES [234]. But also the Auger Observatory is searching for UHE-νs [193]. However, none of them has reached a ν sensitivity sufficient to probe the region in which the proposed ν limits are predicted.

Recently, the Ice Cube experiment has detected the highest energetic cosmogenic ν ever observed. The Ice Cube Collaboration has reported on two PeV-events named Ernie and Bert [1] that have been correlated to AGN cores [243].

2.4 UHE-Photons

Like in the case of ultra-high energy neutrinos, the search for UHE-photons is crucial for our understanding of the origin of UHECR. The determination of the UHE-γ spectrum can potentially reveal the nature of the UHECR production. In the bottom-up scenario, UHE-γ are produced during the GZK-effect. These secondary photons arrive to the earth undistorted by galactic or extra-galactic magnetic fields. Hence, UHE-γ carry valuable information about the direction of the potential production site. Several models exists, predicting the flux of UHE-γ depending on the assumption of the primary. Whether these are protons or heavier nuclei. Again, E^{max}_{source} plays an important role as well as the opacity of the medium of the acceleration site. These models impose a limit on the UHE-γ flux.

In contrast to that, the top-down models again predict a much higher UHE-γ ratio. Due to the decay process of the X-particles, about 90 % of the produced particles consist of neutrinos and photons. Depending on the type of X-particle, the UHE-γ fluxes are characteristic and allow for a discrimination between the different models.

The technique behind UHE-γ detection is the same as for UHECR. When UHE-γ strike the earths atmosphere, they create avalanches of secondary particle. The EAS

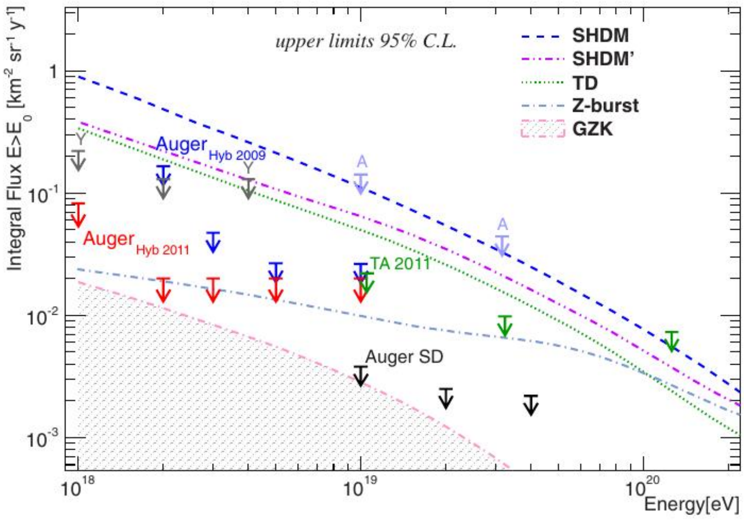

Figure 2.4.1: Upper limits on the integral photon flux by the Pierre Auger Observatory (hybrid and surface detector, only) plotted with other experiments i.e. AGASA, Yakutsk and TA. The dashed lines show the predictions for GZK and "top-down" models: super-heavy dark matter, topological defects and Z-bursts. Taken from [232, and references therein].

can be observed by fluorescence telescopes or ground detectors. However, an UHE-γ shower behaves differently from a UHECR induced EAS. Two effects make the detection of UHE-γ induced air showers especially challenging. Both effects lead to a phenomenological diversity of these showers, making it difficult to reconstruct the properties of the primary in an unequivocal manner. The Landau, Pomeranchuk and Migdal (LPM) effect suppresses the electromagnetic cross-section at energies $E > 10^{19}$ eV. Therefore, the first interaction is delayed (see Chap. 2.6.3). Hence, the EAS is far less developed when reaching the sea level. A second effect is the $e^{\pm}$ pair production because of photon interaction with the geomagnetic field. Secondary electrons produce γ rays by synchrotron radiation. These in turn, trigger an electromagnetic cascade in the earth's magnetic field. The pair production effect depends on two parameters, E_{γ}^{2} and the perpendicular component of the magnetic filed lines. Thus, additionally to the zenith angle, there is an azimuthal dependency of the γ incoming direction. These effects are imposing serious uncertainties on the determination of the primary [223].

Currently, the large UHECR experiments are therefore monitoring the sky for UHE-γ signatures [156]. However, in the EHE regime no detection of γ has been claimed so far by any of the current experiments. This lack of EHE-γs imposes severe constraints

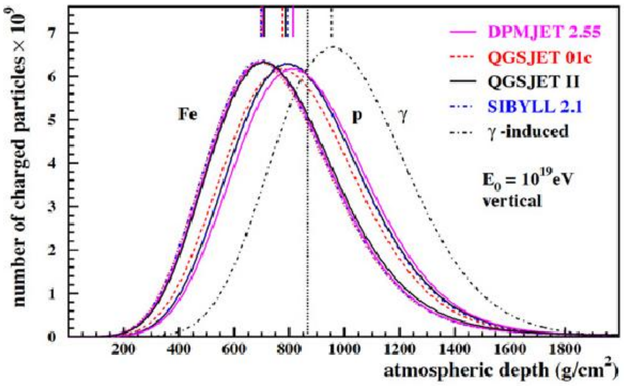

Figure 2.4.2: The average longitudinal profile for Monte Carlo showers induced by photon and nuclear primaries differ significantly. Plot for different hadronic interaction models. Taken from [232].

on the top-down models. Nonetheless, given the exposures of the current experiments, the existence of EHE-γs can certainly not be ruled out.

2.5 Propagation in Space

While propagating from their production site to earth, UHECR are affected by extragalactic and galactic magnetic fields which alter their trajectory. Moreover, UHECR are subject to interaction with the cosmic backgrounds. Hence, the flux suffers from attenuation and secondary particles such as neutrinos and photons are produced.

2.5.1 GZK and Photo Disintegration

In 1966, shortly after the discovery of the 2.73 K cosmic microwave background radiation by Penzias and Wilson [205], Greisen [120] and independently Zatsepin and Kuz'min[279] predicted an interaction of UHE-protons with the relic photons of the cosmic microwave background. This effect is called the GZK-effect. According to this theory, from the threshold of $E \approx 6 \cdot 10^{19}$ eV on, the UHE-proton and the γ_{CMB} will interact via a delta-resonance and create eventually 3 neutrinos with 5 % of the initial proton's energy in one third of the cases. In another two thirds of the cases, two photons with an energy of about 10 % are produced. [23] This mechanism carries away most of the original energy of the proton an therefore limits the horizon of protons above the threshold to about 100 Mpc. There are three possible decay channels [172,

p. 532]:

$$\gamma_{CMB} + p_{UHE} \rightarrow \Delta^{+} \rightarrow n + \pi^{+} \tag{2.16}$$

$$\gamma_{CMB} + p_{UHE} \rightarrow \Delta^{+} \rightarrow p + \pi^{\circ} \rightarrow p + \gamma + \gamma \tag{2.17}$$

$$\gamma_{CMB} + p_{UHE} \rightarrow \Delta^{+} \rightarrow p + N\pi \tag{2.18}$$

Geisen, Zatsepin and Kuz'min predicted a suppression of the cosmic ray flux above the energy threshold of $E \approx 6 \cdot 10^{19}$ eV. Indeed, a strong attenuation of the UHECR flux has been confirmed in the majority of experimental setups. However, it is remarkable that a distinct amount of trans-GZK events, significantly exceeding the threshold energy, has been measured. The reason for that is not clear. Furthermore, the fact that up to now no UHE-neutrino or photon has been recorded raises additional concerns about the predicted GZK cut-off. Alternative ideas to explain the observed spectral feature have been proposed. For instance, an effective maximum acceleration energy E_{max} of the cosmic accelerators is under discussion.

PHOTO DISINTEGRATION OF NUCLEI heavier than protons can be induced due to interaction with the CMB photons — comparable to the GZK-effect. Furthermore, they can interact with infrared (IR), visible light and ultraviolet photons of the extragalactic background light (EBL) [244]

$$A + \gamma_{CMB,EBL} \rightarrow (A - nN) + nN \tag{2.19}$$

[18, 22, and references therein]. Essentially, four processes are responsible [13, 15]:

1. The giant dipole resonance (GDR) is the main contributor, due to a relatively low energy threshold of $E^{\gamma}_{thresh} \approx 8$ MeV. The nucleus looses one or more nucleons or alpha-particles.

2. Quasi-deuteron processes (QDP): At photon energies of $E^{\gamma}_{thresh} = 20 - 150$ MeV. A virtual pion interacts with a nucleon pair within the nucleus. The pair is consequently ejected.

3. Baryonic resonances (BR): At $E^{\gamma}_{thresh} > 150$ MeV, a pion interacts with a nucleon which is thrusted out. While being ejected, it interacts with more nucleons and ejects them as well. For iron, such a process emits 6 nucleons on average.

4. Photo-fragmentation (PF): Together with the BR, the PF contributes at highest energies. At $E^{\gamma}_{thresh} \sim$ GeV a nucleus breaks into many fragments when hit by a γ.

The photo-erosion of nuclei alters the chemical composition of the injected UHECR flux (Fig. 2.5.1). Thus, the effect can serve as a probe for extragalactic and galactic B-fields.

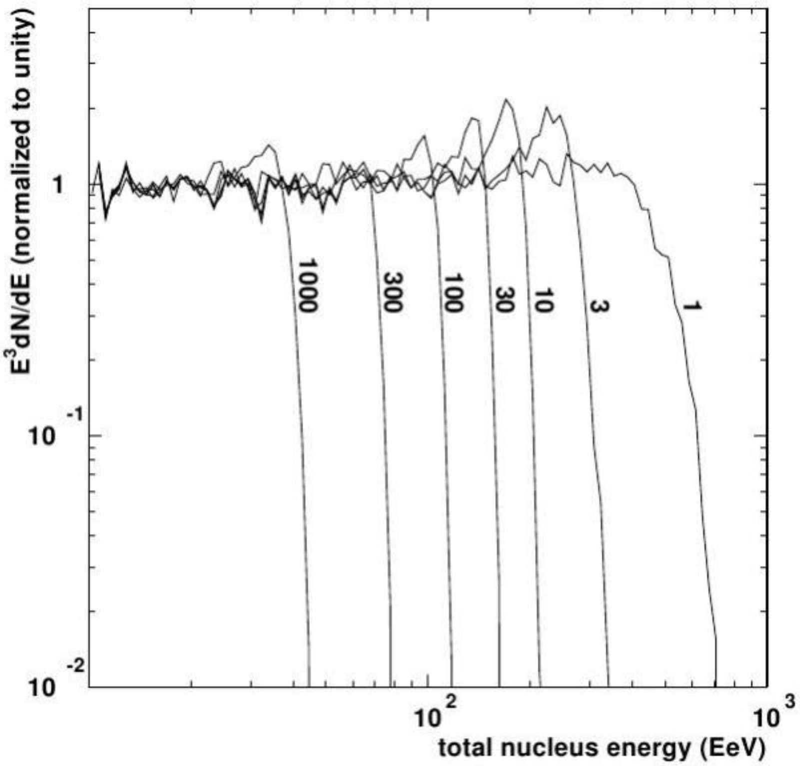

Figure 2.5.1: Differential spectra of UHCR that were emitted as ^{56}Fe nuclei after propagation. The distance is indicated for each curve in Mpc. The source spectrum is assumed to be a power law, $N(E) \propto E^{-3}$, over the interval 10 – 1000 EeV. Taken from [244].

2.5.2 Pair Production

UHE-γ with energies of the order of 10^{19} eV propagating through the ISM experience an effective energy loss on length scales such as 10 Mpc. The interaction is mainly driven by pair production

$$\gamma_{UHE} + \gamma_{EBL} \longrightarrow e^{+} + e^{-} \tag{2.20}$$

and the inverse Compton process

$$e^{\pm} + \gamma_{EBL} \longrightarrow e^{\pm} + \gamma. \tag{2.21}$$

The UHE-γ decay into electron/positron pairs, because of photon interaction with the extra-galactic magnetic field. These secondaries produce γ rays by inverse Compton process and synchrotron radiation at a later stage. This mechanism leads to an effective dilution of the UHE-γ flux. The evolving electromagnetic cascades bring down the energy to GeV or Tev region. For the multi-messenger approach, this means that due to the different cross-sections of the different particle types, the UHE-gammas are carriers of information about the local universe, whereas UHE-neutrinos serve as probes for the cosmological distances. However, also the down-cascaded GeV photons can serve as an indirect secondary messenger [23].

A significant feature of the UHECR spectrum is the dip between 10^{18} to $5 \cdot 10^{19}$ eV, right before the GZK cut-off (Fig. 2.5.2). According to the dip-model, this is an effect

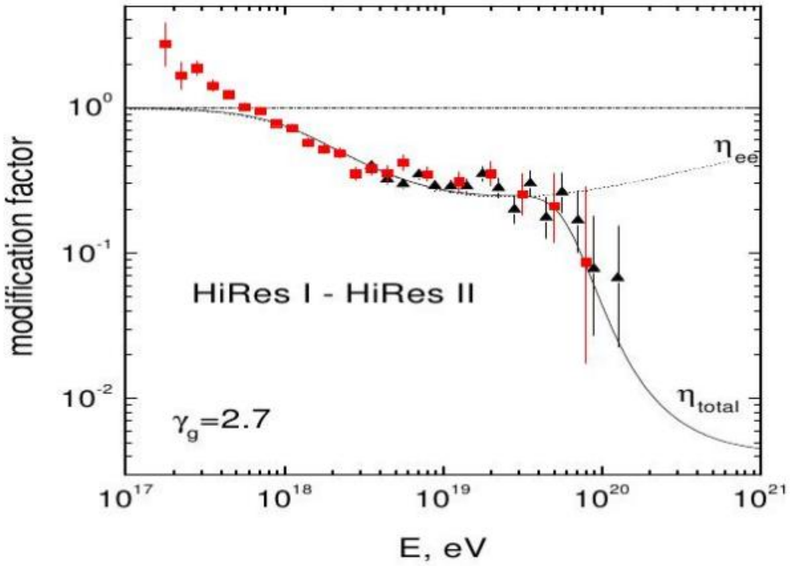

Figure 2.5.2: Pair-production dip and GZK cutoff in terms of modification factor in comparison with the HiRes observational data (HiRes 2 monocular - boxes, HiRes 1 monocular - triangles). Curves η_{tot} and η_{ee} show the total spectrum and the spectrum calculated with only adiabatic and pair-production energy losses included, respectively. Fig. and caption taken from [20, and references therein].

caused by pair production by protons (PPP) [43]

$$p^+ \gamma_{CMB} \rightarrow p^+ e^+ e^- . \tag{2.22}$$

This claim is supported by data of the HiRes and the KASKADE-Grande measurements [20, 253]. However, in other experiments the feature cannot be seen as clearly. If the particles at these energies are heavier nuclei instead of protons the PPP process is certainly not the reason for the feature observed.

2.5.3 Magnetic Fields

Since UHECR are predominantly charged particles, their trajectories are influenced by the various magnetic fields traversed. For the feasibility of the UHECR source determination, it is therefore of vital importance to estimate the impact of those fields on their propagation to earth. Hence, any kind of future UHECR astronomy therefore depends on our understanding of the magnetic field behaviour. We can distinguish between a number of different magnetic field scenarios:

1. Source and its environment: It is an essential factor for the understanding of the UHECR production. Despite of its role in the acceleration process, it does not affect the trajectory of the particles after ejection into the ISM;

2. Intergalactic magnetic field (IGMF): It is regarded as potentially very influential. Nonetheless, its strength and distribution is largely unknown;

3. Magnetic field of the galactic halo: Is a part of the galactic magnetic field (GMF) and plays a vital role for our understanding of the origin;

4. Magnetic field of the galactic disc: Being also a part of the GMF which can confine particles up to very high energies;

5. Magnetic field of the heliosphere: Compared to the two latter contributions it is a small scale field and could only be responsible for small deflections. Therefore, it can be neglected in our estimates;

6. The magnetosphere of the earth: Being also a small scale field, it can be neglected for our estimates of the UHECR trajectory. Nevertheless, it plays a role for the air shower development.

From these considerations it is apparent that in our understanding of the UHECR propagation the two major contributions come from the IGMF and the GMF.

THE GALACTIC MAGNETIC FIELD is difficult to be observed, due to our position inside our galaxy [254]. The overall picture we have gained so far is only reliable within 2-3 pc. The current methods for magnetic field strength measurement are the observation of the Zeeman splitting of radio and maser lines. Also Faraday rotation measurements from pulsars and extragalactic sources serve as indicators. The GMF is far from being homogeneous. It consists of regular and turbulent components [113], such as random local inhomogeneities of unclear origin. Even the symmetry of the GMF is unclear. Thus, the model of the local volume we have cannot be imposed on the entire galaxy. By observation of other spiral galaxies we can try to find a model for our own. Such a model would allow for a parametrization of the GMF. We could then trace back the trajectory of the UHECR.

The assumptions on the galactic magnetic field are varying. For a field strength of the order of some μG, the gyro-radii of UHECR with energies below 10^{18} eV would be much smaller than the thickness of the galactic disc. Therefore, they would be effectively confined. This is the main reason why the sources of these particles are thought to be within our galaxy. For energies exceeding 10^{19} eV, protons have gyro-radii at minimum 5 times larger than the thickness of the galactic disc. Thus, they are not confined to the plane of the galaxy. The highest energy cosmic rays with $E \approx 10^{20}$ are barely deflected by the galactic magnetic field. Hence, their trajectories must remain almost unaffected. For protons with $E = 1 \cdot 10^{20}$ eV, the intrinsic error is less than 1°, for instance. Since the UHECR measured on earth so far do not come from the galactic

Rigidity, R (V)	Gyro-radius of a proton	Gyro-radius of an iron nucleus
10^{15}	0.36 pc	0.014 pc
10^{17}	36 pc	1.4 pc
10^{19}	3.6 kpc	140 pc
10^{21}	360 kpc	14 kpc

Table 2.5.1: Radii of curvature of cosmic ray protons and iron nuclei in a magnetic field with the flux density $3 \cdot 10^{-6}$G. For ultra-relativistic energies, the rest mass of the particle becomes negligible. Thus, the rigidity of a proton in volts is the same as its energy in electron-volts. Data taken from [172, p. 530].

centre, but even show arrival direction from high latitudes, we can conclude an extragalactic origin of these particles [172, p. 530]. However, this behaviour depends on the charge of the primary. Iron will suffer very large deflections, even at energies $2.5 \cdot 10^{20}$ eV, e.g.. This effect could produce multiple images from the same source. It is called magnetic lensing. It could occur frequently and complicate the search for individual sources.

INTER-GALACTIC MAGNETIC FIELD estimates are extremely difficult to obtain. The universe is homogeneous and isotropic on large scales. Within the GZK cut-off though, the matter is inhomogeneously distributed. This can be seen by the distribution of luminous matter. In the local universe, we observe superclusters, walls, filaments and voids. Their coordinates are well known. And so is supposedly the distribution of UHECR sources. We know that magnetic fields are widespread in the universe due to synchrotron emission and multi-wavelength radio polarization measurements. But we do not yet know the overall large scale structure of the field. Available limits depend on the model we assume. We can imagine two extreme scenarios:

If the field had a laminar structure, it would be confined to the regions of high density such as filaments, walls and clusters. The voids in turn would feature fields of negligible strength. The upper limit of the resulting fields within the high density regions could range from 0.1 to 1 μG though. This would be comparable to the GMF values of the interstellar medium [254].

If the field had a cellular-structure, the space would be divided into neighbouring cells. The magnetic field inside each cell would be uniform, but randomly oriented. Also low density regions like voids would be pervaded by a weak magnetic field. The IGMF could be characterized by small changes of the field between 10^{-10}G inside the voids to $10^{-9} - 10^{-8}$G inside walls and filaments. The highest field strengths could appear within or nearby clusters of galaxies by approximately $0.1 - 1$ μG. [254]

Unfortunately, due to the limited observations available, we cannot distinguish between these two models. We must therefore take them as upper and lower boundaries for our assumptions on the overall magnetic field strength of the IGMF. But they are only poorly constraining the expectations. Hence, the range for deflections of UHECR reaches from negligible to many degrees, even for 10^{20} eV protons [113]. The laminar scenario would mark the worst case for UHECR observations. Any interpretation of the angular data would become extremely complicated and biassed by strong systematics. The identification of individual sources would become utterly challenging [254].

On the contrary, in the cellular scenario, gyro-radii of 100 EeV protons reach the size of the GZK sphere. We can take the field strength by 10^{-11} Gauss and apply a random walk propagation scenario [254, 273]

$$\theta(d, E) \approx 0.025^{\circ} \left(\frac{d}{\lambda}\right)^{\frac{1}{2}} \left(\frac{\lambda}{10 Mpc}\right) \left(\frac{B}{10^{-11} G}\right) \left(\frac{E}{10^{20} eV}\right). \tag{2.23}$$

Here, d denotes the distance to the source, λ is the coherence length and B the magnetic field strength [254]. In this case, only small particle deflections occur. Hence, this scenario would allow for an easy identification of the sources and therefore provide excellent conditions for UHECR astronomy.

Both, the galactic and the inter-galactic magnetic field can potentially strongly affect UHECR trajectories. Certainly, the sciences of UHECR physics and cosmic magnetic fields are closely interlinked and can hardly be disentangled. In order to increase our knowledge on UHECR, we have to gain a better understanding of the cosmic magnetic fields and vice versa.

2.6 INTERACTION IN ATMOSPHERE

When UHECR reach the earth, they most likely interact with our atmosphere by striking air molecules. The probability of interaction depends on the cross-section of the particle which is linked to its energy and species. I.e., heavy nuclei such as iron interact relatively high up in the atmosphere, whereas protons will interact later, after traversing a larger grammage of air. Neutrinos in the most extreme case might traverse the entire atmosphere and the planet without interacting at all. When an UHECR hits a nitrogen or oxygen molecule it is split into parts. The fragments carry the kinetic energy of the primary and interact again with the surrounding molecules. An avalanche of secondary particles is triggered and develops into the direction of the initial momentum at velocities exceeding the speed of light in air. This is called an extensive air shower (EAS). Due to the superluminal speed, a pencil beam of Cherenkov light is emitted in direction of the shower axis. The collision excitation and consequent de-excitation of the molecules leads to fluorescent light emission. It is distributed isotropically into all directions. Both radiations are mostly UV light.

2.6.1 SHOWER DEVELOPMENT

The physical processes of the developing air shower can be divided into three different kinds. The nucleonic cascade of the spallating molecules, the leptonic cascade of pions and muons and the electromagnetic cascade of electron-positron pairs and γs (Fig. 2.6.1).

The shape and timing of the shower can be approximated by empirically derived functions. These functions are tuned in accordance to Monte Carlo simulations. The underlying hadronic interaction models are extrapolations of models describing the interaction in accelerator experiments. Due to the limitations of man-made accelerators regarding the maximum reachable energy, a confirmation of the validity of these models for ultra high energies is difficult to achieve. Furthermore, the multitude of interactions to be accounted for (electromagnetic, weak and strong interactions) make it impossible to compute the shower developments as a whole. Hence, we rely on assumptions as well as on empirical parametrizations in order to describe the phenomenology of these showers. However, a precise understanding of these showers is vital for a meaningful UHECR measurement. This applies especially to the mass and type of the primary particle which determines the maximum slant depth X_{max} of the shower [16]. X_{max} is the cumulated slant depth X at the shower maximum. I.e., the thickness of the air which has already been traversed

$$X = \frac{X_{vertical}}{\cos \Theta} \left[\frac{g}{cm^2}\right] \tag{2.24}$$

with $X_{vertical}$ denoting the vertical thickness of the atmosphere and Θ, the shower zenith angle [63].

The Gaisser-Hillas function [107] parametrizes the number of charged particles in the shower as function of penetration depth in the atmosphere.

$$N(X) = N_{max} \left(\frac{X - X_0}{X_{max} - X_0}\right)^{\frac{X_{max} - X_0}{\Lambda}} exp \left(\frac{X_{max} - X}{\Lambda}\right) \tag{2.25}$$

The number of charged particles reaches its peak N_{max} at the shower maximum with the corresponding slant depth X_{max}. $\Lambda = 70$ denotes a shower development parameter [63]. Using this parametrization to fit the observed air showers enables us to measure the altitude at which the EAS reaches its brightest point. Therefore, we have an indicator to indirectly determine the cross-section of the primary.

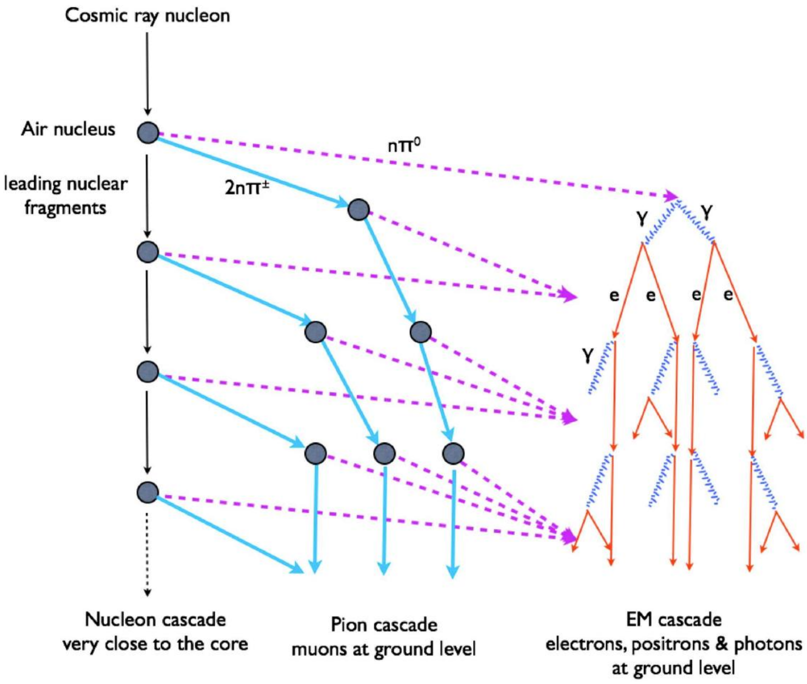

Figure 2.6.1: Schematic sketch of shower development. At each step about 1/3 of the energy of the hadronic shower component is transferred to the electromagnetic one. Taken from [165].

During the spallation of oxygen and nitrogen molecules into secondary particles, pions are produced. They have a short life time of $2,603 \cdot 10^{-8}$ s before decaying into γs or muons plus neutrinos.

$$\pi^{\circ} \rightarrow \gamma + \gamma \tag{2.26}$$

$$\pi^{+} \rightarrow \mu^{+} + \nu_{\mu} \tag{2.27}$$

$$\pi^{-} \rightarrow \mu^{-} + \bar{\nu}_{\mu}. \tag{2.28}$$

Hereafter, the muons (lifetime $2,196 \cdot 10^{-6}$ s) decay into electrons and neutrinos

$$\mu^{+} \rightarrow e^{+} + \nu_{e} + \bar{\nu}_{\mu} \tag{2.29}$$

$$\mu^{-} \rightarrow e^{-} + \nu_{\mu} + \bar{\nu}_{e}. \tag{2.30}$$

However, this life time is sufficiently long, taking into account the relativistic time dilatation, to reach the ground and to be detected. Also the kaon decay can produce muons or pions:

$$K^{\pm} \rightarrow \mu^{\pm} + \nu \tag{2.31}$$

$$K^{\pm} \rightarrow \pi^{\circ} + \pi^{\circ}. \tag{2.32}$$

2.6.2 Photon Yield

During the development of the shower cascade, a large fraction of energy is deposited in atmosphere by ionization losses. Due to the interaction of the nitrogen molecules with charged particles, they become ionized and consequently re-emit photons during de-excitation. The main component is emitted in the UV range between 300 and 400 nm. It is a discrete line spectrum as shown in Fig. 2.6.2. The higher the energy of the primary UHECR is, the more charged particles are created within the EAS. Thus, the more fluorescence photons are produced. The efficiency of this mechanism is expressed in *photon yield* (Fig. 2.6.2b). A general description of the ionization loss per path length traversed is provided by the Bethe-Bloch-formula

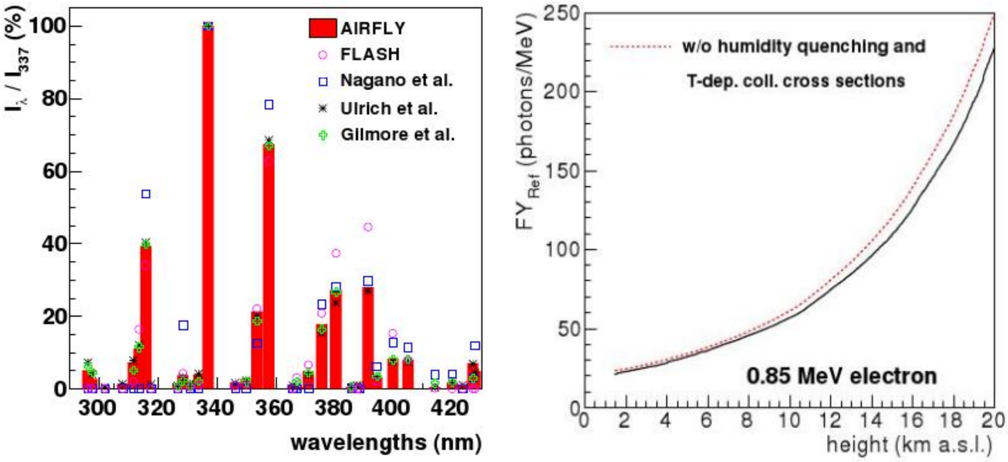

Figure 2.6.2: Left: Relative fluorescence intensities between 300 and 430 nm measured by different experiments. Right: Fluorescence yield for an 0.85 MeV electron. The absolute scale is determined by the fluorescence yield of the 337.1 nm line. The black, solid line represents the fluorescence emission including all known atmospheric dependences. The red, dashed line represents the emission without quenching effect of water vapour. Both taken from [148].

$$-\frac{dE}{dx} = \frac{k\rho Z}{\beta^2 A}\left[ln\frac{\tau^2(\tau+2)}{2(I/(m_ec^2))^2} + F(\tau) - \delta - \frac{2C}{Z}\right] \tag{2.33}$$

with k=0.1535 MeV/(g/cm²), the density ρ, the atomic number Z, mass number of the absorber medium A and the kinetic energy of the incident particle τ $[m_e c^2]$. The function $F(\tau)$ has a different shape for either electron or positron. I denotes the mean excitation potential, δ is the density correction factor [163]. The fluorescence light is an isotropic radiation It can be observed with UV sensitive telescopes.

A smaller amount of energy is converted to Cherenkov light which is produced, whenever a particle traverses a medium with a speed higher than the light speed inside the medium. Therefore, the threshold for Cherenkov light emission depends on the diffraction index of the medium. The Cherenkov light is a beamed component. The pencil beam has an opening angle of

$$\cos(\theta) = \frac{1}{\beta n} + q. \tag{2.34}$$

Here, q denotes the quantum correction factor, n the refraction index of the medium and β the relativistic factor. Cherenkov light has a continuous spectrum that is distributed in the UV and visible range [241].

2.6.3 LPM-Effect

Processes occurring in the electromagnetic cascade are pair production, bremsstrahlung, Compton scattering and synchroton radiation. The electromagnetic cross sections are well described by Bethe[16] and Heitler[17] [59]. However, for very high energies, electromagnetic processes within media cannot be described by the standard formulas any more. Landau, Pomeranchuk and Migdal (LPM) [161, 162, 187] have shown that in the region above energies of $3 \cdot 10^{20}$ eV, the development of EAS in deeper and more dense parts of the atmosphere behaves differently than in the lower energetic cases or at higher altitudes. Electromagnetic processes are characterized by a *formation length* that increases proportional with the energy and the density of the medium. If it is sufficiently long, the process interferes with other in the medium and the coherence is broken. This can happen for multiple Coulomb scattering processes in air, for instance. At very high energies the average scattering points converge and the events begin to interfere. This leads to an effective suppression of the radiation spectrum due to a decrease of the cross-sections for pair production and bremsstrahlung [63].

---

[16] Hans Bethe: ⋆2. Juli 1906 in Straßburg; †6. März 2005 in Ithaca, New York, Nobel price (1967)

[17] Walter Heinrich Heitler: ⋆January 2, 1904 Karlsruhe, German Empire †November 15, 1981 Zollikon, Meilen, Switzerland

In the case of heavy primaries, such as iron e.g., the probability for the LPM-effect to occur is negligible. The energy per nucleon is usually not sufficient to reach the threshold for any LPM suppression. In this case, the electromagnetic cascade is triggered only after the first hadronic shower steps. Thus, the energy range is below the initial energy of the primary and the LPM-effect unlikely to happen.

For UHE-γ on the contrary the probability is by far higher. A photon with an energy exceeding 10^{20} eV is very likely to suffer from LPM suppression. However, the effect depends on the angle between the photons's direction and the magnetic field lines[18] [153]. At the density of the upper atmosphere, the threshold for the LPM-effect (E_{LPM}) is approximately 10 EeV. When the electromagnetic cascade develops into the ground direction, it traverses layers of air with increasing density. Hence, not only the first interaction can be affected, also the consequent shower steps can be retarded. The interaction length increases even more and therefore, the effect is self-amplifying. For photons, the LPM effect leads to a delayed shower development. For high energy neutrinos, the suppression is even stronger. As a consequence, the shower features such as X_{max} can fluctuate even stronger and moreover even create a multiple peak structure of the intensity curve. Instead of one shower maximum, we can observe a number of maxima. As a consequence the energy determination by experiments loses precision. On the other hand it enables the unambiguous identification of neutrino induced air showers.

2.7 Cosmic Ray Detection

The detection of cosmic rays underwent a development of one century of technical evolution. From the first balloon measurements with electroscopes to nowadays observatories, many obstacles have been overcome. The progress in the field of UHECR physics has been a joined approach of both theoreticians and experimentalists. Contributions of the two sides has lead to a better theoretical understanding of the multiple phenomena and has also pushed the barriers of detection farther out. However, as pointed out in the recent chapter, we are still facing many obstacles. In order to measure the trans-GZK events to a meaningful extent, large detector arrays have been built. This chapter is devoted to the introduction of the largest current UHECR experiments in operation.

Successful astro-particle astronomy depends on a precise identification of the prop-

---

[18] The geomagnetic field extends farther out into space than the earth's atmosphere

erties of the messenger particles. The reconstruction of the properties of the air shower is the technique to retrieve this information about the primary — arrival direction, energy and the type of the particle. Key factors for the determination of the primary's characteristics are the direction and the first interaction of the shower, the grammage of the fluorescence light maximum and the total brightness. Moreover, the shape of the shower front and the particle composition yield vital parameters for the event reconstruction.

2.7.1 DETECTION TECHNIQUES

In the low energy regime of cosmic ray physics (i.e., $E \leq 10^{15}$ eV), the cosmic ray flux is sufficiently large to directly collect the events in detectors with balloon experiments or from space. At high energies, the flux is far to low for the direct approach. UHECR observation can only be performed by means of the secondary radiation - the detection of UHECR induced extended air showers (EAS).

EAS can be observed by detecting the secondary particles (predominantly muons) on ground in large arrays of scintillation detectors or Cherenkov tanks. The great advantages of the particle detection is the nearly 100 % duty cycle. The response is independent of weather conditions or day and night time. The technique yields a good sensitivity to showers with low zenith angles. The quality of the recorded events improves with the energy. Usually, each of the ground stations operates independently. The data is transferred to a central data processing unit which applies trigger algorithms to the data set coming from all stations.

Alternatively, EAS can be observed in the UV range, by the fluorescence technique or the Cherenkov technique. The underlying method of the fluorescence technique is calorimetry. The light collected by the UV telescopes serves as a measure for the energy deposited in atmosphere by the primary cosmic ray [278]. Due to the fluorescence effect about four photons per charged particle and per metre of trajectory are isotropically emitted from the shower axis. The photons can be collected by spherical mirrors or lenses and then recorded by a UV-sensitive camera. In an optimal setup, the shower is recorded by multiple telescopes from different directions. Hence, the stereoscopic view allows for a straight forward direction reconstruction of the shower by geometrical considerations. The fluorescence technique is limited to nearly moonless nights for a meaningful detector response. Therefore, depending on geographical and seasonal constraints, the duty cycle is of the order of 10 %. The quality of the recorded events increases with energy and inclination angle, since more light reaches the telescope.

A third option is the radio observation of the showers. EAS emit radio waves due to geo-synchrotron emission. When the shower develops, the created electrons and positrons are deflected by the geomagnetic field causing synchrotron radiation in the radio range. This emission is beamed along the shower axis towards the earth. [111] This technique is the least developed compared to the other two above. However, it could be an extremely helpful tool, since it would provide an additional weather and daylight independent source of information. Moreover, the antennas needed are significantly easier to develop, mount and to maintain than any of the other devices.

In some experiments a combination of different techniques is used in a hybrid approach (Fig. 2.7.1). This bears the advantage of cross-calibration of the methods and additional information for the reconstruction techniques.

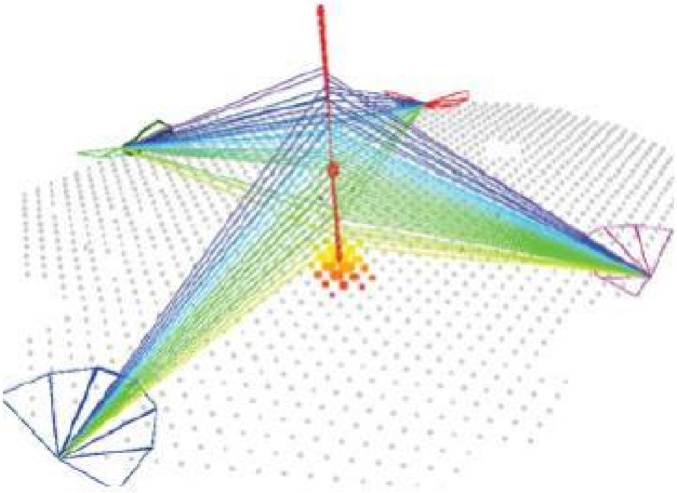

Figure 2.7.1: Hybrid approach: The secondary particles arriving to the earth can be detected by scintillation detectors or Cherenkov water tanks. Simultaneously, the shower development is monitored by UV telescopes. Taken from [177].

2.7.2 EXPERIMENTS

THE PIERRE AUGER OBSERVATORY (PAO), is currently the largest UHECR experiment on earth. It is designed to measure in a hybrid technique using both Cherenkov water tanks and fluorescence telescopes. The surface array consists of 1600 Cherenkov detector stations. A Cherenkov station consists of a cylindrical polyethylene tank with a diameter of 3.6 m and a hight of 1.55 m. It encloses a liner filled with 12 000 l of highly purified water. [2] When secondary particles of the EAS traverse the water, they create Cherenkov light which is detected via photomultiplier counters. These stations are arranged in a grid with a displacement of 1.5 km to the neighbouring station. In total, they cover a total area of 3000 km^2. Additionally, there are four fluorescence telescope stations to monitor the air volume above the grid. Each of the fluorescence station enclosures contains six UV telescopes adding up to 24 telescopes in total. The

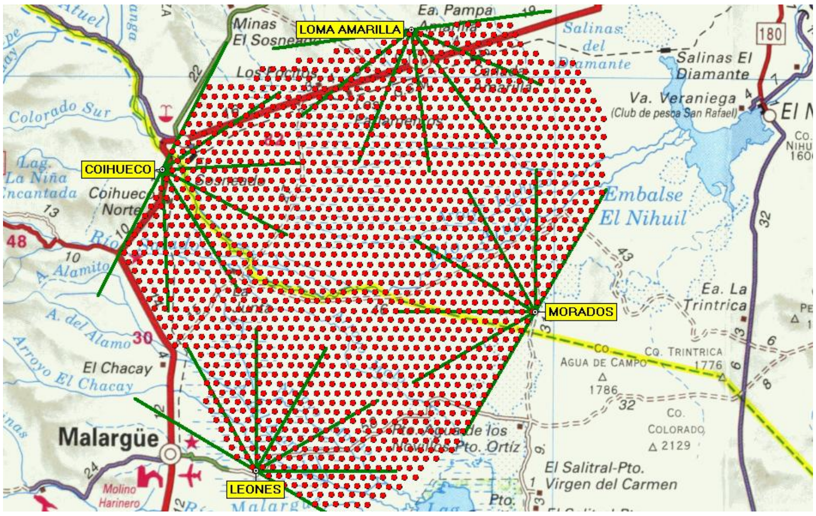

Figure 2.7.2: The Pierre Auger Observatory near Malargüe in Western Argentina. The grid of deployed Cherenkov water tanks is indicated by red dots, the position of the fluorescence telescope stations and their viewing angles by green lines. Taken from [86].

PAO is conceived to measure UHECR over 4 orders of magnitude in energy from 0.01 Eev to above 100 EeV [166]. It has reached an exposure of 40000 km^{2}sr [166]. The fluorescence telescopes have a duty cycle of about 10% [215].

Originally, it had been envisaged to build a second array of the same size as the PAO in the northern hemisphere to have full sky coverage. However, due to financial constraints these plans have been put on hold. Nevertheless, future plans in the framework of AugerNext for the PAO include all sky coverage, the additional use of radio antennas as well as a new generation of muon detectors. [127]

The Telescope Array (TA) is an UHECR experiment, situated in the western desert in Utah, USA. It is a hybrid detector, consisting of a surface detector array of 507 plastic scintillator stations [137]. Each of the stations contain a plastic scintillator of 3 m^2

surface. They can detect the muonic and electromagnetic components of the showers. The stations are arranged in a grid of 1.2 km spacing, covering 700 km². Additionally, three fluorescence detectors monitor the air volume above. In total, there are 38 fluorescence telescopes arranged in 3 stations. [5] The TA experiment is taking data since 2008. This UHECR observatory is the largest in the northern hemisphere. The telescope site is equipped with an on-site accelerator beam for direct calibration of the UV-telescopes [196]. The telescope array site has a long history of cosmic ray experiments. It is actually the 4th renewal of a series, starting with the Fly's Eye experiment in the early 1980s. [28] Following that, the HiRes (High Resolution Fly's Eye) [171] and HiRes II [47] experiments continued. The TA experiment is taking data in hybrid mode since 2008 [253].

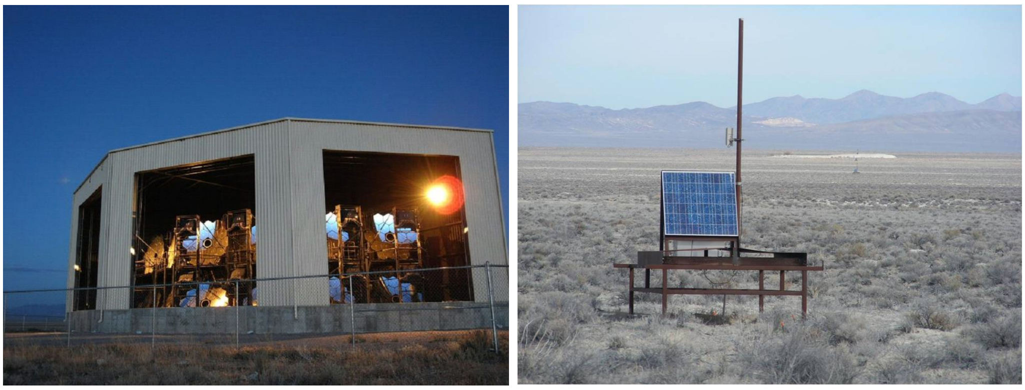

Figure 2.7.3: Left: Fluorescence telescope station at Black Rock Mesa. One unit consists of twelve reflecting spherical mirrors. Right: Surface detector of Telescope Array. It is a plastic scintillator of 3 m². Both taken from [225]

Future plans for TA include low energy extension (TALE). This extension lowers the threshold of the sensitive energy range down to $10^{16.5}$ eV. This will allow to observe the second knee and the predicted galactic-extragalactic transition of dominant sources. Furthermore, at this energy air shower features can be compared to LHC results. Another plan is the exchange of detectors between PAO and TA. This is an approach to better evaluate systematic uncertainties between the two experiments, especially in terms of energy scales and Xmax determination. [196]

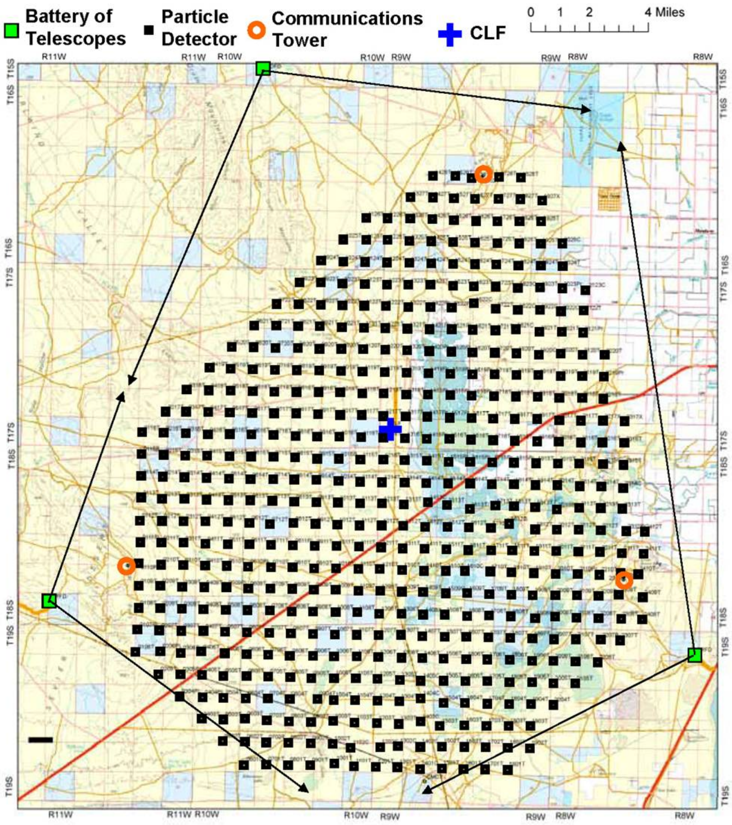

Figure 2.7.4: Map of Telescope Array. Black squares are surface detectors, green squares show fluorescence telescope sites. Taken from [225].

2.7.3 Current Status

In the last 100 years of cosmic ray research amazing discoveries have been made. Especially in the first 50 years cosmic ray science had been on the frontier of nuclear and particle research. New particles have been discovered and new technologies have been developed. Still UHECR research continues to be an active field, breaching the gap between particle and astrophysics.

As pointed out in the above sections, major questions still remain unsolved. The greatest puzzle is certainly the question regarding the origin of UHECR. Due to the data acquired so far, a number of production scenarios have been ruled out, already. However, the question of anisotropy is still open. The data collected by the PAO seem to indicate a correlation of UHECR with the position of AGNs. Nevertheless, the claim is still lacking independent confirmation. Hence, it is too early to claim that the sources of UHECR are anisotropically distributed in the sky. Moreover, we cannot neglect the impact of magnetic fields, galactic or extragalactic, the results strongly depend on the

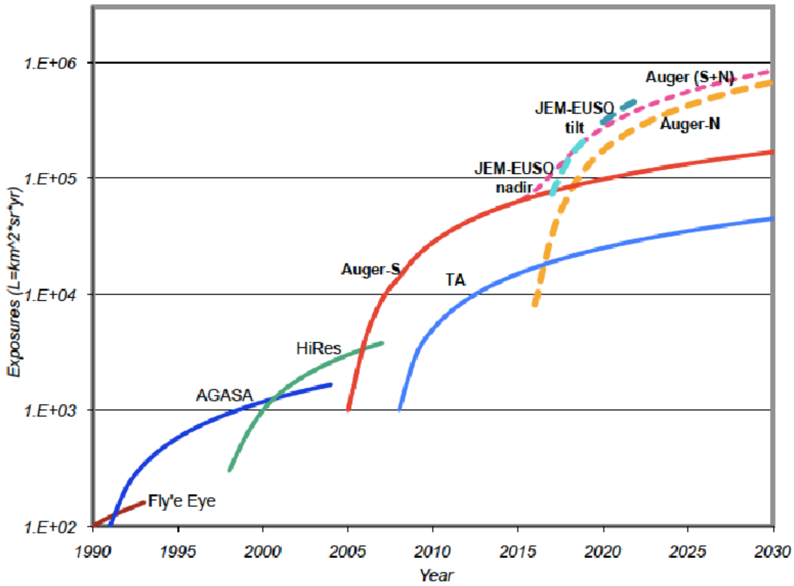

Figure 2.7.5: Exposures of UHECR experiments including the cancelled Auger Northern Observatory. Taken from [156].

methodology. [152] Even if there were discrete sources - the anisotropy might be destroyed due to deflections. This is even more likely if the primaries turn out to be heavier nuclei than protons as suggested by the PAO [90]. However, the question of the type of primary at UHE is still open, due to the fact that the PAO claims have not been confirmed by independent experiments. Nevertheless, the lack of UHE-γ and UHE-ν in current observations could strengthen the position of the PAO. The honest answer to that question is that we do not really know, since the composition analysis is a complicated task. Nowadays experiments yield contradictory answers. HiRes, Telescope Array, HiRes-MIA and the Yakutsk array detectors indicate a proton-dominated flux, while Fly's Eye, Haverah Park and the PAO favour a mixed composition with a large ratio of heavy nuclei, especially for ultra high energies. [22, and references therein] It is important to point out that the entire collection of CR events exceeding $5 \cdot 10^{19}$ eV gathered so far by all experiment worldwide is approximately 200 out of which a small fraction has been observed in hybrid mode [167].

Another open question concerns the maximum energy of UHECR. We know of the existence of particles carrying energies as high as $3 \cdot 10^{20}$eV. Is this the end of the spectrum? And if so, is that due to an intrinsic E_{max} of the sources or does it come from interactions with the ISM on the way to earth? Why do we observe particles with energies above the GZK-limit? All these questions are closely interlinked with each other.

One cannot ask only one and ignore the others at the same time. The nuclear interaction models we are applying during the measurement cannot be verified in accelerator experiments, only for much lower energies. Even if the LHC has helped a lot in improving the predictive power of the models, we cannot know for sure the behaviour of particles interactions in our atmosphere at these energies.

The only way to address these question is the collection of more events in the EHE regime. Even though a great effort has been made, the open problems are closely linked to a lack of statistics. The current experiments are still too small by at least one order of magnitude to measure a sufficient amount of data. Indeed, the planned renovations and extensions will certainly improve the situation, at least in parts. Nevertheless, the current experiments suffer from a major disadvantage. None of them can ever reach a uniform exposure of the entire sky. To overcome the problems summarized here, an entirely novel idea has been proposed — the space based observation of UHECR.

We are all in the gutter, but some of us are looking at the stars.

Oscar Wilde

3

The EUSO Approach

LITTLE DO WE KNOW about the extreme energy end of the cosmic ray spectrum. Hence, a novel approach in the detection of UHECR, to address the open questions regarding the potential sources, composition and energy distribution in the realm of 10^{20} eV, is indispensable.

The idea of a space-borne UHECR detector was first proposed by John Linsley[1] in 1979. The project called SOCRAS (Satellite Observation of Cosmic Ray Air Showers), has been the first proposal for a cosmic ray observatory in space [36, 37, 131]. This space experiment was also supposed to detect UHE neutrinos. Linsley's idea was to use a large reflective mirror of 38 m diameter to observe an area of 10^4 m^2 from an altitude of 500 – 600 km.

In 1995, a workshop to investigate possibilities for space based approach with technologies that had not been available in the 1980s was held at the Marshall Space Flight Center in Huntsville, Alabama in the USA initiated by Yoshiyuki Takahashi[2] [93], John

---

[1] John Linsley ⋆12 March 1925, Minneapolis, Minnesota, USA †25 September 2002, Albuquerque, New Mexico, USA

[2] Yoshiyuki Takahashi ⋆13 September 1947, Amagi-shi, Fukuoka-ken, Japan †12 March 2010,

Linsley and Livio Scarsi[3] [93] (Fig. 3.0.1). Takahashi's idea to use a lightweight Fresnel optics with a wide opening angle forged Linsley's vision into a tangible plan. Following this workshop, the idea of the OWL project [245] emerged in the US, whereas the European approach *Airwatch* was born in Italy.

Figure 3.0.1: From left to right: Takahashi, Linsley, Scarsi. Taken from [93].

The Airwatch project, renamed Extreme Universe Space Observatory (EUSO) at the end of the 90s, was led by Scarsi as the principal investigator (PI) [231]. From 2000 until 2004, a first phase A study was carried out by the European Space Agency (ESA). The EUSO mission was planned to be launched in the first decade of the new century and was supposed to be attached to *Columbus*, the European module of the international space station ISS [256]. The instrument was consisting of a refractive UV telescope with Fresnel lenses and a focal surface detector equipped with multi-anode photomultipliers (MA-PMTs) [207]. It was planned to be transported to the ISS by an American Space Shuttle. Due to programmatic issues, mainly regarding the future of the ISS and the Columbia disaster, the mission was put on hold in 2004. In 2006, the mission was re-established by the name of JEM-EUSO under the leadership of Takahashi, planned for assembly on the Japanese Experiment Module (JEM) at the ISS [93, 251]. The *Extreme Universe Space Observatory on board the Japanese Experiment Module*, is essentially based on the design of the former EUSO mission. However, JEM-EUSO has slightly different dimensions and uses updated technologies.

At the same time, a Russian attempt to measure UHECR from space emerged. The TUS/KLYPVE program aims at comparable objectives but uses a reflective optical system instead (see Chap. 3.8.1) [3, 150, 151].

Nashville, Alabama, USA

[3] Livio Scarsi ⋆25 May 1927, Rocca Grimalda, Italy †16 March 2006, Rocca Grimalda, Italy

3.1 SPACE BASED UHECR OBSERVATIONS

The basic idea of the space-based approach to the exploration of UHECR, is to monitor the earth's atmosphere with an UV telescope from above (Fig. 3.1.1). Depending on the opening angle of the optics and the altitude of the instrument, it can monitor a large fraction of the atmosphere. This air volume serves as a target mass for incoming UHECR. When primary particles strike the nitrogen or oxygen molecules of the atmosphere, an avalanche of secondary particles is triggered and develops into ground direction. This is an extended air shower. By collecting the UV photons of the emitted fluorescence and Cherenkov radiation, the shower can be registered. From the geometrical and timing information of the photons the direction, energy and type of the primary particle can be reconstructed. This idea is appealing in many regards. The UV setup relies on the already well understood fluorescence technique. The Cherenkov signal can serve as an additional source of information. The space approach enables a 4π sky coverage, whereas earth bound detectors only feature a maximum exposure in one of the two hemispheres. Above all, the space borne design yields a high aperture — exceeding the highest apertures reached on earth by at least one order of magnitude. For such a space based instrument, we can think of an instantaneous geometrical aperture up to $A_{eff} \approx 10^6 km^2 sr$. This in an equivalent to a target mass of more than 10^{12} tons [227]. A further advantage is a higher duty cycle compared to earth bound

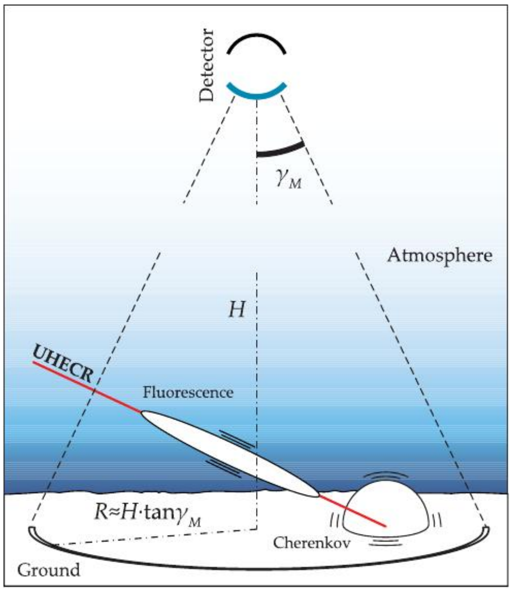

Figure 3.1.1: Schematic sketch of the space approach. Taken from [208].

fluorescence telescopes. A typical EAS fluorescence light maximum develops at an altitude of 3 to 5 km from ground [53]. Thus, the EAS maxima are less obstructed by clouds, when observed from above. Besides, the atmospheric conditions of the upper half of the atmosphere are more stable, since it tends to be less affected by weather disturbances. Therefore, assuming a duty cycle of approximately 20 %, an exposure of $A_{exp} \approx 10^6 km^2 sr\, yr$ can be reached within 5 years of operation [227]. The space approach will furthermore overcome a number of typical problems of ground telescopes arising from the close proximity of the detector to the EAS, such as difficulties in the determination of the solid angle and changing attenuations of the UV light of the same shower in atmosphere. The almost constant fluorescence emission rate at various altitudes below the stratosphere allows for simple approximations of the relation between energy, fluorescence yield and time structure of the emitted photons, and the EAS altitude at which they have been produced. From space, the scattering by aerosols, which is relevant at altitudes below the atmospheric boundary layer, can be neglected [53].

On the downside of space observation are a number of disadvantages, mostly imposed by financial constraints. Since payload mass is a limiting factor in any space mission, a space based observatory will most likely comply of only one detector. Two or more detectors would allow for a stereoscopic mode. This would bear the advantage of an improved angular resolution, as well as X_{max} determination and an improved trigger scheme. The space approach imposes strong limits on the instrument's power supply and data budget. Telemetry constraints require a sophisticated trigger system to transmit only those events to earth that are regarded as potentially valuable. Another challenge is the speed of the moving detector. Depending on the altitude, the pathway of the satellite projected on ground moves at a velocity of the order of some kilometres per second, thus the observation conditions change and the detector and data evaluation have to account for that. A good knowledge of the atmospheric properties is inevitable. Hence, the instrument would need to be equipped with additional detection devices to monitor the atmosphere.

These challenges can be successfully addressed or at least controlled by an advanced detector design and the stake of new technologies. Within the cosmic ray community it is widely agreed upon that a major breakthrough to address the fundamental unanswered questions can be only achieved by increasing nowadays exposure by one order of magnitude [106, 167, 222]. The space approach will effectively meet this demand. This new generation telescope, marks the advent of a new kind of astronomy. So far, the only carrier of information to be used were various forms of electromagnetic radiation.

Space based UV telescopes are the beginning of UHECR astronomy [51].

3.2 THE JEM-EUSO MISSION

JEM-EUSO, the *Extreme Universe Space Observatory on board the Japanese Experiment Module* is a space-borne UHECR telescope. It will use the earth's atmosphere as a large detector target volume to measure cosmic rays with energies around the GZK cut-off [94, 217, 258, 261, 275]. In the current configuration of the mission the launch is planned for 2017 with a Japanese H2B rocket. It will be transferred to *Kibo*[4], the Japanese module, by a H-II Transfer Vehicle (HTV). The telescope will be removed from its hatch of the spacecraft by the Kibo's robotic arm, the JEM remote manipulator system (JEMRMS), and deployed to one of the equipment exchange units (EEUs) of the exposed facility (EF). The exposed facility provides a multi purpose platform where the experiments, which require an open environment, are operating. From here, the JEM-EUSO instrument will observe the earth's atmosphere in the UV range between 300 to 400 nm (Fig. 3.2.1). The instrument consists of an optical system, to focus the light emitted by the EAS on a focal surface detector (FSD). The FSD is equipped with photo-detection modules (PDMs). Each PDM is made of a set of multi-anode photomultiplier tubes. This detector setup has single photon count abilities and a high time resolution. The signal is identified by a trigger system, recorded and transmitted to earth. From the signal characteristics, the properties of the UHECR can be inferred. JEM-EUSO will start its operation in nadir mode and will be tilted in a second phase of

Table 3.2.1: Key facts about the JEM-EUSO mission [227].

Expected Launch	2017
Duration of Mission	3 (+2) years
Launcher	H2B Rocket
Transport Vehicle	HTV
Location	JEM on ISS
Instrument Mass	1938 kg
Power Budget (op./non-op.)	352 W/ 926 W
Data Downlink	285 kbps
Orbit Altitude	~ 400 km
Orbit Inclination	± 51.6°

---

[4] Kibo (jap.): Hope, former name: JEM, http://kibo.jaxa.jp

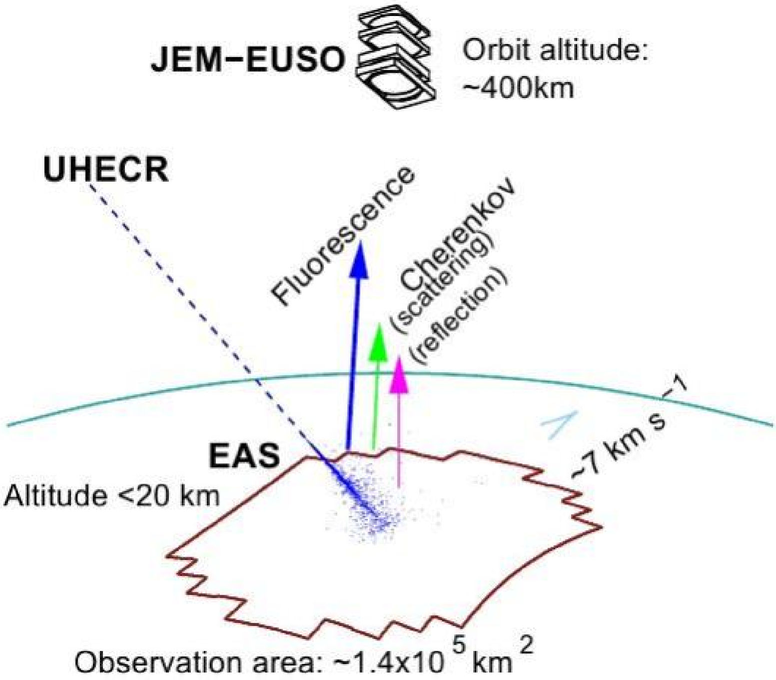

Figure 3.2.1: Concept of the JEM-EUSO mission. Taken from [7, 57].

operation to increase the exposure. The telescope will reach an instantaneous aperture between 65 and 280 times larger than the PAO, depending on the tilting angle. It corresponds to an observational area of $2 \cdot 10^5\ km^2$ in nadir and $7 \cdot 10^5\ km^2$ in tilted mode [93]. The planned operation time will be at minimum three years with a planned extension of two more years. Thus, in the scope of the mission JEM-EUSO is expected to collect approximately 1000 events with $E > 7 \cdot 10^{19}$ eV [53]. It will increase the statistics at the high energy end of the spectrum by an order of magnitude. Its energy threshold of about $5 \cdot 10^{19}$ eV allows for cross calibration with the already existing ground based UHECR observatories. Mounted on the ISS, the telescope moves at a speed of approximately 7 km/s in the latitude range of ± 51° [251]. This will provide a homogeneous exposure to both hemispheres.

JEM-EUSO is the successor of (ESA-) EUSO, but differs in some important regards. First of all, instead of the European Columbus module, the detector is now hosted on board the JEM. The telescope features an improved overall performance. Even though, the instrument design itself differs only slightly, the use of new technologies, such as an improved optical design, new lens material, photomultipliers with a higher quantum efficiency and a revised trigger scheme, decrease the energy threshold to $5 \cdot 10^{19}$ eV.

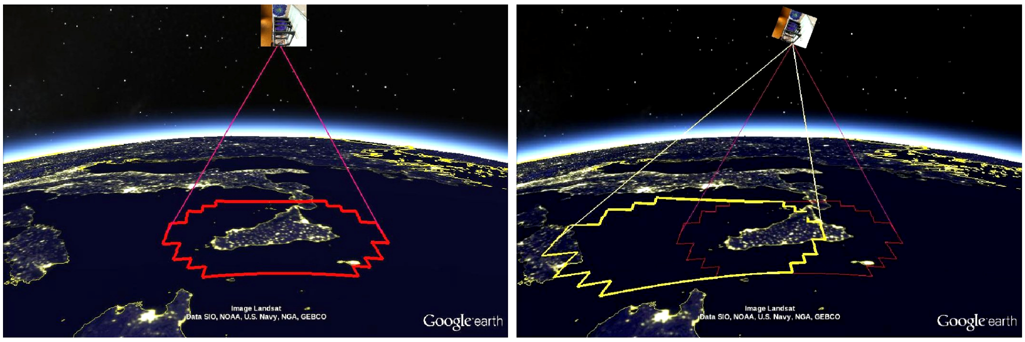

Figure 3.2.2: JEM-EUSO field of view over the Mediterranean sea. left: nadir mode, right: tilted mode, tilting angle of 20°. Pics. are a courtesy of K. Shinozaki.

And finally, by tilting the instrument, the effective area can be enlarged by a factor of 5 [93] (Fig. 3.2.2).

3.3 INSTRUMENT DESIGN

Deployed at the ISS, the extended JEM-EUSO telescope has a cylindrical shape of about 2.6 m in diameter. Its net weight is estimated at the moment with 1983 kg. Its power consumption is expected to be 926 W in operation and 352 W during stand by [81].

The telescope comprises of four major components: The optical system, the focal surface detector, the electronics and the structure. This is accompanied by two subsystems: an atmospheric monitoring system and a calibration system. Systems for energy supply and data downlink are provided by the host module [141, 257].

3.3.1 OPTICAL SYSTEM

The optical system of the telescope is a refractive system of three lenses. Its purpose is to collect the fluorescence and Cherenkov light emitted by the EAS and to focus it onto the focal surface of the telescope. The photons of interest are in the UV range between 300 and 400 nm. Since the signal is extremely faint, a high optics throughput efficiency is required in this wavelength range. At the same time, the optics has to have a large opening angle to cover a volume of air which enables a sufficient exposure of the

---

[5] sidecut optics

Table 3.3.1: Key parameters of the JEM-EUSO telescope [227].

Field of View	± 30°
Aperture Diameter[5]	2.5 m
Focal Surface Area	4.5 m^2
Observational Area	$> 1.3 \cdot 10^5$ km^2
Pixel Field of View	0.075°
Pixel Size on Ground	~ 550 m
Number of Pixels	$3.2 \cdot 10^5$
Time Resolution	2.5μs
Dead Time	$< 3\%$
Optical Bandwidth	300 – 400 nm
Duty Cycle	~ 20%

mission. The size of the lenses is a determining factor for the instrument's collection power. However, in a refractive design, the mass of the system increases with the size, as well. Moreover, exceeding a certain diameter, the lenses become unstable under their own weight. To cope with these preconditions, the JEM-EUSO instrument is equipped with a system of Fresnel lenses. This concept allows for a wide opening angle, slim and therefore lightweight lenses and a point spread function in compliance with the requirements. Currently, different designs are under study. Essentially, the system is made of a set of three lenses. The entrance pupil is a curved Fresnel entrance lens with an iris behind. The second lens is flat with a symmetric diffractive surface on the one side and a Fresnel surface on the other. Its purpose is to correct for chromatic aberration. The third lens is again a curved, double sided Fresnel lens. Furthermore, the optical unit consists of a filter, which selects the wavelengths of interest, the lens frame and housekeeping sensors (Fig. 3.3.2).

The performance requirements imposed on the optical system are the following:

1. The field of view (FoV) of the optics has to be larger than ± 30°, which corresponds to a spatial resolution of ~ 0.1° or less. (This corresponds to approximately to the FOV of a single pixel);

2. The spot size has to be smaller than the pixel size of the focal surface detector;

3. A maximum photon collection efficiency in the UV range between 330 and 400 nm;

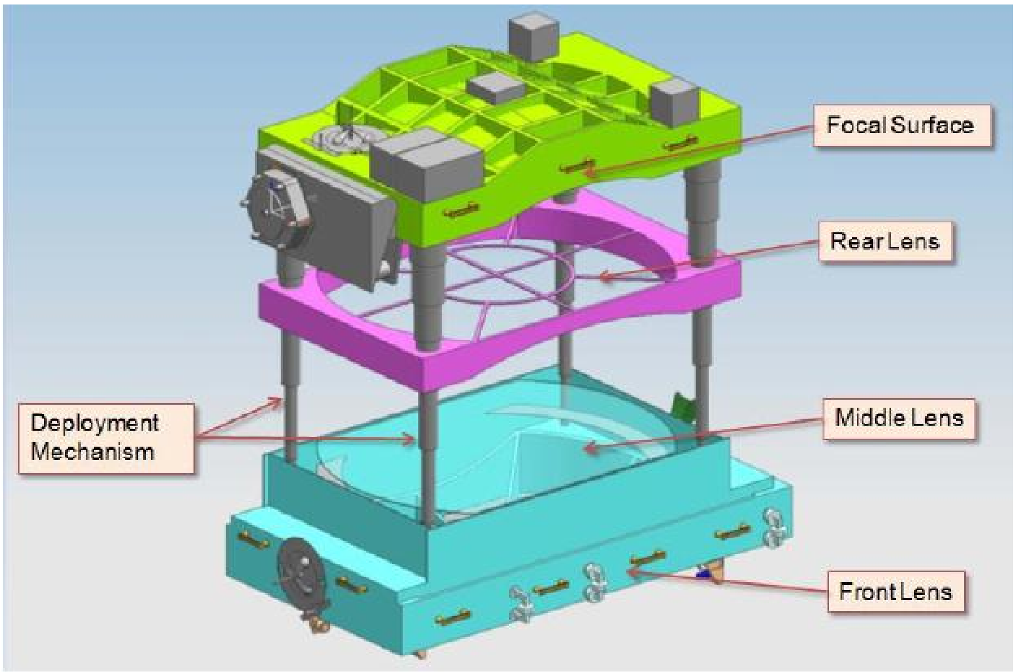

Figure 3.3.1: The optical system of the JEM-EUSO telescope. Taken from [257].

4. The optics must be space qualified for a life span of 5 years or more in the ISS environment.

Two designs have been proposed that fulfil the specifications above - a baseline and an advanced design. In the baseline case, the material is proposed to be polymethyl methacrylate (PMMA)[6]. In the advanced design option, the entrance lens is made of CYTOP[7]. CYTOP bears the advantage of being more radiation resistant than PMMA and having better optical properties. However, this comes at the price of higher costs and almost twice the weight.

The lenses will be shaped with a maximum diameter of 2.65 m. However, by cutting two parallel sides of the lenses to 1.9 m, a so called *side cut* design has been proposed to make the best use of the dimensions of the HTV's cargo bay.

3.3.2 FOCAL SURFACE DETECTOR

The focal surface detector of the JEM-EUSO telescope detects the focused fluorescence and Cherenkov light. It measures the position of the incoming photons as a function of time and follows the spatial and temporal air shower development.

---

[6] PMMA is a product of Mitsubishi Rayon Co., Ltd.

[7] CYTOP is a product of AGC Co., Ltd.

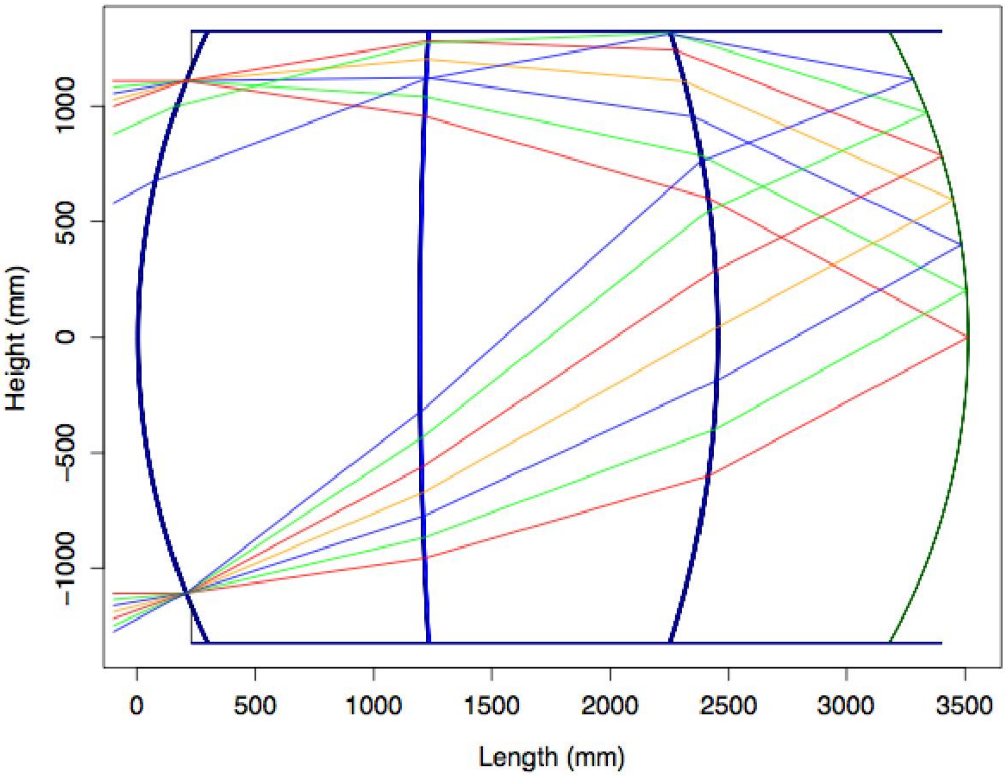

Figure 3.3.2: Cross section of the optics of the JEM-EUSO telescope. Taken from [257].

The focal surface detector is essentially composed of 137 photo detection modules (PDMs), each of which is made of 6 × 6 multi-anode photomultipliers (MA-PMTs). The MA-PMTs are mounted in a support structure that also contains important supply components such as the PDM board with the first trigger level and the readout electronics, the high voltage divider and the high voltage power supply. The entire focal surface detector is supported by the focal surface structure. The PDMs are deployed on the focal surface in a pattern that most efficiently takes advantage of the area, since any dead space between PDMs contribute to detection inefficiencies [147].

Apart from the common requirements for space missions like a high reliability and a stability over the expected duration of the mission, the performance requirements are [147], [257, p. 88]:

- a single-photon sensitivity in the 300 to 400 nm range to detect extremely faint air showers,
- a fast response (below 0.1 μs) to follow the EAS space-time development,

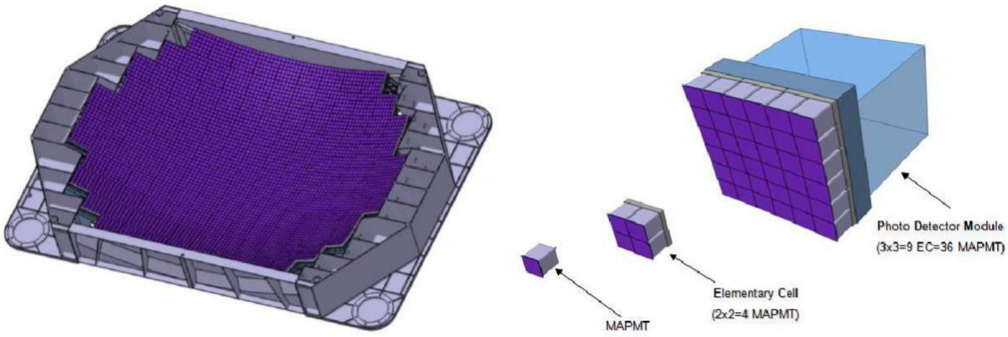

Figure 3.3.3: left: Focal surface detector, right: MA-PMT assembly Taken from [257].

- a noise rate two orders smaller than the rate of the nightglow background,
- a good and uniform overall detection efficiency (averaged over all the FS, shall be $\varepsilon_{PD} \geq 0.12$),
- an optimal cover of the optical focal surface with a maximal sensitive area due to reduced dead or inefficient spaces,
- a low sensitivity to magnetic fields of the order of magnitude of 1 Gauss,
- a high reliability according to space mission requirements over at least a 5 years of operation time.

The centrepiece of the focal surface detector is the MA-PMT (Fig. 3.3.4). Within one PDM, the MA-PMTs are organized in *elementary cells* of 4 × 4 MA-PMTs. Thus, one PDM contains 36 MA-PMTs. The entire FS detector therefore is made up of 137 PDMS $\cdot$ 36 = 4932 MA-PMTs. The envisaged MA-PMT model as the baseline option is the Hamamatsu R11265-M64. It has the size of 26.2 mm × 26.2 mm and a height of 20.25 mm. The mass is 27.3 g. Its 8×8 square pixels have a dimension of of 2.88 × 2.88 mm, resulting in a maximum sensitive area of 23.04 × 23.04 mm [147]. The R11265-M64 is characterized by the following specifications [257, p. 90]:

- The tube is equipped with an ultra-bialkali photo-cathode and a 0.8 mm thick UV- transmitting window;
- The device has a metal channel dynode structure with 12 stages, providing a gain of the order of 10^6 at 0.9 kV with a tapered voltage divider;
- It has a quantum efficiency higher than 35% (maximum 40%);

- The anode pulse rise-time is about 1.5 ns;
- The transit time spread has a duration of 0.3 ns;
- It has a cross talk of approximately 1%.

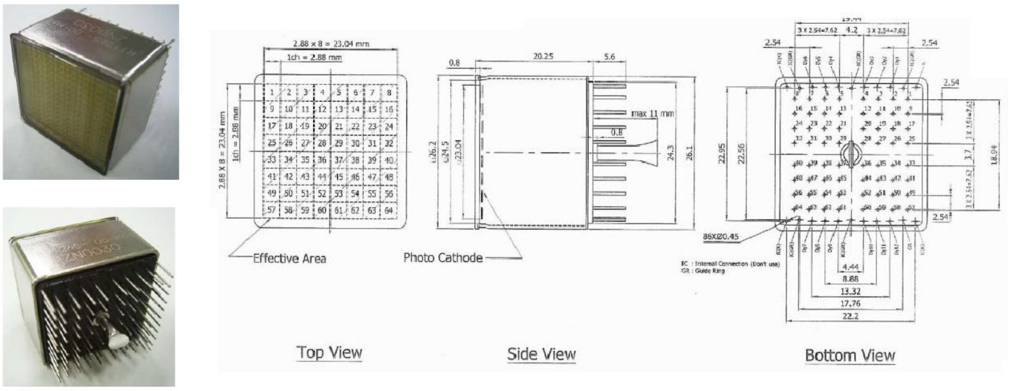

Figure 3.3.4: The Hamamatsu R11265-M64 photomultiplier. Taken from [257, p.90].

In addition to the baseline option using MA-PMTs, a second advanced option is under discussion — the use of silicon photomultipliers (SiPM). The SiPM is a novel type of light detector which bears the advantage of a high quantum efficiency, low mass and compactness at relatively low costs. It is a semiconductor device which needs only a low voltage supply. Up to several ten thousands of avalanche photo-diodes can be accommodated on one chip. These photo-diodes work in Geiger mode at very high speeds [257, p. 108-112]. Different kinds of SiPM have been reviewed and tested regarding their potential deployment in the JEM-EUSO detector. However, the space robustness and radiation hardness are still subject to study. Therefore further investigations are ongoing.

3.3.3 ELECTRONICS AND TRIGGER

The JEM-EUSO control electronics include several sub-systems, among them the ISS communication and power interfaces, housekeeping data system, the thermal control, a position determination system as well as management systems for the control of the atmospheric monitoring system, lid operation and calibration, monitoring and alignment devices management system. We will concentrate here on the scientifically most relevant.

The electronics of the JEM-EUSO detector, responsible for the data acquisition is hierarchically structured on different levels. After activation of the PMTs, the signal is read out and saved into a ring buffer on the PDM board. The PDM board provides the first trigger level (L1). When a trigger is issued, the data is transferred to the *cluster control board* (CCB). This is an important component of the read-out electronics. It bundles the information of about 8 PDM units[8] and accommodates the second trigger level (L2). The main purpose of the CCB is data acquisition from a number of PDM boards, the selection by application of the L2 trigger and further transmission to the mission data processor (MDP). It plays an important role for data reduction [32, 33]. The interface between the PDM board and the CCB board is a bottleneck for the data flow of the entire system. To transmit the event data (around 2.7 Mbit per PDM and event) sufficiently fast, an 8-bit wide, source synchronous data bus running at 40 MHz has been implemented. Commands, configuration and status messages of the PDM can be send via a standard serial peripheral interface (SPI).

After receiving a L1 trigger message from any of the connected PDMs , the CCB broadcasts the signal to the remaining PDMs and requests the contents of their ring buffers. This data is consequently transmitted to the CCB and the L2 trigger is applied in a parallel way. If the CCB trigger is issued for at least one of the PDMs the data is forwarded to the mass memory module of the MDP. CCB and MDP are interfaced by SpaceWire[9], due to its approved reliability [32, 33].

Purpose of the trigger is to discriminate a potential signal from background counts. For a space mission like JEM-EUSO strict criteria are applying, since the downlink data budget is severely limited. Therefore, the trigger algorithm has to act very conservatively, i.e. the ratio of real to fake events should be rather large. At the same time, the event types, JEM-EUSO is primarily looking for are still very precious. Even a high aperture experiment like JEM-EUSO cannot afford to loose a substantial number. Moreover, the algorithm should not consume too much hardware resources and energy.

To process the large amount of data coming from the $\sim 3 \cdot 10^5$ pixels, the JEM-EUSO detector will be equipped with a two-level trigger system. The first trigger level is applied directly at the PDM board. This bears the advantage that the trigger searches for signals just in a small part of the focal surface, but in parallel on every PDM. Each of them is sufficiently large to contain a significant part of a typical signal track.

---

[8] still to be defined

[9] SpaceWire: a network dedicated for spacecrafts, developed by ESA

The first trigger level consists of three sub-levels implemented in an integrated circuit (ASIC) at the PDM board.

1. *The Anode-level trigger*, an analogue discriminator which detects single photoelectron events at each anode. Electronic noise is reduced, since the strong anodic pulses are clearly above the pre-amplifier electronic noise;
2. *The Pixel-level digital trigger*, a gated counter and a digital comparator. Here, a threshold is set according to the background intensity. If the amount single-photoelectrons recorded by an anodic chain within a GTU is higher than the threshold the signal is passed on. This level greatly reduces random light background counts;
3. *The EC digital trigger* is also a gated counter and a digital comparator like the second sub-level. It uses the same technique, but this time for a number of consecutive GTUs and groups of pixels (persistency trigger).

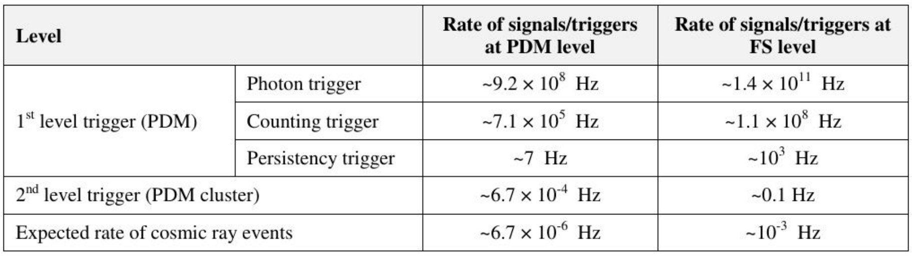

Level		Rate of signals/triggers at PDM level	Rate of signals/triggers at FS level
1^{st} level trigger (PDM)	Photon trigger	~9.2×10^{8} Hz	~1.4×10^{11} Hz
	Counting trigger	~7.1×10^{5} Hz	~1.1×10^{8} Hz
	Persistency trigger	~7 Hz	~10^{3} Hz
2^{nd} level trigger (PDM cluster)		~6.7×10^{-4} Hz	~0.1 Hz
Expected rate of cosmic ray events		~6.7×10^{-6} Hz	~10^{-3} Hz

Figure 3.3.5: Trigger rates of the two-level trigger system of the JEM-EUSO instrument. Taken from [257, p. 115].

The second trigger level is situated at the cluster control board. The data of 8 PDMs arrive at a rate of around 57 Hz, at the CCB. The L2 trigger is programmed within a Xilinx Virtex-4QV FX-140 FPGA[10] onboard the CCB. To distinguish the unique pattern of an EAS from background, the L2 trigger algorithm is trying to identify a moving spot over a predefined time. The PDM electronics will send a starting point, GTU and pixel coordinates from the L1 trigger. These coordinates are used by the L2 as a *trigger seed*. It moves small integration box around this seed into a predefined set of directions and integrates the number of photon counts in time . The L2 trigger is issued, once the integrated number exceeds a pre-set threshold value [97, 99]. The integration box is

---

[10] Field Programmable Gate Array

made of 3 × 3 pixels that is moved into 67 directions and integrates ± 7 GTUs. The triggering events are transmitted to the onboard CPU at a rate of 5 mHz [33].

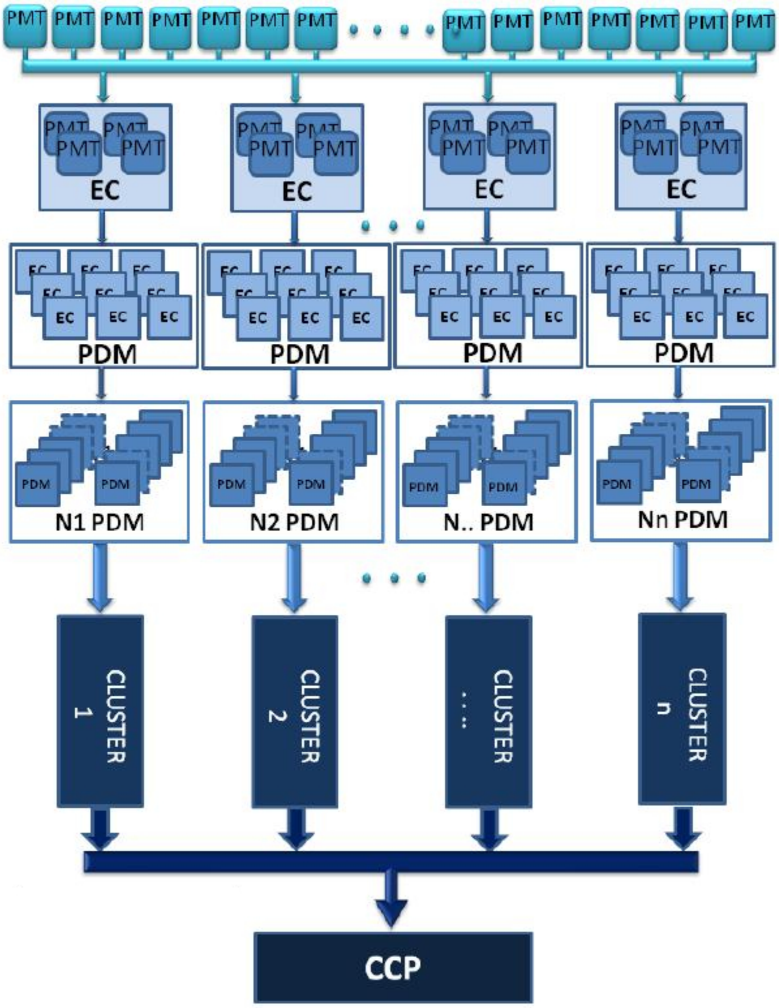

Figure 3.3.6: The hierarchical scheme of the focal surface of the JEM-EUSO instrument. Taken from [257, p. 119].

3.3.4 CALIBRATION

In the course of the mission, the instrument is expected to suffer from a number of deficiencies, among them are uncertainties in the atmospheric conditions, background levels, as well as timing uncertainties. Moreover, parameters of the instrument can be affected, e.g. the tilt angle, pointing errors (due to the attitude instability of the ISS), temperature variations and the age of the instrument [8]. Two different calibration systems will provide information on these uncertainties.

The internal calibration of the instrument components will be conducted by means of built in UV light sources. A light source is made of a LED, placed together with a calibrated photo diode within an integrating sphere. A number of these light sources is placed behind the optics to directly illuminate the focal surface detector. Another set of sources is installed at the edges of the focal surface to emit in the direction of the optics. The light passes the optics and is reflected by the inner side of the closed lid, propagates back through the optics and onto the focal surface. These two setups allow for both, calibration of the MA-PMTs and the optics. However, both methods are relative calibrations to monitor the degradation of the components in time. An absolute calibration of the different parts of the instrument will be performed before launch [118, 226].

To inquire more global information of the setup of instrument and atmosphere, a ground calibration system (or Global Light System - GLS) of xenon flashers and lasers is planned to regularly provide well determined portions of light from different regions of the earth's surface [8, 195] (Fig. 3.3.7). The laser beams can mimic EAS tracks of

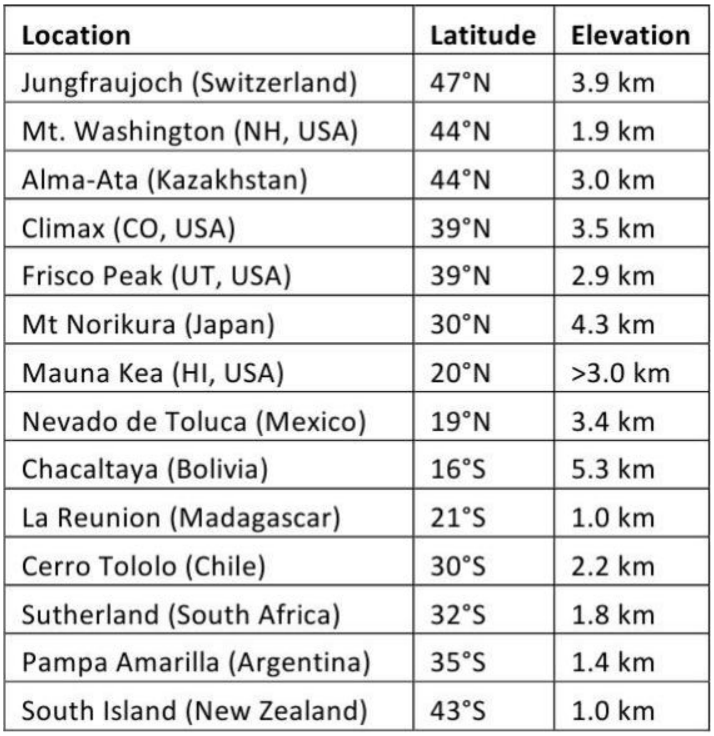

Location	Latitude	Elevation
Jungfraujoch (Switzerland)	47°N	3.9 km
Mt. Washington (NH, USA)	44°N	1.9 km
Alma-Ata (Kazakhstan)	44°N	3.0 km
Climax (CO, USA)	39°N	3.5 km
Frisco Peak (UT, USA)	39°N	2.9 km
Mt Norikura (Japan)	30°N	4.3 km
Mauna Kea (HI, USA)	20°N	>3.0 km
Nevado de Toluca (Mexico)	19°N	3.4 km
Chacaltaya (Bolivia)	16°S	5.3 km
La Reunion (Madagascar)	21°S	1.0 km
Cerro Tololo (Chile)	30°S	2.2 km
Sutherland (South Africa)	32°S	1.8 km
Pampa Amarilla (Argentina)	35°S	1.4 km
South Island (New Zealand)	43°S	1.0 km

Figure 3.3.7: Candidate sites for the GLS units. Taken from [8].

UHECR. Recorded by JEM-EUSO, the angular reconstruction accuracy can be determined and corrected if necessary. The xenon flash lamps provide UV light flashes of well defined intrinsic luminosities as a standard candle. Using this knowledge, the accuracy of the energy reconstruction of UHECR events can be improved [8]. It is envisaged to mount one laser and xenon flasher unit on board of an aircraft. This provides a flexible and mobile solution and enables the possibility to mimic horizontal and downward showers.

3.3.5 ATMOSPHERIC MONITORING

The observational properties of EAS depend on the conditions of the atmosphere. Especially the impact of clouds on the reconstruction of its properties is a major determining factor, due to the scattering and attenuation of the signal light. In order to discriminate well-recorded events from insufficient ones or to correct accordingly, a good knowledge of the cloud's position and the cloud top altitude is inevitable. (See Chap. 3.5) To retrieve this information, JEM-EUSO is equipped with an atmospheric monitoring system, consisting of an infrared (IR) camera and a light detection and ranging (LIDAR) device. In the broader sense, also the GLS (see 3.3.4) can be regarded as part of the AM system, since it will also deliver information on the atmospheric conditions. Moreover, JEM-EUSO will make use of meteorological data by weather forecasting services, like the National Centers for Environmental Predictions (NCEP), the Global Modeling and Assimilation Office (GMAO) and the European Centre for Medium-Range Weather Forecasts (ECMWF) [218, 266].

THE IR CAMERA will deliver information on the cloud coverage and retrieve the altitudes of optically thick clouds. It collects IR photons emitted by the cloud top to estimate its altitude. This can be inferred, due to the effect that the target temperature and emissivity are correlated to the clouds altitude. This works best in the troposphere, where there is a linear dependence of 0.6 K per 100 m of height.

The IR camera setup is a refractive optics, made of germanium and zinc selenide and an uncooled microbolometer [257, p. 180] (Fig. 3.3.8). It takes data in the wavelength band of 10 – 12 μm. Its FOV is identical to the one of the main telescope, with an angular resolution of about 0.1°. The camera accomplishes an accuracy of 3 K, which corresponds to an error of 500 m in cloud top estimation. It has a frame rate of 1/30 s and transfers the data every 30 s, which corresponds to half of the FoV of the telescope, due to the movement of the ISS.

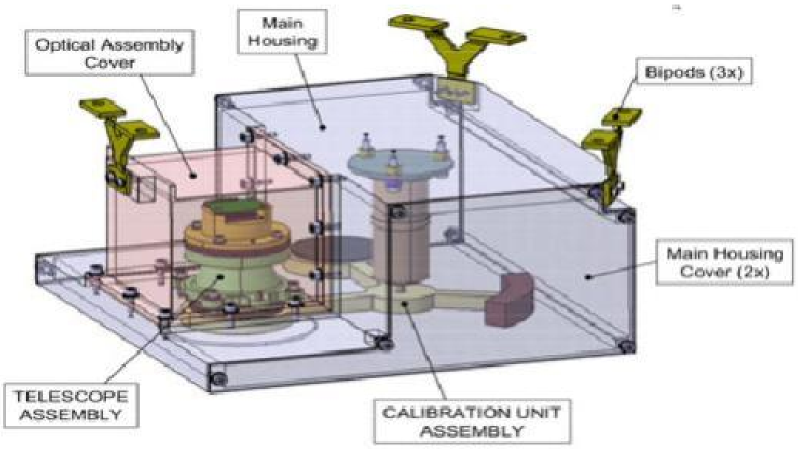

Figure 3.3.8: The JEM-EUSO Infrared Camera. Taken from [218].

THE LIDAR will infer the altitudes of optically thin cloud tops and the optical depth. The device uses a Nd:YAG laser and a pointing mechanism which steers the beam by a mirror in the direction of the EAS event, once a trigger occurs. It is operated at a wavelength of 355 nm. The main telescope acts as the receiver for the reflected lidar beam.

3.4 SCIENTIFIC OBJECTIVES

The JEM-EUSO mission has been developed to address the exigent questions in UHECR research. It will investigate the nature of the extreme energy side of the universe. However, due to its unique design, the telescope is prepared to deliver data on other scientific objectives at the same time. JEM-EUSO is a high aperture and high sensitivity instrument. Its MA-PMTs have single photon count abilities and a fast temporal resolution. This novel setup for UV imaging of the atmosphere can be suitable for atmospheric science, as well as for geophysical research [276].

3.4.1 Main Objectives

The identification of single sources is the main mission goal of JEM-EUSO. The exposure of JEM-EUSO in combination with its angular resolution accuracy will decisively distinguish between the isotropic and the anisotropic scenario. In the latter case, it will collect a meaningful amount of UHECR to effectively identify the potential sources. Owed to the $4\,\pi$ coverage of the celestial sphere, it can therefore map the entire sky. Its data will allow to correlate the cluster of arriving UHECR with astronomical objects [257, p. 7].

The spectroscopy of individual sources is the next step after their identification. Most of the recent experiments have confirmed a strong suppression of the UHECR flux at $6 \cdot 10^{19}$ eV. However, it is unclear whether this steepening is a feature of the GZK effect or resulting from an potential acceleration limit. JEM-EUSO can perform a spectral analysis of different spatially separated regions of the sky. This will enable us to constrain acceleration and emission mechanisms [257, p. 11]. JEM-EUSO will for the first time enable astronomy through the particle channel.

3.4.2 Exploratory Objectives

The detection of UHE-γ is the top exploratory objective of the mission. The composition of UHECR arriving to the earth should, at least to some extent, include UHE-γs. These photons are either produced as a propagation feature, by means of the GZK-effect or directly in the sources as secondary products. A third scenario, predicts UHE-γ as a result of the decay of super-heavy dark matter.

The ratio of expected UHE-γ strongly depends on the production process of UHECR. In the first case, γ appear as secondary particles when UHE-protons interact with relic photons of the cosmic microwave background. (See Chap. 2.5.1) In this case, the ratio of UHE-γ is estimated to be of the order of 10%. Thus, for conventional UHECR observatories, the UHE-γ flux is far too low for a clear measurement. Due to its large aperture, JEM-EUSO has a sensitivity, sufficient for the detection of fractional fluxes (Fig. 3.4.1). Moreover, it would allow even for the detection of secondary γ from individual sources. Therefore, JEM-EUSO will help to further constrain exotic models.

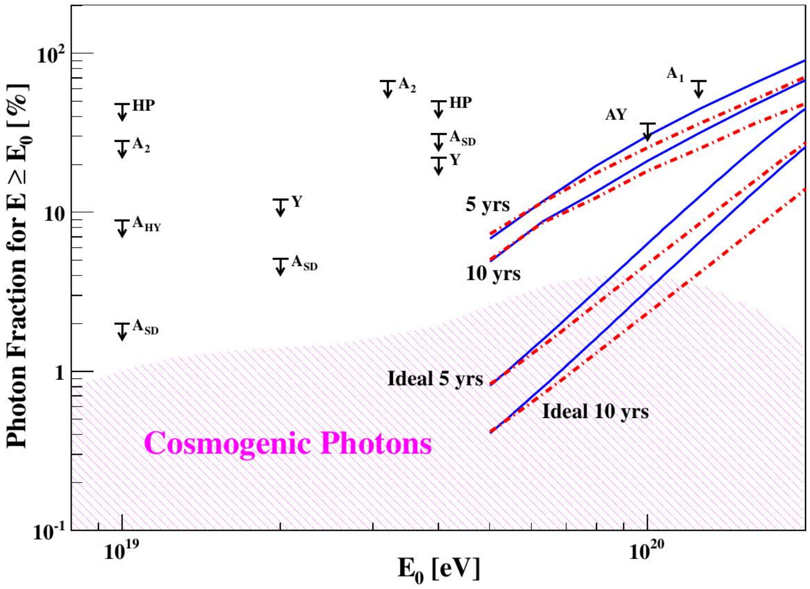

Figure 3.4.1: Upper limits on the fraction of photons in the integral cosmic ray flux at 95% confidence level as a function of primary energy. Solid lines correspond to the expected upper limits for JEM-EUSO in Nadir mode and dot-dash-dot lines correspond to a combination of Nadir and Tilted modes. A Gaussian uncertainty on the determination of the X_{max} parameter of 100 g cm^2 is assumed for the calculations. The shaded region indicates the prediction for GZK photons. Black arrows are experimental limits, HP: Haverah Park, A1 and A2: AGASA, AHY and ASD: PAO, AY: AGASA-Yakutsk, Y: Yakutsk. Pic. and caption taken from [247].

UHE-γ, being neutral particles are interesting messengers, since their trajectories are not distorted by magnetic fields and will therefore pinpoint the direction of their creation sites [247].

THE DETECTION OF UHE-ν is the second exploratory goal of the mission. Due to the GZK-effect or to the nuclei disintegration effect (described in Chap. 2.5) cosmogenic neutrinos are steadily produced. Thus, detecting these cosmogenic neutrinos can give a better understanding of the primary composition of UHECR. By detecting extreme energy neutrinos, we can observe sources far beyond the GZK horizon, since there is no magnetic bending. Moreover, apart from the cosmological red shift, no energy losses occur on their way through the interstellar medium [257, p. 20]. Both processes, GZK and nuclear disintegration have characterizing imprints on the neutrino spectrum. An experiment, highly sensitive to neutrinos, could therefore discriminate the models from another. In case of top-down models an even larger fraction of neutrinos is expected. Many of them have been ruled out already on the base of the existing data from ground experiments. A high aperture experiment like JEM-EUSO can effectively reduce these limits and help to further constrain top-down models.

However, two problems arise for the successful detection of neutrinos. First of all, since their cross section is very low, a huge target volume is required to observe a relevant number of them. Additionally, the discrimination of neutrinos from other particles such as protons or nuclei by taking advantage of the EAS maximum is a sophisticated task. Large efforts have been invested to study the neutrino observation capabilities of JEM-EUSO [see 64, 139, for details] and are still ongoing. A recent study has shown the neutrino trigger capabilities of JEM-EUSO [247] (Fig. 3.4.2).

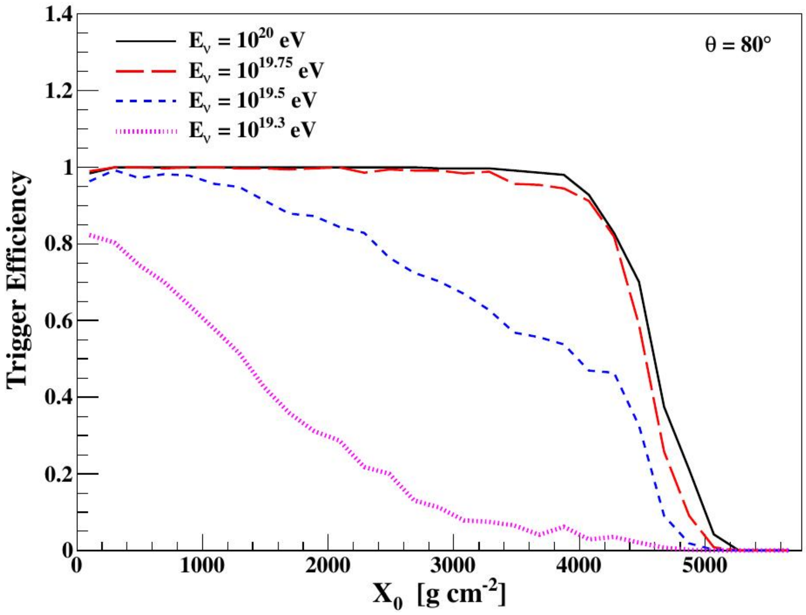

Figure 3.4.2: Trigger efficiency as a function of the grammage of the first interaction point corresponding to electron neutrino showers that hit the ground on the center of the field of view of the JEM-EUSO telescope in Nadir mode. The zenith angle of the showers is $\theta = 80°$. Pic. and caption taken from [247].

The study of magnetic fields is another mission objective. JEM-EUSO can play a key role to probe the magnetic fields between the emitter of UHECR and the earth. The spatial distribution of the potential UHECR sources carries information on the galactic and extra-galactic fields. By analysing the smearing of the image created by UHECR

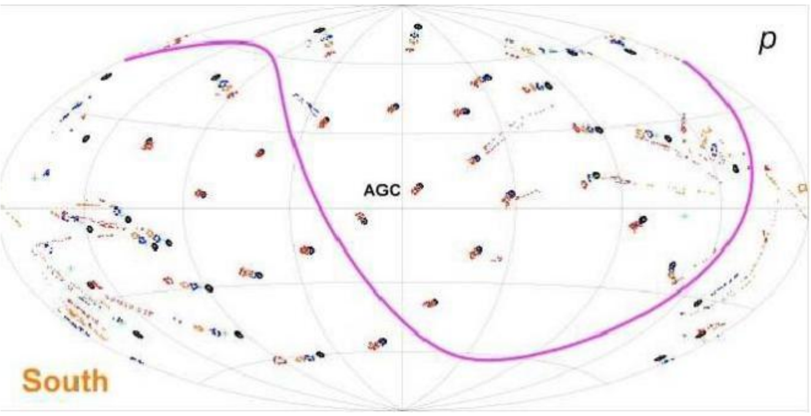

Figure 3.4.3: Deformation of the point spread function of individual sources as a function of energy and location on the sky for a certain possible realization of the Galactic magnetic field. Black corresponds to the highest energy, 10^{20} eV and red to the lowest, $10^{19.4}$ eV. Different realizations produce distinctive patterns. Pic. and caption taken from [179].

of different energies, the direction and strength of the traversed magnetic field can be inferred [257, p. 24] (Fig. 3.4.3).

THE VERIFICATION OF THE GENERAL THEORY OF RELATIVITY (GTR) is regarded as a potential task for the mission. UHECR are understood as a tool to probe the theory of general relativity for Lorentz factors of $\gamma \approx 10^{11}$. The spectral shape of trans-GZK events may be forged by non-standard physics. These features would be disguised from current ground experiments simply by the scarcity of events exceeding 10^{20} eV. By an increase of statistics by at least one order of magnitude, JEM-EUSO could serve as a key experiment to discover new physics at the highest energies [257].

ATMOSPHERIC PHENOMENA can be observed by JEM-EUSO due to its designated design since it is essentially a large UV camera that monitors the atmosphere with a high time resolution. The IR-system and the lidar provide additional information on the observed air volume. This combination of instruments allows for the observation of atmospheric events including meteors, meteoroids and other atmospheric phenomena [67, 276].

Meteors arrive to the earth at hypersonic speeds between 11 and 73 km/s. While traversing the atmosphere, their kinetic energy is converted to heat and light via collisions of the body with air molecules. The temperatures reach up to 2500 K. Thus, along the trajectory ions and free electrons produce light by de-excitation. The wavelengths of the emitted radiation are in the visible, but also in the IR and UV range. The spectrum consists of a black body component and discrete emission lines of nitrogen, oxygen, but also metals injected by the meteor itself [58, 83]. The distribution of their size and inventory is a major concern of modern planetary science. This knowledge is important to constrain theories of the evolution of the smaller bodies in the solar system. Moreover, these studies are vital to evaluate impact hazards on the terrestrial biosphere [257, p.30].

High energetic meteors create dangerous dust clouds that can potentially harm aircrafts. An efficient fireball detection system could help to ease the threads of meteorite impacts for human life and infrastructure. Current meteor observatories are networks of ground based telescopes. Space-borne observation facilities can provide coverage of a wider area of the sky with respect to ground based detectors. Their dependence on weather condition is less strong, due to the fact that a large portion of the atmosphere is above the clouds. Due to its high sensitivity in the UV range between 300 and 400 nm, JEM-EUSO can be an efficient tool to observe these events. It can serve as a pathfinder for a future space-based detection system of meteors and fireballs [58, 83].

TRANSIENT LUMINOUS EVENTS (TLE) were first proposed in the 1920s. However, it took until 1989 for the first observations. TLE, are a classification for various electric discharge phenomena in the upper atmosphere:

- *Sprites* are bright flashes at altitudes of 40 - 90 km. They occur in groups above thunderstorm clouds and last typically a few ms. The mechanism behind is not fully understood. Observation in the μs order could help to explain their origin and development;

- *Halos* occur above sprites at altitudes of 75- 85 km. They are diffuse bright regions with extensions of 100 km;

- *Elves* are the most common among TLE. They are rapidly expanding light discs at altitudes around 85 - 95 km. The extension of the discs can reach diameters up to 200 km;

- *Blue jets* are flashes ejected by centre regions of thunderstorms that are not going down to earth but upwards in the ionosphere. They can reach total energies of the order of 30 MJ;

- *Terrestrial gamma ray flashes* have first been recorded in 1994 by the Compton Gamma Ray Observatory. They are most likely produced at the top of thunderstorm clouds.

By monitoring TLEs, JEM-EUSO would contribute to our understanding of the atmospheric plasma structure [257].

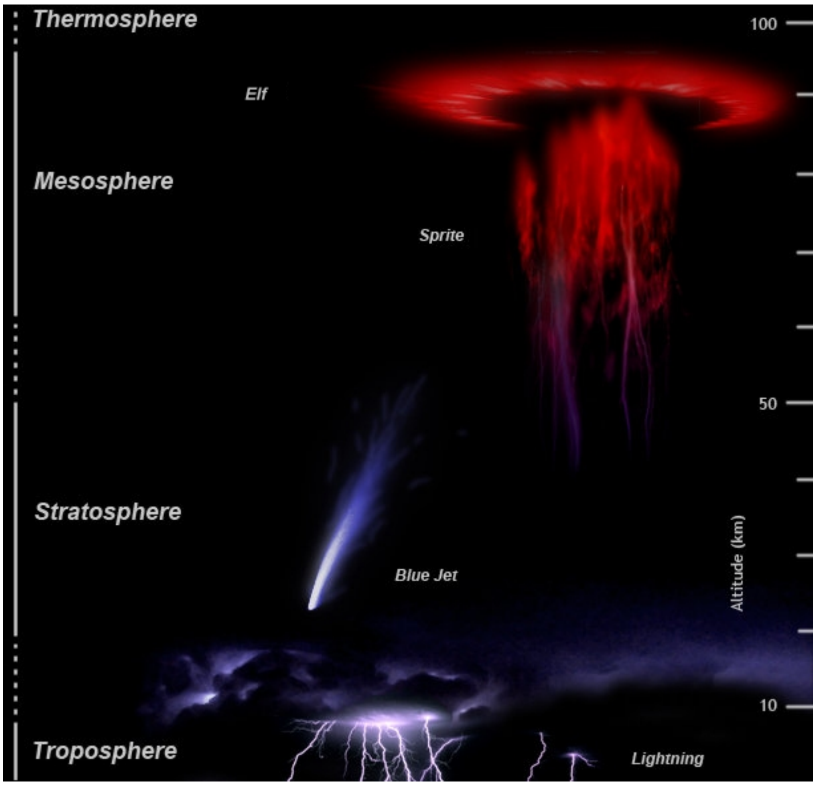

Figure 3.4.4: Transient luminous events (TLE) in the upper atmosphere. Taken from [257].

3.5 EXPECTED PERFORMANCES

The JEM-EUSO mission will effect unprecedented performances in UHECR detection, owed to outstanding gains in both aperture and exposure with respect to any current ground observatory [7, 54, 55, 57]. The expected performance has been evaluated by means of extensive simulation studies. These estimates aim not only at quantifying the exposure, but also on the angular, X_{max} and energy resolution. In this chapter we briefly report on the exposure as well as on the X_{max} / energy resolution. The angular resolution, being the essence of this dissertation, is extensively discussed in the following chapters.

3.5.1 EXPOSURE

To estimate the exposure of the telescope, the aperture is calculated, first of all. The aperture is convoluted with other determining factors, such as observational duty cycle, cloud efficiency and the expected loss of coverage. In a high statistics study, UHECR events have been simulated in an area, significantly larger than the actual FOV. The geometrical aperture is defined by:

$$A(E) = \frac{N_{trigg}}{N_{inject}} \cdot S_{inject} \cdot \Omega_o \tag{3.1}$$

with the ratio of triggered to injected events, $\Omega_o = \pi\, sr$, the solid angle acceptance for $0° < \theta < 90°$ and S_{inject} the area in which the showers are injected [7, 57] (Fig. 3.5.1).

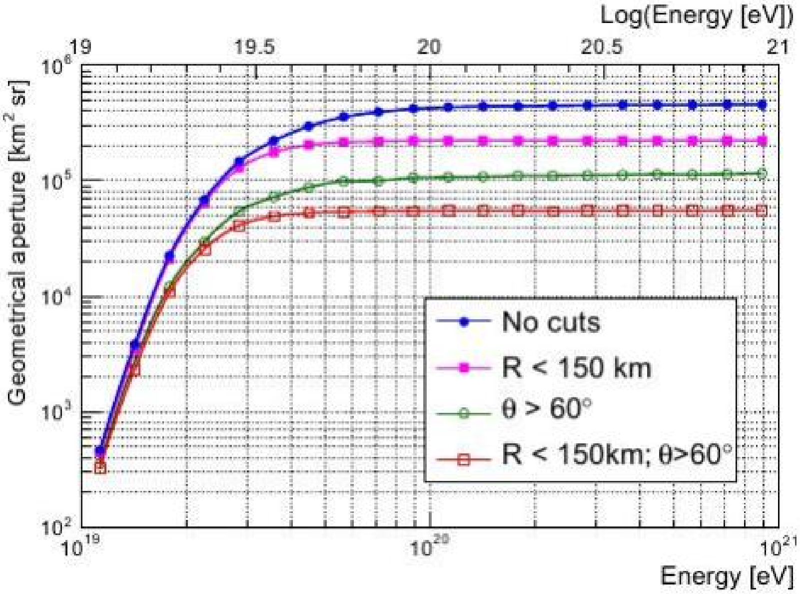

Figure 3.5.1: Geometrical aperture as a function of energy. The filled circles and squares indicate geometrical apertures for the entire observation area and R $<$ 150 km respectively, where R indicates the distance of the impact location of the EAS from the center of FoV. The open circles and squares include a zenith angle cut of h $>$ 60°. Pic. and caption taken from [7, 57].

A major determining factor for the exposure is the role of clouds. In cloudy conditions, it is affected depending on cloud-top altitude and optical depth. The extent to which clouds impact the observation, depends on the zenith angle of the UHECR. The steeper the particle arrives, the more likely it is that the EAS fluorescence light maximum might develop below the cloud top [124].

Low-clouds might only obstruct the end of an air shower. As long as the major part of the shower is visible to the telescope, information on energy and X_{max} can still be recovered. In some light-polluted environments, low clouds might even improve the measurements by attenuating parasitic photons originating from man-made light sources. The AM system will play a vital role to locate cloud distributions and to determine their top altitudes. Using this information, together with the Cherenkov footprint, allows for an improved estimate of the EAS impact position on the cloud [124].

Also high altitude clouds with small optical depths are not expected to strongly interfere with the EAS detection. However, due to a slight attenuation, the energy reconstruction could be affected. To overcome this potential problem, the AM system will identify problematic scenes and allow to correct the data. A clear atmosphere (32% of the cases) provides good conditions for measurements. Considering the additional low cloud occurrences, 61% of the events can be used for analysis in 'good scene' conditions, while 20% of the cases can be regarded as cloudy. Nevertheless, a significant part of the signal can still reach the detector [124, 224]. These events can be discriminated from those observed in good condition by the use of data acquired by the AM system. Most likely, the determination of E and X_{max} will suffer from extinction losses.

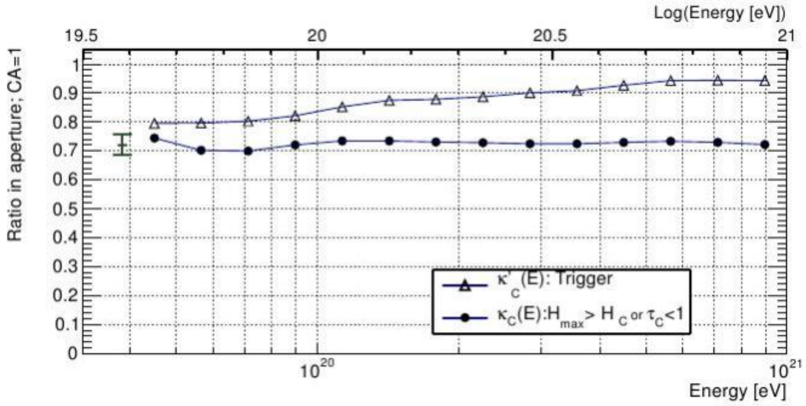

Figure 3.5.2: Ratio of the geometrical aperture for averaged cloudy condition (circles) to that from clear atmosphere (triangles) as a function of energy. For the cloudy case, $H_C < H_{max}$ or $\tau_C < 1$ are required for triggering EAS events. The error bars denote an estimated uncertainty on κ_C. Pic. and caption taken from [124, 224].

Despite that, angular reconstruction with a less precise quality will still be possible to some extent. To conclude, the overall cloud efficiency κ_C has been estimated as 72 % [124, 224]. It is a major parameter determining the exposure (Fig. 3.5.2).

An additional parameter affecting the exposure in the observational duty cycle. Since the altitude of the ISS is at about 400 km, one orbit takes about 90 minutes [251]. During the ISS daytime, the instrument's lid has to be closed to prevent damage of the PDMs due to bright sunlight. Also at night, phases with too much moonlight can render the observation impossible. Based on the data of the Tatiana satellite [108, 109], a study has been conducted to estimate the duty cycle of the JEM-EUSO mission [55]. The observational duty cycle is defined as the time fraction in which less than 1500 photons $m^{-2}sr^{-1}ns^{-1}$ enter the telescope. It has been estimated as $\eta_\circ$ =20% — a rather conservative assumption [see 7, 57, for details]. Further losses of coverage are induced by lightnings ($\sim$ 2%), auroras ($\sim$ 1%) and anthropogenic light sources ($\sim$ 7%) are summarized as the overall loss of coverage f_{loc} =10% [7, 57].

Taking into account κ_C, the observational duty cycle $\eta_\circ$ = and the overall loss of coverage f_{loc}, the annual exposure can be defined as as

$$\text{Annual Exposure} \equiv A(E) \cdot \kappa_C \cdot \eta_\circ \cdot (1 - f_{loc}) \cdot (1[yr]). \qquad (3.2)$$

(Fig. 3.5.3)

3.5.2 ENERGY AND X_{max} RESOLUTION

The ability to reconstruct the energy of the primary particles is one of the key performance parameters of the mission. Two complementary methods, the slant depth method and the Cherenkov method have been investigated and yield comparable results. Especially for high energies and high zenith angles for which the results improve in general, both methods are complementary [see 99, for details]. In the most recent study [102], the energy resolution of the instrument has been estimated for events distributed on the whole field of view and for energies in the range 10^{19} – 10^{21} eV and zenith angles between 0° and 90° distributed as $\sin(2\theta)$ (Fig. 3.5.4).

The overall energy resolution is around 20 to 30% above $7 \cdot 10^{19}$ eV. Considering only those events in the centre of the FOV (± 20 km), the energy resolution is even improved. Here the resolution yields between 5 to 20% [102]. Applying cuts on the

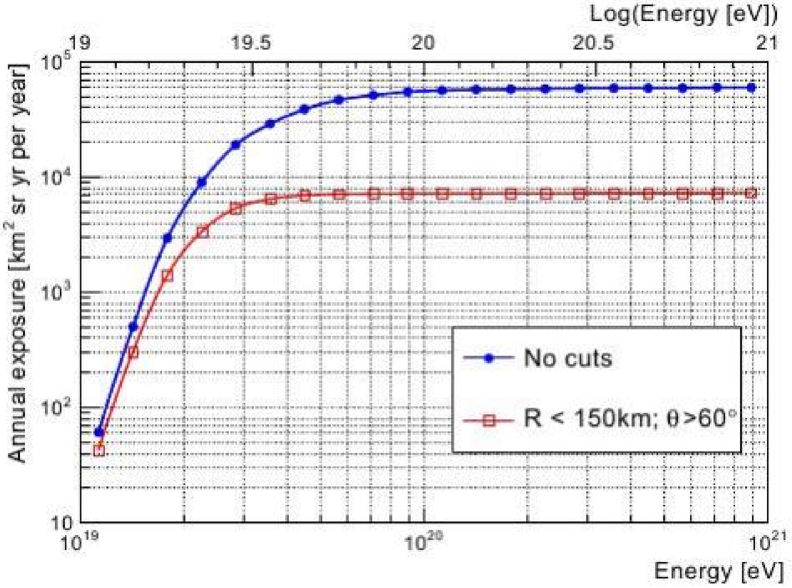

Figure 3.5.3: Annual exposure as a function of energy obtained for the two extreme conditions shown in Fig. 3.5.1: (a) entire observation area (filled circles); (b) cut on distance R $<$ 150 km and on zenith angle h $>$ 60° (open squares). Pic. and caption taken from [7, 57].

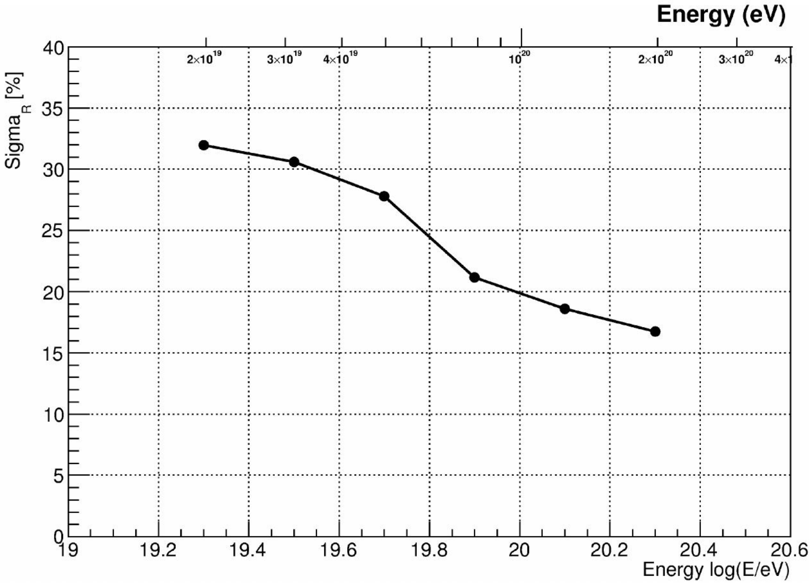

Figure 3.5.4: JEM-EUSO energy resolution with the slant depth method: σ of (E_{reco}-E_{real}) · /E_{real} for all event sample and entire FOV. Events selected with DOF $>$ 4 χ^2 /Ndf $<$ 3. Taken from [102].

number of DOF and on χ^2 /Ndf can discriminate successfully reconstructed events from failed ones. However, the application of quality cuts decreases the reconstruction efficiency by about 15% [99] (Fig. 3.5.5).

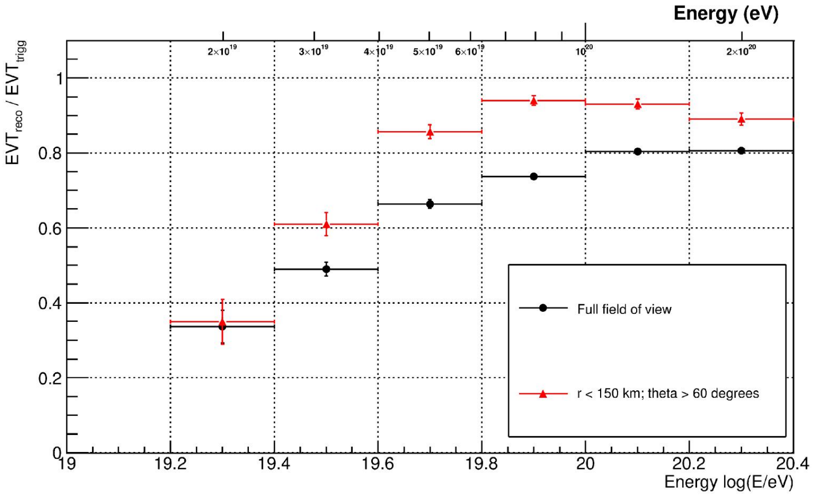

Figure 3.5.5: The fraction of events surviving the cut DOF > 4 χ^2 /Ndf < 3. The fraction is shown with respect to the triggered events. Black dots: full FOV, red triangles: inside a FOV radius of 150 km and zenith angles $> 60°$. Taken from [102].

In the same study, the X_{max} resolution has been assessed for the FOV region within a box of (x: ± 150, y: ± 150) km. The events have been simulated with zenith angle between 0° and 90° and for various energies. The X_{max} have been reconstructed by means of their Cherenkov mark. In general, the Cherenkov method can be considered as more solid for the X_{max} determination. The overall X_{max} resolution is of the order of $\sim$ 100 g/cm^2 (Fig. 3.5.6). By the application of quality cuts as described above, the resolution can be further increased [99].

The science requirements for the angular resolution capabilities of the telescope are defined as $\leq 2.5°$ for showers with zenith angles exceeding 60°. The scope of this thesis is to verify if this requirement can be met.

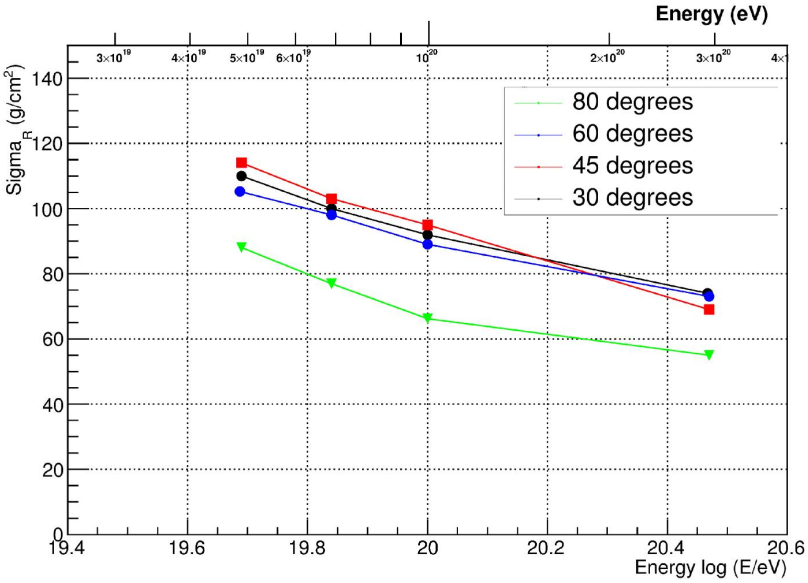

Figure 3.5.6: JEM-EUSO X_{max} resolution for various zenith angles and energies with the slant depth method:. Events are impacting in the centre area of the FOV. The geometry has been reconstructed with the slant depth method. Pic. and caption taken from [102].

3.6 PATHFINDER MISSIONS

Three pathfinder missions are going to be conducted within the framework of the JEM-EUSO preparations. All three pathfinders are essentially scaled down versions of the large telescope. In each setup a small version of the focal surface detector works in combination with an optical system that also resembles the one of JEM-EUSO. Two of the pathfinders are technically relatively identical. Having a diameter of 1 m, the EUSO-Balloon and TA-EUSO are both approximately of the same size. Mini-EUSO, the third pathfinder, is considerably smaller.

The pathfinders serve to illustrate the technical readiness potential of the mother mission. They carry key components of JEM-EUSO such as the MA-PMTs, electronics and the optical system. While operating, realistic end-to-end tests of the setups are obtained. The EUSO-Balloon will play a special role, since it will conduct the measurements under quasi-space conditions. This yields an even better argument for the maturity of the JEM-EUSO concept [126]. Moreover, the tests conducted by the pathfinder missions will help to configure the main instrument. The EUSO-Balloon and Mini-EUSO are expected to deliver information on the atmospheric background conditions.

3.6.1 EUSO-BALLOON

The EUSO-Balloon is a scaled down version of the JEM-EUSO detector. It is constructed of components, identical to the ones of the JEM-EUSO detector [259, 271] (Fig. 3.6.1). The EUSO-Balloon is a UV refractor telescope, mounted on a stratospheric balloon gondola. A system of three Fresnel lenses made of PMMA focuses the incoming light onto a single PDM on the focal surface. PDM, MA-PMTs, PDM readout board, CCB and data processor resemble the corresponding JEM-EUSO components [200, 201]. The instrument does not have a circular lens system but a squared one. Its field of view is 12° × 12°.

Beginning in summer 2014, a number on stratospheric balloon flight will be conducted at altitudes up to 40 km. The balloon will fly above various kinds of ground conditions. This allows for a deep analysis of how the background conditions change with the ground composition.

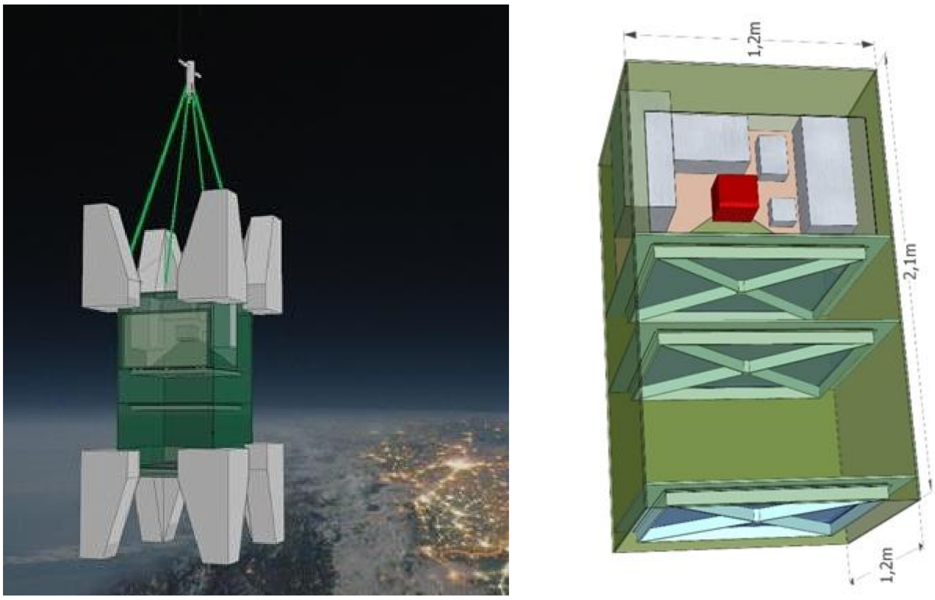

Figure 3.6.1: Left: EUSO-Balloon equipped with floating pads for a soft touch down and buoyancy in case of a water landing. Taken from [201]. Right: EUSO-Balloon Scheme. Taken from [126].

The scientific goal of the mission is to conduct a background study with varying ground conditions such as urban areas, sea, forests, etc. Due to its relatively small effective aperture, the possibility of the actual observation of a real UHECR event is regarded as minor. During the mission however, it is planned to test the trigger algorithms, the near real time analysis (NRTA) software and reconstruction techniques by using artificial EAS. These EAS will be induced by a laser mounted on a helicopter. The major advantage is that the timing as well as the energy and the spectrum are exactly known, making it easier to calibrate the detector accordingly [270, 271].

The first balloon launch is scheduled for summer 2014 in Timmins, Ontario in Canada. In the future, multiple flights will be conducted under the guidance of the French Space Agency CNES[11] [126, 259].

3.6.2 TA-EUSO

Like the EUSO-Balloon, Telescope Array EUSO (TA-EUSO) is a scaled down version of the JEM-EUSO instrument. It is identical to the Balloon-EUSO pathfinder with two exceptions: The optical system is made of only two lenses. The middle lens (diffractive lens) is not necessary in this setup, since the field of view is more narrow (± 4°) with respect to EUSO-Balloon. However, the other lenses are square Fresnel lenses with the side length of 1 metre. The PDM is the same as for the EUSO-Balloon, Mini-EUSO and JEM-EUSO [79]. This pathfinder is deployed at the Telescope Array site in Utah, USA [80, 126] (Fig. 3.6.2).

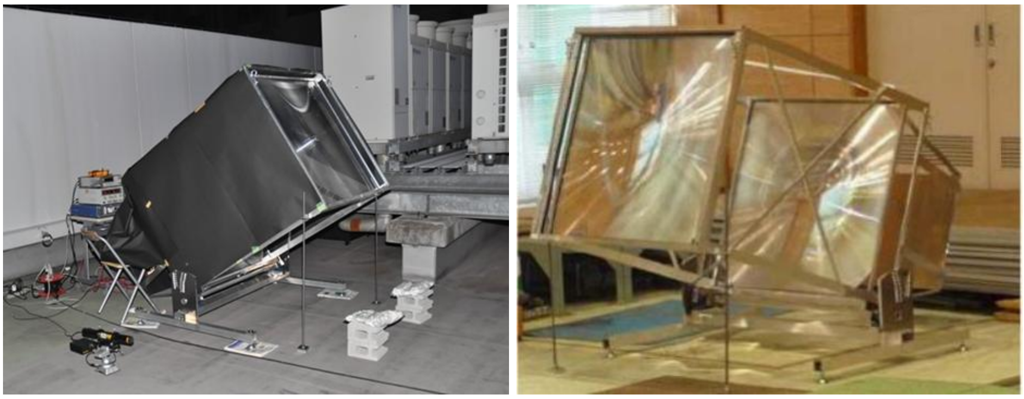

Figure 3.6.2: left: TA-EUSO, right: TA-EUSO Optical system. Pic. taken from [126].

The purpose of this pathfinder is to demonstrate via an entire end-to-end setup the advanced state of the proposed JEM-EUSO components. The TA-EUSO pathfinder takes advantage of the already existing infrastructure of the TA site, i.e. the electron

---

[11] CNES: Centre National d'Etudes Spatiales

beam facility and a ground laser for calibration [264], [79]. The utilization of the same calibration devices allows for cross-calibrations between the two detectors and an absolute energy calibration [237]. Also different from the EUSO-Balloon pathfinder, TA-EUSO is equipped with an external trigger line [79]. Thus, whenever TA records an UHECR event and the FOV is identical, it should also be registered by TA-EUSO.

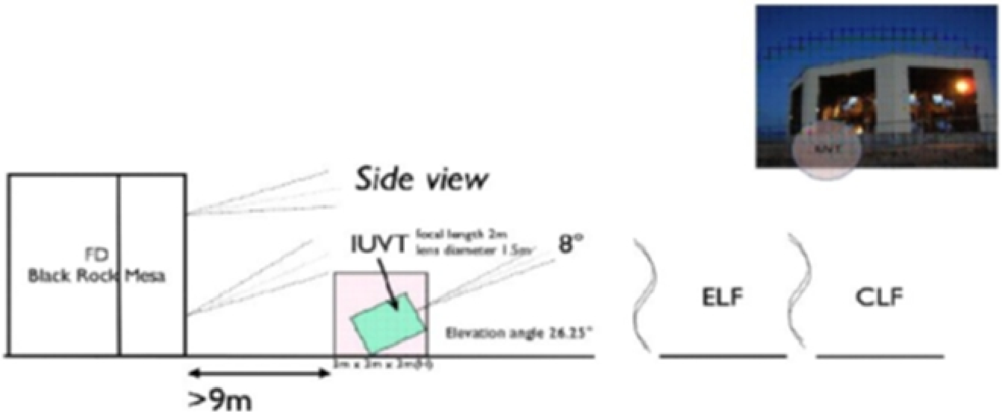

Figure 3.6.3: The TA-EUSO detector deployed at the TA site in front of the Black Rock Mesa station. Electron light facility (ELF) and central laser facility (CLF) indicated.

3.6.3 MINI-EUSO

The third pathfinder under construction, is the Mini-EUSO mission. Being approximately 10 times smaller than the JEM-EUSO instrument, it will consist of 1 PDM and the corresponding readout and data processing electronics like the other pathfinder missions. The optical system, made of two Fresnel lenses, will have a diameter of 25 cm (Fig. 3.6.4). Mini-EUSO will be transported to the ISS by one of the supply carriers that arrive at the space station regularly [52]. Accessible by the astronauts, it will be used to monitor the earth's atmosphere from inside the pressurized section through one of its UV transparent windows. Currently, it is planned to make use of the Russian module *Zvezda* and to look downwards to earth to the nadir. The intention of the mission is to validate the duty cycle for ISS based UHECR experiments and to determine the energy threshold. It is not supposed to search for UHECR events — this is out of the scope of this mission. It is rather a possibility to study the UV background from the altitude of the ISS. The current background data available have been measured by the Tatiana satellites [108, 109]. However, it has been measured without an optical system. Mini-EUSO will be able to make an absolute calibration of the MA-PMTs in flight and to set the shower energy threshold. Even though, Mini-EUSO will most likely not be able to observe any UHECR induced EAS, due to its low aperture (limited by the window size), it will certainly perform measurements of atmospheric phenomena like lightnings and perhaps meteors [260].

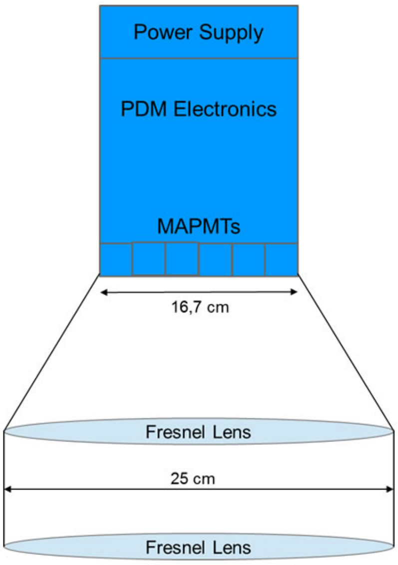

Figure 3.6.4: Cross-section of the Mini-EUSO detector. Taken from [260].

The Mini-EUSO phase A study is at present under evaluation of the ROSCOSMOS Scientific Committee. The final approval is still pending [260].

3.7 ACCOMODATION STUDY: SPACEX

Even though, originally planned to be launched by the Japanese H2B rocket and transferred to the ISS by means of the HTV, the accommodation on the SpaceX *Dragon* Spacecraft is being discussed as a potential alternative. SpaceX is a commercial space contractor [74]. It is the first private company which has accomplished to deliver cargo to the ISS [268] (Fig. 3.7.1). In future, it is envisaged that also manned spacecrafts will be launched by SpaceX.

The Dragon has a payload capacity of 6 t. It has a pressurized and an unpressurized part. The JEM-EUSO instrument can be accommodated in the unpressurized section of the Dragon, called the Trunk. Since the Japanese HTV and the Dragon of SpaceX

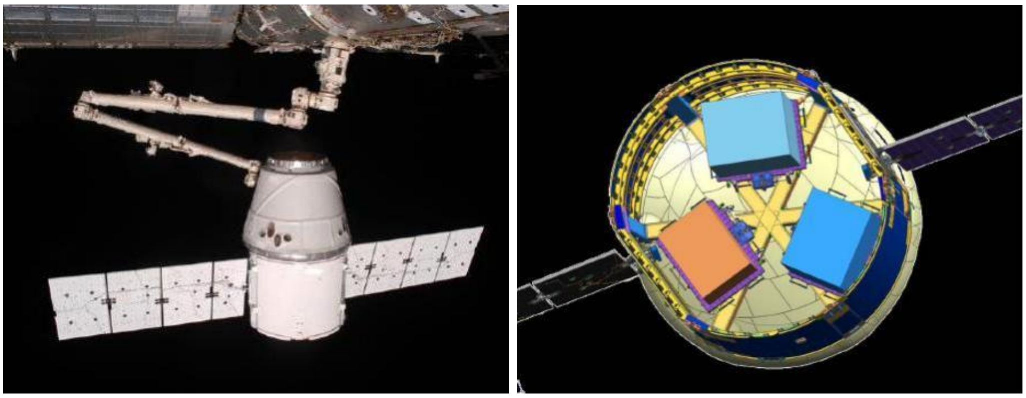

Figure 3.7.1: left: The Dragon Spacecraft of SpaceX, right: The Trunk of the Dragon with three payloads. Pics. taken from [9] and references therein.

are differently structured, certain design changes of the telescope will be necessary.

Usually, the payloads transported by the Dragon are delivered by the flight releasable attachment mechanism (FRAM). Unfortunately, the mass of JEM-EUSO requires another solution, since the FRAM cannot handle such heavy weights. Thus, a custom made solution is proposed [9].

Another change of the telescope's design is imposed by the different shapes of cargo bays of the two spacecrafts. The original instrument has been proposed with a side cut optics and a diameter of 2.65 m to fit in the hatch of the HTV. The Dragon on the contrary allows for a circular optics design, due to its annular shape. It would be possible to maintain the same aperture, while decreasing the diameter of the optics. This bears the advantage of less weight and increased stability. Another benefit is the attachment of the payload in the Trunk. The telescope could be attached to the Trunk at its focal surface end, which is the most heavy part of the instrument. The HTV configuration would require an attachment at the opposite side. This means that the forces imposed on the instrument during the launch phase, would need to be withstand by the tube structure of the telescope body. Therefore, in the Dragon configuration a less stable tube structure is sufficient which saves additional mass [9]. For additional information of the space available in the Dragon Trunk, see appendix 7.2.

3.8 OTHER UHECR MISSIONS

3.8.1 TUS AND KLYPVE

In parallel to (ESA-)EUSO/JEM-EUSO, the TUS/KLYPVE program emerged in Russia in the first decade of the 21st century [149, 150].

The program comprises of a sequence of missions for the observation of transient luminous event phenomena and energetic particles impacting the upper atmosphere [203]. Two small pathfinder missions, Tatiana and Tatiana 2 have been launched into space already [108–110]. Both missions were supposed to conduct UV background measurements, using PMTs alike the later, large missions. Unfortunately, the first Tatiana measurements have not been successful, due to technical errors. The second Tatiana mission, however has provided precious information on the UV background, though it is important to note that the measurements have been performed without any focusing optics [108, 109].

Table 3.8.1: Key parameter of TUS and KLYPVE. Data from [93, 150, 151].

	Mission	
	KLYPVE	TUS
Orbit Altitude	~ 400 km	$350 - 600$ km
Mirror Area	10 m^2	1.4 m^2
Focal Distance	3 m	1.5 m
Optics Aperture	10 m^2	1.8 m^2
Geom. Aperture	$2.2 \cdot 10^4$ km^2 sr	$2.0 \cdot 10^4$ km^2 sr
Annual Exposure	3000 linsl. yr^{-1}	2700 linsl. yr^{-1}
Pixel Angular Size	$< 0.2°$	$0.6°$
Field of View	$12° \times 12°$	$9° \times 9°$
Number of Pixel	2304	256
Time Resolution	0.4 μs	0.8 μs

TRACK UV SETUP (TUS) relies on a reflective optics using Fresnel mirrors [3, 151] (Fig. 3.8.2). Its launch is scheduled for 2014 [154]. It is a pioneering mission for the observation of UHECR, TLEs and the analysis of the UV background from space. Accommodated on board the Lomonosov satellite[12], it will orbit the earth at an altitude

---

[12] Another payload on this platform is the UFFO (Ultra-Fast Flash Observatory) detector. Devel-

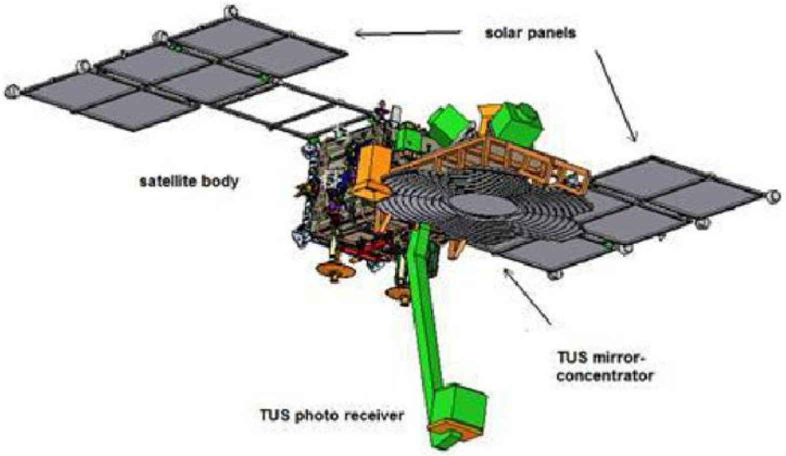

Figure 3.8.1: The TUS detector as payload on board the Lomonosov satellite. Taken from [151].

of 350 – 600 km. TUS can be regarded as a pathfinder for the JEM-EUSO mission in the sense that it uses the same observation approach [93, 145]. Having a mirror area of

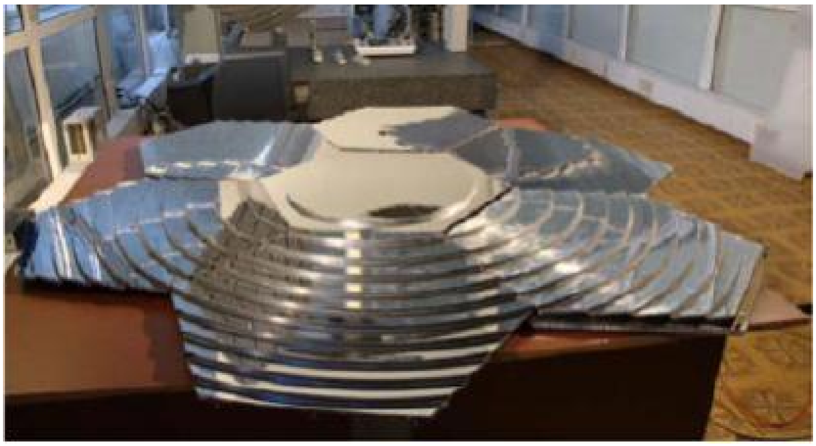

Figure 3.8.2: Segmented Fresnel mirror of the TUS detector. Taken from [93].

1.4 m^2, TUS is expected to observe about 50 UHECR events per year from the energy of $5 \cdot 10^{19}$ eV on. It is equipped with a Hamamatsu R1463P photomultiplier of 16×16 (=256) pixels. According to simulations, it will be able to discriminate UHECR events with energies $> 10^{20}$ eV from background, even in moonlit nights [150].

---

oped in parts by the Korean members of the JEM-EUSO Collaboration, it is an instrument to search for gamma-ray bursts. The trigger part of UFFO uses the PMT and electronics which will be used in the JEM-EUSO mission [121].

KLYPVE is the main mission for UHECR observation. Instead of being part of a free flyer satellite, it is going to be hosted by the Russian module *Zvezda* on board the ISS. It is scheduled for launch not exceeding 2017. Like TUS, it uses a Fresnel mirror to focus the UV light emitted by the EAS onto the focal surface detector. The mirror has a diameter of 4 metres and consists of 16 segments as the current baseline. They will be assembled by Astronauts/Kosmonauts in space [93]. Due to its larger collection power it will have an energy threshold lower than TUS, of approximately 10^{19} eV [150]. Moreover, its accuracy in the determination of the EAS properties will be higher than the one of TUS, since it is equipped with about 10 times more pixels. It is estimated to be $\sim 5^\circ$ in arrival direction determination of the UHECR and $\Delta E/E \sim 20\%$ in energy for particle energies above 30 EeV. The KLYPVE mission is expected to measure about twice the event rate as TUS, ~ 100 events per year.

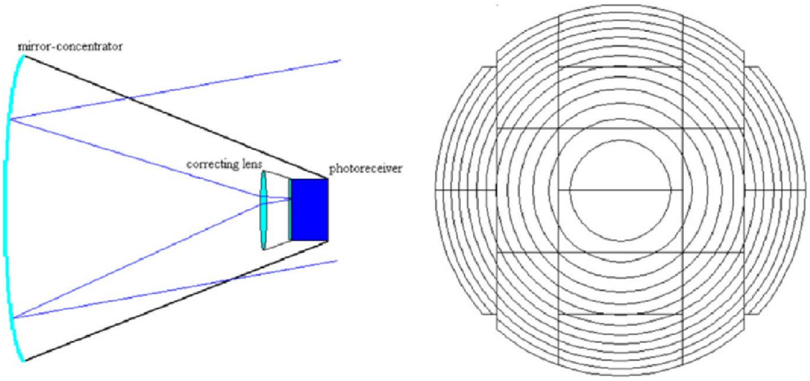

Figure 3.8.3: Scheme of the KLYPVE optics and the segmented Fresnel mirror. Taken from [93].

3.8.2 SUPER-EUSO

The Super-EUSO (S-EUSO) mission has been proposed in the context of the ESA Cosmic Vision Program 2015 – 2025 [228]. Its observation principle is the same as in (ESA-) EUSO, JEM-EUSO or the Russian space missions. However, S-EUSO is conceived as a free flyer. This has a number of advantages compared to ISS missions. (See Fig. 3.8.4) The orbit of such a mission can be tailored for this instrument, exclusively. Besides, there are less stringent constraints in terms of power consumption or the data rate. For S-EUSO an altitude of $\sim 800 - 1100$ km has been proposed. This altitude allows for a higher aperture compared to JEM-EUSO. It is envisaged to either choose an elliptical orbit, having the perigee at ~ 800 km and the apogee at ~ 1100

km or a circular orbit with variable altitudes. A variable orbit exploits the idea of an ultra-high aperture at high altitudes and a high aperture and high precision at lower altitudes [53, 208]. For the optics a Schmidt design is under study. This is a deployable catadioptric system — a combination refractive lenses and mirrors. Pure reflective designs have the disadvantage of a blind spot on the mirror, due to the shadow caused by the receiver. Hence, the telescope has to have a certain size, sufficient to compensate for this intrinsic inefficiency. A purely refractive system on the other hand bears the problem of heavy weight and instability for very large instruments. Therefore, this design dictates an upper limits for the detector size. Using a Schmidt design, as proposed for S-EUSO, facilitates the realization of various sizes of the instrument without major changes to the overall optics structure.

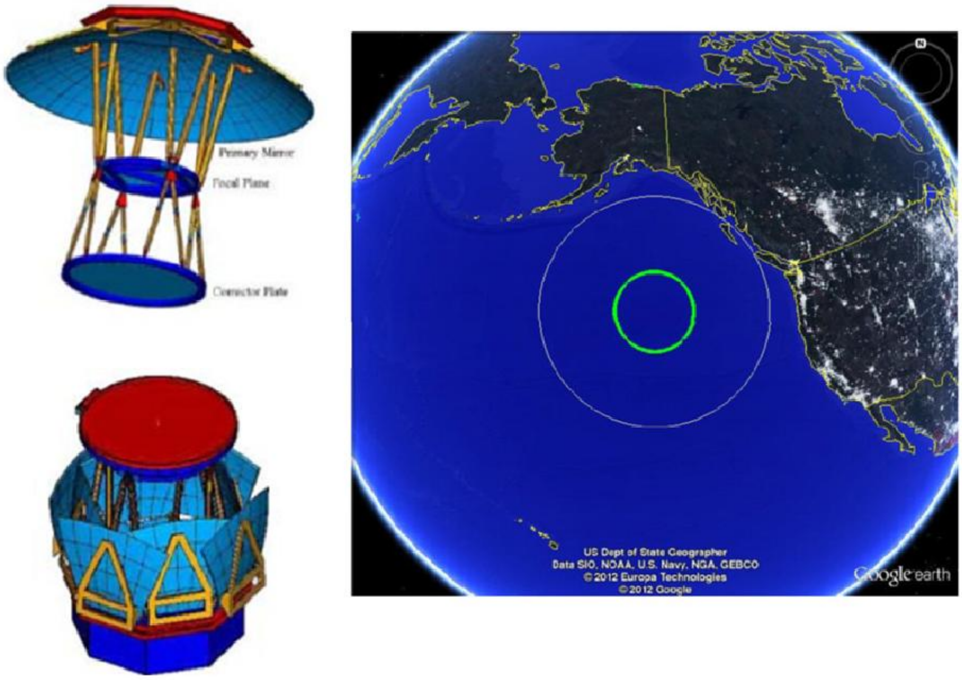

Figure 3.8.4: The Super EUSO detector. left: The instrument is conceived as a free flyer mision using a Schmidt-Optics. right: The telescope reaches an aperture of $1.3 \cdot 10^6$ km^2 sr. Pics. taken from [93].

At the moment, an entrance pupil diameter of ~ 7 metre has been proposed. The opening angle will be between ± 20° – ± 25°. This reflects the fact that at high altitudes, the EAS signal will appear extremely faint. Therefore, an improved optics throughput efficiency is needed [208]. For the same reason, a next generation photomultiplier with a high quantum efficiency is required, most likely silicon-based Geiger-mode photodetectors (SiPM) are a suitable choice. To reach a pixel granularity on ground, comparable to the one of JEM-EUSO, but from a higher orbit, about 1 million pixels are necessary [208]. This setup will allow for an energy threshold of $\sim 10^{19}$ eV. The observed area at apogee will be $\sim 0.8 \cdot 10^6$ km^2 with an instantaneous geometrical aperture of $2 \cdot 10^6$ km^2 sr, depending on the orbit and the FoV [208].

Table 3.8.2: Parameters of the S-EUSO [181].

Orbit Altitude	800 – 1100 km
Operation Period	5 – 10 years
Orbital Period	100 min
Duty Cycle	0.1 – 0.2
Optical Band Width	330 – 400 nm
Main Mirror Diameter	11 m
Pupil Diameter	7 m
Field of view	$\sim\pm 25°$
Focal Surface Diameter	4 m
Optics Structure	catadioptric
Photomultiplier	Si-PMT
Aperture (800 km)	$1.3 \cdot 10^6$ km^2 sr

3.8.3 OWL / GREAT OWL

The Orbiting Wide-angle Light Collectors (OWL) mission, is a concept design study that employs the launch of two identical satellites, each having an aperture of 3 metres and a viewing angle of 45°. The satellites fly in circular, near-equatorial orbits ($\sim 10°$) at initially at 1000 km. The two satellite setup enables stereoscopic observation. This makes the event reconstruction tolerant to atmospheric conditions, since the atmospheric light absorption and scattering can be corrected. Nevertheless, the satellites will have a lidar system to monitor the atmospheric depths and the cloud distribution. The information of the atmospheric conditions is complemented by data received from infrared satellites [157]. The monocular mode yields a high reliability and a larger aperture (Fig. 3.8.5).

The OWL concept makes use of SiPM, as well. The 4.9 m^2 focal surface will be equipped with $\sim 5 \cdot 10^5$ pixels. Like the proposed S-EUSO telescope, OWL has a Schmidt optics. To save weight, the optics structures are planned to be inflatable. The

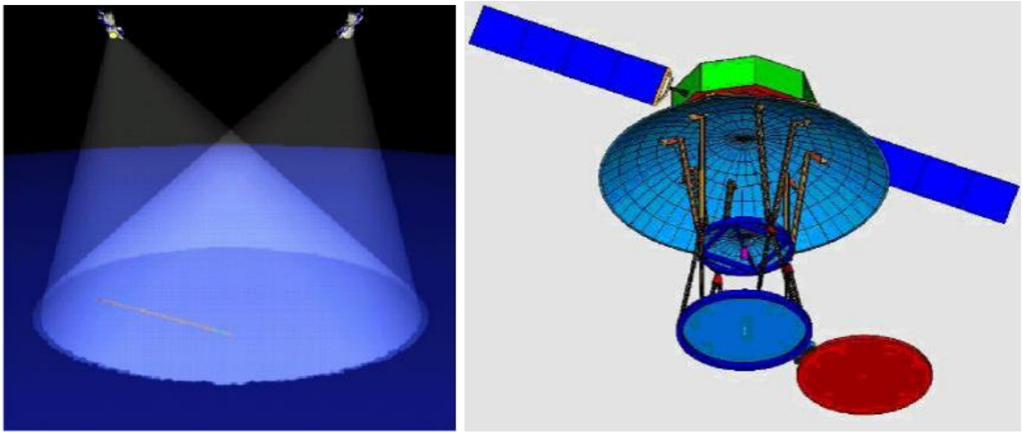

Figure 3.8.5: left: The stereoscopic view of the OWL concept, right: The OWL instrument. Pics. taken from [157].

primary mirror has a diameter of 7.1 m, this enables an effective aperture of 3.4 m^2. This corresponds to a projected surface area on ground of $\sim 10^6$ km^2, and an instantaneous aperture of $\sim 2 \cdot 10^6$ km^2 sr. With a duration of the mission assumed as 5 years, an exposure of $\sim 10^6$ km^2 sr yr is reached. The energy threshold is estimated to be $6 \cdot 10^{19}$ eV [157].

Great OWL is a even more visionary approach to measure GZK-cosmogenic neutrinos. For this up scaled version of the OWL detector, the energy threshold should be lowered to $< 10^{18}$ eV. This requires the optics to be enlarged by a factor of ~ 6, i.e. a 42 m diameter primary mirror, 18 m corrector and 13.8 m focal plane is required. Due to payload restrictions, it would be impossible to realize a telescope of that size, using conventional technologies. Thus, the entire instrument would have to be made of inflatable structures, employing techniques developed for large-area antenna and solar power systems [157].

Truth is stranger than fiction, but it is because fiction is obliged to stick to possibilities; Truth isn't.

Mark Twain

4

ESAF

The expected performance of JEM-EUSO is evaluated by means of extensive computer simulations. The end-to-end approach allows for a detailed assessment of the efficiency of the telescope's single components and their interfaces. Thus, in the scope of the simulations, every aspect of the UHECR measurement from space must be covered by the software package in detail.

The EUSO Simulation and Analysis Framework (ESAF) had originally been developed in the context of the former ESA-EUSO mission [38, 72, 262, 263]. It is written in an object oriented way. Main parts of the code are programmed in C++, other in Fortran. Moreover, it uses libraries of the ROOT[1] package [75]. ESAF is organized in modules, each of them devoted to simulate a specific part of the entire simulation chain. Due to this modularity, it is relatively simple to exchange one module with another. This yields the advantage that this software is not bound to simulate only the original EUSO mission. For the simulation of the JEM-EUSO mission, a new model

---

[1] ROOT is a data analysis software developed in the context of the Large Hadron Collider at CERN. [http://root.cern.ch]

of the telescope has been designed to replace the original [100]. Furthermore, we use the same software to simulate the pathfinders of JEM-EUSO.

Not only the technology of the detectors — may they be space-borne or not — can be substituted. Also the modules describing the 'physics' can be interchanged. For instance, the use of different kinds of air shower generators or models of the atmosphere helps us to better understand the behaviour of the expected signal. Interchangeable components of the telescope, such as lenses or focal surface detector components, allow for a better performance estimation and optimization of the instrument.

The sequence of the modules is organized in a hierarchical order. Generally, the simulation part is separated from the reconstruction part. This is important for a completely independent assessment of the performance of the telescope. Both sequences share only a collection of parameters describing the instrument and atmospheric databases.

A full end-to-end study begins with the interaction of the UHECR particle in the atmosphere. Next steps are the development of the air shower, fluorescence and Cherenkov light production and the photon propagation in atmosphere. This includes different kinds of scattering , reflection and attenuation effects. Once, the photons arrive to the entrance pupil of the telescope, the whole chain of events within the instrument is addressed. Photon propagation through the optical system, photoelectron creation and signal readout as well as the trigger chain is simulated. After the detector response data is written to disc, the reconstruction chain can be executed to reconstruct the properties of the UHECR primary by following a step by step approach. First of all, the signal must be disentangled from electronic noise and background photons. Secondly, the position and direction of the EAS is reconstructed which also allows for a particle type determination. Eventually, the energy of the particle can be computed.

Additionally, to the simulation/reconstruction part of the software package, a small collection of utilities is included in ESAF. They offer some analysis features as well as macros to generate vital allocation tables needed for the computation parts:

- The *opticsresponse* macro generates a database of optics throughput efficiencies, depending on the arrival angle of the photons to the lenses, by shooting a predefined number of test photons onto the optics;

- *MakePixelAngleMapPhotonFile* is a macros to create the pixel-angle-map table. In this table, every pixel on the focal surface detector is correlated to a certain arrival direction of photons to the entrance lens and the corresponding errors

$(\mathrm{Pixel}_i \;\rightarrow\; n_i(\theta_i^{FOV}, \varphi_i^{FOV}), \sigma(\theta_i^{FOV}), \sigma(\varphi_i^{FOV}))$

- *EEventViewer* is an analysis tool to visualize the output of intermediate simulation steps, such as the distribution of charged particles within the air shower or the spectrum of photons arriving to the detector site.

4.1 EVENT SIMULATION

The simulation part of ESAF begins with the particle interaction in atmosphere and ends with the instrument's measurement data written to disc, including the trigger information. For each of the intermediate simulation steps a variety of interchangeable packages is available. Depending on the purpose of the simulation, the single modules are selected in accordance. This allows to quick check certain parts of the simulation chain or to conduct full end-to-end studies, e.g..

The sequence of the simulation part of the framework is guided by the *SimuApplication*. It is the program part which executes the required modules in a logical order. It basically consists of two parts — *Detector* and 'nature', represented by the *LightToEuso* part (Fig. 4.1.1). The LightToEuso part is again subdivided into a handful of modules, responsible for the generation of the shower, creation of photons and light transfer to the telescope (Fig. 4.1.2). For a specific simulation run, the order of modules and the

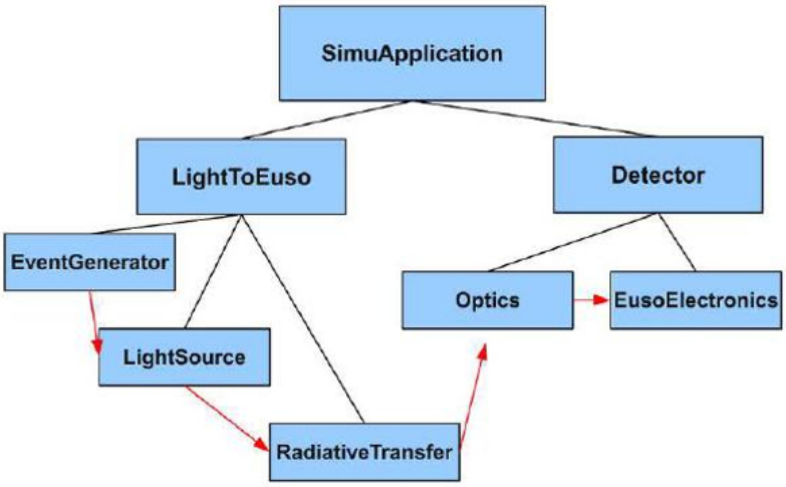

Figure 4.1.1: Schematic sketch of the simulation part of the ESAF framework. Taken from [99].

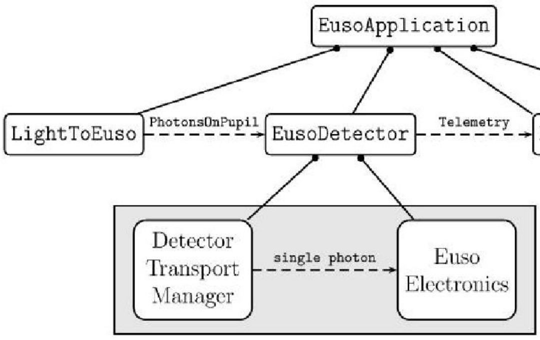

Figure 4.1.2: The LightToEUSO application calls a number of sub-packages. Taken from [97].

setup of the single modules themselves is defined by means of their dedicated configuration file. I.e., threshold values, multiplication factors, methods and the location of databases are saved within it (List. 4.1).

Listing 4.1: Example of a simulation config file

```
# config file for ShowerLightSource object
#
ShowerLightSource.FluoCalculator = nagano
ShowerLightSource.CrkCalculator = simple
ShowerLightSource.fLambdaMin = 250
ShowerLightSource.fLambdaMax = 485
ShowerLightSource.EnergyDistributionType = parametrized
ShowerLightSource.EnergyDistributionName = giller
ShowerLightSource.LateralDistributionName = NKGhadron
ShowerLightSource.AngularDistributionName = baltru
ShowerLightSource.fUseAngDev = no
```

For a complete listing of the parameters utilized in simulation runs, see appendix 7.2. In this chapter, we will only briefly mention packages and procedures that are part of ESAF but have not been used in the scope of this thesis. Instead, we will put the emphasis on the description of the packages that have been utilized in this study.

4.1.1 Shower Simulation

The simulation part of the entire chain begins with the generation of the air shower. Within ESAF, we can utilize the built-in solution provided by the *SLAST* shower generator. Alternatively, already existing air showers generated by external shower generators can be imported to ESAF via dedicated interfaces: *CONEX* [12, 50, 210, 211], *CORSIKA* [129] or *UNISIM* [71].

SLAST is a shower generator that uses parametrizations to simulate the distribution of charged particles. Depending on the energy and zenith angle of the UHECR, the longitudinal development is described by a parametrization according to the Greisen, Ilina, Linsley (GIL) function [170]. The formula dates back to the Greisen parametrization describing the longitudinal shower development of UHE-γ [220]. Modified by Ilina in 1992, it was set to describe nuclei initiated showers [138]. In 2001, Linsley proposed the following version [82, 170]:

$$N_e = \frac{E}{E_1} \cdot e^{-[t - t_{max} - 2\, t \cdot ln(s)]} \tag{4.1}$$

with the slant depth $t = \frac{x - x_1}{x_0}$, $x_0 = 37.5 g/cm^2$, E_1=11.45 GeV, the shower age:

$$s = \left[\frac{\frac{1+t_{max}}{t}}{2} \right]^{-1}, \tag{4.2}$$

and t_{max} defined by

$$t_{max} = a + b \cdot \left[ln\left(\frac{E}{\varepsilon}\right) - lnA \right]. \tag{4.3}$$

Here, a=1.7 denotes an offset constant, b=0.76 the elongation rate and ε= 81 MeV, the critical energy. The GIL function (Eq. 4.1), is visualized in (Fig. 4.1.3). The lateral

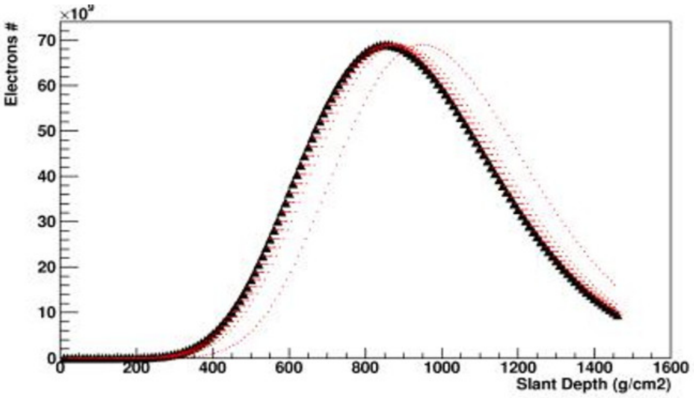

Figure 4.1.3: Greisen Ilina Linsley (GIL) parametrization for longitudinal development of extended air showers. Taken from [99].

distribution of charged particles follows the *NKGhadron* parametrization according to

Kamata and Nishimura [146] and Greisen [119]:

$$f(x) = \frac{\Gamma(4.5-s)}{2\pi\Gamma(s)\Gamma(4.5-2s)} \left(\frac{r}{r_1}\right)^{(s-2)} \left(1+\frac{r}{r_M}\right)^{(s-4.5)} \tag{4.4}$$

with r, the distance to the shower core in metres and r_M being the Molière radius:

$$r_M = E_s \frac{X_1}{\varepsilon} \tag{4.5}$$

with the scale energy $E_s \approx 21$ MeV and the radiation length in air $X_1 = 37\, cm^{-2}$. The local Molière radius is obtained by $r_M/\rho(h) \approx 9.6\, g\, cm^{-2}/\rho(h)$. The NKG function is however a modified version, fine tuned by a scale factor as in [116] to fit Monte Carlo simulations. This is in good agreement with the JNC function [76, 77].

Depending on the age parameter s, the shape of the particle spectrum for energies between the critical energy and the energy of the primary electron or photon that triggers the electromagnetic cascade $\varepsilon \ll E \leq E_0$ is

$$\frac{1}{N_e}\frac{dN_e}{d\ln E} \sim E^{-s}. \tag{4.6}$$

It can be analytically expressed according to Nerling [194], Giller [115, 274] or Hillas [133]. The Giller distribution follows Monte Carlo simulation between 10^{19} to 10^{20} eV, describing the electron energy spectra depending on the shower age:

$$\frac{1}{N_e}\frac{dN_e}{d\ln E} = C(s) \cdot \left\{1 - a \cdot exp\left[-f(s) \cdot \frac{E}{\varepsilon}\right]\right\} \cdot \left(1 + \frac{E}{\varepsilon}\right)^{-\left[s + b \cdot \ln\left(\frac{E}{c \cdot \varepsilon}\right)\right]} \tag{4.7}$$

with N_e, the total number of electrons, a=1.005, b=0.06, c=189, f(s)= 7.06 · s + 12,48 and C(s)=0.111 · s + 0.134 for 0.7 $\leq$ s $\leq$ 1.3 (Fig. 4.1.4). The Giller parametrization is taken as the standard particle energy spectrum within ESAF, since the other parametrizations do not seem to reproduce the Monte Carlo results above 10^{19} eV sufficiently.

The angular distribution of the Cherenkov light follows the empirical formula developed by Baltrusaitis et al. in the context of the Fly's Eye experiment [29].

$$\frac{dN}{d\Omega} \propto \frac{exp\left(-\frac{\theta}{\theta_0}\right)}{2\pi\theta_0 \sin(\theta)} \tag{4.8}$$

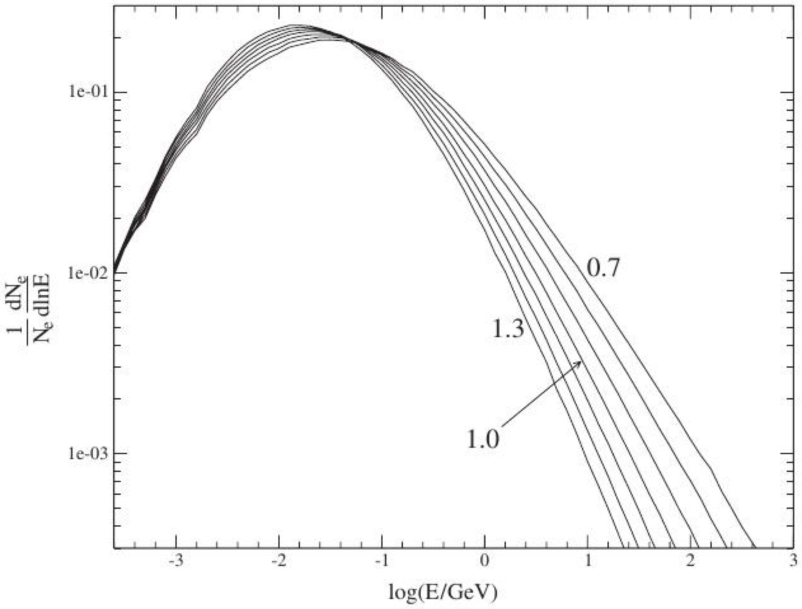

Figure 4.1.4: Electron Energy Spectrum according to Giller [115, 274] for various shower ages. Each curve represents the average of 10 proton showers of 10^{19} eV. Taken from [115].

with the emission angle θ (relative to shower axis) and θ_0=4.0 ± 1.2° the multiple scattering parameter for $20 \leq E_T \leq 60$ MeV, the threshold energy for Cherenkov light emission.

$$\theta_0[rad] = a \cdot E_T[MeV]^{-b} \tag{4.9}$$

E_T depends on the refraction index of the medium traversed.

$$E_T = 0.511[2(n-1)]^{-1/2} \tag{4.10}$$

The parameters a and b have been approximated by different studies according to Tab. 4.1.1. The merit of SLAST, with the built-in parametrized approach, is a very quick and efficient solution for the shower production. The shower can be produced within

Table 4.1.1: θ_0 parameters a and b. From [29, and references therein].

	a	b
[242]	0.83	-0.67
[96]	0.77	-0.65
[96, 133]	0.85	-0.66

seconds, whereas the more sophisticated generators consume far more computing resources. Of course, the Monte Carlo methods yield a more realistic outcome. However, since the GIL formula is tuned in accordance to Monte Carlo simulations, the results are comparable [82]. Therefore, SLAST can be regarded as a robust and convenient tool for code testing, evaluation of the reconstruction algorithms and to give first estimates on the instrument's performance.

CONEX is a one-dimensional hybrid shower generator for high energy air showers [12, 50, 210, 211]. At the first stages of the shower development, the high energy particle interaction is computed by a Monte Carlo simulation. For the less energetic subshowers CONEX relies on solving the hadronic and electromagnetic cascade equations numerically [50]. This yields the advantage of saving computing time compared to a full Monte Carlo simulation, especially at ultra high energies. The two parts of the program are steered by the same physics. Different hadronic interaction models can be selected: SIBYLL 2.1 [11], QGSJET01 [144], QGSJETII-04 [199] and EPOS LHC [31, 68, 212] are implemented for the high energy part, GHEISHA [103] for the low energy part. The high energy electromagnetic part is computed by the built-in EGS4 code and additional LPM-effect supplements [12]. Photo-nuclear interaction and muon production follow the CORSIKA program. Once, the secondary particle energy falls below a pre-set threshold, the particles behaviour is described by cascade equations for the interaction processes like bremsstrahlung, Compton effect and pair production. CONEX yields remarkably similar results as the full Monte Carlo CORSIKA code (Fig. 4.1.5). CONEX can not only simulate proton induced air showers, but also UHE neutrinos and photons [246].

CORSIKA, being a full Monte Carlo simulator for cosmic ray induced air showers, certainly yields the most natural results [129]. It has a choice of various built-in hadronic interaction models such as NEXUS, SIBYLL 2.1, QGSJET01, QGSJET II-3 and EPOS 1.6. The CORSIKA output can be injected into ESAF by means of a designated interface. However, CORSIKA requires a computing time by orders of magnitudes higher than SLAST or CONEX.

UNISIM had been developed at the time of (ESA-) EUSO, to provide proton and neutrino showers to ESAF [71]. A number of studies has been carried out so far [64, 229].

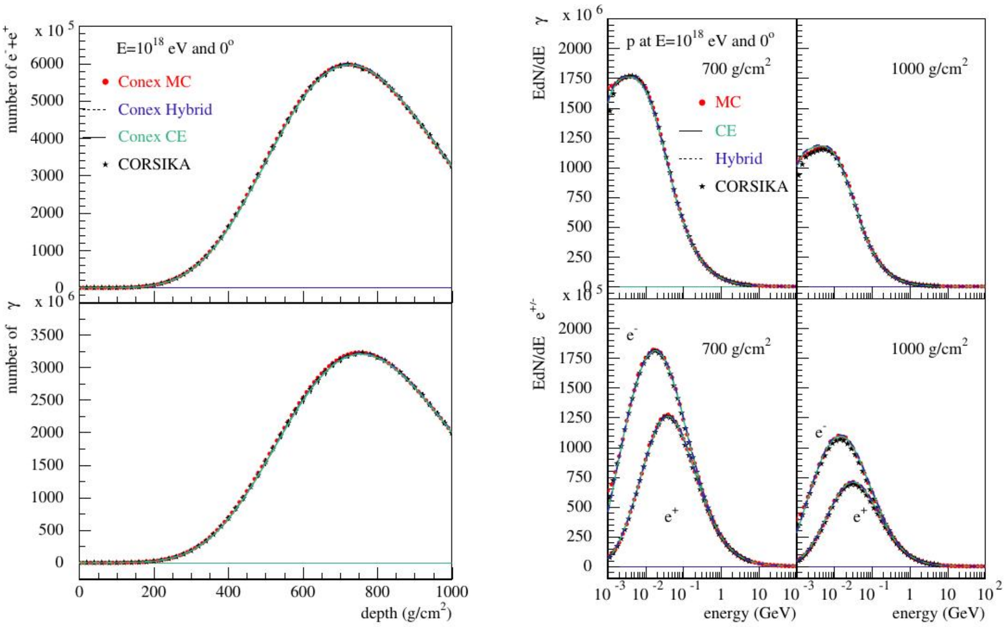

Figure 4.1.5: Figure 5: Left panel: Average longitudinal profiles of charged particles and photons of energies above 1 MeV for proton-initiated vertical showers of $E_0 = 10^{18}$ eV. Right panel: Particle energy spectra of photons, electrons, and positrons for the atm. depths $X = 700$ and 1000 g/cm^2. Shown are the results from the hybrid calculation (dashed line), pure MC simulation (points), and numerical cascade Eqs. solution (full line). In addition CORSIKA predictions are given by stars. Pic. and caption taken from [50].

However, since the code is not supported any longer, current and future neutrino simulation studies are being conducted, utilizing the CONEX code instead [139, 247].

4.1.2 LIGHT GENERATION

After the shower generation by SLAST or import of a generated shower by an external code such as CONEX, the distribution of particles and their energy distribution is handed over to the *ShowerLightSource* module. Its task is the production of fluorescence and Cherenkov photons. Two photon bunches are assigned to each shower step; one for fluorescence, the second for Cherenkov photons. The light yield is calculated for each of the shower bunches.

FLUORESCENCE LIGHT is produced by taking into account the number of electrons in the shower step N_e according to GIL (Eq. 4.1) and integrate the spectral distribution of the electron energies $\frac{1}{N_e}\frac{dN_e}{dE}$ as well as the fluorescence yield FY_λ^L [38]

$$\frac{dN_{fluo}}{dL} = N_e(s) \int_E \left[\left(\frac{1}{N_e}\frac{dN_e}{dE}(s) \right) \int_\lambda FY_\lambda^L(E,P,T)\,d\lambda \right] dE. \tag{4.11}$$

For the fluorescence yield, either the Kakimoto parametrization [142] or the Nagano parametrization [191, 192] can be used.

The Kakimoto parametrization fits the measurements performed by Kakimoto et al. in 1996 [142]:

$$FY_\lambda^L = \frac{\left(\frac{dE}{dx}\right)}{\left(\frac{dE}{dx}\right)_{1.4\ MeV}} \cdot \rho \left\{ \frac{A_1}{1+\rho B_1\sqrt{T}} + \frac{A_2}{1+\rho B_2\sqrt{T}} \right\} \tag{4.12}$$

with dE/dx, the electron energy loss, $(\mathrm{dE/dx})_{1.4\ MeV}$ evaluated at 1.4 MeV respectively, the air density ρ [kg m^{-3}] and the temperature T [K]. The constants $A_{1,2}$, $B_{1,2}$ can be inferred from Tab. 4.1.2

Table 4.1.2: Yield parameters $A_{1,2}$ and $B_{1,2}$. Taken from [142].

A_1	89.0 ± 1.7 m^2 kg^{-1}
A_2	55.0 ± 2.2 m^2 kg^{-1}
B_1	1.85 ± 0.04 m^3 kg^{-1} K$^{-1/2}$
B_2	-0.66 ± 0.33 m^3 kg^{-1} K$^{-1/2}$

The Nagano parametrization follows the measurements by Nagano et al. [191, 192]:

$$FY_\lambda^L = \frac{\left(\frac{dE}{dx}\right)}{\left(\frac{dE}{dx}\right)_{0.85\ MeV}} \frac{A_i\,\rho}{1+\rho B_i\sqrt{T}} \tag{4.13}$$

with

$$A = \frac{\left(\frac{dE}{dx}\right)_{0.85\ MeV} \Phi^\circ}{h\nu} \quad \text{and} \quad B = \frac{R_{N_2}\sqrt{T}}{p_i'} = \frac{4\sigma_{nn}\tau_0 R_{N_2}}{\sqrt{\pi k M}}, \tag{4.14}$$

where R_{N_2}=296.9 m^2 s^{-2}K^{-1} is the specific gas constant for nitrogen and the air pressure ρ. The electron energy deposit dE/dx, required by both yield parametrizations is calculated according to [235]

$$\frac{dE}{dX} = -\rho \frac{0,153536}{\beta^2}\frac{Z}{A} B\, E_{kin}. \tag{4.15}$$

For a direct comparison of the fluorescence yields as computed in ESAF see Fig. 4.1.6.

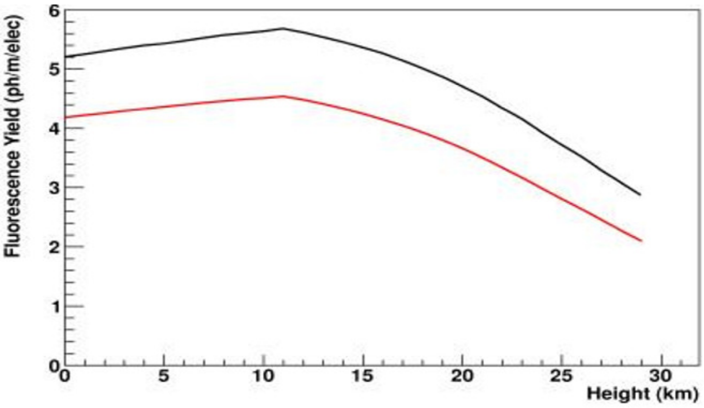

Figure 4.1.6: Fluorescence yield according to Kakimoto and Nagano. Taken from [99].

Cherenkov light is produced whenever a charged particle traverses a dielectric medium at a velocity exceeding the speed of light within it. It is emitted in a pencil beam along the direction of motion of the particle [49, p. 443]. In ESAF, the photon production is computed in analogy to the fluorescence case

$$\frac{dN_{Ckov}}{dL} = N_e(s)\int_{E_{thresh}}^{\infty}\left[\left(\frac{1}{N_e}\frac{dN_e}{dE}(s)\right) CY^L(E,n)\right] dE. \tag{4.16}$$

were $CY^L(E,n)$ is the integrated Cherenkov yield. It is described by

$$CY^L(E,n) = 2\pi\cdot\alpha\cdot 2\delta\left(1-\left(\frac{E_{thres}}{E}\right)^2\right)\cdot\left(\frac{1}{\lambda_{min}}-\frac{1}{\lambda_{max}}\right), \tag{4.17}$$

with $\delta = \rho(h)/\rho(0)$, the ratio of air densities at altitude h and on ground level, the threshold energy for Cherenkov light production E_{thres} and the fine structure constant α [38] (Fig. 4.1.7). The opening angle of the Cherenkov cone has a few degrees and depends on the altitude.

4.1.3 ATMOSPHERIC TRANSPORT

The atmosphere used for simulation within ESAF can be selected from either the

1. *U.S. Standard Atmosphere 1976* [198] or

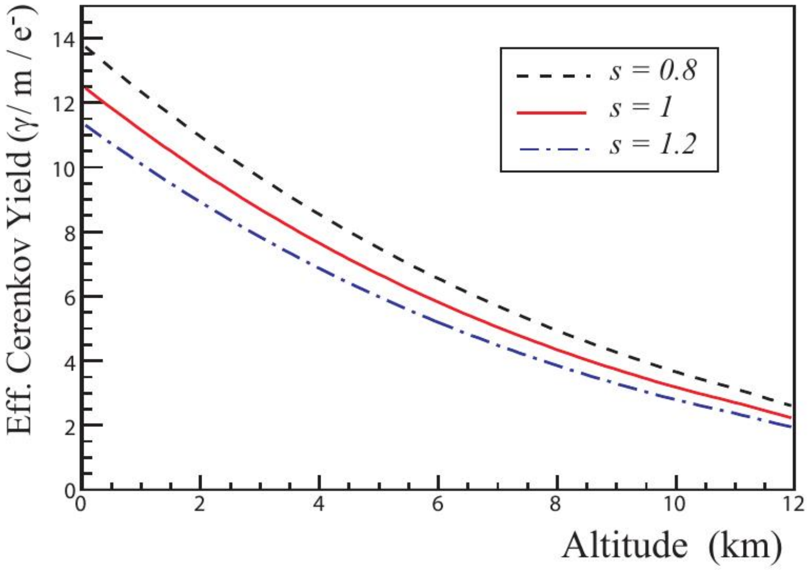

Figure 4.1.7: Cherenkov yield as calculated in ESAF for three shower ages s. Taken from [38].

2. the *MSISE empirical model of the atmosphere* [130, 209].

The Rayleigh scattering and ozone absorption is computed with help of the LOWTRAN7[2] [24] atmosphere package [99]. Every photon bunch of the shower has its unique position and direction as well as certain photon properties in terms of spectral, longitudinal, lateral and angular distribution. The propagation of photons through the atmosphere to the instrument can be conducted by two possible atmospheric transport modules — the very fast, parametrized *Bunch* algorithm or the *Monte Carlo* transfer. The latter, being significantly slower and demanding in terms of computing power, but certainly closer to nature than the first. The evaluation of the differences between the two algorithms and the impact on the angular resolution has been part of this work.

THE BUNCHTRANSFER, uses a parametrized approach. It is a very fast and efficient way to propagate the photons to the detector. The idea behind the algorithm is to consider not the single photons, but the entire bunch. The three major types of photons arriving to the detector are treated by the algorithm: 1) the fluorescence photons, directly propagated onto the first lens of the detector without undergoing any further atmospheric interactions. 2) The Cherenkov photons impacting on ground and being reflected to the instrument. 3) The Cherenkov photons arriving to the detector after scattering

---

[2] LOWTRAN: Low Resolution Transmittance Code

with aerosols or molecules. The bunch algorithm neglects additional components of fluorescence light which is scattered or reflected from ground [38, 189]. The direct fluorescence component is propagated towards the detector in a simple approach. Among the many fluorescence photons produced, only an extremely small fraction reaches the first lens. This is owed to the fact that the photons are homogeneously emitted in every direction and the ~ 5 square metre detector entrance is ~ 400 km away. Simple geometrical considerations show that only

$$\frac{\text{lense surface} \cdot 100}{4\pi \cdot (\text{ISS altitude})^2} = \frac{\sim 5\,m^2 \cdot 100}{4\pi \cdot (\sim 4 \cdot 10^5\,m)^2} \approx 10^{-10}\% \tag{4.18}$$

of the photons can reach the detector on a straight line. Thus, instead of tracking each photon and analyze its probabilities to be scattered or attenuated, the candidate photons are taken and propagated towards the detector. The single photons inherit their properties from their parent bunch. Now, only the probability of being attenuated on the way is calculated according to its wavelength and distance.

The Cherenkov component is computed in a similar way. However, in this case a single scattering interaction is taken into account. Typically, within each Cherenkov-bunch, a sub sample of photons is scattered in such a way that the new direction of the photon intersects the instrument's entrance pupil. Usually, the pathway in atmosphere is much longer than for the fluorescence component. Of the reflected component, only a minor part reaches the detector. Due to the earth's albedo of about 5% [84], a large fraction of the photons is lost. Furthermore, since it traverses the low layers of the atmosphere, reflected Cherenkov light is affected by ozone absorption. For the fluorescence photons it usually does not play a major role. In nature, all photons are subject to scattering processes of both Mie and Raleigh scattering. The bunch algorithm however, does only take scattering effects for the Cherenkov photons into account. This is an approximation, owed to the fact that calculating scattering effects for such a large amount of photons over some scattering orders consumes a large amount of computing time. This algorithm has nevertheless proven to be very useful in evaluating the expected performances of the detector and in a number of important tests.

THE MONTE CARLO transport of photons in atmosphere is the more advanced approach. Here the interaction of the photons in the atmosphere is taken into account up

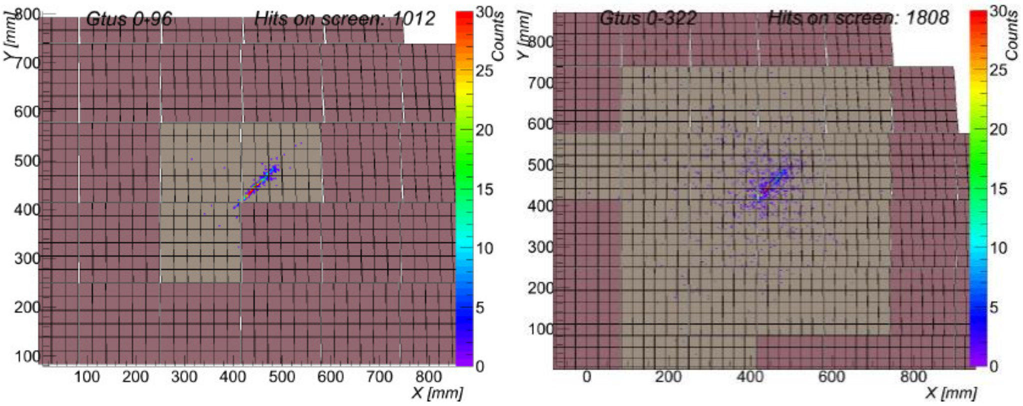

Figure 4.1.8: Signal tracks of the same shower event (proton, E=10^{20} eV, θ=60°) on the JEM-EUSO focal surface. Left: Bunch algorithm for transport of photons in atmosphere. Right: Monte Carlo algorithm taking into account five scattering orders.

to the nth order. For each photon, its properties like wavelength, position and direction within the bunch must be assigned by the help of a random generator, weighted with the corresponding physical distribution. For each interaction, the probability to become attenuated or scattered within 4 π direction is again randomly determined. This happens for each photon up to the pre-set nth order or to the point when the detector is reached. To avoid the computing for all of the photons generated within the shower, a reduced version of the full Monte Carlo mechanism is applied [38, 190] (Fig. 4.1.11). This simplification is valid since the detector is not part of the scattering medium but rather distant. I.e., between the top of the atmosphere and the detector, no Monte Carlo calculations are needed and for those photons leaving the atmosphere, only those have to be considered that fall into the (very small) solid angle of the telescope. The method has been evaluated and compared to similar atmospheric simulations by [38]. Due to the contributions of higher scattering orders, the signal tracks appear broader on the focal surface and more outstretched in time (Fig. 4.1.8).

4.1.4 DETECTOR

The telescope simulation consists of a number of modules, each responsible for the simulation of a specific part of the detector and its sub-components. Major parts are the optics, the focal surface detector and the readout electronics. An additional, but important sub-system for the JEM-EUSO mission is the atmospheric monitoring system,

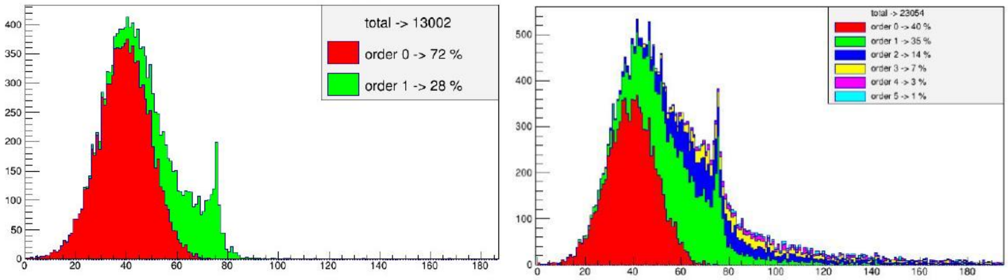

Figure 4.1.9: Light curve of the same shower event (proton, E=10^{20} eV, θ=60°) and its components observed by JEM-EUSO. Left: Bunch algorithm for transport of photons in atmosphere. The fluorescence light is not affected by any scattering interaction, whereas the Cherenkov light is assumed to undergo one single interaction, either scattering or ground reflection. Right: Monte Carlo algorithm taking into account five scattering orders.

i.e. the LIDAR and the IR camera. The AM system, however, is at the moment only partly implemented within ESAF. The LIDAR simulations can be performed within the framework, the necessary simulation for the infrared camera are carried out by a stand-alone code [219, 265].

The optics of the JEM-EUSO telescope can be simulated by utilizing three different possible options; a parametrized optics implementation and two kinds of optics ray-traces.

The first and most simple solution is the parametrized optics. Tracking the photons through the optics by means of mathematical functions bears the advantage of negligible computing time. The parametrized approach yields the simplistic picture of an ideal optics and thus focusses the signal in a perfect manner without any perturbations one would expect in reality. Therefore, it is not used for any serious performance estimate. However, it can be used as a first step when setting up the entire end-to-end simulation for the first time for a new detector.

Advanced options are the *RIKEN ray-trace* and the *Dubna ray-trace* optics. The *Dubna ray-trace* is based on Geant4[3]. The *RIKEN ray-trace* does not require any further libraries. Both ray-trace codes yield virtually indistinguishable results from one another. In the scope of this dissertation, we have been using the *RIKEN ray-trace*, exclusively.

---

[3] Geant4 is a toolkit for the simulation of the passage of particles through matter. Its areas of application include high energy, nuclear and accelerator physics, as well as studies in medical and space science. It is developed at CERN. [http://geant4.cern.ch]

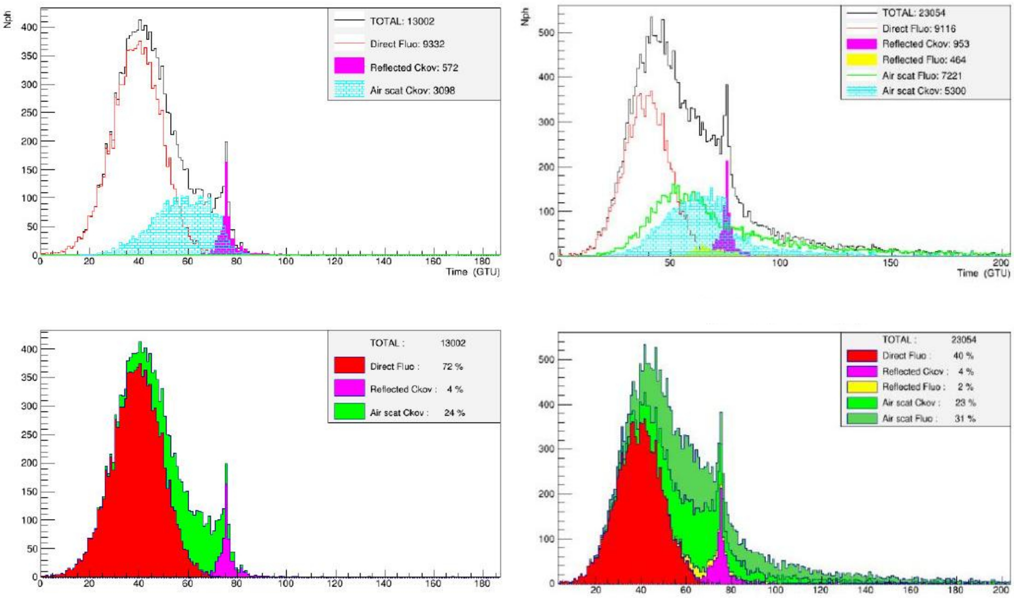

Figure 4.1.10: Signal components of the same shower event (proton, E=10^{20} eV, θ=60°) on the telescope's entrance pupil. Left: Bunch algorithm for transport of photons in atmosphere. Right: Monte Carlo algorithm taking into account five scattering orders.

THE FOCAL SURFACE DETECTOR The description of the focal surface detector comprises the layout file which contains vital information on the PMTs. Arranged on an ideal focal surface (Fig. 4.1.12), each of them has a unique identifier. The FS layout file is an allocation table which connects the unique ID of each PMT to a specific PDM, whose position and pitch in three dimensions is also given here. The simulation of the single PMTs is done in accordance to database tables containing the parameters of the PMTs, such as dimensions and efficiencies, cross-talk, etc.. The type of PMT can be easily exchanged, given that the data of the specific model is made available by the producer. The current baseline used for simulations in the scope of this work is the Hamamatsu R11265-M64.

THE ELECTRONICS simulation treats every step of the detector readout part. Starting at the level of the PDM electronic board where the signal is read out in the form of anode currents, the simulation include the electronic processing, addition of background and the application of the trigger algorithms. The signal readout is done within an *el-*

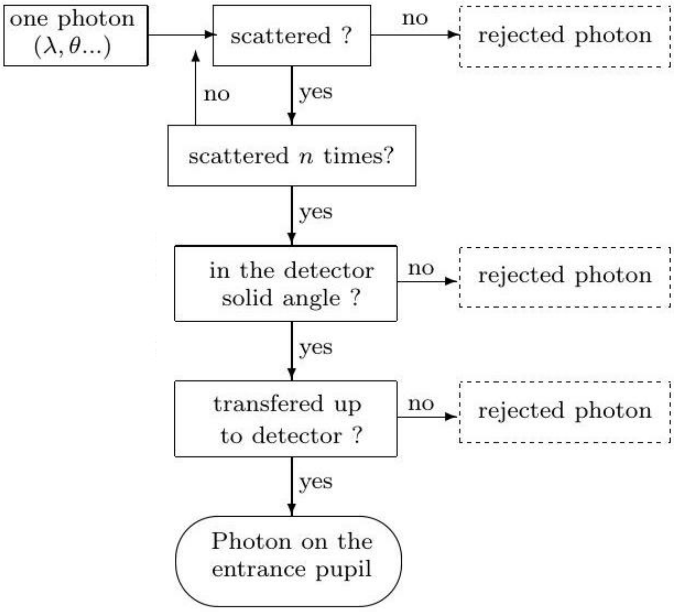

Figure 4.1.11: Working scheme of the Monte Carlo algorithm to simulate photon transport in atmosphere for n scattering interactions. Taken from [38], modified.

ementary cell, a matrix of two by two MA-PMTs by an ASIC[4] [87]. The ASIC is part of the PDM board which controls the data flow for the entire PDM. At this stage, the background is added, to circumvent the problem of simulating the many background photons in atmosphere. The resulting background pattern on the focal surface is relatively homogeneous, characterized by Poissonian fluctuations. In reality we expect to observe an intensity maximum at the centre of the focal surface and a decrease in background intensity in the outer parts. This is owed to a decrease in throughput efficiency for larger optics radii. At the moment a constant background is taken into account, though. Furthermore, at the PDM-board, the first trigger level L1 is applied, reducing the data rate by a factor of about $6 \cdot 10^4$ [87]. The L1 trigger is called persistent track trigger (PTT). It checks inside a box of three by three pixels for signals that last longer than a preset time duration of typically five consecutive GTUs. If this is the case and the total number of counts within this box exceeds another preset threshold value, a trigger signal is issued. When a signal passes the first trigger stage, the data is sent to the cluster control board (CCB). Here, the data of about seven PDMs[5] is collected, scanned by the second trigger level L2 and sent to the main CPU in case a trigger signal given. The L2 is called linear tracking trigger (LTT). It searches for pixels exceeding

---

[4] ASIC: Application-specific integrated circuit

[5] decision on the number of PDMs pending

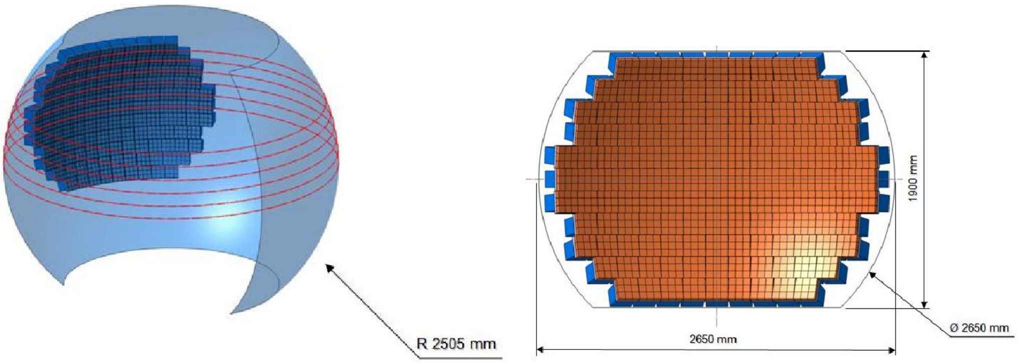

Figure 4.1.12: Left: The shape of the focal surface is described by a sphere of ~ 2.5 m radius. Right: The PDMs are arranged on the FS in an x,y layout with a centre PDM. Taken from [257].

a certain threshold. Once, such a *red* pixel is found, an integration box of three by three pixels is moved along predefined paths intersecting it. Again, a second threshold must be passed to issue the trigger. This is supposed only to happen for the case when the integration box moves approximately along the axis of a signal track and not for clusters of background [99].

Following the digitization of the signal by the ASICs, the electronics simulation is carried out in a parametrized way. This is considered as appropriate, since no significant signal losses or distortions are expected after this stage [99]. The event data, including intermediate results from the single simulation steps, are saved in an output file and written to disc.

4.2 Event Reconstruction

The reconstruction part of the ESAF software aims at estimating the direction, X_{max} position and energy of the primary UHECR. Like the *Simu* part of the framework, also the *Reco* part is subdivided into several modules, each of them responsible for a specific sub task (Fig. 4.2.1). In the course of the event reconstruction process, the modules used for the simulation of the event data remain untouched. All relevant actions necessary for the reconstruction are performed independently from the simulation part of the framework. Starting from the raw data, read out from the ROOT file, the reconstruction sequence first checks for the trigger information and tries to recover the actual signal track within the distribution of background counts. Following that, from the position, shape and timing information of the track, the direction can be inferred

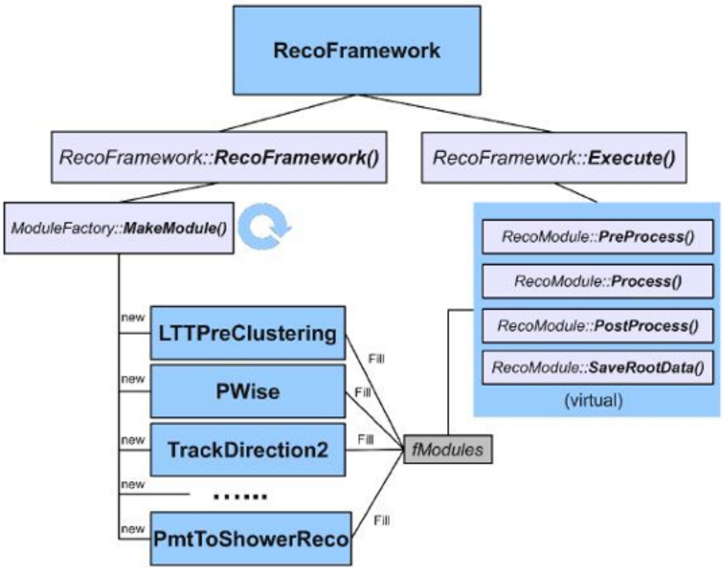

Figure 4.2.1: Schematic sketch of the reconstruction part of the ESAF framework. Taken from [99].

by the dedicated angular reconstruction module. Knowing the position and direction of the EAS in the atmosphere, an estimate of the *Xmax* and energy can be computed. For the different tasks within the reconstruction chain, a number of modules have been developed. Some of the date back to the time of (ESA-)EUSO, others have been developed to suit the needs of the new mission. Thus, for every task a choice of designated modules exist. Like in the simulation part, the sequence of modules is defined within a configuration file (List. 4.2).

Listing 4.2: The RecoModuleList configuration file

```
# PATTERN RECOGNITION MODULES:
#
Module = LTTPreClustering
Module = PWISE
#Module = RobustModule
#Module = HoughTransform
#
# TRACK DIRECTION MODULES: either TD2 or TDPlane+TD.
#
#Module = TrackDetectorPlane
#Module = TrackDirection
Module = TrackDirection2
#
```

```
# ENERGY MODULES:
#
Module = PmtToShowerReco
```

4.2.1 Pattern Recognition

The motivation behind the pattern recognition module is to extract the real signal track from background and noise. Atmospheric background photons originate from the atmospheric night glow, weather phenomena or human light sources. The noise is introduced by the electronic components of the detector itself. Its contribution to the overall background is relatively small.

Originally, ESAF had been equipped with two kinds of pattern recognition: *cluster analysis* [174] and *Hough transform* [136, 175]. Some preliminary results have been obtained using these methods [181, 182]. However, in the scope of the simulation studies conducted in the framework of JEM-EUSO the existing pattern recognition modules have proven to be insufficient to meet the JEM-EUSO scientific requirements. Therefore, three new modules have been developed to facilitate an appropriate pattern recognition — the *PWISE* module [62, 123], the *Robust* module [61] and the *LTT-PreClustering* module [56, 62].

Peak and WIndow SEarching (PWISE) is the recently developed signal filter for the ESAF reconstruction [125]. Unlike the former, original pattern recognition modules it does not search for logically connected groups of neighbouring pixels, but analyses each of them individually in time. The technique works in three major steps [122, 123]:

1. Among the many pixels derived from the triggered PDMs, PWISE takes only those into consideration with a maximum photon count exceeding the *peak-threshold*.
2. Now, a time interval is identified that maximizes the signal-to-noise ratio (SNR) defined by

$$SNR = \left(\frac{1}{\Delta\tau \cdot RMS}\right) \sum_{\Delta\tau} pc(t), \tag{4.19}$$

with pc(t), the photon-counts at the time t, $\Delta\tau$, the width of the time window around the maximum count peak of the pixel and the root-mean square RMS of the photon-counts.

3. Only if the maximum SNR is above a pre-set *SNR-threshold*, the counts in this time window are regarded as signal counts and passed on to the direction reconstruction.

The rejection power depends on the fine tuning of the two thresholds. Focus of its development was to provide a clean track with sufficient signal counts for the angular reconstruction. A relatively conservative threshold setting comes at the expenses of loosing a fraction of the actual signal track [123]. A great advantage of the PWISE is its power to reject multiply scattered photons that produce counts far off the main sequence of the signal track and introduce uncertainties in its subsequent fitting. Like scattered photons originating from perturbations of the optics these counts contribute to a fuzzy image of the signal track. Moreover, they are characterized by delayed arrival times due to the multiple scattering and can therefore have a negative impact especially on the Θ reconstruction (Fig. 4.1.9).

The Linear Tracking Trigger Pre-Clustering technique can be applied beforehand the actual signal identification. The underlying technique is according to the same algorithm as implemented in the second trigger level — the *Linear Tracking Trigger*. However, since the event reconstruction is not affected by time or power budget constraints, the same logic is applied with higher accuracy, delivering more sophisticated results [56, 62, 117].

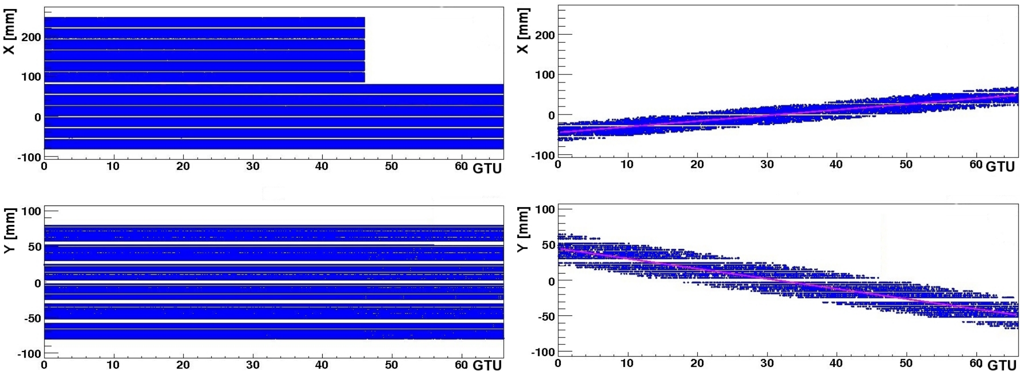

Figure 4.2.2: x-t and y-t plots of the focal surface with a signal track embedded in background. Left: before and Right: after LTT Pre-Clustering selection. Both taken from [56].

Like the LTT, it searches for *red* pixels with a maximum number of counts. In the next step, it takes an integration box and moves it into a number of directions intersecting this pixel. In this step the major difference from the LTT arises, due to the fact that computing power on earth allows for many more directions than onboard the telescope. The module finally selects the path which maximizes the number of counts. It does not extract the signal from background but significantly reduces the area of the focal surface massively which potentially contains the track (Fig.4.2.2).

Only a narrow track of pixels is passed on to the PWISE module or another pattern recognition. The other pixels are neglected. A box of the size of about eight by eight pixels reduces the amount of pixels to be analysed by the successive module to about 3 %, relatively independent of the energy of the EAS. At the same time it conserves more than 90 % of the signal counts originating from the UHECR. LTT-PreClustering can further enhance the performance of the angular reconstruction under some circumstances [62].

4.2.2 Direction Reconstruction

Once the signal is extracted from background, the spatial and timing information of the signal counts allow to reconstruct the position and direction of the air shower. The only information for the reconstruction chain to start with comes in the form of front end electronics objects (FEE). One FEE consists of the pixel ID and the recording time of the signal.

The pixel-angle-map is an allocation table that comprehends the information, which pixel on the focal surface is connected to a specific arrival angle of photons to the first lens (Fig. 4.2.3). Thus, the FEEs are effectively converted to information in terms of incoming direction of photons to the detector in spherical coordinates and its error.

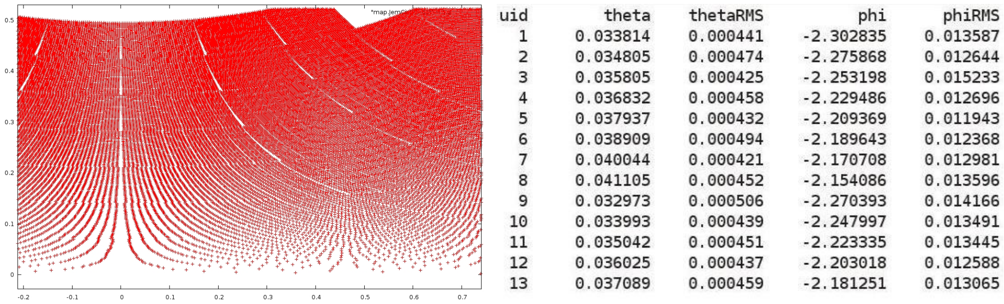

uid	theta	thetaRMS	phi	phiRMS
1	0.033814	0.000441	-2.302835	0.013587
2	0.034805	0.000474	-2.275868	0.012644
3	0.035805	0.000425	-2.253198	0.015233
4	0.036832	0.000458	-2.229486	0.012696
5	0.037937	0.000432	-2.209369	0.011943
6	0.038909	0.000494	-2.189643	0.012368
7	0.040044	0.000421	-2.170708	0.012981
8	0.041105	0.000452	-2.154086	0.013596
9	0.032973	0.000506	-2.270393	0.014166
10	0.033993	0.000439	-2.247997	0.013491
11	0.035042	0.000451	-2.223335	0.013445
12	0.036025	0.000437	-2.203018	0.012588
13	0.037089	0.000459	-2.181251	0.013065

Figure 4.2.3: Left: Plot showing the position of pixel on the FS. Right: First entries of the pixelanglemap lookup table. Both taken from [181].

For every pixel i, we obtain

1. the zenith angle θ_i^{FOV} and its error $\sigma_{\theta_i^{FOV}}$,
2. the azimuth angle and its error $\sigma_{\varphi_i^{FOV}}$,
3. the number of signals N_i^{hits},
4. and the time of arrival of the photons t_i

[181, 206, 250, and references therein].

THE TRACK DETECTOR PLANE (TDP)[6] is a mathematical concept of a plane, intersecting both the shower axis and the detector It is defined by the two unit vectors $\hat{V} \perp$ TDP and $\hat{W} \parallel$ TDP (Figs. 4.2.4 and 4.2.5). Using the TDP as an intermediate reconstruction step, reduces the problem to two dimensions (Fig. 4.2.5). Thus, the direction reconstruction algorithms applied hereafter, first aim at reconstructing the angle β inside the TDP (Fig. 4.2.5). Then, from β, using the knowledge of $\hat{V}$ and $\hat{W}$, we can

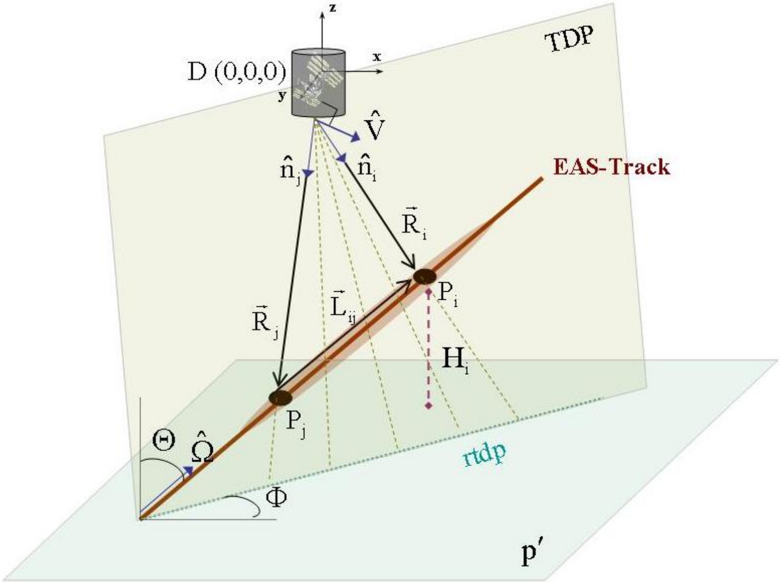

Figure 4.2.4: Direction Reconstruction System and the position of the TDP. Taken from [56, 181].

---

[6] Track Detector Plane: in some other UHECR experiments also referred to as Shower Detector Plane (SDP)

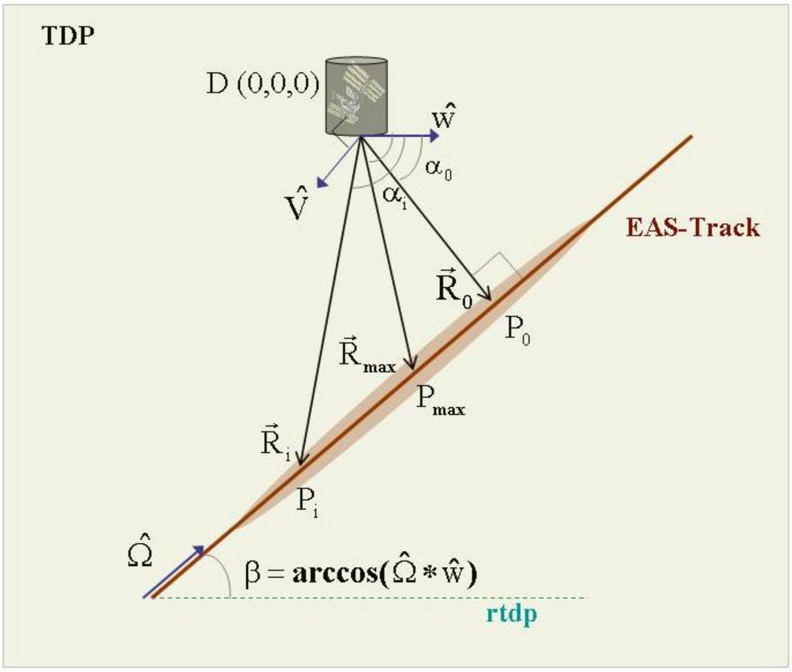

Figure 4.2.5: The Track Detector Plane (TDP) and the relevant vectors and angles within it. Taken from [56, 181].

retrieve $\hat{\Omega}(\Theta, \Phi)$ by

$$\hat{\Omega}(\Theta, \Phi) = \hat{W} \cdot \cos\beta + \hat{V} \cdot \sin\beta. \tag{4.20}$$

To infer the vector $\hat{V} \perp$ TDP, the air shower is approximated as one-dimensional. The signal track is projected into the x-t- and y-t planes. The spatio-temporal information can be retrieved by a linear fit [181, 250]

$$\sin(a_{ij})\hat{V} = \hat{n}_i \cdot \hat{n}_j. \tag{4.21}$$

The method uses the arrival times of the photons t_i to the detector in combination with the arrival directions $\hat{n}_i$ corresponding to certain pixels. The x- and y- components of the signal track are related to the photon's arrival angles θ^{FOV} and φ^{FOV} by:

$$x = -\tan\theta^{FOV} \cos\varphi^{FOV} \tag{4.22}$$

$$y = -\tan\theta^{FOV} \sin\varphi^{FOV}. \tag{4.23}$$

The knowledge of the x-t and y-t behaviour enables us to estimate the position of the

TDP. The point were the plane intersects the detector is defined to (0,0,0). Now, the position can be fixed with the help of the line rtdp which is established when the TDP intersects the earth's surface (Fig. 4.2.5). May the plane p' be tangent to the ground below the telescope's nadir. Then, rtdp can be parametrized by its slope M and its intersection point Q (0,0,0), by

$$\begin{aligned} x(t) &= v_x t + x_0 & (4.24)\\ y(t) &= v_y t + y_0 & (4.25)\\ \Longrightarrow rtdp : 0 &= \left(\frac{v_y}{v_x}\right) x - y + \left(y_0 - \frac{v_y}{v_x} x_0\right) & (4.26)\\ 0 &= M \cdot x - y + Q. & (4.27) \end{aligned}$$

The plane in 3-dimensional space is described by

$$0 = ax + by + z \qquad (4.28)$$

Since its intersection with the plane p' equals rtdp, the system can be solved. $\hat{V}$ is determined as

$$\hat{V} = \left(M\frac{H_{ISS}}{Q}, -\frac{H_{ISS}}{Q}, 1\right) \qquad (4.29)$$

The determining vector $\hat{W}$ is fixed by the intersection of the TDP with the plane parallel to the ground at the altitude of the ISS. Inside the TDP we use the angles α_i and β. α_i is defined by

$$\alpha_i = \arccos(\hat{n}_i \cdot \hat{W}). \qquad (4.30)$$

β is the angle between $\hat{\Omega}$ and $\hat{W}$

$$\beta = \arccos(\hat{\Omega} \cdot \hat{W}). \qquad (4.31)$$

Once β is determined, Θ and Φ can be easily computed. A system with two unknowns ($\hat{\Omega}$ and β) must be solved.

$$\begin{cases} \hat{V} \cdot \hat{\Omega} = 0 \\ \hat{W} \cdot \hat{\Omega} = \cos\beta \end{cases} \qquad (4.32)$$

as explained in [181, 249, 250].

Within the *TrackDirection2Module*, there are currently five different algorithms implemented. The first two approximate the angular velocity of the shower as constant and make an analytical attempt to solve the problem, the next two try to reconstruct the direction by means of a numerical approach [249].

- *Analytical Approximate 1* (AA1): approximates the angular velocity of the track projected in the x-t and y-t planes as constant to infer the primary's arrival direction in an iterative approach;
- *Analytical Approximate 2* (AA2): approximates the velocity projected on a plane perpendicular to the detector as constant;
- *Numerical Exact 1* (NE1): uses the arrival time of photons to the instrument to make a χ^2 minimization to reconstruct the shower direction $\hat{\Omega}$;
- *Numerical Exact 2* (NE2): uses the arrival angle of photons to the instrument to make a χ^2 minimization to obtain $\hat{\Omega}$;
- *Analytical Exact 1* (AE1): exploits the exact relations between photon arrival times and pixel viewing directions.

NE2 and AE1 are independent of the TDP. All of the methods require AA1 to be executed, first of all. Its result is then used as a starting point for further calculations.

THE REFERENCE SYSTEM to express the origin of the cosmic rays uses a right handed coordinate system with its z-axis aligned to the nadir point of the telescope. The arrival direction of the primary is defined by

$$\hat{\Omega} = \begin{pmatrix} \sin\Theta\cos\Phi \\ \sin\Theta\sin\Phi \\ \cos\Theta \end{pmatrix} \tag{4.33}$$

Thus, the vector $\hat{\Omega}(\Theta, \Phi)$ points up in the sky, where the UHECR has come from. In the scope of the reconstruction we also use the coordinate system having its origin in the detector to describe the arrival directions of the shower photons to the detector.

$$\hat{n} = \begin{pmatrix} \sin\theta^{FOV}\cos\varphi^{FOV} \\ -\sin\theta^{FOV}\sin\varphi^{FOV} \\ -\cos\theta^{FOV} \end{pmatrix} \tag{4.34}$$

We define the unit vector $\hat{n}_{max}$ pointing from the telescope to the shower maximum, the altitude of the shower maximum H_{max} and P_c, the Cherenkov impact point or shower core. P_i and P_j are two generic points of the air shower. Their distances to the detector are R_i and R_j and the shower segment between P_i and P_j is

$$|\vec{L}_{ij}| = |\vec{R}_i - \vec{R}_j|. \tag{4.35}$$

With this relation, the origin of the primary $\hat{\Omega}$ is linked to the emission site of the fluorescence photons:

$$\vec{R}_j - \vec{R}_i = \vec{L}_{ij} \rightarrow R_j\hat{n}_j - R_i\hat{n}_i = L_{ij}\hat{\Omega}. \tag{4.36}$$

Hence, we can relate the photon arrival time to the telescope with the shower direction

$$c(t_i - t_j) = L_{ij} + R_i - R_j \tag{4.37}$$

with $L_{ij} > 0$ for $t_i > t_j$. The shower velocity is approximated as the speed of light c. Using (Eq. 4.37) within the TDP, we receive an expression that displays the arrival time of photons in dependence of β

$$t_i(t_j, R_j, \alpha_j, \alpha_i, \beta) = t_j - \frac{R_j}{c} \cdot \left[\frac{\sin(\alpha_j - \alpha_i) + \sin(\alpha_i + \beta) - \sin(\alpha_j + \beta)}{\sin(\alpha_i + \beta)}\right]. \tag{4.38}$$

For a more detailed derivation see [250, and references therein].

THE ANALYTICAL APPROXIMATE 1 algorithm is the first direction reconstruction algorithm. It can either be executed as a first approach, providing essential information to the following algorithms or it can be run, exclusively. It makes use of the TDP and reconstructs the arrival direction first in the coordinate system of the TDP and translates the outcome in a second step into the reference frame in terms of $\hat{\Omega}(\Theta, \Phi)$. The AA1 works in an iterative approach by alternately reconstructing H_{max} and β. Differentiating the function (Eq. 4.38) with respect to α_i and replacing the jth pixel for the pixel pointing to the shower maximum $t_i^{teo}(t_{max}, \alpha_{max}, R_{max}, \alpha_i, \beta)$ yields

$$\omega = \frac{d\alpha_i}{dt_i} = -\frac{c}{R_{max}}\left[\frac{\sin^2(\alpha_i + \beta)}{\sin(\alpha_{max} + \beta) \cdot [\cos(\alpha_i + \beta) - 1]}\right]. \tag{4.39}$$

Neglecting the α_i dependence of ω and conceiving it as constant is an approximation which is feasible due to the fact that the detector is very remote from the EAS. Thus, for short EAS α_i changes only slightly from point to point and therefore we approximate

$\alpha_i \approx \alpha_{max}$. Now, (Eq. 4.39) can be simplified. Hence, we can write ω as function of α_{max}, R_{max} and β which is constant for the entire signal track.

$$\omega \approx -\frac{c}{R_{max}} \frac{\sin(\alpha_{max} + \beta)}{\cos(\alpha_{max} + \beta) - 1} \tag{4.40}$$

and we get

$$\beta = 2 \arctan \left(\frac{c}{\omega \cdot R_{max}} \right) - \alpha_{max}. \tag{4.41}$$

To obtain ω, we perform a linear fit of $\alpha(t)$. The slope of the fit yields the angular velocity. To retrieve β we have to infer R_{max}, the distance between the telescope and the EAS maximum

$$\begin{aligned} R_{max} = {} & \left(R_{\text{♁}} + H_{ISS}\right) \cdot \cos \theta_{max}^{FOV} \\ & - \sqrt{\left(R_{\text{♁}} + H_{max}\right)^2 - \left(\left(R_{\text{♁}} + H_{ISS}\right) \cdot \sin \theta_{max}^{FOV}\right)^2}, \end{aligned} \tag{4.42}$$

first of all. Here, $R_{\text{♁}}$ stands for the radius of the earth and H_{max} the altitude of the shower maximum. θ_{max}^{FOV} is the θ-component of the unit vector $\hat{n}_{max}(\theta_{max}^{FOV}, \varphi_{max}^{FOV})$ pointing from the detector to the shower maximum. The shower maximum is inferred by a Gaussian fit of the light curve, thus we get $\hat{n}_{max}(\theta_{max}^{FOV}, \varphi_{max}^{FOV})$. Since H_{max} is unknown, it has to be initially assumed to be 5 km — a typical value for protons. This enables us to compute β with Eq. 4.40. Knowing β, we can easily calculate a first estimate of the shower direction $\hat{\Omega}$ using (Eq. 4.20) [249, 250]. This is the first iteration within the AA1 reconstruction cycle as shown in Fig. 4.2.6.

Now, we can recalculate H_{max} by utilizing a simple parametrization of the atmosphere[7] which is a function of the zenith angle of the shower Θ and its slant depth X_{max}:

$$H_{max} = c \cdot \log \left[\frac{(X_{max} \cdot \cos \Theta - a)}{b} \right]. \tag{4.43}$$

As a first approximation, X_{max} is assumed to be 831 g/cm², the parameters a, b, c are inferred from (Tab. 4.2.1). X_v is calculated by $X_v = X_{max} \cdot \cos \Theta$.

Now, using the more realistic H_{max} value, we can recalculate β and translate it into the arrival direction of the primary particle $\hat{\Omega}(\Theta, \Phi)$ using (Eq. 4.20) [181, 249, 250].

---

[7] conducted by John Linsley, based on experimental data of the US Standard Atmosphere

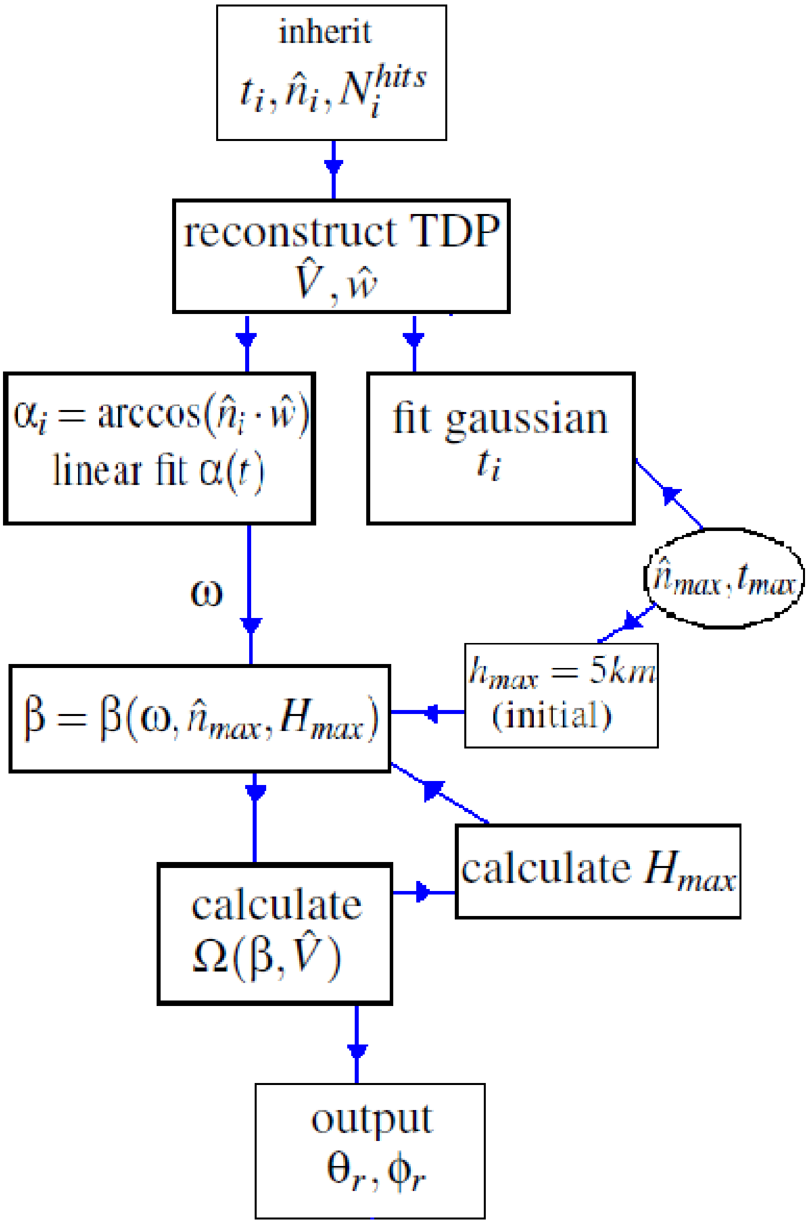

Figure 4.2.6: Schematic sketch of the AA1 direction reconstruction algorithm. Taken from [181].

Table 4.2.1: a,b,c parameters of Linsley's atmospheric parametrization. X_0=1036.1 g/cm², X_4=631.1 g/cm² and X_{10}=271.1 g/cm². From [249].

	$X_v < X_{10}$	$X_{10} < X_v < X_4$	$X_4 < X_v < X_0$
a	0.61	-94.92	-186.56
b	13.05	1144.91	1222.66
c	6.36	8.78	9.94

THE ANALYTICAL APPROXIMATE 2 algorithm requires the position of the TDP, together with the knowledge of α_{max}, inherited from the AA1 algorithm. Like AA1 it reconstructs the direction of the shower by fitting the angular velocity of the signal. However, AA2 uses the plane perpendicular to the shower axis and assumes the speed as constant. An iterative approach is not necessary here, since some information has already been provided by AA1. First of all, AA2 fits the speed in x(t) and y(t) components by a least squares fit. Then it retrieves the x and y speeds from the slope of the fitting function.

$$v_x = \text{slope}[x(t)] \quad v_y = \text{slope}[y(t)] \quad \Longrightarrow \quad v = \sqrt{v_x^2 + v_y^2} \tag{4.44}$$

and using α_{max}

$$\gamma = 2 \cdot \arctan\left(\frac{v}{c} \cdot \sin\ \alpha_{max}\right) \tag{4.45}$$

then β can be calculated by

$$\beta = -\ \gamma\ + \alpha_{max} \quad (if\, 90^\circ - \alpha_{max} < \beta < 90^\circ) \tag{4.46}$$

$$\beta = \gamma\ + \alpha_{max} \quad (if\, \beta > 90^\circ - \alpha_{max},\ \beta > 90^\circ). \tag{4.47}$$

From β we can calculate the primary's arrival direction, using (Eq. 4.20) [249, 250].

THE NUMERICAL EXACT 1 algorithm tries to retrieve the shower direction within the TDP by performing a χ^2-minimization between the arrival times of photons from the measured data and photons expected from a theoretically computed signal track

$$t_{exp} = t_1 - \frac{R_{max}}{c}\left[\frac{\sin(\alpha_1 - \alpha_i) + \sin(\alpha_i + \beta) - \sin(\alpha_1 + \beta)}{\sin(\alpha_i + \beta)}\right]. \tag{4.48}$$

The R_{max} value is inherited from previous modules, the β as computed by the algorithms before is used as a starting point. The algorithm varies the parameters of the above function to minimize

$$\chi^2(t_0, R_{max}, \beta) = \sum_{i=1}^{n_{FEE}} \frac{(t_i^{data} - t_i^{exp})^2}{\sigma_i^2} \cdot N_i^{hits}. \tag{4.49}$$

The β that minimizes the χ^2-function matches the true shower at its best. To translate β from the TDP coordinate system in the detector system, we use (Eq. 4.20) and obtain $\hat{\Omega}(\Theta, \Phi)$ [70, 249, 250].

The Numerical Exact 2 algorithm works independently of the TDP. However, it requests the values for Θ and Φ, as reconstructed by the AA1 algorithm, as a starting point. Now, it takes advantage of the endpoint of the shower (this can be the Cherenkov mark or simply the end of the track, where the shower is assumed to hit the ground) as a fixed reference point (Fig. 4.2.7). By varying the free parameters Θ and Φ of a theoretical shower and comparing the arrival angles of photons coming to the detector to the arrival angles in the data of the measured shower we can estimate the

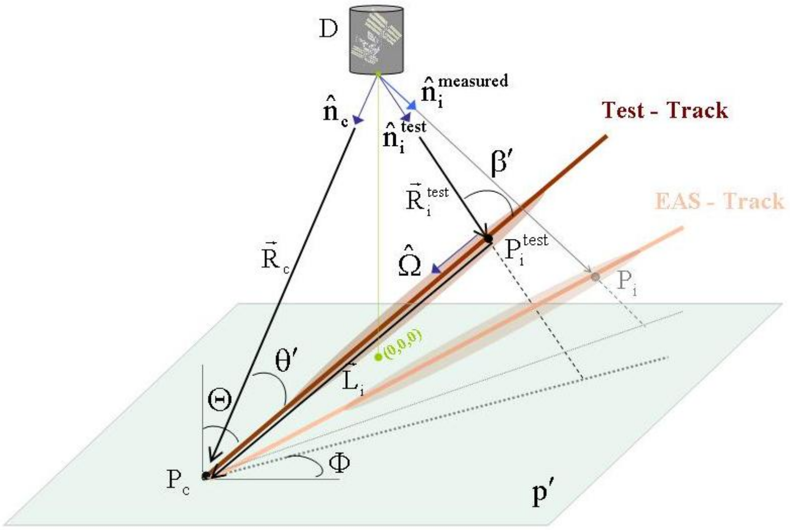

Figure 4.2.7: The vectors and angles used by the NE2 algorithm. Taken from [56, 181].

direction of the true shower. First of all, $\vec{L}_i$ the vector between P_c and P_i is defined as

$$\begin{aligned} x_i &= x_c + L_i \sin\Theta \cos\Phi && (4.50)\\ y_i &= y_c - L_i \sin\Theta \sin\Phi && (4.51)\\ z_i &= z_c - L_i \cos\Theta && (4.52)\\ \Longrightarrow L_i &= R_c \left(\cos\theta' - \frac{\sin\theta'}{\tan\beta'} \right) && (4.53) \end{aligned}$$

for $t_i < t_c$, L_i is positive. θ' can be expressed as a function of the unit vector $\hat{\Omega}(\Theta, \Phi)$ and the coordinates of P_c, the endpoint (or Cherenkov mark) of the track

$$\theta' = \arccos\left(\frac{\vec{R}_c}{|\vec{R}_c|} \cdot \hat{\Omega}(\Theta, \Phi) \right). \tag{4.54}$$

Using (Eq. 4.37), we can plug in t_i and express the angle β' by

$$\beta' = 2 \operatorname{arccot}\left(\frac{c(t_i - t_c)}{R_c \sin\theta'} + \cot\left(\frac{\theta'}{2}\right) \right). \tag{4.55}$$

The formulas in (Eq. 4.50) express the coordinates of every P_i as function of the angles Θ and Φ. Thus, the vector $\vec{R}_i^{test}$ which connects P_i to the detector can be computed due to the knowledge of the coordinates of the endpoint of the shower

$$\vec{R}_i^{test} = \vec{R}_c + \vec{L}_i. \tag{4.56}$$

For every pixel, the angle ψ_i which lies between $\hat{n}_i^{measured}$ and $\hat{n}_i^{test} = \frac{\vec{R}_i^{test}}{|\vec{R}_i^{test}|}$, can be calculated

$$\psi_i(\Theta, \Phi) = \arccos\left(\hat{n}_i^{measured} \cdot \frac{\vec{R}_i^{test}}{|\vec{R}_i^{test}|} \right). \tag{4.57}$$

The χ^2 function

$$\chi^2(\psi_i) = \sum_{i=1}^{n_{pixel}} \frac{\psi_i^2(\Theta, \Phi)}{\sigma_i^2} \cdot N_i^{hits} \tag{4.58}$$

has a minimum, once the arrival angles of the photons from the theoretical track match the ones of the measured track. The Θ and Φ of the test track are then taken as the incoming direction $\hat{\Omega}(\Theta, \Phi)$ of the true shower [70, 181, 249, 250].

THE ANALYTICAL EXACT 1 algorithm (AE1) is independent of the TDP. However, it requires the knowledge of the direction of the shower maximum $(\hat{\theta}^{FOV}_{max}, \hat{\varphi}^{FOV}_{max}, \vec{R}_{max}, t_{max})$ from previous modules. We define L$_i$ as the distance between a generic point of the shower $P_i = R_i \cdot \hat{n}_i$ and P_m. This yields a system with two unknowns, $\vec{L}_i$ and $\vec{R}_i$ [250]:

$$\begin{aligned} |P_{max} - P_i|^2 &= L_i^2 && (4.59) \\ c(t_{max} - t_i) &= \vec{R}_{max} + \vec{L}_i - \vec{R}_i. && (4.60) \end{aligned}$$

In a loop over all the pixels containing the shower track, we can calculate for every pixel with $(t_i < t_{max})$

$$\vec{R}_i = \frac{2c \cdot (-t_i + t_{max}) \cdot \vec{R}_{max} - (c \cdot (t_i - t_{max}))^2}{2 \cdot [\vec{R}_{max} \cdot (-1 + \cos\delta) + c \cdot (-t_i + t_{max})]} \tag{4.61}$$

and

$$\vec{L}_i = \sqrt{\vec{R}_i^2 + \vec{R}_{max}^2 - 2 \cdot \vec{R}_i \cdot \vec{R}_{max} \cdot \cos\delta}, \tag{4.62}$$

with δ, the angle between the two vectors $\vec{R}_i$ and $\vec{R}_{max}$

$$\cos\delta = \cos\theta_i^{FOV} \cdot \cos\theta_{max}^{FOV} + \sin\theta_i^{FOV} \cdot \sin\theta_{max}^{FOV} \cdot \cos(\varphi_i^{FOV} - \varphi_{max}^{FOV}). \tag{4.63}$$

For arrival times of photons $(t_i > t_{max})$ we calculate for every pixel pixel

$$\vec{R}_i = \frac{2c \cdot (-t_i - t_{max}) \cdot \vec{R}_{max} + (c \cdot (t_i - t_{max}))^2}{2 \cdot [\vec{R}_{max} \cdot (1 - \cos\delta) + c \cdot (t_i - t_{max})]} \tag{4.64}$$

and

$$\vec{L}_i = -\sqrt{\vec{R}_i^2 + \vec{R}_{max}^2 - 2 \cdot \vec{R}_i \cdot \vec{R}_{max} \cdot \cos\delta}. \tag{4.65}$$

Now, for every arriving photon we have the relation to the originating position of the shower track in dependence of the maximum position. The coordinates and their errors are expressed by

$$\begin{aligned} x_i &= R_i \cdot \sin\theta_i^{FOV} \cdot \cos\varphi_i^{FOV} & \sigma_{x_i} &= \frac{0.1}{N_i^{hits}} && (4.66) \\ y_i &= R_i \cdot \sin\theta_i^{FOV} \cdot \sin\varphi_i^{FOV} & \sigma_{y_i} &= \frac{0.1}{N_i^{hits}} && (4.67) \\ z_i &= R_i \cdot \cos\theta_i^{FOV} & \sigma_{z_i} &= \frac{0.1}{N_i^{hits}} && (4.68) \end{aligned}$$

with the field of view of a pixel ~ 0.1. By performing a linear fit of x_i, y_i, z_i we finally retrieve $\Omega(\Theta, \Phi)$ [249, 250].

Due to the different approaches of the five algorithms, their performance varies depending on the circumstances of the showers. Factors like energy, zenith angle and field of view position have an impact on the precision of the estimate. The fine tuning and the assessment of the performance of the different angular reconstruction algorithms is one of the major tasks of this work.

4.2.3 ENERGY AND X_{max} RECONSTRUCTION

The module to infer the X_{max} of the air shower and the energy of the primary particle is called *PMTToShowerReco*. As the name suggests, it starts with the PMT signals and tries to inversely process the way of the signal and photons respectively through the photomultiplier tubes, optics, atmosphere and shower, by applying correction functions to account for the several perturbations they are undergoing on their way to the instrument's readout (Fig. 4.2.8) [56, 98, 99, 102].

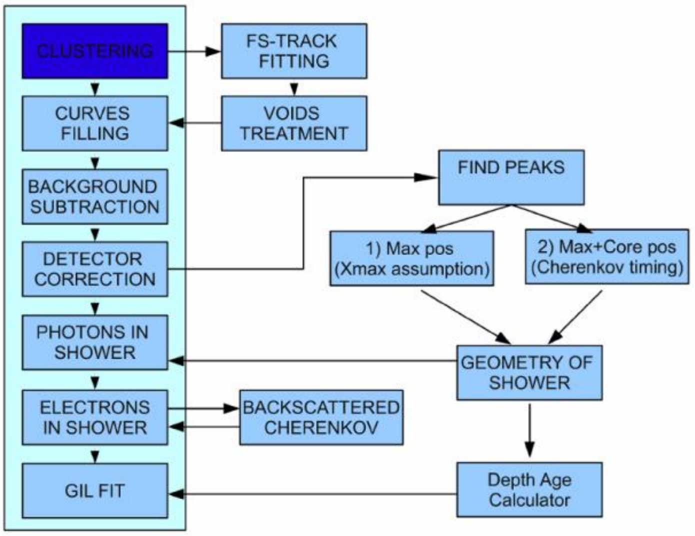

Figure 4.2.8: Overview on the PMTToShowerReco module. Taken from [102].

First of all, the module reads the trigger information and takes only the triggered events into account for further processing. The process chain begins from the signal distribution in time (signal curve) and corrects the sudden drops of the curve which are created when the signal traverses gaps between the PMTs and the larger voids between the PDMs on the focal surface. Therefore, the module retrieves the position of the track on the FS. The corresponding parts of the signal track that touch dead areas are ignored for the further processing. Now the background is subtracted. It is a fixed value for each pixel-gtu which is calculated as the square root of the amplitude value. Following that, the module tries to recover both the fluorescence maximum and the Cherenkov peak, if there is any. Unfortunately, the identification is not always possible. The procedure can be challenging due to signal fluctuations. Thus, a sophisticated identification algorithm has been developed [99]. The algorithm assumes the particle to be a proton first of all.

To reconstruct the light curve on the focal surface level, the efficiencies of the front-end electronics and the PMTs have to be taken into account, as well as the transmittance of the optical filter (BG3). The correction is performed by a multiplication of the single contributing factors.

To reconstruct the light curve at the entrance pupil level, the algorithm has to account for the optics inefficiencies, by utilizing the *opticsresponse*. This is a data table which contains the probabilities to focus the photons into a spot with the radius of 3 mm, weighted by the throughput efficiency. Both abilities depend on the zenith angle of the photons arriving to the telescope. This 'trigger throughput' is also affected by the lateral expansion of the shower. Moreover, the algorithm uses information of the *pixelanglemap*. This allows the estimation of an efficiency factor for each point of the signal track. By now, the global efficiency of the telescope is taken into account and treated respectively [99].

The shower luminosity, the total number of photons within the shower, can only be obtained if the distance to the detector is known. Due to geometrical reasons the distance affects the estimation of the photons flux by a factor of $1/d^2$. Thus, the intermediate task is the estimation of the X_{max} position (Fig. 4.2.9). There are two possibilities:

1. *The Cherenkov method*: uses the Cherekov peak (if properly identified) and takes the time delay between the photons arrival times coming from the maximum and the ones coming from the Cherenkov reflection mark to compute X_{max}.

2. *The slant depth method* fits the shape of the shower with a shower parametrization (GIL) and reads out the X_{max} value. This method requires the angular reconstruction data [99].

Knowing the X_{max} position, the atmospheric transmission is calculated by use of the LOWTRAN code. It delivers the photon distribution at the shower site. However, we cannot distinguish between fluorescence and Cherenkov photons. Therefore, to give

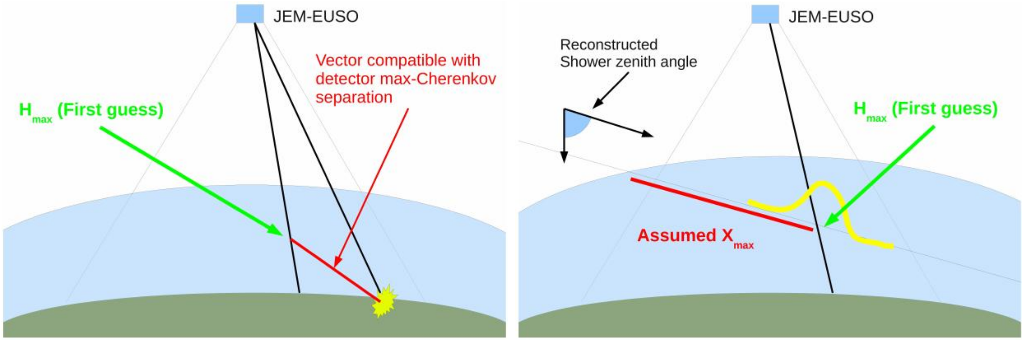

Figure 4.2.9: H$_{max}$ Reconstruction in the PMTToShowerModule. Left: The Cherenkov method. Right: The slant-depth method. Both taken from [102].

a proper estimate of the shower electrons, the problem of determining the amount of Cherenkov photons must be solved. Since this number is interlinked with the number of shower electrons, the problems have to be disentangled by an iterative approach. It starts with the ansatz of assuming no Cherenkov contamination, at all. Thus, the electron number is calculated by using the Nagano [191] fluorescence yield parametrization. From the obtained electron distribution the created Cherenkov photons can be computed. They are subject to absorption and scattering. The scattered ones are considered as contamination in the next step. Those Cherenkov photons that are neither absorbed, nor scattered are considered in the next step. The amount of electrons can be recalculated by using the fluorescence yield with the corrected amount of photons. This procedure is carried out step by step iteratively for the entire shower. The shower electron distribution is fitted with the GIL [170] function to obtain the energy and X$_{max}$ of the shower [99].

The whole reconstruction process described here can simply be expressed by

$$\frac{dN_{pe}}{dL} = \int_{\lambda_{min}}^{\lambda_{max}} \left\{ N_e\left(X(L), X_{max}, E\right) \varepsilon_{FY}^{\lambda}\left(H(L), s(L)\right) \frac{1}{4\pi} + \Psi_{CH}(\lambda, \vec{P}(L)) \right\} \frac{A_{opt}\cos\theta}{R^2} \cdot T_s(\lambda, \vec{P}(L), \vec{D}) \cdot T_a(\lambda, \vec{P}(L), \vec{D}) \varepsilon_{opt}(\lambda, \theta, \pi) T_{BG3}(\lambda) \varepsilon_{PMT}(\lambda) \varepsilon_{FE}\, d\lambda. \tag{4.69}$$

The above formula displays the relation between the number of signal counts of the front-end electronics N_e and a step of the EAS. The parameter $\varepsilon_{FY}^{\lambda}$ represents the differential fluorescence yield. Major determining factors of the detector are A_{opt} the lens surface area, ε_{opt} the optics throughput efficiency, T$_{BG3}$ the transmission of the optical band filter, ε_{PMT} the efficiency of the photomultiplier (which is determined by the quantum efficiency and the covering factor) and ε_{FE} the efficiency of the front end electronics. Ψ_{CH} describes the Cherenkov component:

$$\begin{aligned}\Psi_{CH}(\lambda, \vec{P}(L)) = \\ \int_0^L \left[N_e\left(X(l), X_{max}, E\right) \varepsilon^{\lambda}_{CH}\left(H(l), s(l)\right) \cdot T_s(\lambda, \vec{P}(l), \vec{P}(L)) T_a(\lambda, \vec{P}(l), \vec{P}(L))\right] dl \\ \cdot \left(-\dot{T}_s(\lambda, \vec{P}(L)) dl\right) \alpha_{anys}. \quad (4.70)\end{aligned}$$

This formula convolutes the electrons in each shower step with the differential Cherenkov yield $\varepsilon^{\lambda}_{CH}$. The terms T_s and T_a denote transmission losses due to scattering and attenuation [56, 98, 99, 102].

Double, double toil and trouble; Fire burn, and cauldron bubble.

Macbeth (Act IV, Scene I)

5

Angular Resolution: Nadir Mode

THE DETERMINATION OF THE ORIGIN of UHECR can be regarded as the primary objective behind any future UHECR observatory — this applies to the space borne experiments as well. Ground based observatories can rely on hybrid techniques and stereoscopic vision. Hence, their spatial resolution capabilities will largely remain unmatched, whereas in space, several constraints arise. These are imposed mainly due to limitations in payload, power consumption and data budget. Moreover, the safety related policies of the space agencies only allow the deployment of space qualified hardware. Therefore, novel technologies can only be implemented to some extent. Thus, in terms of pure spatial resolution, a space based detector cannot rival the already well established experiments. It is only by means of its unprecedented exposure in combination with a sufficient angular resolution that a space telescope can prevail over the ground based experiments. Hence, it will be the key experiment to identify the sources of UHECR.

This dissertation aim to quantify the potential angular resolution performance of the JEM-EUSO instrument. We place a special emphasis on the evaluation, how the measurement is affected by Rayleigh scattering of the fluorescence photons. In addition to this, we estimate the impact on the angular resolution when the instrument is tilted from its nadir alignment by 20° and 40° (see Chap. 6).

Within the context of JEM-EUSO, a number of pathfinders and potential alternative setups have emerged in the course of mission development. Smaller in size and weight, these instruments serve as technology demonstrators (EUSO Balloon, TA-EUSO) or possible alternatives to the originally developed instrument (SpaceX EUSO, EUSO500). While focussing on the JEM-EUSO baseline instrument, we have conducted end-to-end simulations for these instruments as well and addressed their expected performance in terms of their angular resolution capabilities.

A MEASURE of the instrument's angular resolution is defined by means of the separation angle γ (Fig. 5.0.1). It is the angle between the true arrival direction of the cosmic ray $\hat{\Omega}(\Theta, \Phi)$ and the reconstructed $\hat{\Omega}_r(\Theta_r, \Phi_r)$. It is always positive by definition.

$$\gamma = \sphericalangle(\hat{\Omega}, \hat{\Omega}_r) = \arccos\left((p_2 \cdot p_3) + (p_4 \cdot p_5) + p_1\right) \tag{5.1}$$

with

$$\begin{aligned} p_1 &= \cos\Theta \cdot \cos\Theta_r \\ p_2 &= \sin\Theta \cdot \sin\Theta_r \\ p_3 &= \cos\Phi \cdot \cos\Phi_r \\ p_4 &= \sin\Phi \cdot \sin\Phi_r \\ p_5 &= \sin\Theta \cdot \sin\Theta_r \end{aligned}$$

In our study we use the separation angle γ to express the angular resolution in two ways. First of all, we display the mean value in combination with its standard deviation calculated by

$$\sigma(\gamma) = \sqrt{\left(\frac{1}{N}\right) \cdot \sum_{i=1}^{N} (\gamma_i - \gamma_{mean})^2} \tag{5.2}$$

Moreover, we use the γ^{68} value which expresses the cumulative distribution of γ reaching 68% of the reconstructed events. I.e. 68% of all reconstructed events have a separation angle $\gamma \leq \gamma^{68}$.

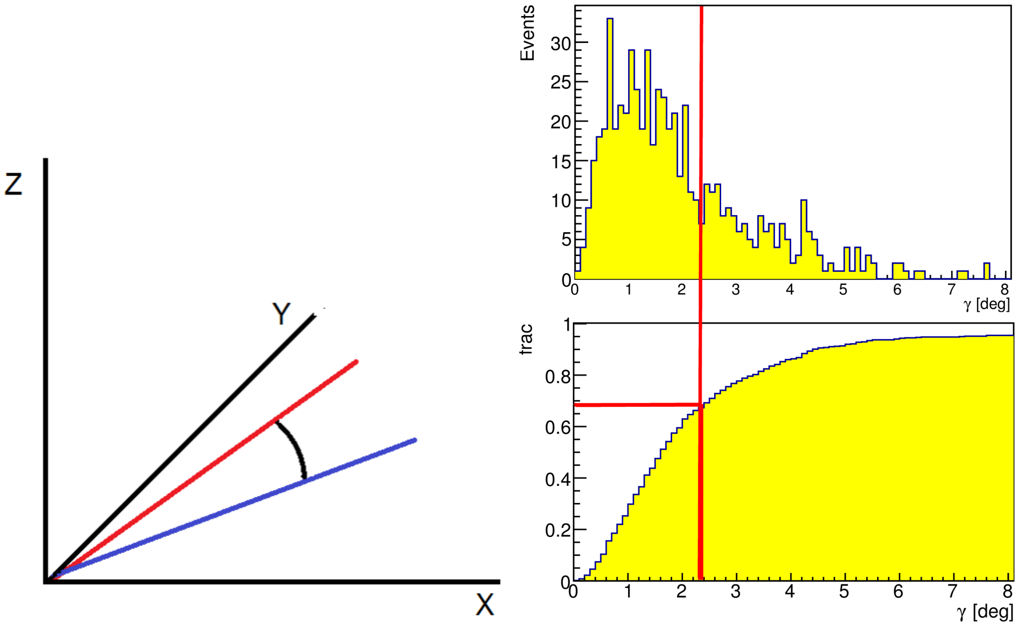

Figure 5.0.1: The separation angle γ lies between the vector of the true incoming direction and the reconstructed. It is positive by definition (left). To compare the angular resolution of JEM-EUSO to other detectors we define γ^{68}. Here, the cumulative distribution of γ reaches 68% of the reconstructed events (right).

Being a practical tool for intercomparison of different detectors at a glance, we cannot rely upon the separation angle only. Neither does it differentiate between statistical fluctuations and systematics, nor does it contain any information on the Θ and Φ resolution. Therefore, a holistic picture of the detector performance only emerges if we consider both $\langle\gamma\rangle$, γ^{68} and additionally $\langle\Theta\rangle$ and $\langle\Phi\rangle$ in combination with their standard deviations

$$\sigma(\Theta_r) = \sqrt{\left(\frac{1}{N}\right) \cdot \sum_{i=1}^{N} (\Theta_{r,i} - \langle\Theta_r\rangle)^2} \tag{5.3}$$

and

$$\sigma(\Phi_r) = \sqrt{\left(\frac{1}{N}\right) \cdot \sum_{i=1}^{N} (\Phi_{r,i} - \langle\Phi_r\rangle)^2}. \tag{5.4}$$

5.1 JEM-EUSO: NADIR MODE SIMULATIONS

The JEM-EUSO telescope will begin its operation aligned to the nadir direction. At a second stage, the instrument is planned to be tilted from its nadir to increase the exposure. The assessment of the expected performances of the instrument in nadir mode, is therefore the first objective of this thesis. For a good understanding of the reconstruction performances it is inevitable to address the analysis of the signal behaviour.

5.1.1 SIGNAL BEHAVIOUR

The detector for the measurement of UHECR must be understood as an entity comprising of the atmosphere acting as the detector volume and the actual telescope itself. During the course of the signal analysis it is therefore vital to examine the output of the intermediate steps of the measurement chain in close detail. Each of the intermediate steps can be parametrized by the utilization of dedicated models. Each of them has the potential to introduce systematic errors in the final results.

The shower development in this study uses the *SLAST* parametrization for the generation of the shower as described in Chap. 4.1.2. For illustration of the virtual measurement we follow a *standard shower*[1] event through the entire end-to-end chain. First of all, a distribution of particles along the shower is created (Fig. 5.1.1).

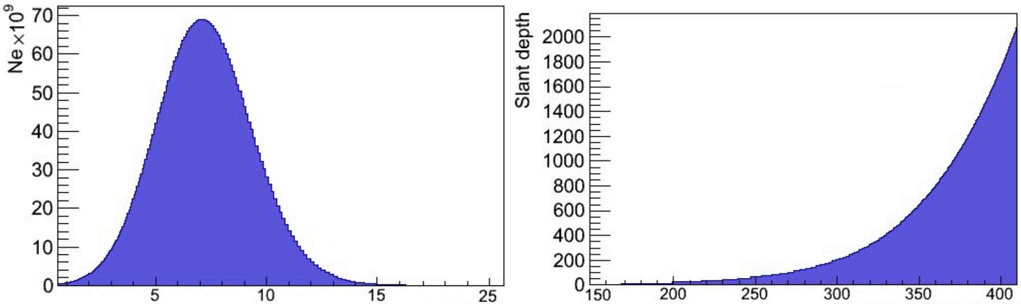

Figure 5.1.1: Standard shower: Number of electrons/positrons per altitude (left) and the temporal development (right).

From the distribution of charged particles, the numbers of fluorescence photons and Cherenkov photons are generated (Fig. 5.1.2) according to the corresponding light yields (Fig. 5.1.3).

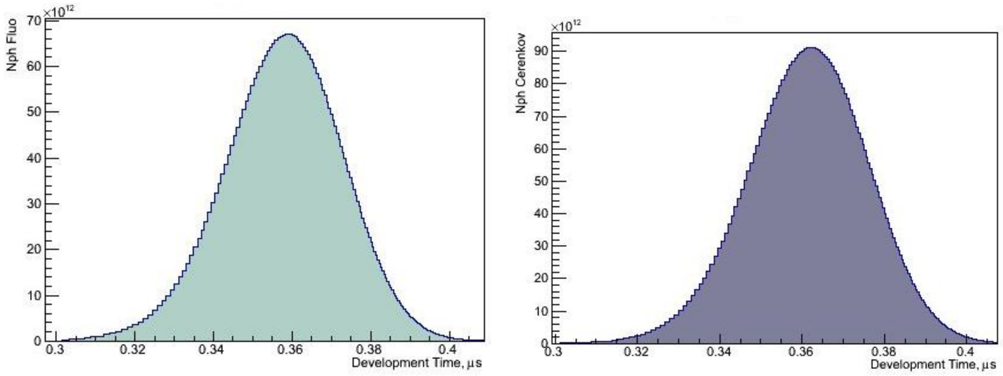

Figure 5.1.2: Standard shower: Fluorescence (left) and Cherenkov Photons (right)

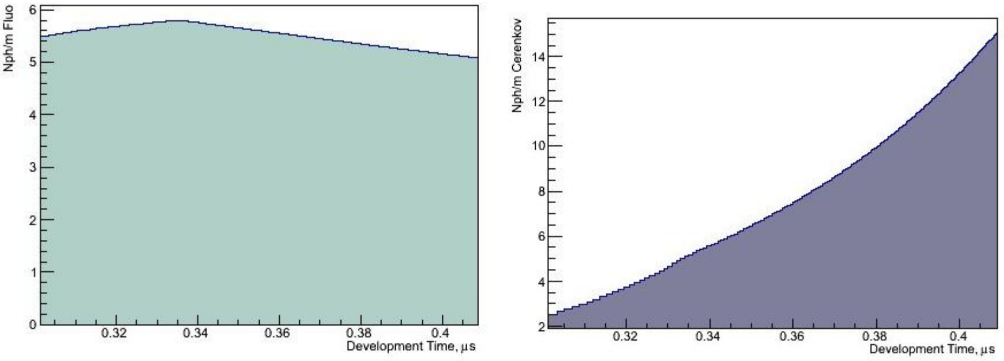

Figure 5.1.3: Standard shower: Fluorescence (left) and Cherenkov Photon Yield (right).

The spectrum of the fluorescence photons is a discrete line spectrum with the major contribution in the UV range between 300 and 400 nm, whereas the Cherenkov spectrum is continuous (Fig. 5.1.4).

Since the atmospheric part of the process chain is impossible to describe in perfect detail, we essentially rely upon approximations. These can be relatively simple such as parametrizations derived from former atmospheric measurements. Another, more sophisticated approach is the use of Monte Carlo computation methods which try to reproduce the numerical results in a stochastical approach by repeated sampling. Of course, even the most sophisticated Monte Carlo simulations are only able to predict within their limited abilities imposed by the underlying physical models assumed.

---

[1] A standard shower event is induced by a proton with an energy of 10^{20} eV and a zenith angle of 60°.

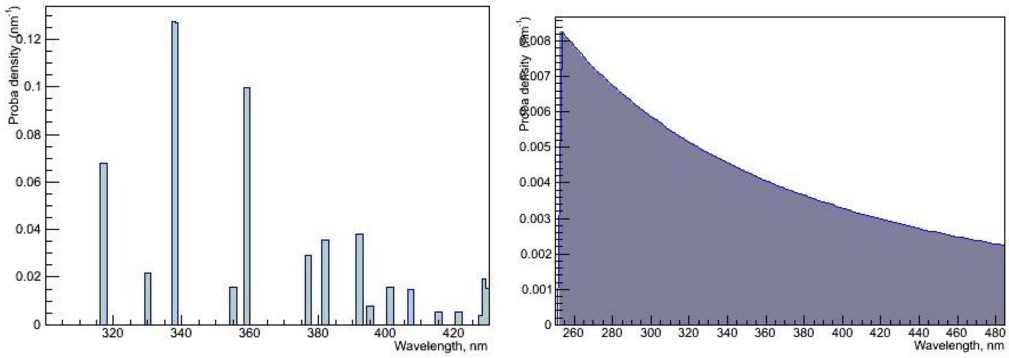

Figure 5.1.4: Standard shower: Fluorescence (left) and Cherenkov Photon Spectrum (right).

On their way to the detector, the photons suffer from losses due to atmospheric attenuation. The transmittance is wavelength dependent (Fig. 5.1.5).

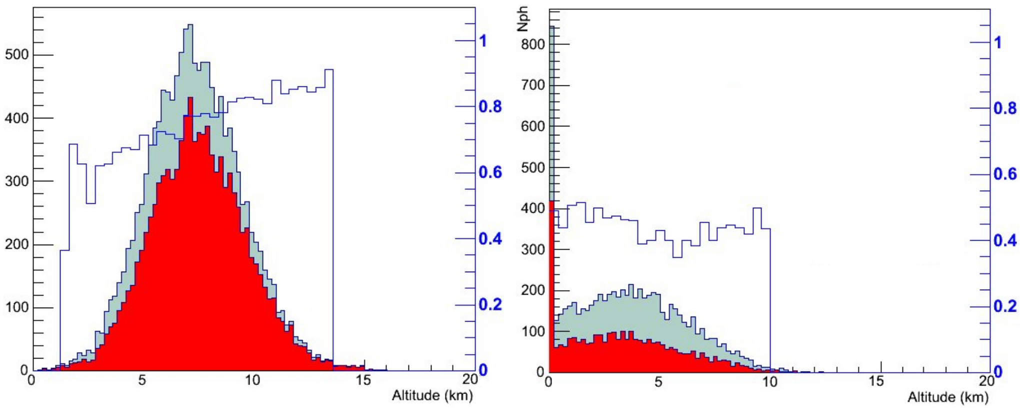

Figure 5.1.5: Standard shower: Fluorescence (left) and Cherenkov Photon Transmittance (right). In gray photons before atmospheric transport, in red hereafter. The blue line indicates the ratio of the two distributions.

Once the photons reach the instrument stage of the measurement, we have the advantage of a relatively precise knowledge of the instrument's properties. Here, the intermediate results can be computed by means of analytical formulas or the help of databases. Hence, this part of the measurement chain is not expected to introduce major uncertainties to the final estimate. The photons arriving to the first lens are transported through the optics via a ray-trace code. The losses due to attenuation in the lens material and the scattering on the Fresnel surfaces are taken into account (Fig. 5.1.6).

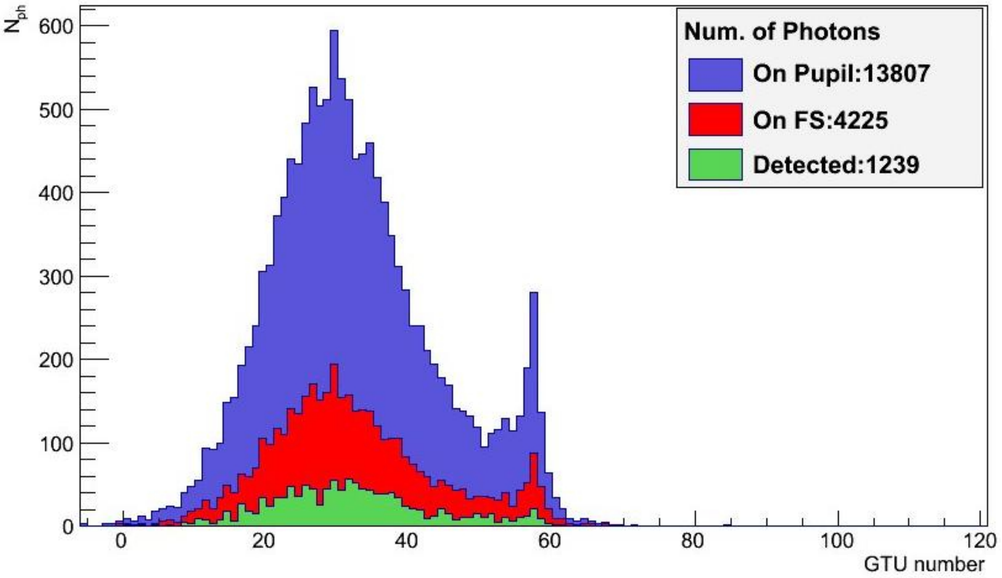

Figure 5.1.6: An example for a standard shower, E=10^{20} eV, Θ= 60°: photon distribution in time on the first lens (purple), reaching the focal surface (red) and making signal (green). The event has been placed in the centre of the FOV.

5.1.2 Angular Resolution

To evaluate the expected angular resolution performance of the JEM-EUSO telescope we have generated a database of UHECR induced extended air showers with five different fixed energies and four different fixed zenith angles. The energy ranges from $5{\cdot}10^{19}$ eV, $7{\cdot}10^{19}$ eV, $1{\cdot}10^{20}$ eV, $3{\cdot}10^{20}$ eV to $5{\cdot}10^{20}$ eV. The simulated zenith angles include 30°, 45°, 60° and 75°. The azimuth angles are randomly chosen between 0 and 360°. All primaries are exclusively proton events. The events have been distributed within an area which is well larger than the actual field of view (FOV) of the telescope. The idea behind is to provide a more realistic scenario with stray light reaching the detector and causing possible triggers without without having a real shower event recorded, but also to investigate the impact of those air showers that appear not entirely inside the FOV but intersect its boundaries. The shower impact points have been set inside x= ± 270 km × y= ± 190 km.

The angular resolution measured in terms of the γ^{68} shows a clear dependence on the different energies and zenith angles (Fig. 5.1.7). In general, the relation is evident. The more energy the primary deposits in the atmosphere, the more photons are produced. Hence, more photons reach the detector and consequently more information is

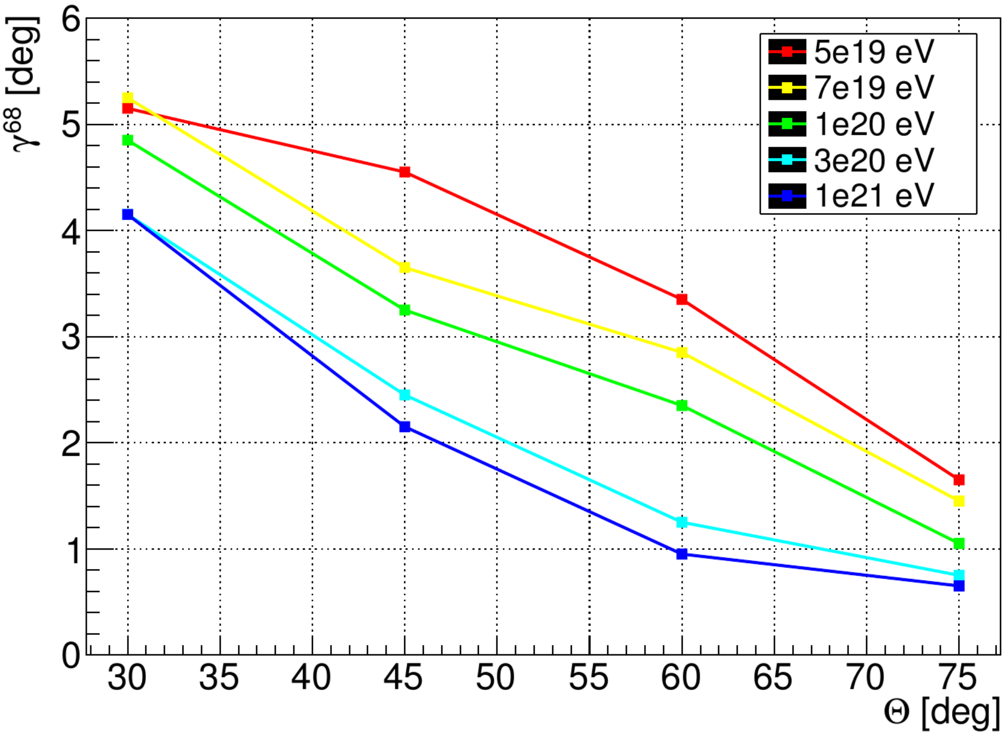

Figure 5.1.7: JEM-EUSO nadir mode: Angular resolution in terms of γ^{68}, obtained by the NE2 algorithm for proton events plotted against the true zenith angle for different energies (colour coded).

delivered to the reconstruction modules. The argument of the zenith angles is similar but slightly different. The more inclined the showers are, the longer the tracks become. This is due to the fact that they develop higher in the atmosphere, where the air pressure is lower. Therefore, there are less targets and so the secondary particles and the produced photons are distributed over a longer track. Furthermore, since the showers develop beneath the telescope, the viewing angle of the shower with reference to the detector changes in such a way that the shower is better seen from the side, whereas for low inclinations this component appears in a rather unfavourable way.

In Fig. 5.1.8, we show the trigger efficiency (blue), the reconstruction efficiency (green) and the product of the two, the effective efficiency (red). It is important to point out that the trigger efficiency as shown here should not be mistaken for the real expected trigger efficiency. The trigger efficiency as defined in this work means simply the ratio of triggered events to simulated events without taking the proper FOV geometry into account. A number of showers might appear partially inside the FOV of the instrument's optics, without being in the FOV of a PDM. This is simply due to

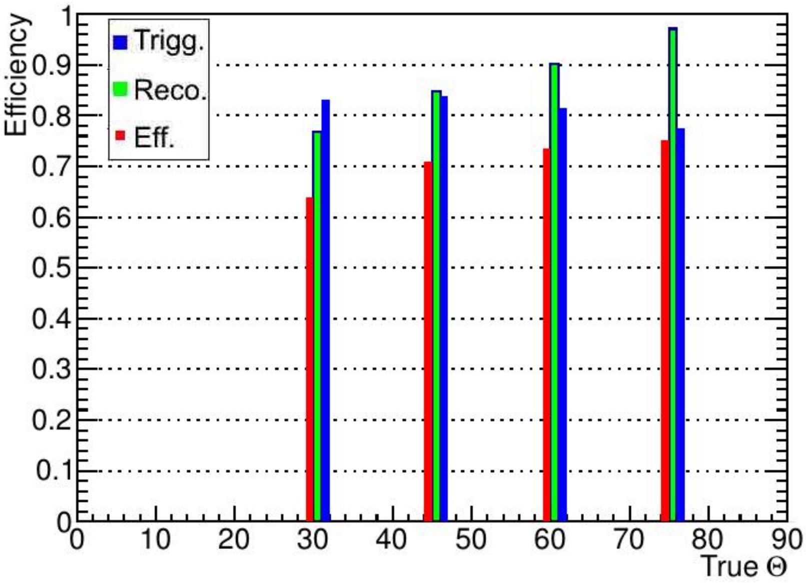

Figure 5.1.8: JEM-EUSO nadir mode: trigger efficiency (blue), reconstruction efficiency (green) and the effective efficiency (red) for the different zenith angles and cumulative energies.

the fact that the rectangular PDM layout only roughly approximates the shape of the side-cut circular optics. We can assume, if properly calculated, the trigger efficiency of the 10^{20} eV, Θ=60° standard event to be 100% [99]. Thus, the efficiency plots shown here, serve to illustrate the differences between the detector configurations tested in this work and not as absolute numbers. The reconstruction efficiency denotes the ratio of reconstructed events to triggered events. Reconstructed means that during the fitting procedure of the track which has been identified by the pattern recognition before, the fit has converged and there is a sufficient amount identified signal counts for the direction reconstruction module to apply the algorithms. However, it does not express a quality evaluation. For instance, an event can be triggered, labelled as reconstructed but point 20° away from the true incoming direction of the primary particle even though this is relatively unlikely.

The angular resolution in Fig. 5.1.7 has been estimated by the NE2 algorithm which proves to be the overall best performing algorithm in this setup. However, depending on the circumstances which are primarily the zenith angle and the energy but also the position of the shower inside the FOV, another algorithm can be the better choice for the direction reconstruction. Figs. 5.1.9 and 5.1.10 show the dependencies.

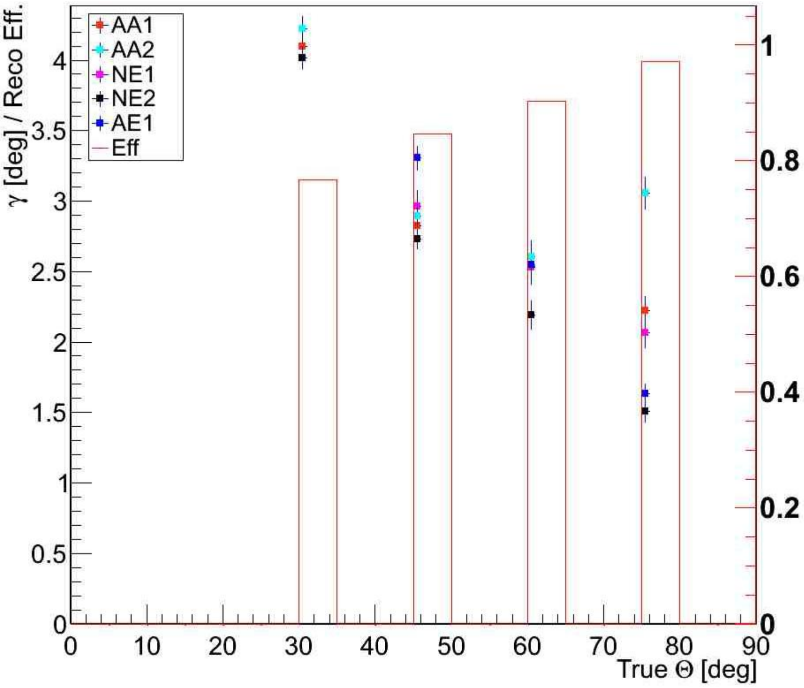

Figure 5.1.9: JEM-EUSO nadir mode: $\langle\gamma\rangle$ for the five algorithms (colour coded)and their standard deviation plotted as function of the true zenith angle together with the reconstruction efficiency (red bars).

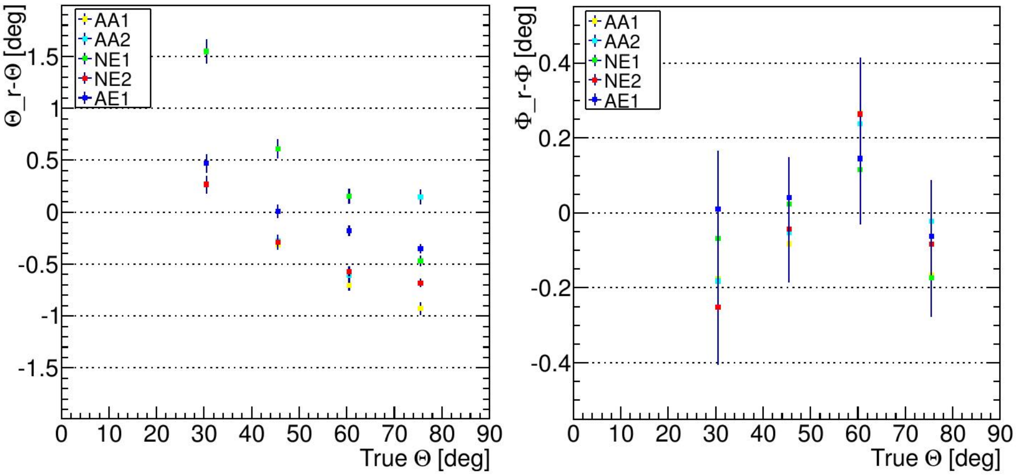

Figure 5.1.10: JEM-EUSO nadir mode: reconstructed $\langle\Delta\Theta\rangle$ (left) and $\langle\Delta\Phi\rangle$ distributions (right) for cumulative energies. The colours represent the five different algorithms to show their individual performance. The error bars indicate the standard deviations.

The angular resolution performance of the JEM-EUSO telescope also features a dependency on the position inside the FOV. In the very centre of the FOV, the reconstruction module performs at its best and so does the trigger algorithm. The more the events are displaced from the centre, the lower the resolution becomes and the less efficient both trigger and reconstruction efficiency are (Fig. 5.1.11). The reason for this comes partly from the effect that events occurring in the outer ring of the FOV, have a greater possibility to intersect the boundaries of the FOV and appear therefore only in parts. This applies mostly to the red events in Fig. 5.1.12. Another factor introducing difficulties is the degradation of the optics throughput efficiency. In the centre about 30% of the photons reach the focal surface, whereas in the remote regions it drops to less than 20%. Moreover, events in this area are also farther displaced from the telescope's nadir point and thus, less photons arrive even to the entrance pupil of the instrument. In Fig. 5.1.12, we plot the population of the maxima of the events that (1) did not trigger (in red), (2) have been triggered, but not reconstructed (yellow) and (3) have been successfully reconstructed (green).

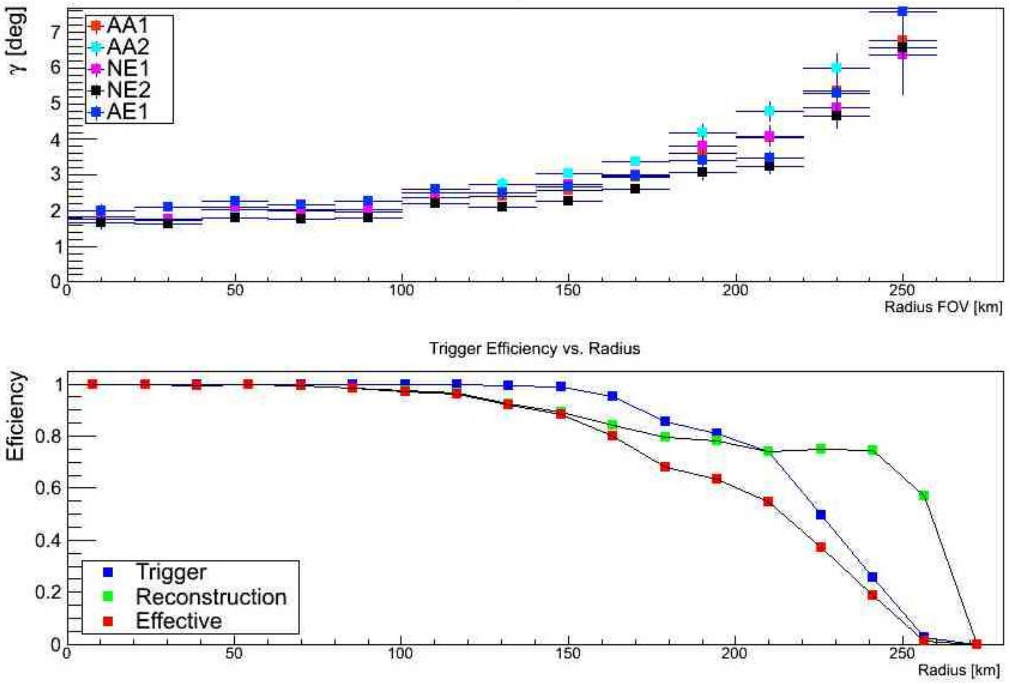

Figure 5.1.11: JEM-EUSO nadir mode: top: $\langle\gamma\rangle$ for the five algorithms (colour coded) and their standard deviation plotted as function of the FOV radius. bottom: trigger (blue), reconstruction (green) and effective efficiency (red) as function of the FOV radius.

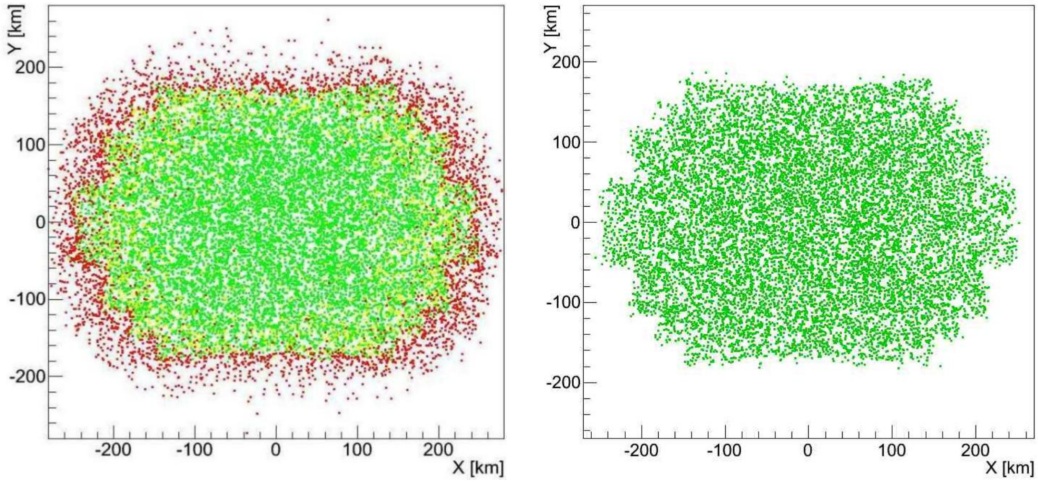

(a) FOV position of event maxima: superimposed view

(b) Reconstructed events

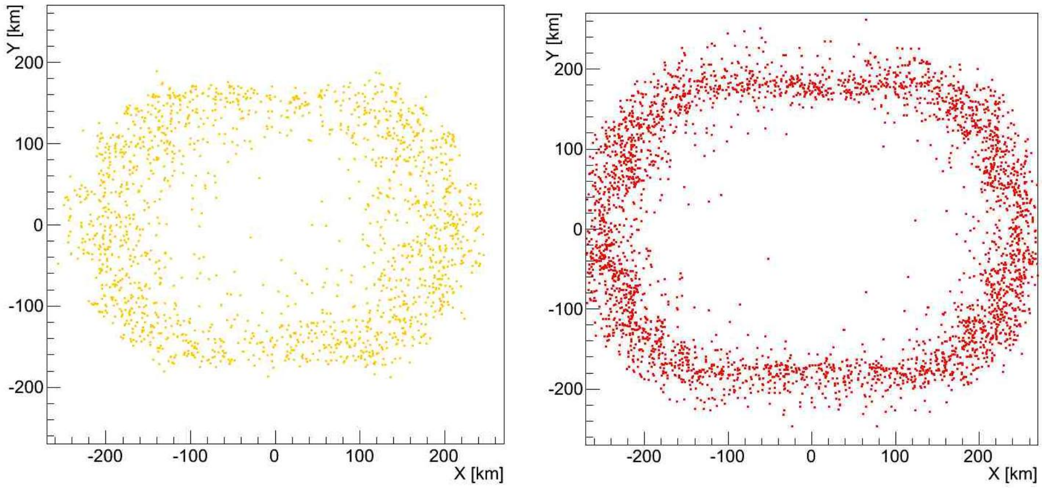

(c) Failed events

(d) Non-triggering events

Figure 5.1.12: JEM-EUSO nadir mode: shower maxima positions within the telescope's FOV. Red: Population of non-triggering events. Yellow: Events, triggered but not reconstructed. Green: Events, triggered and successfully reconstructed.

5.1.3 QUALITY CUTS

The precision to which the UHECR direction of origin can be reconstructed depends on a variety of variables within nature such as energy of the primary or the zenith angle and position of the resulting shower with reference to the telescope. Besides that, the design of the instrument itself imposes certain inefficiencies which alter or attenuate the signals. Hence, the quality of the reconstruction data ranges from poor in some cases to excellent in others. To better quantify the impact of the shower position within the telescope's field of view on the reconstruction quality, we have analyzed a sub-class of events having their shower maximum within a radius of 150 kilometres. Within this reduced FOV, we expect the resolution to improve with regard to the overall event reconstruction quality due to two different effects mostly: First of all, these events occur within an area inside the FOV in which the optical system of the instrument features its highest throughput efficiency. Hence, less photons suffer from attenuation while being propagated through the optics. Secondly, taking into account these events only prevents us from accidentally trying to reconstruct signal tracks of which major parts are missing due to intersecting the FOV borders (Fig. 5.1.13).

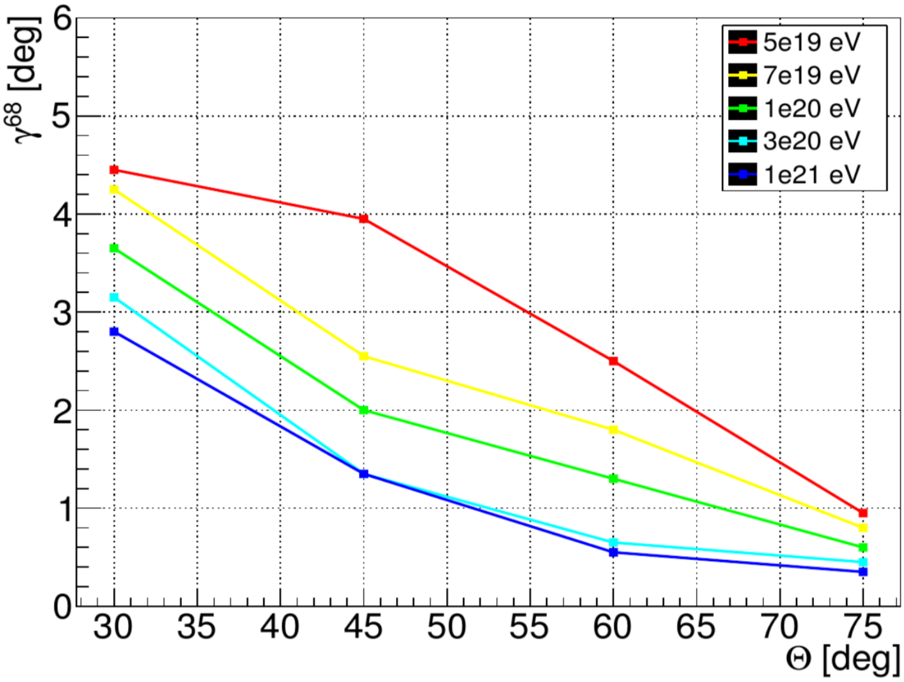

Figure 5.1.13: JEM-EUSO nadir mode: Angular resolution in terms of γ^{68} inside a 150 km radius from the centre. Results obtained by the NE2 algorithm in dependence of the true zenith angle for different energies (colour coded).

A second sub-class of events analyzed are the bright events. Depending on the factor pointed out above, we expect to observe extremely luminous events on the one hand, but also a number of events which have either intrinsically or attenuation-imposed a rather faint or short signature on the focal surface. For this estimate we have chosen only those events, having a minimum of 20 pixels belonging to the integrated track (Fig. 5.1.14). The populations of both quality cut analyses made arguably overlap in parts. For instance, events occurring at the very edge of the FOV and appearing only partially will certainly fall into both categories. Furthermore, events with relatively low energy and zenith angles that occur more than 150 km displaced from the centre of the FOV and are therefore stronger attenuated by the less efficient optics than their centre-placed counterparts, might also only produce signal tracks with less than 20 pixels. However, we could not find a clear correlation between these two quality cuts imposed. Both describe the behaviour of their own class of events in their own way and are therefore important tools to assign reconstruction quality labels on real events in the future.

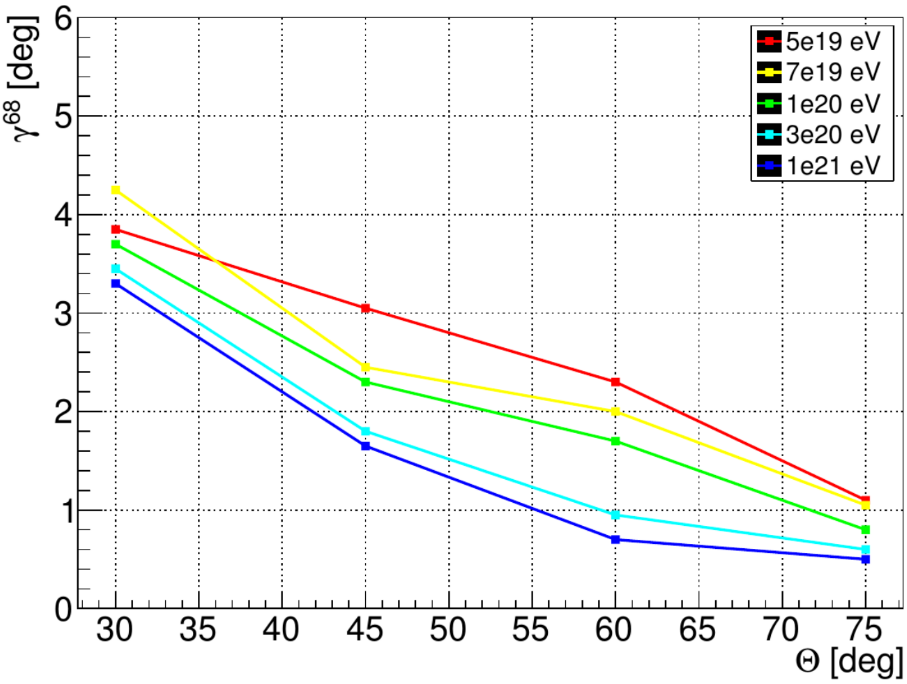

Figure 5.1.14: JEM-EUSO nadir mode: Angular resolution in terms of γ^{68} for events with a minimum of 20 pixels selected. Results obtained by the NE2 algorithm in dependence of the true zenith angle for different energies (colour coded).

5.2 JEM-EUSO: Impact of Rayleigh Scattering

The recently published angular resolution study as presented in Chap. 5.1.2, has been simulated without addressing the expected air scattering effects of the fluorescence light component. This is a valid approach in the sense that the majority of photons reach the detector without undergoing any scattering effects. Moreover, this kind of study primarily aims at demonstrating the feasibility of the end-to-end simulation of the entire mission, while giving a first well-established evaluation on the potential angular resolution of the instrument. However, in nature the signal photons are expected to undergo interaction with air molecules up to a number of times. In order to evaluate the impact of these scattering effects on the reconstruction quality this chapter is devoted to a study in which a Monte Carlo treatment is invoked during the transport of photons from the air shower through the atmosphere to the telescope. We analyse the effects on the recorded signal and present the extent to which those changes potentially affect the expected angular reconstruction performance.

5.2.1 Signal Tracks of Scattering Events

The *Bunch* algorithm used in many prior studies does not account for the scattering effects of the fluorescence light photons. This effect might be of less importance for ground based experiments due to the close proximity of the showers. However, for a telescope located more than 400 km away, scattering up to multiple orders are expected to have a non-negligible impact on the signal behaviour. We have therefore employed Monte Carlo simulations with successively higher scattering orders to understand the extent to which the scattering order impacts the signal (Figs. 5.2.3 and 5.2.4). The events with a Monte Carlo simulation of photons in atmosphere differ from those using the *Bunch* transfer in some important regards. First of all, the total number of photons reaching the detector is significantly higher — in a number of configurations about twice as many. See Tab. 5.2.1 for the detailed account. However, the total number of photons arriving to the telescope can be misleading. It cannot be understood in the sense that the tracks appear twice as bright. In fact, the now additional photon component appears to be spread over a much wider area than the *Bunch* track. Many photons appear in close vicinity of the track axis, causing a broadening of the track. However, a large fraction is dispersed all over the focal surface (Figs. 5.2.2 – 5.2.4).

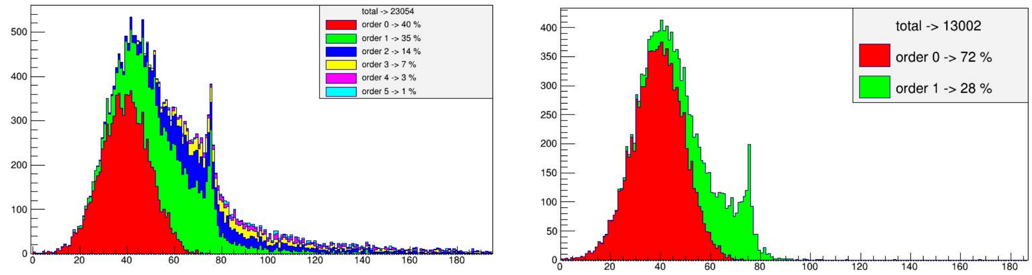

(a) MC: photon fraction

(b) Bunch: photon fraction (includes Cherenkov photons scattering, only.)

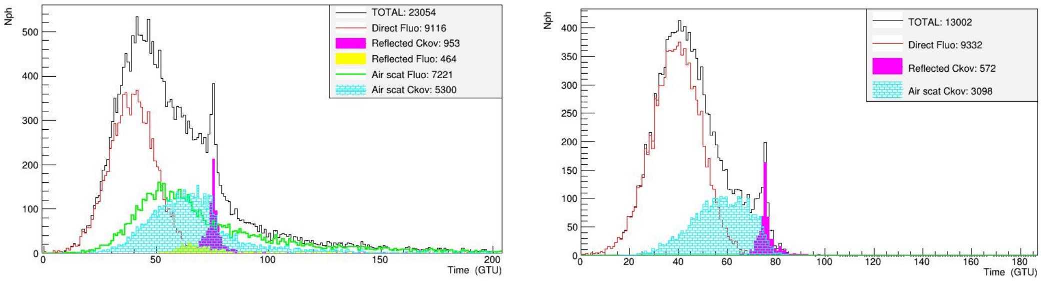

(c) MC: photon numbers

(d) Bunch: photon numbers

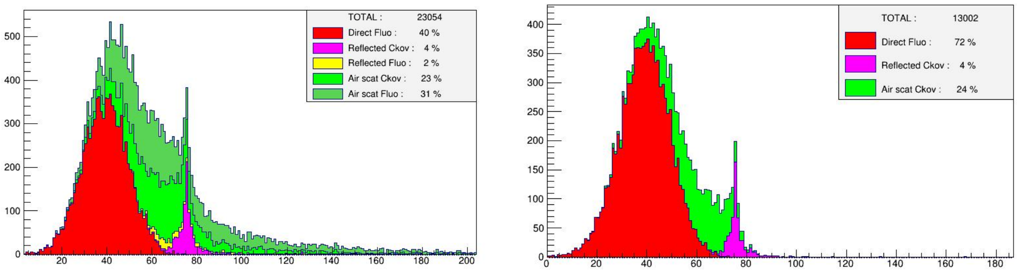

(e) MC: signal components, pupil

(f) Bunch: signal components, pupil

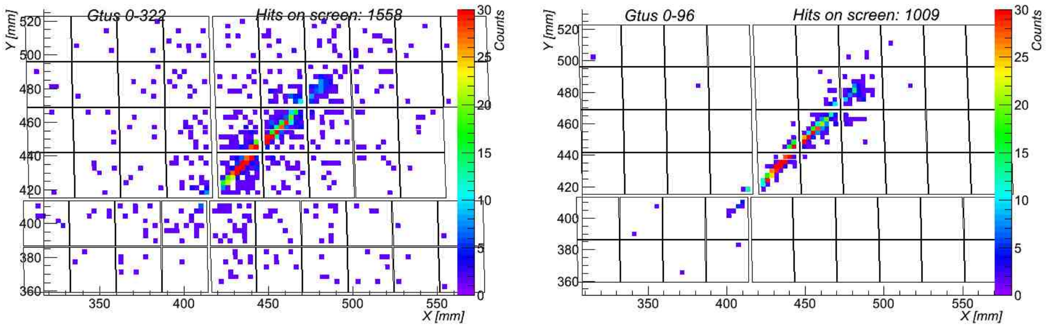

(g) MC: signal track

(h) Bunch: signal track

Figure 5.2.1: Direct comparison between two standard showers with Monte Carlo transfer of photons in atmosphere simulating 5 scattering orders (left) and Bunch without scattering of fluorescence light, only Cherenkov (right) .

Table 5.2.1: Intermediate results of the simulation chain. The numbers are average values from a statistics of 100 events distributed over the entire FOV.

simulation stage	# of particles			
	Bunch		*Monte Carlo*	
$e^{\pm}$ in shower	$4.4 \cdot 10^{12}$			$4.4 \cdot 10^{12}$
photons produced	$9.9 \cdot 10^{15}$			$9.8 \cdot 10^{15}$
photons emitted to detector	direct	10256	direct	10188
	scatt.	5181	scatt.	15837
	refl.	1041	refl.	2202
	total	16478	total	28227
photons on pupil	10219			18641
photons on focal surface	2427			4223
signals created	650			1145
PDMs hit	2			11

The Monte Carlo signals do not only differ from the *Bunch* tracks regarding their geometrical properties but also in their timing. Since the scattered photons travel longer distances in atmosphere in comparison to their counterparts reaching the instrument on a straight trajectory, their arrival time is delayed. This effect extends the duration of the entire event from the detector point of view up to factors of 10. For instance, a 10^{20} eV, Θ=60° event without any scattering effect taken into account, such as the one shown in Fig. 5.2.3 c, d, the duration takes 59 GTUs, whereas if five scattering orders are taken into account the same events last up to 481 GTUs as shown in Fig. 5.2.4 e, f.

The three effects pointed out, contribution to background photons around the signal, broadening of the track and dilation of the signal timing occur in dependence of the energy and the zenith angle of the shower, since it is related to the overall number of photons (Fig. 5.2.2). Moreover, the effect depends on how many scattering orders are being considered. In our simulations we have found that for up to five orders of scattering, we can see an obvious contribution, however with ever decreasing significance (Figs. 5.2.3 and 5.2.4). Due to the fact that higher scattering orders exceeding the fifth, contribute only marginally, we have selected five scattering orders as the reasonable number for taking the scattering into account for the present study. Any higher order would not influence the signal in a significant way, but increase the computing

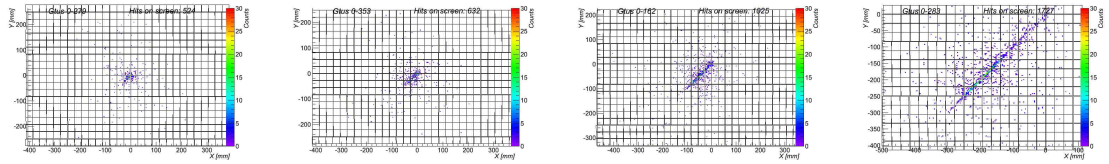

(a) 5e19 eV, 30° **(b)** 5e19 eV, 45° **(c)** 5e19 eV, 60° **(d)** 5e19 eV, 75°

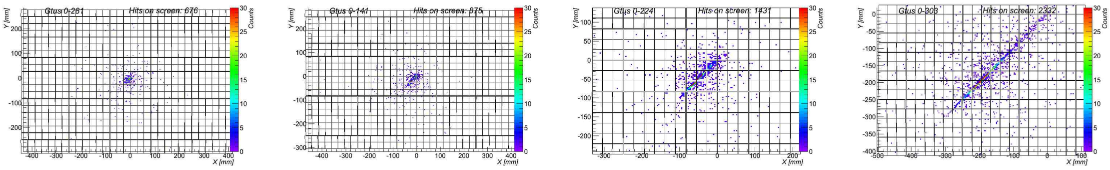

(e) 7e19 eV, 30° **(f)** 7e19 eV, 45° **(g)** 7e19 eV, 60° **(h)** 7e19 eV, 75°

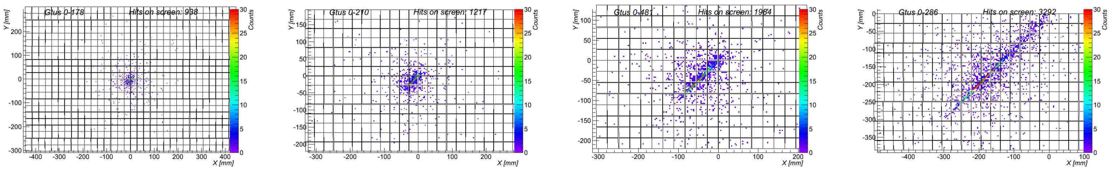

(i) 1e20 eV, 30° **(j)** 1e20 eV, 45° **(k)** 1e20 eV, 60° **(l)** 1e20 eV, 75°

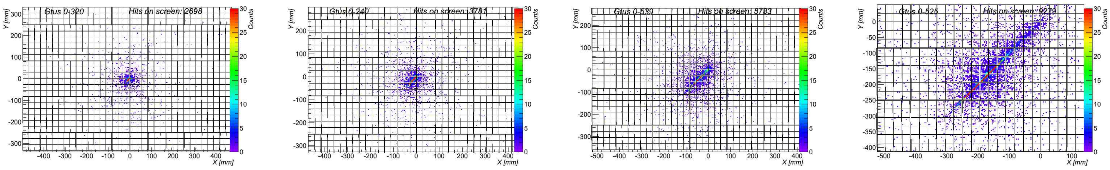

(m) 3e20 eV, 30° **(n)** 3e20 eV, 45° **(o)** 3e20 eV, 60° **(p)** 3e20 eV, 75°

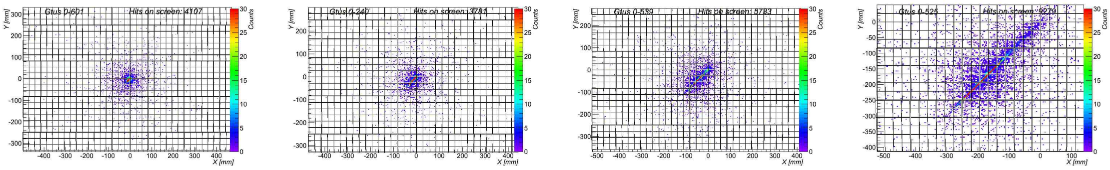

(q) 5e20 eV, 30° **(r)** 5e20 eV, 45° **(s)** 5e20 eV, 60° **(t)** 5e20 eV, 75°

Figure 5.2.2: Shower tracks on the focal surface for different energies and zenith angles using Monte Carlo transfer of photons to simulate five scattering orders.

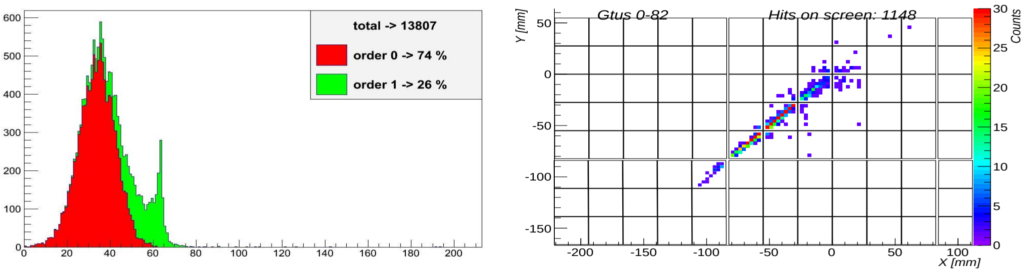

(a) Bunch: light curve **(b)** Bunch: track

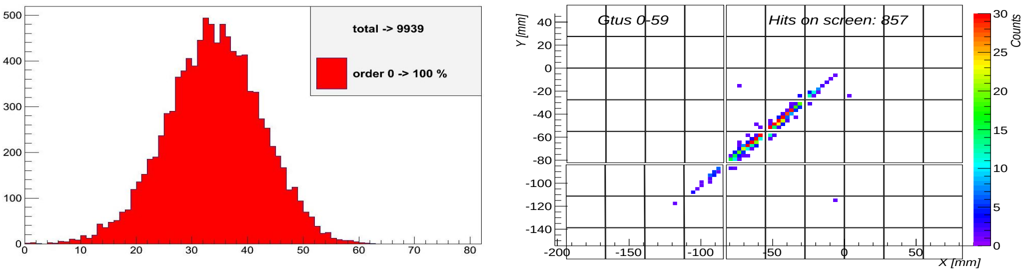

(c) MC, order 0: light curve **(d)** MC, order 0: track

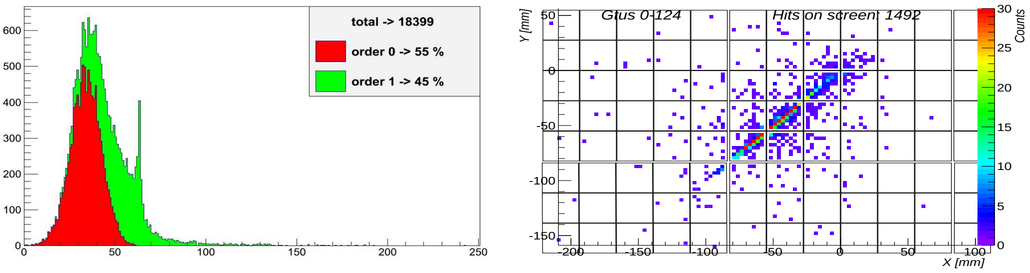

(e) MC, order 1: light curve **(f)** MC, order 1: track

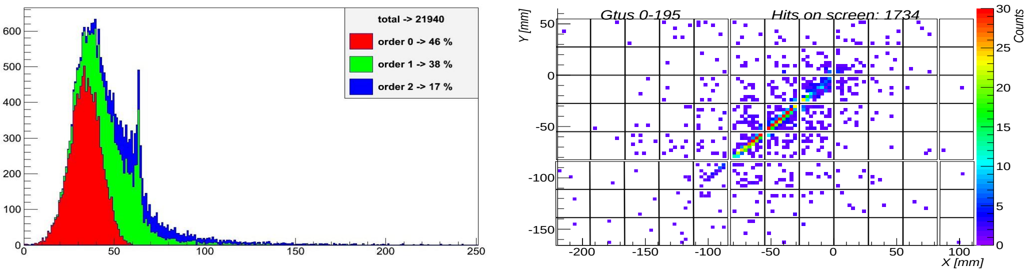

(g) MC, order 2: light curve **(h)** MC, order 2: track

Figure 5.2.3: The influence of the scattering order on the light arriving to the telescope: Light curves (left) and signal tracks (right). a) and b) show the case of a Bunch track which includes Cherenkov light as 1^{st} order scattered light. c) and d) show the case of no scattering effect at all.

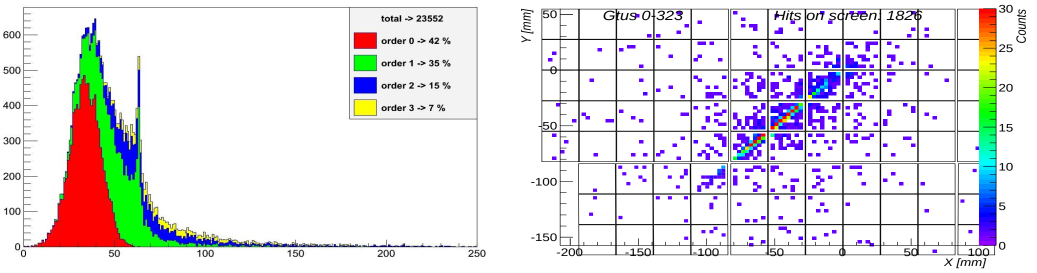

(a) MC, order 3: light curve **(b)** MC, order 3: track

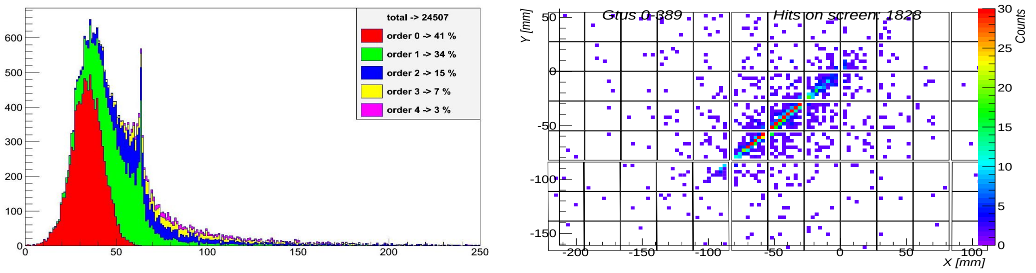

(c) MC, order 4: light curve **(d)** MC, order 4: track

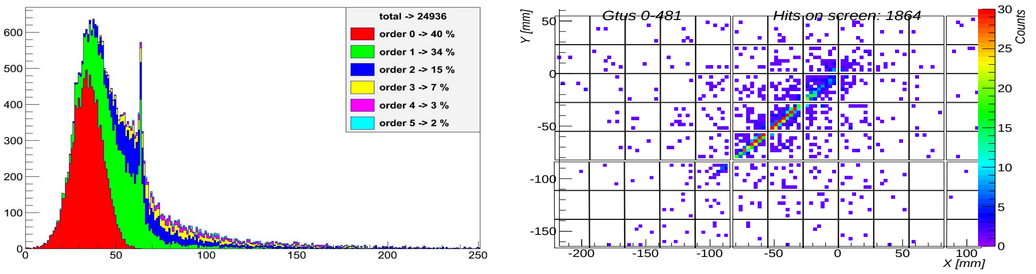

(e) MC, order 5: light curve **(f)** MC, order 5: track

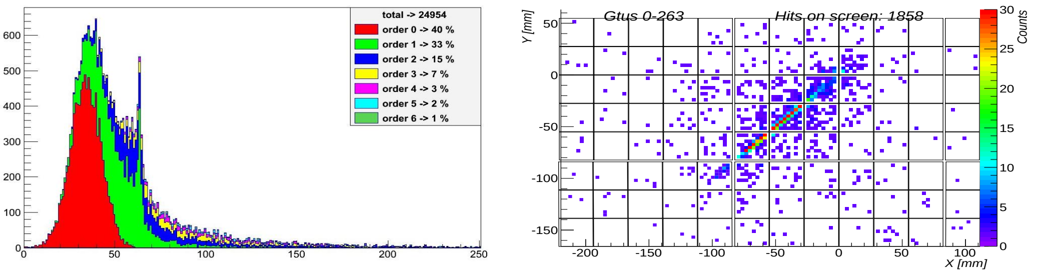

(g) MC, order 6: light curve **(h)** MC, order 6: track

Figure 5.2.4: The influence of the scattering order of Monte Carlo events. Up to five orders of scattering, we can see an obvious contribution, however with ever decreasing significance. Left: light curves on pupil, right: signal tracks.

time to an unreasonable extent.

Since the properties of the signal change both geometrically and temporally due to the scattering effects, the tasks for the pattern recognition and the angular reconstruction modules differ from the *Bunch* scenario. The dilation of the signal timing does not play a major role, since one snapshot of the telescope lasts for 128 GTUs. Thus, the event will be truncated. However, this will not affect the measurement in a negative way. The visible light curve itself may be outstretched by about 20 or 30 % compared to the *Bunch* events. Nevertheless, the entire rest of the decaying light curve is hardly above the background noise. Thus, loosing the GTUs after the 128^{th} will not play any role. The effect of the photons scattered far out of the signal track, landing somewhere on the focal surface will neither affect the pattern recognition process, nor the angular reconstruction. This effect basically contributes to the overall background of different sources. Its contribution however is negligible compared to the other far more dominant components such as the atmospheric night glow. Most likely, these PDMs will not even be triggered. Hence, their data will not be transmitted down to earth. The broadening of the track however, will definitely have an impact on both the pattern recognition and the fitting procedure of the track direction module. To estimate this potential impact an entire end-to-end study has been conducted.

5.2.2 RECONSTRUCTION OF SCATTERING EVENTS

A comparable database of showers as simulated in Chap. 5.1.2, has been produced for a Monte Carlo transport of photons in atmosphere to the detector. This time the highest energy is represented by $5 \cdot 10^{20}$ eV. The area in which the shower impact points have been set has been chosen as x: ± 260 km × y: ± 180 km compared to x: ± 270 km × y: ± 190 km in the previous study. The margin is still considered as suitable, but the amount of showers simulated outside the FOV is therefore minimized. When we compare the γ^{68} distribution of the Monte Carlo events (Fig. 5.2.5) compared to the γ^{68} distribution of the *Bunch* events (Fig. 5.1.7), we can immediately see that the angular resolution has decreased by about 0.5° to 1°. The effect apparently affects all the energies simulated to the same extent. In terms of zenith angle dependency, we note that the small zenith angles are stronger affected than the large ones. For 30° we observe a worsening of about 1° in resolution, whereas the 75° inclined events suffer from about 0.5° degradation at maximum.

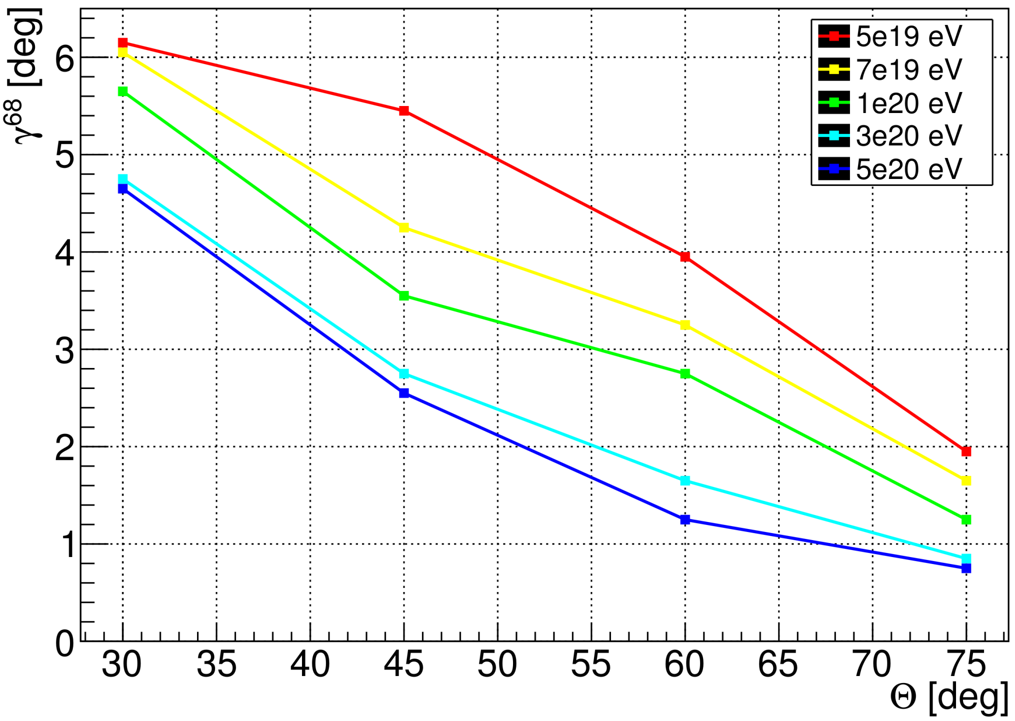

Figure 5.2.5: JEM-EUSO nadir mode, multiple scattering: Angular resolution in terms of γ^{68} obtained by the NE2 algorithm for proton events plotted against the true zenith angle for different energies (colour coded).

The effective efficiency is substantially reduced in comparison to the Bunch events. This limitation is mainly imposed by the reconstruction efficiency. The trigger efficiencies have remained stable at around 80%. The reconstruction efficiencies have decreased from 75% to 45% for the 30° showers, from 85% to 60% for the 45° showers and from 90% to 70% for the 60° showers. Only for the 75° showers it remains at a 90% reconstruction efficiency (Fig. 5.2.6). When we compare the angular resolution between the two scenarios in terms of the mean γ values, it becomes obvious that the resolution has degraded even more than indicated by the γ^{68} plots. For the low zenith angles at 30°, the difference between the γ^{68} resolution of the Bunch events and the γ^{68} resolution of the Monte Carlo events is approximately 1° to 1.5°. For the highest zenith angles the worsening is about 0.5°. Now comparing the mean γ distribution to one another, the difference is about 2° to 2.5°. This means that on average the resolution worsens by about 2°, even if for the best 68% the decline is smaller. Thus, the spread of the reconstruction quality within the population of reconstructed events has become larger.

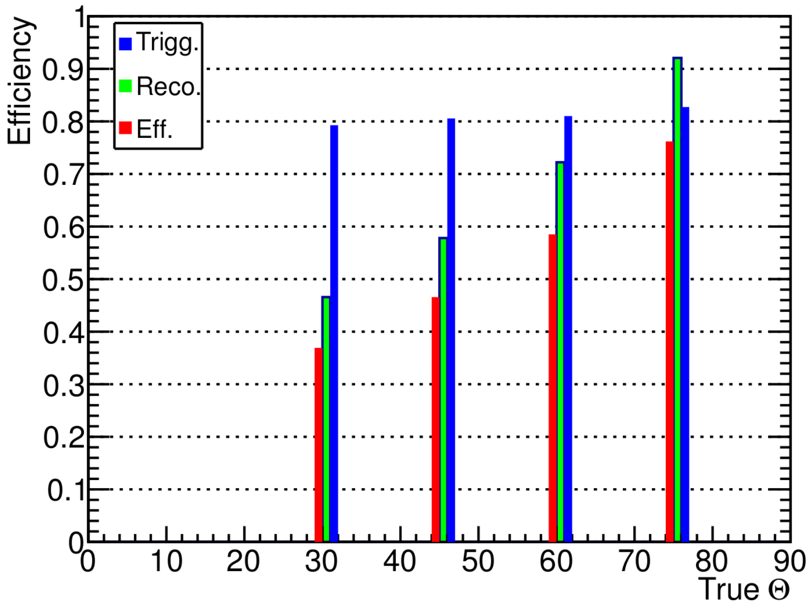

Figure 5.2.6: JEM-EUSO nadir mode, multiple scattering: trigger efficiency (blue), reconstruction efficiency (green) and the effective efficiency (red) for the different zenith angles and cumulative energies.

Comparing the radius dependencies of the separation angle and the efficiencies of the two scenarios, we can confirm that the detector's trigger response to both shower types remain at a level of almost 100% with the first 150 km of radius. Then, both feature a sudden but slight jump to 85% due to the side-cut. From here on, the trigger curve decreases to 50% at 220 km and features a cut-off at 250km, the edge of the FOV in the x-direction. The reconstruction efficiency curve however, looks clearly different. In the *Bunch* scenario, we can reconstruct almost every event within a radius of 100km. Afterwards we witness a steady decline to 80% at 240 km with a sharp cut off at the edge. In the multiple scattering scenario, the reconstruction efficiency begins already at the centre at a level of 80% and features a slight decrease until 100 km. From here on, it decreases to about 60% at the rim of the FOV which resembles the behaviour of the non-scattering case. Thus, it is obvious that for the centre region the relatively low reconstruction efficiency for Monte Carlo events dominates the effective efficiency. From about 200 km on, the trigger filters out many events and thus leaves only the very bright showers for reconstruction (Fig. 5.2.9). Comparing the population of the shower maxima of the reconstructed, the failed and the non-triggering events between the two scenarios it becomes even more obvious that it the outer region of the telescope's FOV, we loose the events mainly due to a low trigger efficiency, whereas in

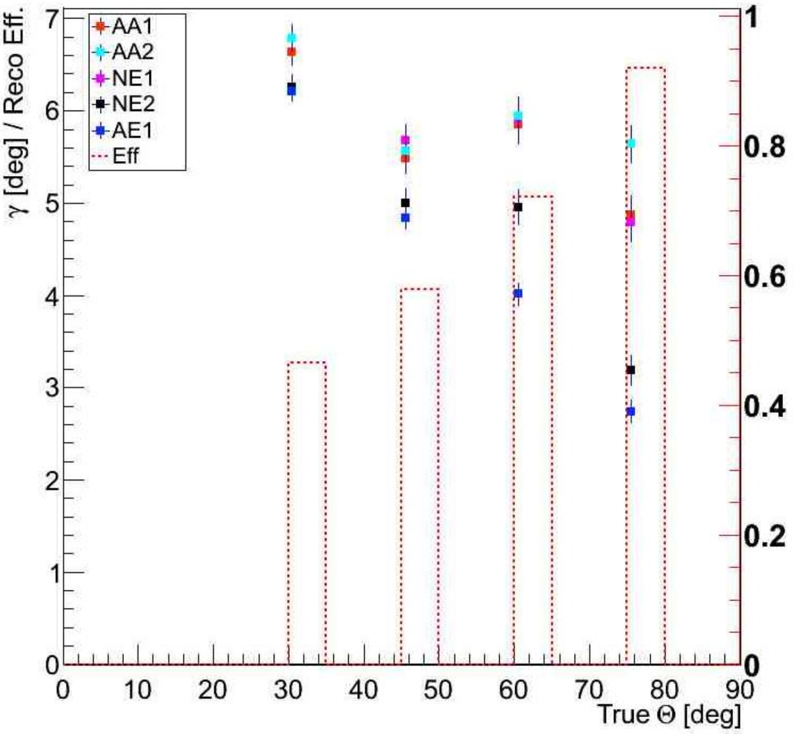

Figure 5.2.7: JEM-EUSO nadir mode, multiple scattering: $\langle\gamma\rangle$ for the five algorithms (colour coded)and their standard deviation plotted as function of the true zenith angle together with the reconstruction efficiency (red bars).

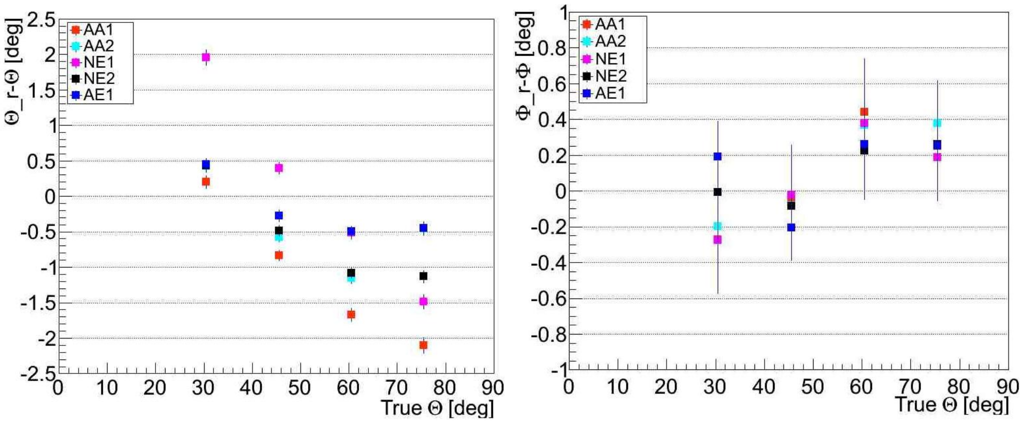

Figure 5.2.8: JEM-EUSO nadir mode, multiple scattering:reconstructed $\langle\Delta\Theta\rangle$ (left) and $\langle\Delta\Phi\rangle$ distributions (right) for cumulative energies. The colours represent the five different algorithms to show their individual performance. The error bars indicate the standard deviations.

the central area the lower reconstruction efficiency dominates. For the *Bunch* showers however, within a radius of 150 km this applies only to an almost negligible extent (Fig.

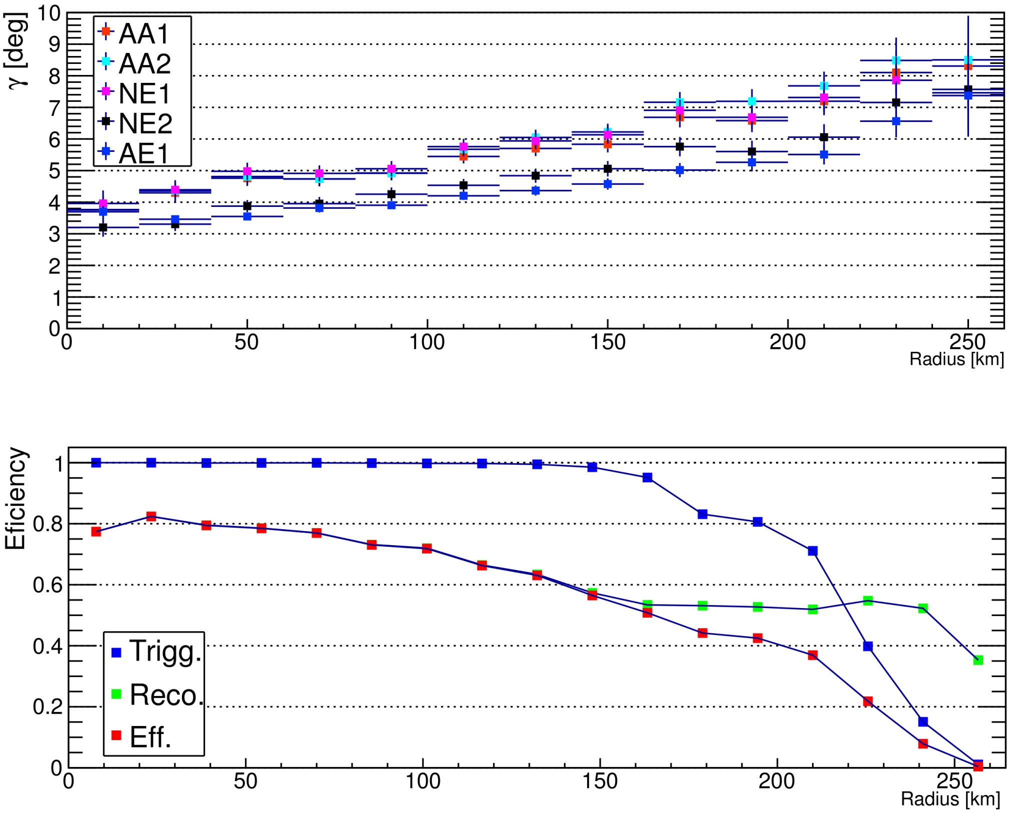

Figure 5.2.9: JEM-EUSO nadir mode, multiple scattering:top: $\langle\gamma\rangle$ for the five algorithms (colour coded) and their standard deviation plotted as function of the FOV radius.
bottom: trigger (blue), reconstruction (green) and effective efficiency (red) as function of the FOV radius.

5.2.10).

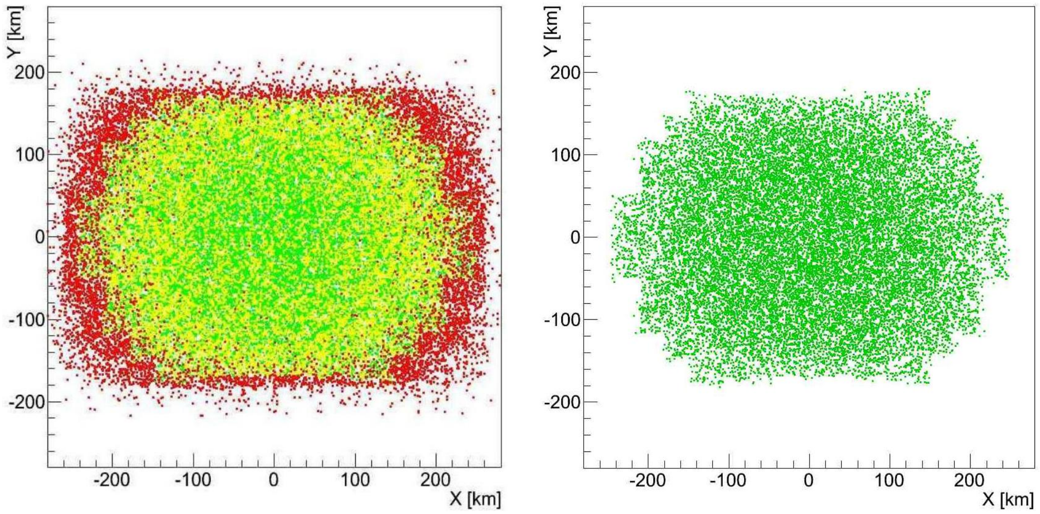

(a) FOV position of maxima, superimposed view

(b) Reconstructed events

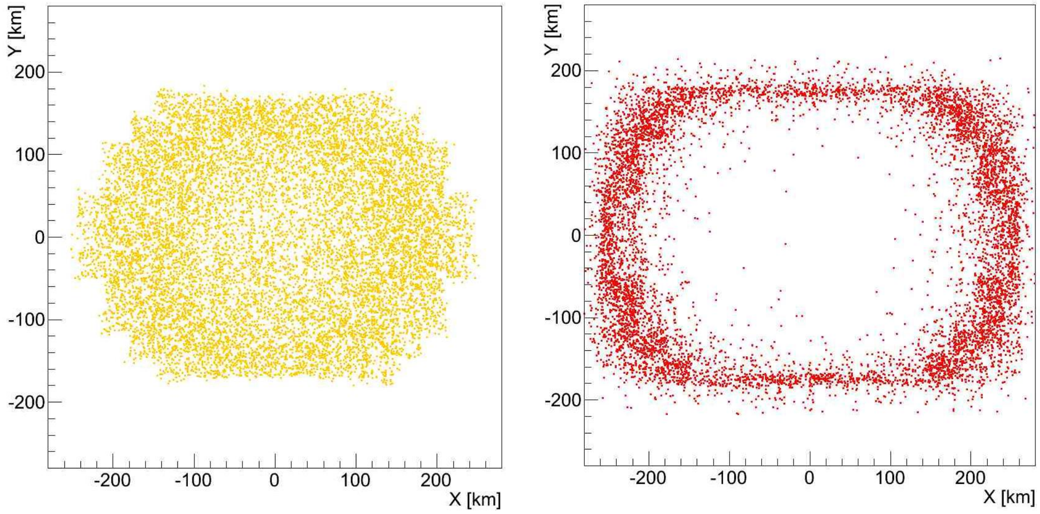

(c) Failed events

(d) Non-triggering events

Figure 5.2.10: JEM-EUSO nadir mode, multiple scattering: shower max. positions within the telescope's FOV. Red: Population of non-triggering events. Yellow: Events, triggered but not reconstructed. Green: Events, triggered and successfully reconstructed.

5.3 SPACEX EUSO

The accommodation of the JEM-EUSO detector on board the SpaceX spacecraft *Dragon* requires an updated instrument design as described in detail in Chap. 3.7. The most important changes which are expected to have an impact on the instrument's performance are listed in Tab. 5.3.1. The new focal surface layout is basically a rearrangement of the outermost PDMs. Some of them have been relocated, others have been removed entirely. The bottom line employs 129 PDMs instead of 137 (Fig. 5.3.1).

Table 5.3.1: Key parameter of JEM-EUSO and SpaceX EUSO simulations. Parameters and components from K. Shinozaki and [78].

	Mission	
	JEM-EUSO	SpaceX EUSO
Lens dimensions	2650 × 1900 mm	2500 mm circular
Lens area	4.4 m^2	4.9 m^2
Focal surface layout	137 PDM	129 PDM
Pixel-angle-map	accordingly	accordingly
Focal surface diameter	2650 × 1900 mm	2200 mm circular shape
Lens thickness	10 mm	7 mm

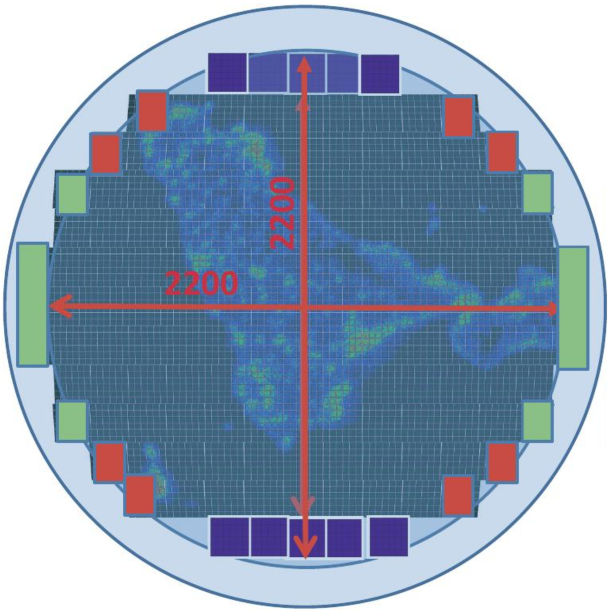

Figure 5.3.1: SpaceX EUSO: focal surface layout. Blue: Added PMTs, Green removed (moved), Red: removed (cut). Pic. taken from [78].

5.3.1 ANGULAR RESOLUTION OF SPACEX EUSO

To assess the angular resolution performance of the slightly modified detector, a study comparable to the one for the baseline JEM-EUSO instrument has been conducted. To meet the changed geometry of the field of view of the instrument, the showers impact points have been placed within a square of x: ± 240 km × y: ± 240 km. The energies and zenith angles have the same configuration as the previous Monte Carlo studies. The primarie's energies are set to $5 \cdot 10^{19}$ eV, $7 \cdot 10^{19}$ eV, $1 \cdot 10^{20}$ eV, $3 \cdot 10^{20}$ eV and $5 \cdot 10^{20}$ eV. The simulated zenith angles include 30°, 45°, 60° and 75°. The primaries are protons only and the Φ directions of the showers are randomly set between 0 and 360°. The overall angular resolution clearly improves with respect to the JEM-EUSO baseline detector (Fig. 5.3.2). This applies to all zenith angles, except for the highest. At 75° and supposedly beyond, we cannot observe any improvement with respect to the side-cut

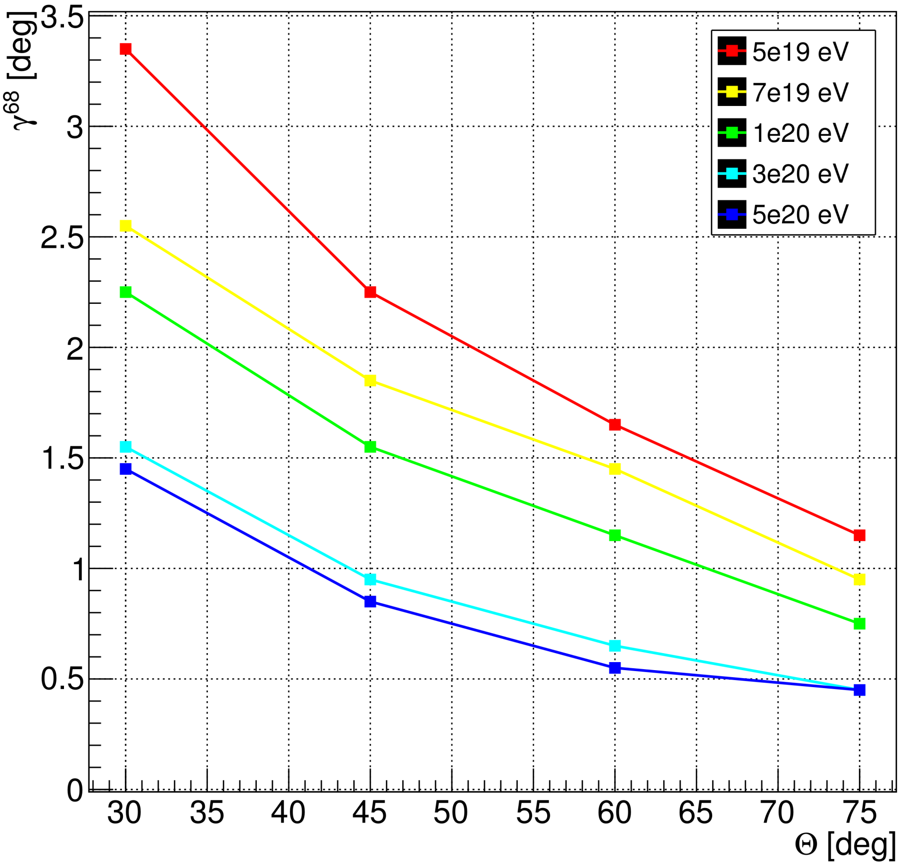

Figure 5.3.2: SpaceX EUSO: Angular resolution in terms of γ^{68} obtained by the NE2 algorithm for proton events plotted against the true zenith angle for different energies (colour coded).

case. Here the resolution remains the same, independent of the energy of the primary. On the contrary, for all lower zenith angles we can confirm a strong improvement of the resolution. Most remarkably, in particular the higher energies benefit more than a factor of 2. Beyond that, also the lower energies gain between 1° and 1.5° in resolution. In terms of efficiencies the situation changes only slightly. The trigger efficiencies remain comparable to the side-cut instrument and therefore very good. Regarding the lower zenith angles 30°, 45°, 60° however, we note a small but significant decrease in efficiency. This leads to a decrease of the effective efficiency for these configurations by 10 % to 15 %.

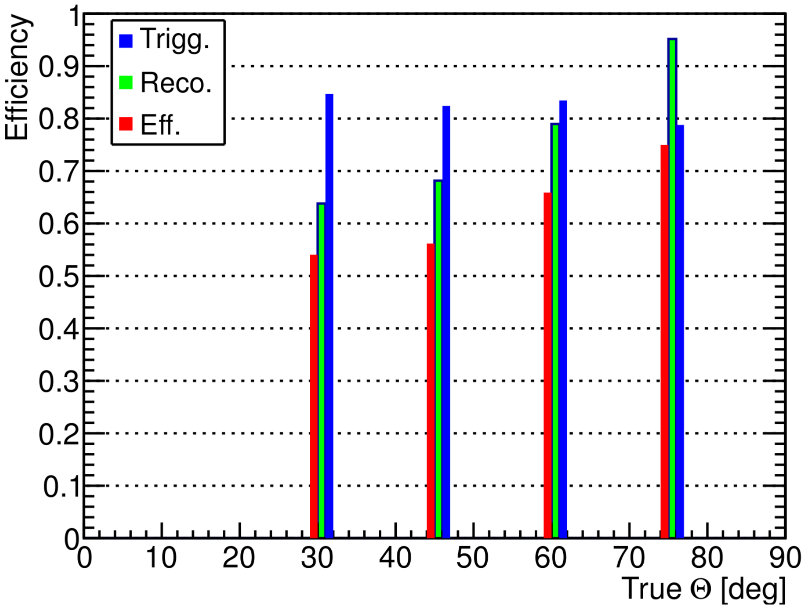

Figure 5.3.3: SpaceX EUSO: trigger efficiency (blue), reconstruction efficiency (green) and the effective efficiency (red) for the different zenith angles and cumulative energies.

Naturally, like the γ^{68} distribution, also the mean γ distribution improves (Fig. 5.3.5). Like in the side-cut case, the different algorithms agree to a good extent in their angular determination and the errors are small. This also applies when we check the performance of the individual Θ and Φ determination of the single algorithms. In the side-cut instrument we could not observe a severe systematics nor a high variation of the results. Likewise, in the circular case there are only small deviations from the mean value (Fig.

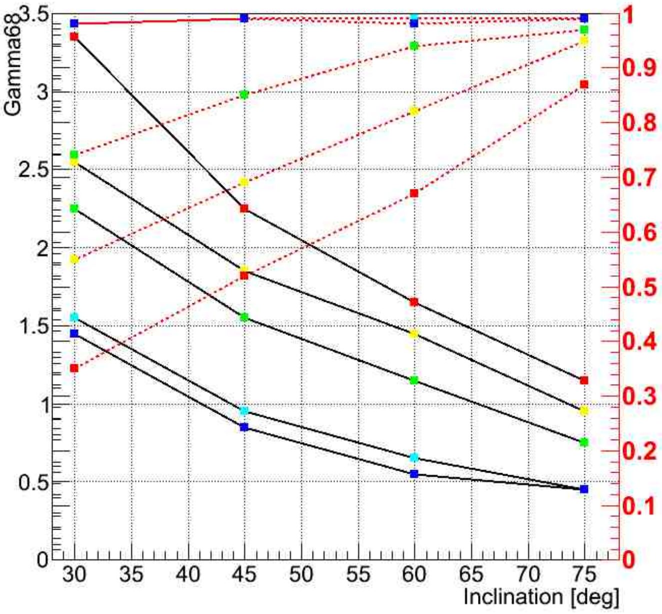

Figure 5.3.4: SpaceX EUSO: γ^{68} vs zenith angle for the different energies (colour-coded). The values have been obtained by the NE2 algorithm. Additionally, the reconstruction efficiencies for the single energies have been plotted with reference to the right y-axis.

5.3.5). Analysing the impact of the FOV radius on the angular resolution and the efficiencies, we can spot the difference between the circular and the side-cut instrument. In the baseline instrument we could observe a distinctive jump at the radius where the side-cut applies (at 160 km), whereas the circular instrument features a very smooth curve both for the resolution as well as for the efficiency (Fig. 5.3.7). The trigger efficiency remains at a very high level of almost 100% up to a radius of 170 km. Only in the border region of the FOV it clearly decreases. The reconstruction efficiency decreases from a smaller radius on (~ 80 km). This is owed to the decreasing throughput efficiency of the optics. However, it reaches 50% only at about 180 km from the centre. Due to the circular shape, more events than in the side-cut case remain inside this area.

The interpretation above is clearly supported when we analyse the maximum position of the showers within the FOV (Fig. 5.3.8). The distribution of the shower maxima of the non-triggering events (in red), the events which the algorithms failed to reconstruct (yellow) and the distribution of successfully reconstructed events (green). It illustrate very well the behaviour we have already seen from the previous plot. Inside

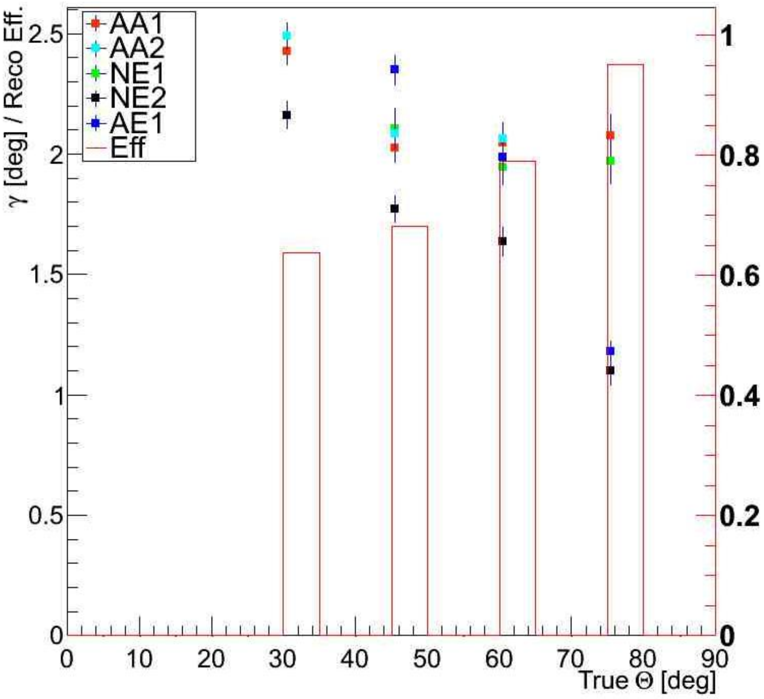

Figure 5.3.5: SpaceX EUSO: $\langle\gamma\rangle$ for the five algorithms (colour coded)and their standard deviation plotted as function of the true zenith angle together with the reconstruction efficiency (red bars).

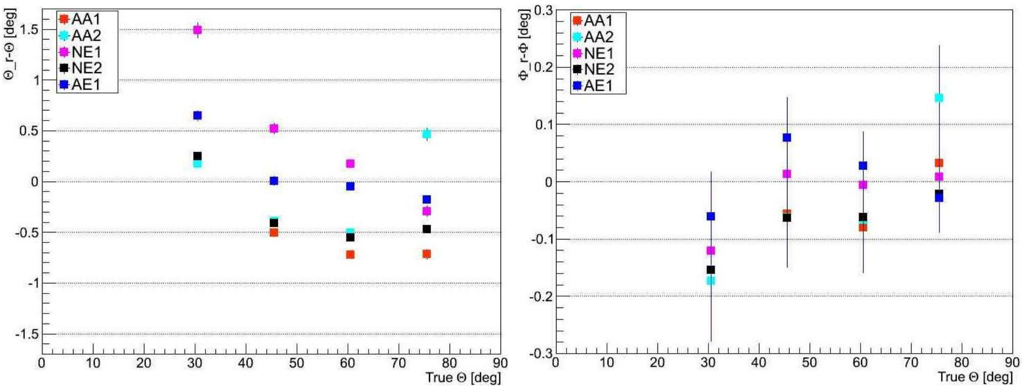

Figure 5.3.6: SpaceX EUSO: reconstructed $\langle\Delta\Theta\rangle$ (left) and $\langle\Delta\Phi\rangle$ distributions (right) for cumulative energies. The colours represent the five different algorithms to show their individual performance. The error bars indicate the standard deviations.

the central area of the field of view, there is almost no event without a trigger. Moreover, the density of failed events is small and increases only slowly towards the outer regions. Having the highest density in the central part, their behaviour is complemen-

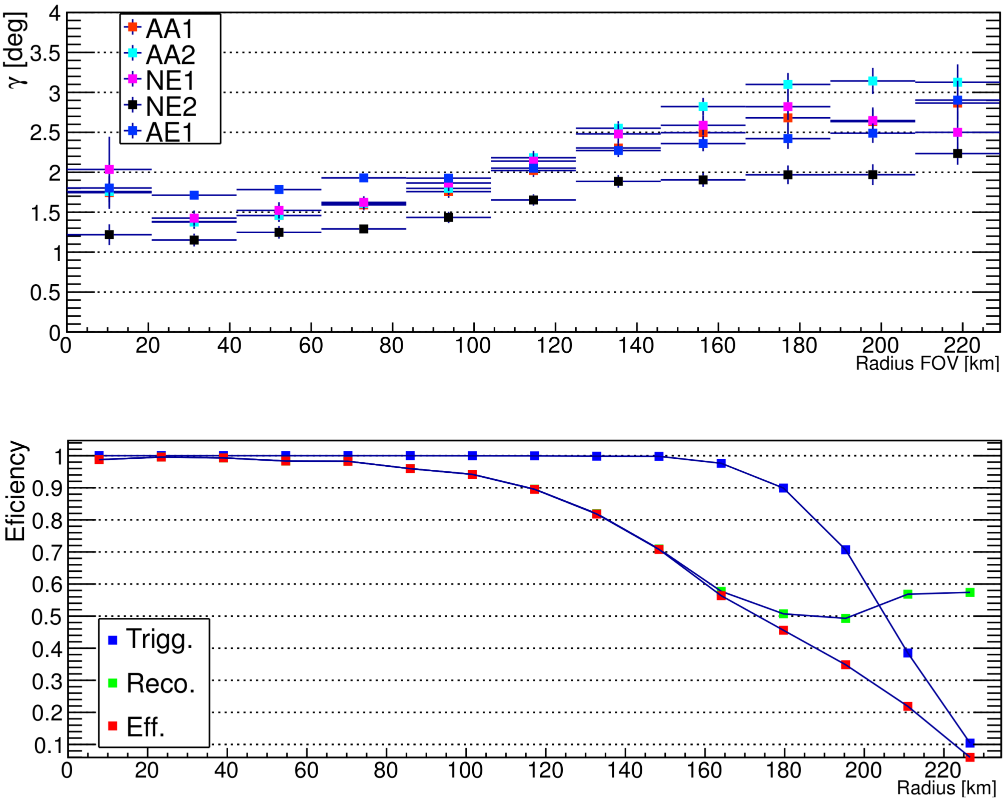

Figure 5.3.7: SpaceX EUSO: top: $\langle\gamma\rangle$ for the five algorithms (colour coded) and their standard deviation plotted as function of the FOV radius.
bottom: trigger (blue), reconstruction (green) and effective efficiency (red) as function of the FOV radius.

tary to the population of reconstructed events. Still, from the pattern of the green population it becomes evident that there are no PDM parts which lie within a blind area.

The reason behind this rather convincing performance of the circular instrument with respect to the side-cut telescope can be understood in the context of the tilted mode studies (Chap. 6). Also for the nadir instrument the same determining factors apply. First of all, the distance of the event from the telescope has a major impact. In comparison to the side-cut instrument, the circular telescope observes showers that are closer to the detector, on average. Events that appear on the very outer parts (X= -200 – -230 km and X= 200 – 230 km) of the side-cut instrument's FOV, are not visible to the circular detector due to its smaller FOV diameter. On the other hand, the regions that were formerly cut (Y= -170 – -200 km and Y= 170 to 200 km) do observe shower events now. Therefore, the detector receives more light per event than before.

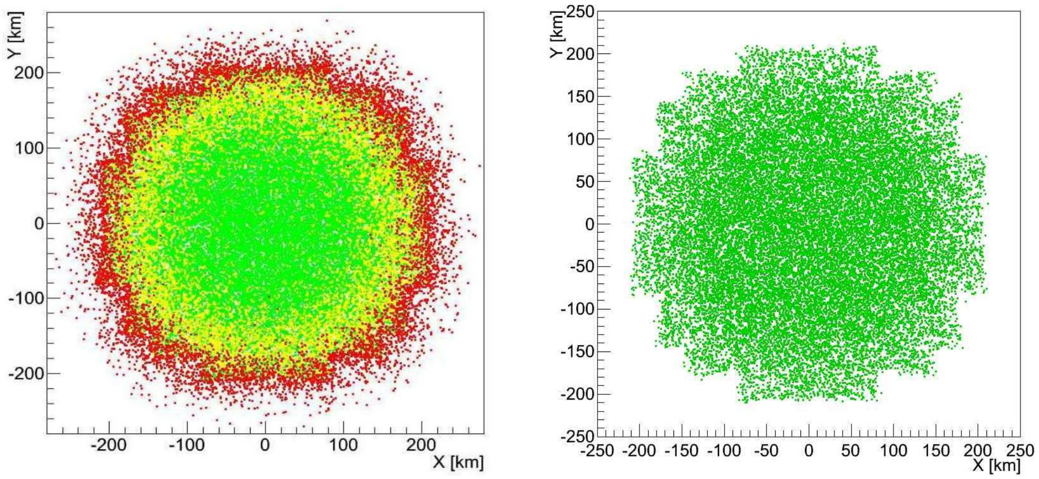

(a) Position of maxima, superimposed view

(b) Position of maxima, reconstructed

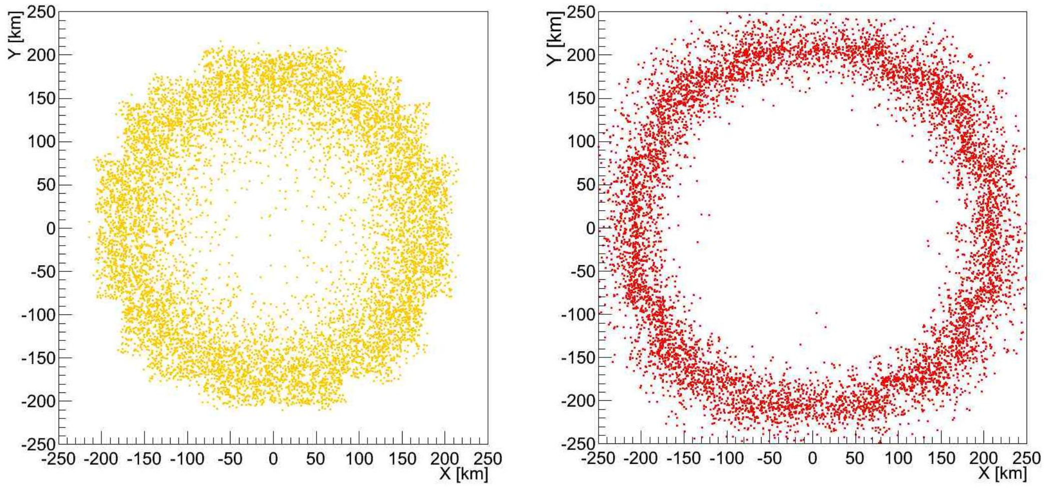

(c) Position of maxima, failed

(d) Position of maxima, not triggered

Figure 5.3.8: SpaceX EUSO: Detector FOV, projected on ground. Shower fluorescence light maximum distribution in the FOV of the tilted instrument for the reconstructed events (green), the failed (i.e. triggered but not successfully reconstructed) events (orange) and the non-triggering events (red).

Moreover, the optics throughput efficiency has a less severe impact on the outer FOV events due to its smaller diameter. Thus, there is an extra gain of light for those events. And especially those events are responsible for the worsening of the angular resolution when we evaluate the overall performance of the instrument. Hence, it is not surprising and serves as a good confirmation for the results obtained for the circular detector, when we compare them to the results obtained with the baseline instrument and restrict ourselves to the quality cut events as presented in Chap. 5.1.13.

5.4 EUSO500

Since the original instrument accumulates to almost 1.8 tons the JEM-EUSO collaboration was trying to meet the demand of a downscaled instrument. Thus, during the course of mission planning, a light weight and smaller version of the JEM-EUSO detector had been evaluated. The technology resembles the one of the JEM-EUSO baseline instrument at large but only weights approximately 500 kg. Now, the diameter of the lenses was supposed to be 1 metre, the entire outer ring of PDMs was removed. Hence, the focal surface detector now complied of 101 PDMs, arranged in a circle. Having these specifications, the FOV corresponds roughly to the quality cut (150 km) of the side-cut baseline instrument. However, EUSO500 has a smaller optics diameter than JEM-EUSO (Fig. 5.4.1). As expected, poorly reconstructed events populate the outer FOV parts of both telescopes. In the EUSO500 case, there are more of them even in the central part. This is a feature owed to the much smaller optics. EUSO500 receives less

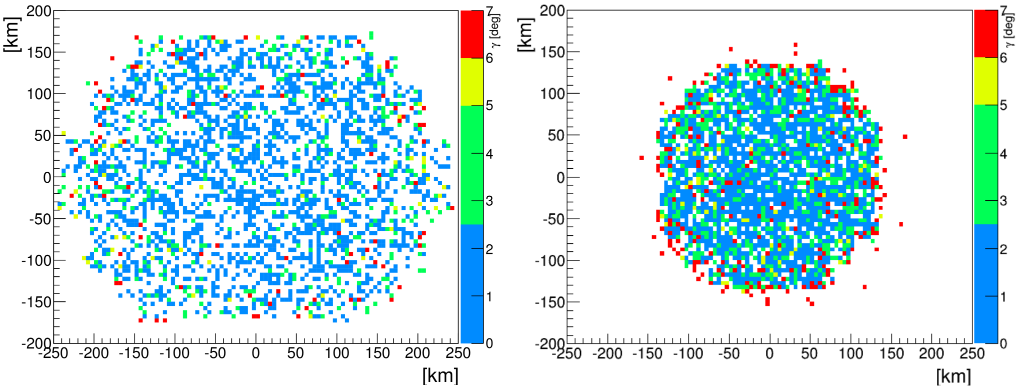

Figure 5.4.1: left: JEM-EUSO FOV, right: EUSO500 FOV. The colour code indicates the resolution expressed in $\langle\gamma\rangle$.

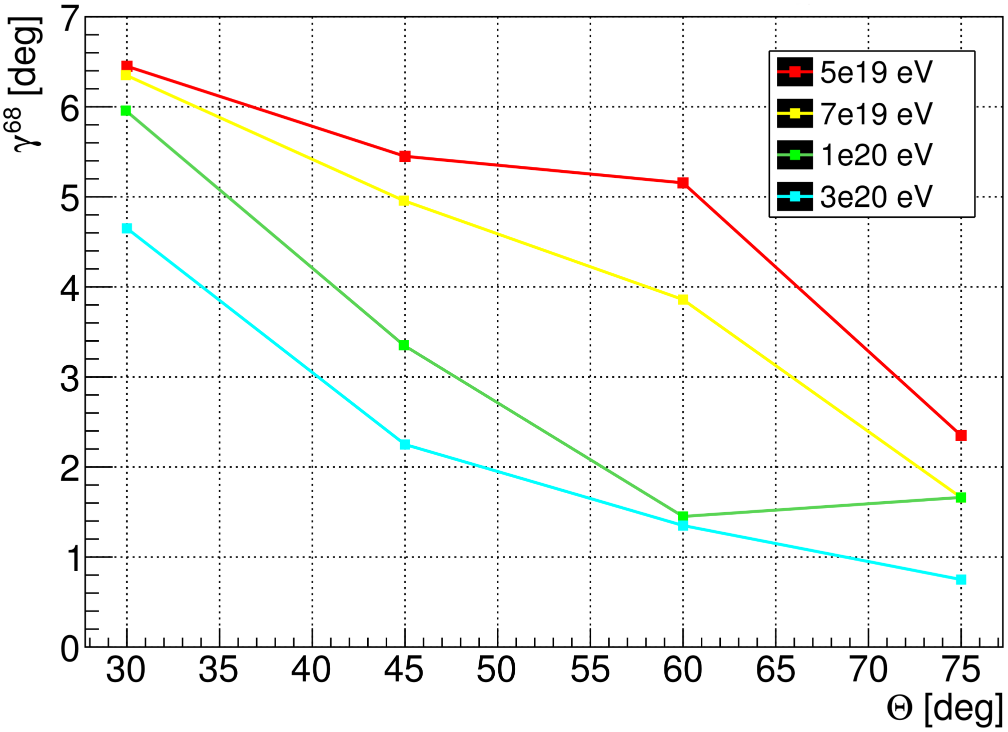

Figure 5.4.2: EUSO500:Angular resolution in terms of γ^{68} obtained by the NE1, NE2, AE1 algorithms for proton events plotted against the true zenith angle for different energies (colour coded).

light then its larger counterpart. Hence, less bright events, even in the centre might suffer from a lower efficiency. To evaluate the potential performance of such a light weight instrument, we have created a preliminary virtual test setup of a 500 kg version — EUSO500. Most of the components used, were simply downscaled parts of the JEM-EUSO instrument. For instance, we have used the same focal surface, this time though we have deactivated the outer ring of PDMs. To estimate the angular resolution performance of this setup, we have conducted a small study, similar to the previously presented, but with a lower statistics and without a proper characterization of the signal behaviour. Comparing the angular resolution in terms of the γ^{68} values, we can see that the resolution decreases by a factor of 1° to 2° with respect to the side-cut instrument. Especially the lower energies are affected (Fig. 5.4.2). On the contrary, the overall efficiency is well comparable and even slightly higher than the baseline instrument (Fig. 5.4.3).

Analysing the reconstruction of the Θ and Φ components, we can immediately see

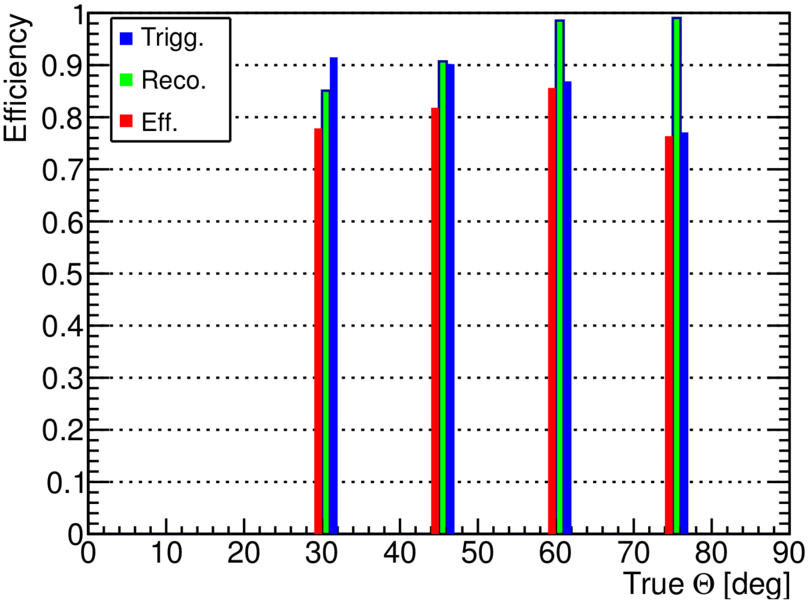

Figure 5.4.3: EUSO500: trigger efficiency (blue), reconstruction efficiency (green) and the effective efficiency (red) for the different zenith angles and cumulative energies.

clear differences compared to the baseline instrument. The results of the different algorithms for the Θ estimation differ by more than 3° for the 30° inclined showers. (The difference is only 1.5° for the side-cut instrument) Also the standard deviation of the Φ reconstruction is about twice as large as for the original telescope (Fig. 5.4.4).

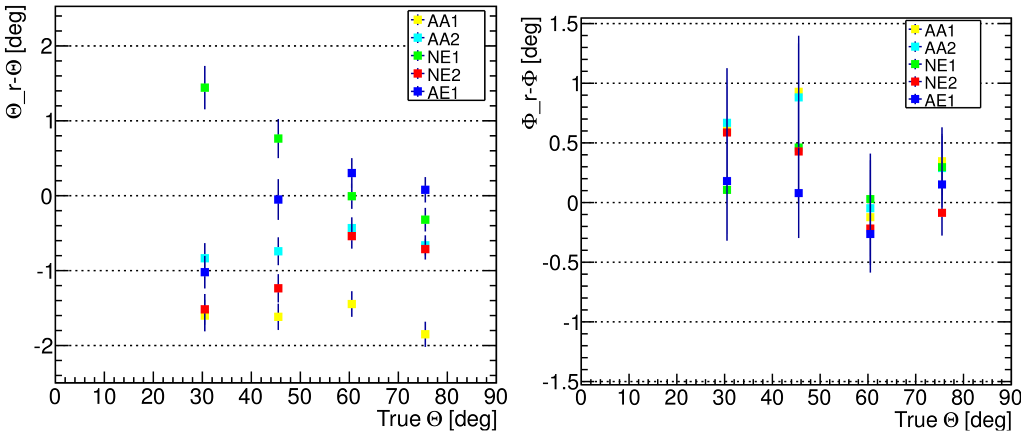

Figure 5.4.4: EUSO500: reconstructed ⟨ΔΘ⟩ (left) and ⟨ΔΦ⟩ distributions (right) for cumulative energies. The colours represent the five different algorithms to show their individual performance. The error bars indicate the standard deviations.

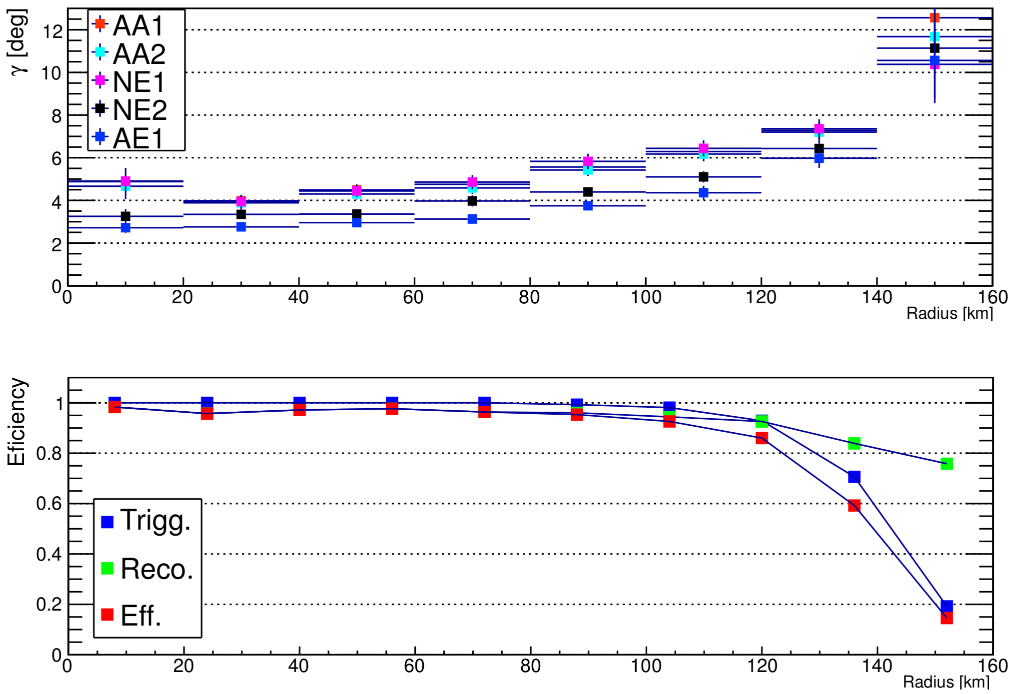

Figure 5.4.5: EUSO500: top: $\langle\gamma\rangle$ for the five algorithms (colour coded) and their standard deviation plotted as function of the FOV radius.
bottom: trigger (blue), reconstruction (green) and effective efficiency (red) as function of the FOV radius.

Inside the FOV, the trigger and reconstruction efficiencies are remarkably constant with a sharp decrease at the rim. The angular resolution starts already at the centre with 3° to 4° $< \gamma >$ and increases up to 10° for the outer radii. (Fig. 5.4.5). The reason for this stable efficiency at most focal surface radii can certainly be explained by a smaller dominance of the proximity effect. Since the field of view of the EUSO500 instrument is relatively small, it does not play a large role compared to the side-cut instrument. The overall angular resolution, however is reduced due to the smaller amount of photons collected.

5.5 JEM-EUSO Balloon

5.5.1 Potential Resolution of the EUSO-Balloon

For the simulation of the EUSO Balloon, we have used a downscaled version of the JEM-EUSO detector, replaced the optical system with the one of the balloon and removed all but the central PDM from the focal surface. Although this exercise is an approximation, it is expected that the real instrument will perform in a comparable way. As described in Chap. 3.6.1, the EUSO-Balloon was not designed as a UHECR mission. Its purpose is to demonstrate the readyness potential of the main instrument's technology and to perform background measurements. Moreover, it will record fake showers, produced by a laser device. The probability to measure real EAS is very small for a flight time of some hours. Nevertheless, this small study aims to determine the potential angular resolution performance of the EUSO-Ballon for UHECR induced air showers. In general this should also apply to the reconstruction of the laser induced events as well. In this study we have used air showers with energies between 10^{18} eV and 10^{19} eV and with inclination angles between 10° and 60°. Showers with higher energies are extremely unlikely to be observed due to the small exposure of the balloon. The small focal surface with only one PDM does not permit to measure strongly inclined showers simply due to spatial constraints. In Fig. 5.5.1, we can see a 10^{19} eV shower with a zenith angle of 20° which already occupies two thirds of the entire PDM. Thus, even for the unlikely case that the balloon observed an UHECR event the focal surface might not contain the entire signal track, especially for the larger zenith angles. This behaviour can clearly be seen when we analyze the separation angle in dependence of the radius of the FOV. In general, the balloon can resolve the arrival direction of the showers to a very high precision of about 1°. But this is only possible if the showers are placed right in the centre of its FOV. Once, the track is not fully contained, the

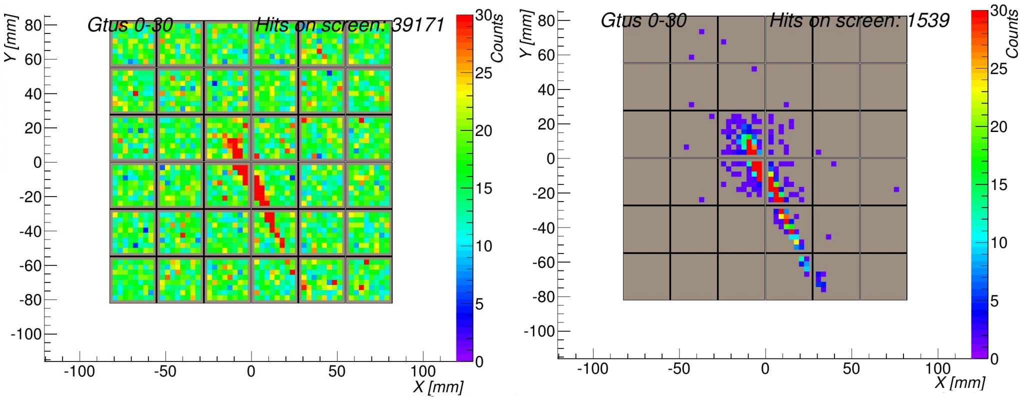

Figure 5.5.1: EAS signal track of 1e19 eV, 20 deg proton event as it could appear within the balloon's FOV with background included (left) and without (right).

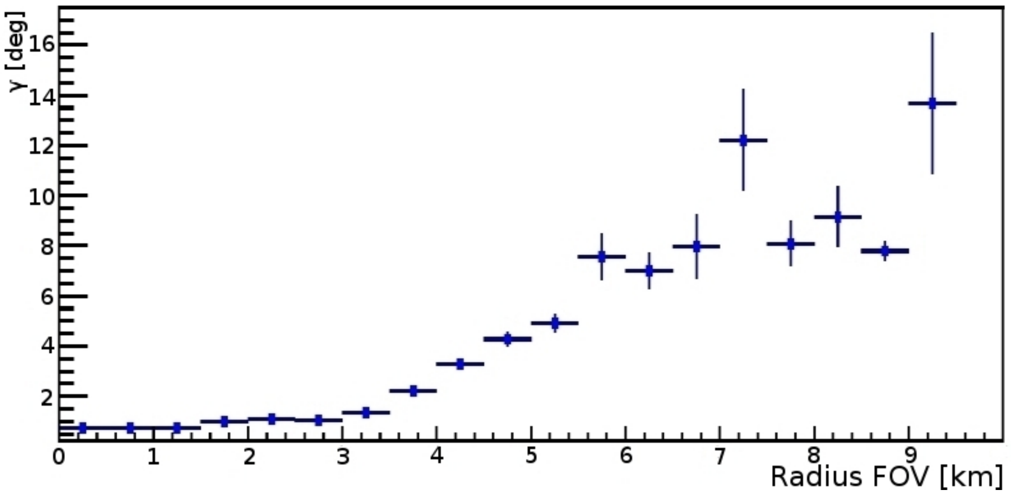

Figure 5.5.2: EUSO Balloon: $\langle\gamma\rangle$ of the best algorithm plotted as function of the FOV radius. The error bars indicate the standard deviation.

resolution rapidly worsens. Evaluating the angular resolution capabilities as a function of the zenith angle of the showers, we can see a similar response. The steep showers, leaving short tracks can be reconstructed, but from about 30° on the Θ resolution declines rapidly. This is owed to the fact that the Θ reconstruction depends on the proper knowledge of the timing which is lost when significant parts of the signal track are missing. The Φ reconstruction on the contrary is still possible with a smaller part of the track, since the track length is less important for its reconstruction (Fig. 5.5.3).

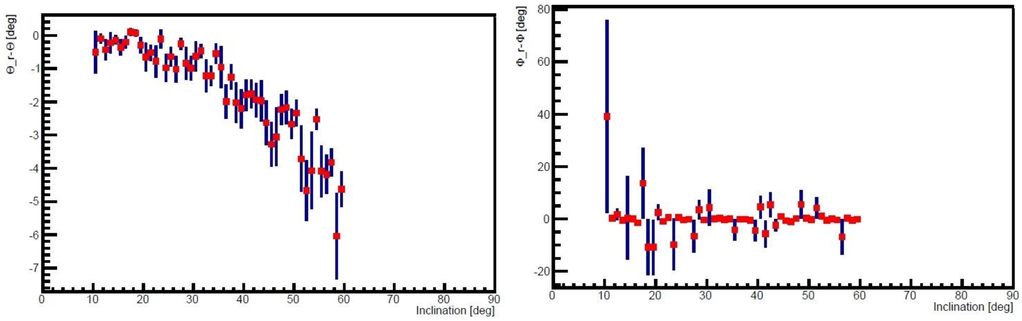

Figure 5.5.3: EUSO Balloon: reconstructed $\langle\Delta\Theta\rangle$ (left) and $\langle\Delta\Phi\rangle$ distributions (right) for cumulative energies. Data points show the results of the NE2 algorithm. The error bars indicate the standard deviation.

It is by the fortune of God that, in this country, we have three benefits: freedom of speech, freedom of thought, and the wisdom never to use either.

Mark Twain

6

Angular Resolution: Tilted Mode

The notion of a tilted UV telescope allowing to further increase the already large detection area by some factor is an important programmatic aspect of the JEM-EUSO mission. This idea is strongly appealing for the reason that without further instrument design improvements, the exposure to UHECR above 10^{20} eV could be raised considerably. It could yield a sufficient exposure even for the observation of UHE neutrinos. Certainly, the energy threshold would increase and the angular reconstruction quality is expected to decay. To quantify the effect on the angular resolution, we have conducted an extensive study to analyse the effect of an operation mode tilted by 20° and by 40°.

6.1 Photon and Signal Analysis 20°

To evaluate how the signal behaviour is affected by tilting the instrument by 20° from the nadir axis, we have first conducted a study on the incoming signal photons. We use an air shower with an energy of 10^{20} eV and a zenith angle with Θ=60° as a standard candle. The brightness of the shower using SLAST in combination with the *Bunch* photon transfer module can be regarded as almost constant, making it a good tool for this purpose. We inject 44000 showers within the greater field of view of the telescope and check how many photons per event reach the telescope, pass through the optics make a signal on the focal surface detector and give a trigger signal in the end. In Fig. 6.1.1, we observe that those showers which develop right below the telescope yield the highest rate of photons reaching the instrument. The further away showers are placed from the telescope, the less photons per event arrive, simply owed to geometrical reasons — the number scales with $1/d^2$. The events located right beneath the telescope are now shifted away from the centre of the instrument's FOV and are situated in a part of the optics which is not as efficient as the centre. The throughput of the optical

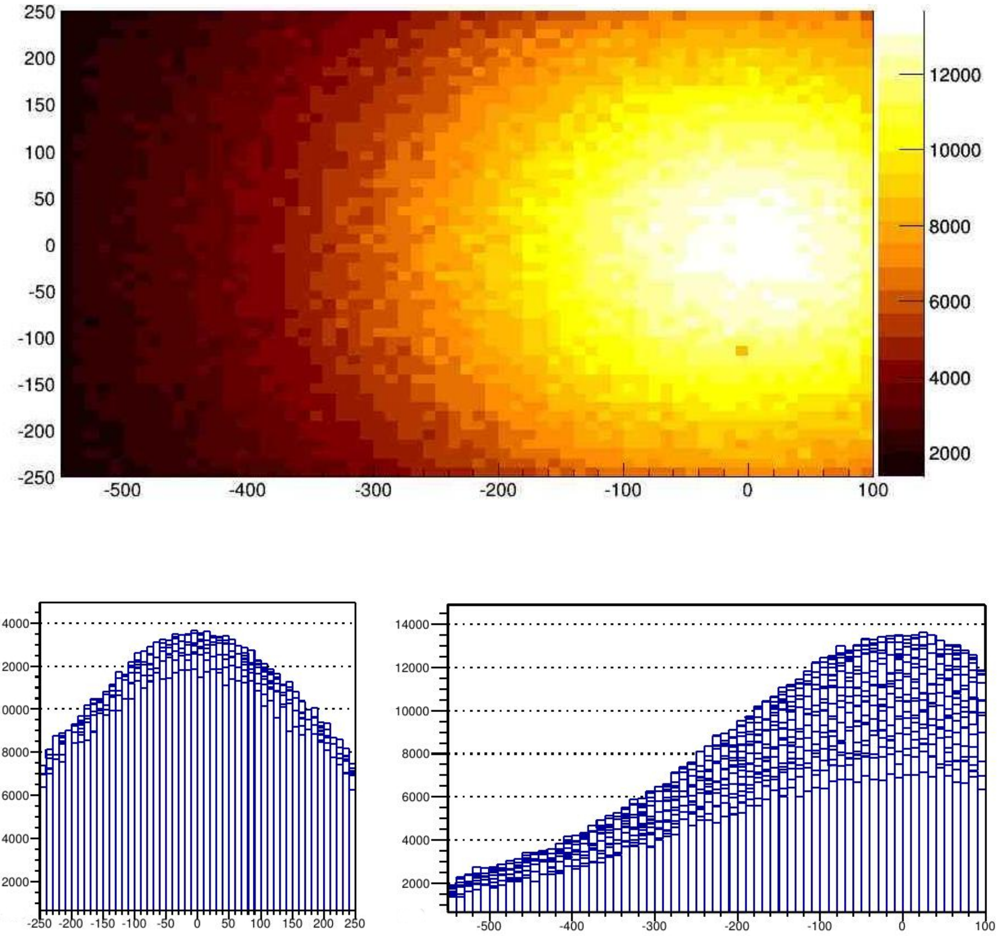

Figure 6.1.1: JEM-EUSO tilted mode, 20°: distribution of photons arriving to the instrument. Top: FOV as seen from above, amount of photons per event is colour coded, bottom left: y-profile of the FOV, bottom right: x-profile of the FOV.

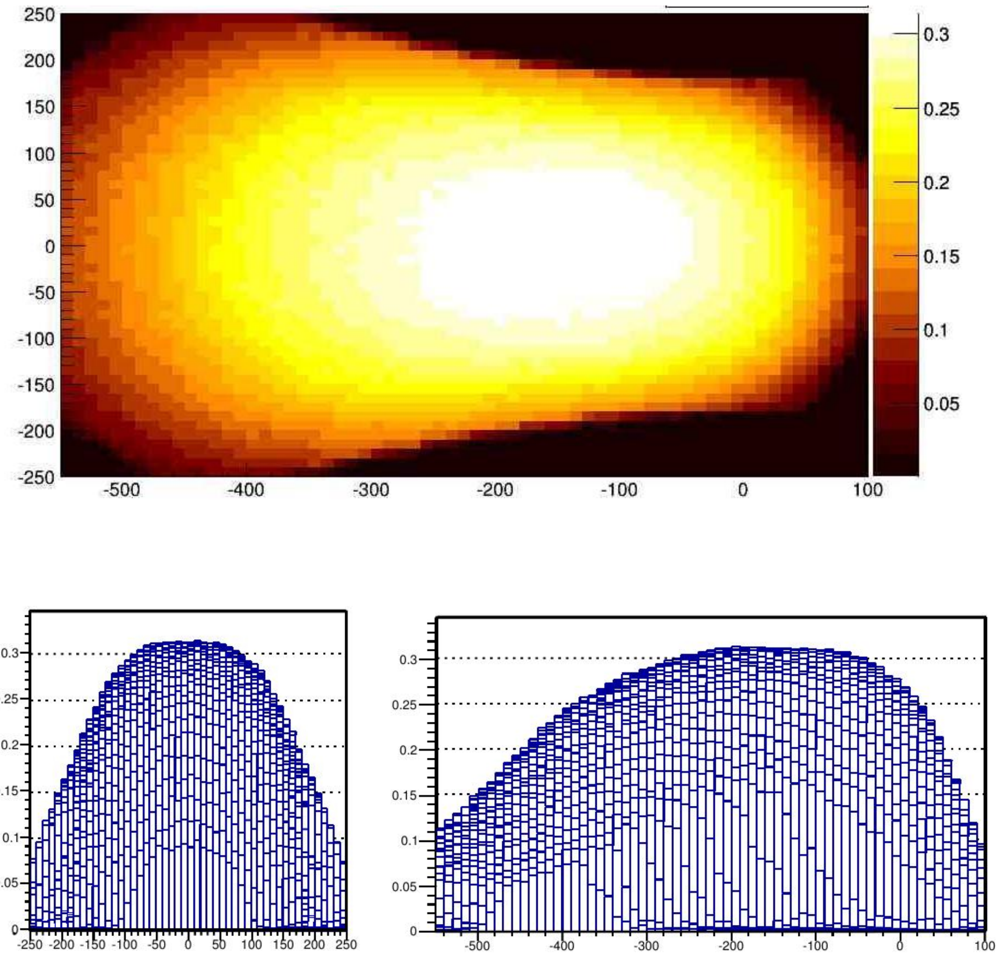

Figure 6.1.2: JEM-EUSO tilted mode, 20°: Optics efficiency. Top: FOV as seen from above, optics efficiency is colour coded, bottom left: y-profile of the FOV, bottom right: x-profile of the FOV.

system depends on the inclination angle under which the light hits the first lens. For photons arriving orthogonal to the entrance pupil, the probability of arriving on the focal surface is around 30 %. However, with increasing inclination, it drops to 10 % at the very edge of the FOV at approximately 30° inclination. This corresponds to a distance of about 500 km on ground from the detector's nadir position. From Fig. 6.1.2c, we note that now a larger part of the FOV lies within an area where the optics is not as efficient as in the centre. This bears the consequence that those showers, already shining fewer photons to the telescope, suffer more from optical losses than those showers which are in closer proximity to the telescope (Fig. 6.1.3). Thus, the relatively steep decrease in photons per event reaching the focal surface is a result of two effects. First,

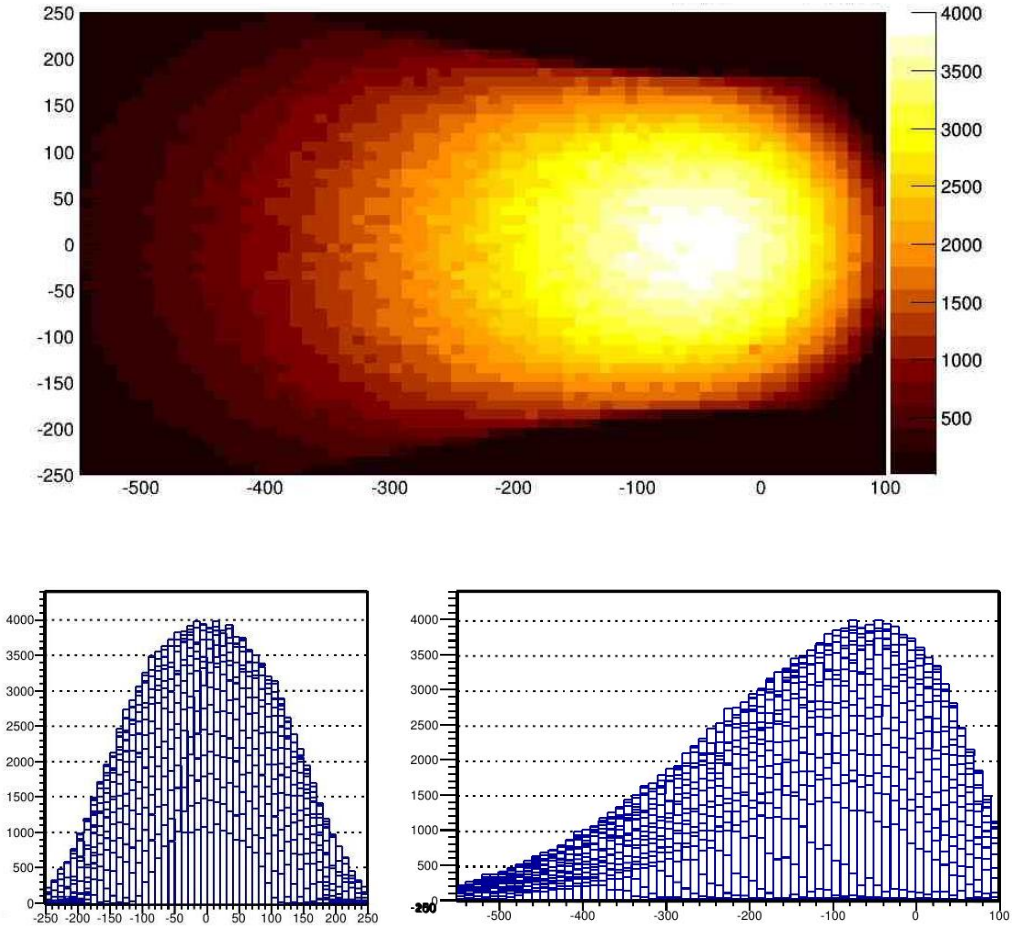

Figure 6.1.3: JEM-EUSO tilted mode, 20°: photons/event distribution on focal surface. Top: FOV as seen from above, amount of photons per event is colour coded, bottom left: y-profile of the FOV, bottom right: x-profile of the FOV.

the geometrical effect and second, the additional optical loss factor. Analysing the distribution of signal counts per event in dependence of the FOV position of the showers yields a similar result. The shape of the decreasing 'signal curve' (Fig. 6.1.4) resembles the one of the 'photons on the focal surface curve' (Fig. 6.1.3). The difference in total numbers derives from the quantum efficiency multiplied by the covering factor[1] which yields the total collection efficiency. This total efficiency however, is the same over the whole focal surface and has no angular dependence. Hence, the probability of photons to create a signal is the same, independent of their actual field of view position . Plotting only those events that trigger the PDMs, the actual field of view of the tilted

---

[1] The covering factor denotes the ratio of sensitive area to dead spaces on the focal surface.

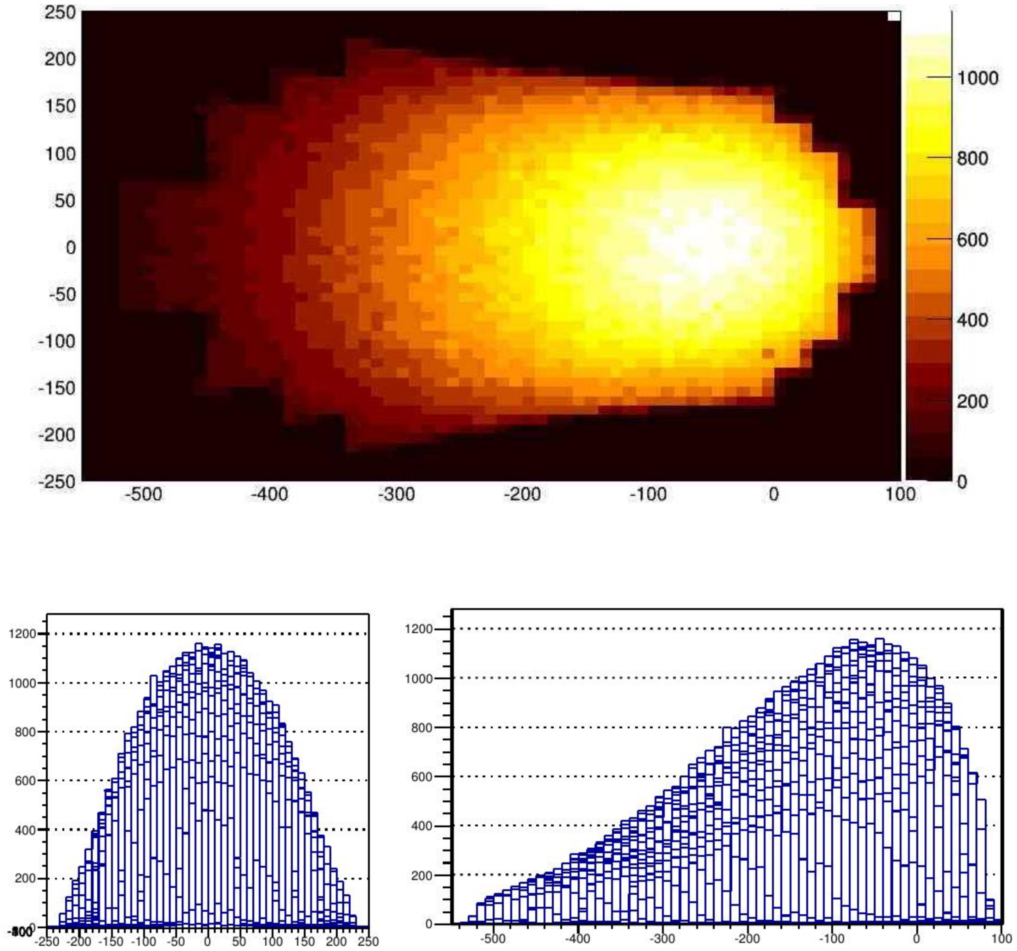

Figure 6.1.4: JEM-EUSO tilted mode, 20°: signals/event distribution on focal surface. Top: FOV as seen from above, number of signals per event is colour coded, bottom left: y-profile of the FOV, bottom right: x-profile of the FOV.

instrument becomes visible (Fig. 6.1.5). Moreover, we can see that at the very end of the remote part of the field of view we are loosing a small amount of events. In this part, the signal is very weak due to the different factors explained above. For those events, intersecting the borders of the FOV, the remaining visible track can be too short to issue a trigger. Events with energies and zenith angles below 10^{20} eV and Θ=60° are affected even stronger.

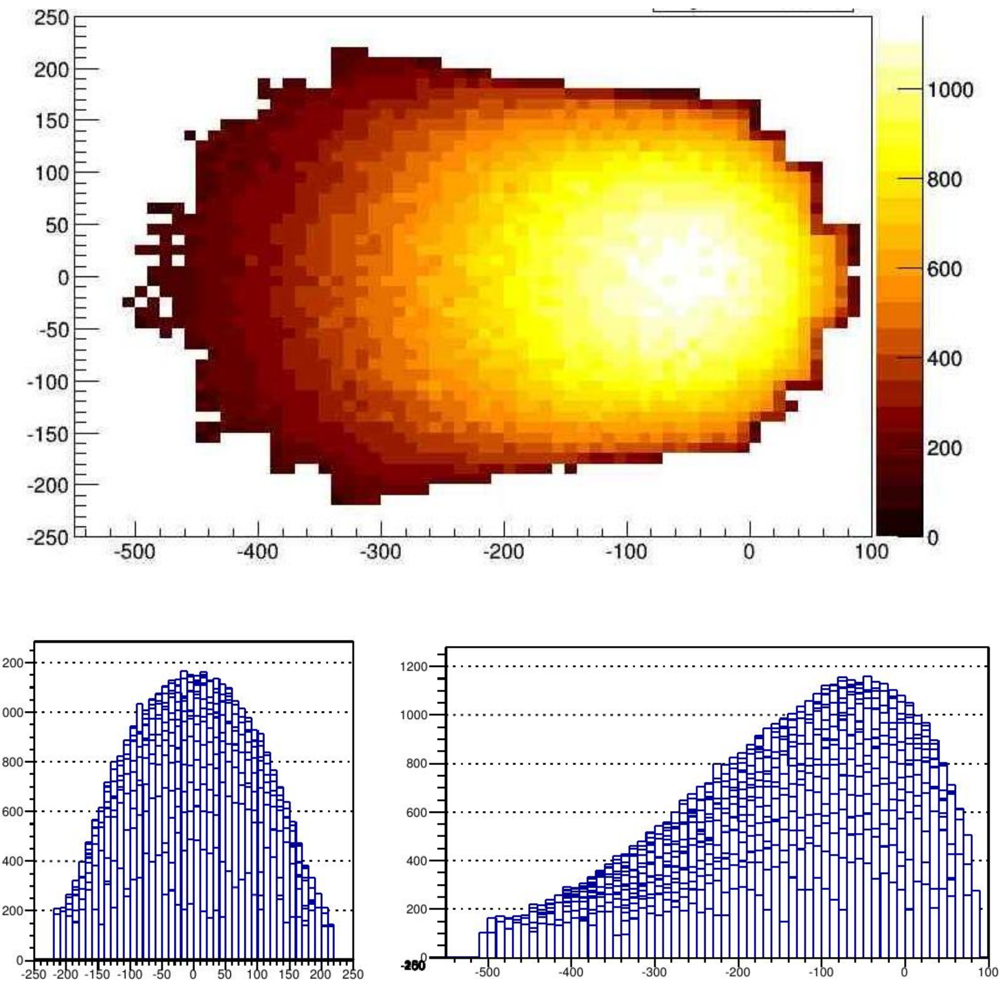

Figure 6.1.5: JEM-EUSO tilted mode, 20°: signals/triggering event distribution on focal surface. Top: FOV as seen from above, number of signals per triggering event is colour coded, bottom left: y-profile of the FOV, bottom right: x-profile of the FOV.

6.2 ANGULAR RESOLUTION: 20° TILTING

For the scenario of a tilted telescope with an angle of 20°, we have created a shower database with the same energies and zenith angles as in the previous study. For this setup however, the impact points of the showers have been placed within a rectangular area of x: -550 km – +100 km × y: -250 km – +250 km. This is again larger than the actual FOV of the tilted instrument. For each of the energy/zenith angle combinations the amount of triggering events is of the order of 2000 or higher. The higher statistics of events compared to the nadir mode study is owed to the increased field of

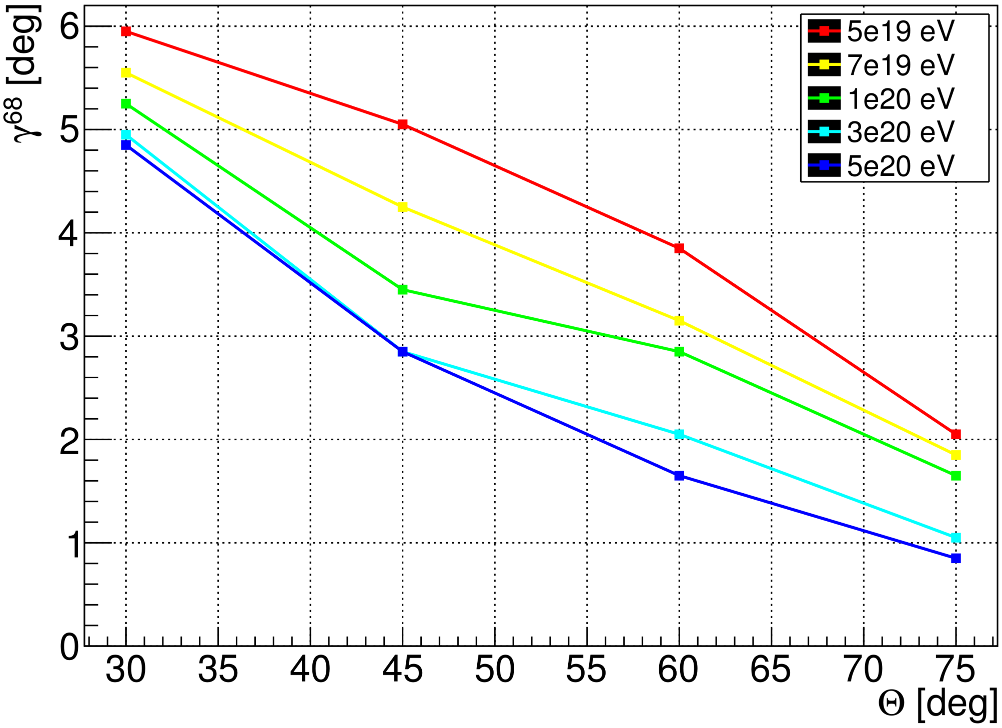

Figure 6.2.1: JEM-EUSO tilted mode, 20°:Angular resolution in terms of γ^{68} obtained by the NE2 algorithm for proton events plotted against the true zenith angle for different energies (colour coded).

view. The angular resolution of the tilted (20°) telescope decreases compared to the nadir instrument. The effect mainly depends on the zenith angle of the showers, to a smaller extent on the energy. On average we observe a worsening of the angular resolution by approximately 1°. The low zenith angle showers experience a shift by about 1.5°. The findings are in fact relatively similar to the numbers of the nadir instrument while taking into account the multiple scattering orders using Monte Carlo transport of photons in atmosphere. This picture also applies to the efficiencies (Fig. 6.2.2). The effective efficiency, being the product of trigger and reconstruction efficiency, drops by almost 40% for the low zenith angles. However, in this scenario the trigger efficiency has become a determining factor. While in the Monte Carlo scenario, the trigger efficiency remained at a relatively high level and the reconstructability of the triggered events rapidly dropped, for the tilted mode it is the contrary. We can see a decrease of the trigger efficiency even for the 75° events and a strong decline for 30° events. The various reconstruction algorithms react differently to the tilted scenario in compari-

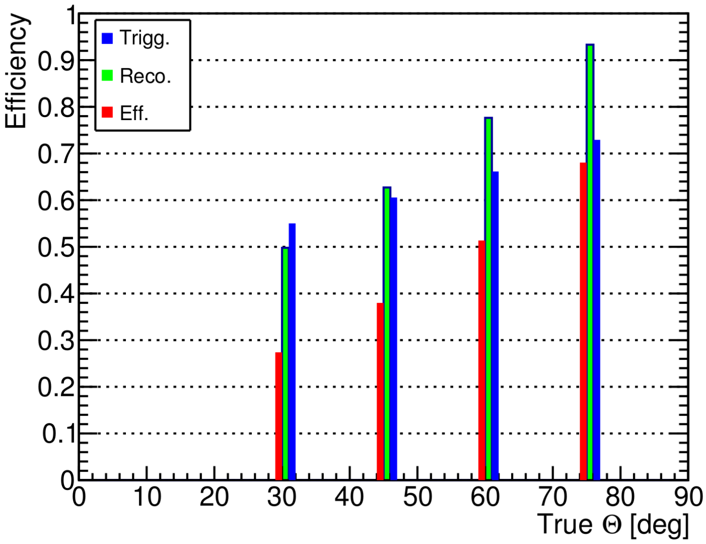

Figure 6.2.2: JEM-EUSO tilted mode, 20°: trigger efficiency (blue), reconstruction efficiency (green) and the effective efficiency (red) for the different zenith angles and cumulative energies.

son to the Monte Carlo case. We can clearly see that for a specific zenith angle, the 5 different reconstruction algorithms yield more diverse results than for the nadir case. However, for the nadir configuration and Monte Carlo transfer, the answer has been even more diverse with additionally a stronger variance of the single algorithms. (Figs. 6.2.3 and 6.2.4) Investigating the cause for the significant loss of both efficiency and angular resolution, we consider the field of view position of the shower. In Fig. 6.2.5, we can see that the overall angular reconstruction performs relatively constant with only a small increase as function of the FOV radius. Starting from a radius of about 350 km however, there is a slightly stronger increase towards the outer FOV regions. For the efficiency, though, we observe an almost linear dependence with the radius. With a full trigger efficiency and a high reconstruction efficiency ($\sim 90\%$) at the very centre, there is a severe decline to almost zero at 500 km radius. Up to a radius of about 300 km, this is mostly due to the very clear decrease of the reconstruction efficiency. However, from there outwards the trigger efficiency decreases rigorously. Hence, for the FOV parts beyond 300 km, the few events that pass the trigger, yield a relatively high reconstruction efficiency. This picture becomes even more clear, when we plot the maximum position of the showers within the tilted FOV (Fig. 6.2.6). The distribution of the shower maxima of the non-triggering events (in red), the events the software

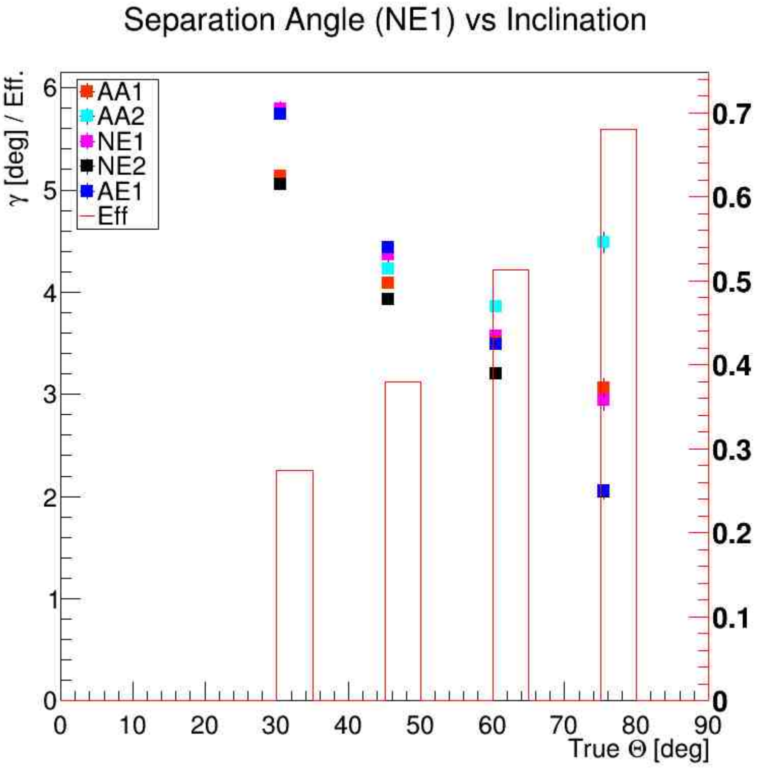

Figure 6.2.3: JEM-EUSO tilted mode, 20°: $\langle\gamma\rangle$ for the five algorithms (colour coded)and their standard deviation plotted as function of the true zenith angle together with the reconstruction efficiency (red bars).

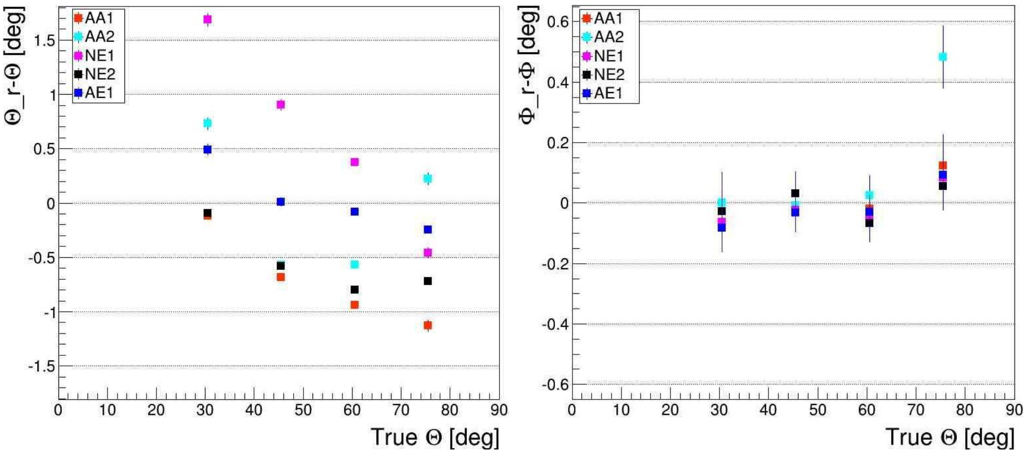

Figure 6.2.4: JEM-EUSO tilted mode, 20°: reconstructed $\langle\Delta\Theta\rangle$ (left) and $\langle\Delta\Phi\rangle$ distributions (right) for cumulative energies. The colours represent the five different algorithms to show their individual performance. The error bars indicate the standard deviations.

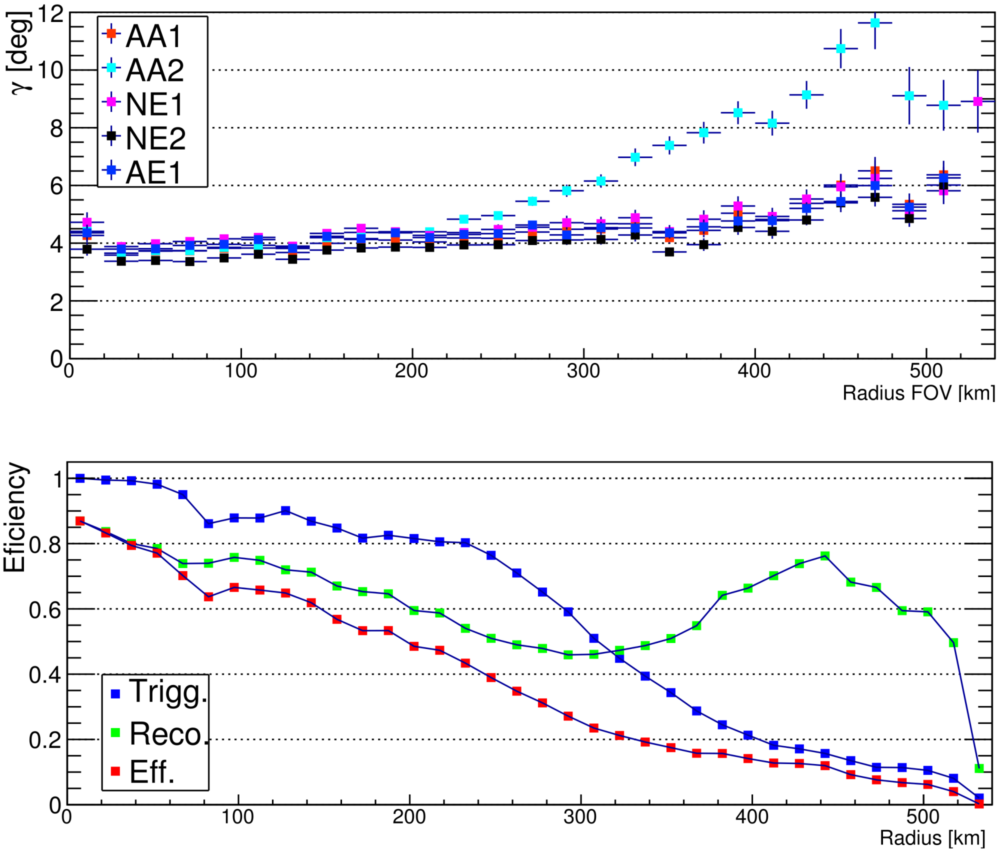

Figure 6.2.5: JEM-EUSO tilted mode, 20°: top: $\langle\gamma\rangle$ for the five algorithms (colour coded) and their standard deviation plotted as function of the FOV radius. bottom: trigger (blue), reconstruction (green) and effective efficiency (red) as function of the FOV radius.

failed to reconstruct (yellow) and the distribution of successfully reconstructed events (green) clearly confirm the study conducted for the photon behaviour during the simulation part. There is an area inside the FOV, where there are almost no non-triggering events and the density of failed events is small, as well. This is the area in which almost every event has been both triggered and reconstructed. Among those events populating this area that have not been triggered we still can see a rectangular pattern. These are events with low energies and zenith angles, falling into the dead spaces between PMTs and PDMs. For the outer FOV parts at -350 km to 500 km, on the contrary, we can be sure that the events that were triggered and succesfully reconstructed in the end were among the ones with highest energies and zenith angles. When we compare the area in which both triggering and reconstruction works on a high level, to the same area

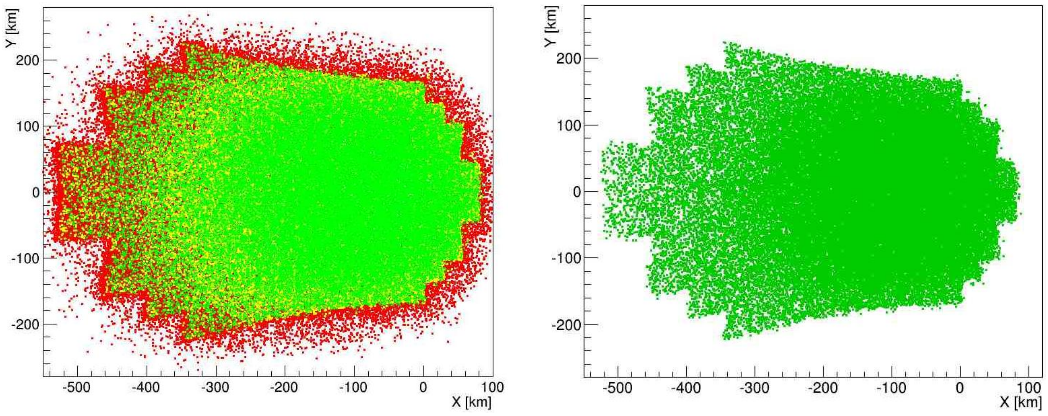

(a) FOV position of maxima, superimposed view

(b) Reconstructed events

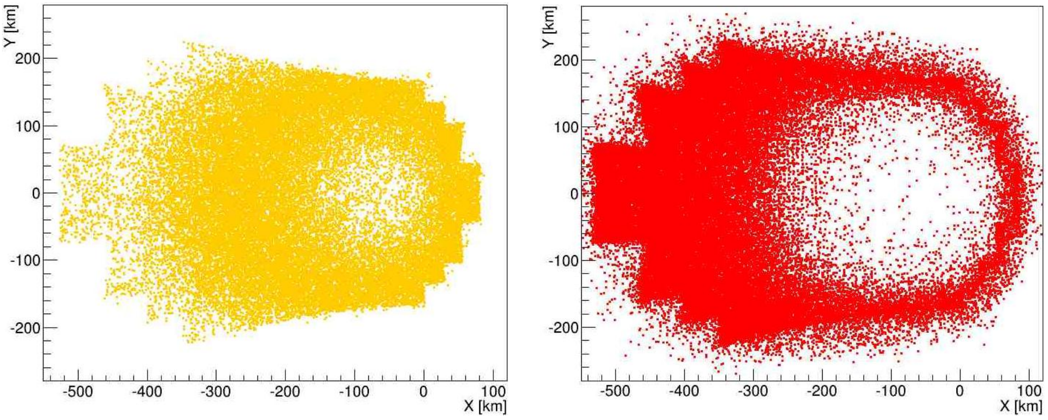

(c) Failed events

(d) Non-triggering events

Figure 6.2.6: JEM-EUSO tilted mode, 20°:shower maxima positions within the telescope's FOV. Red: Population of non-triggering events. Yellow: Events, triggered but not reconstructed. Green: Events, triggered and successfully reconstructed.

in the nadir case, we must note that it is smaller in the tilted case.

However, we have identified the lack of photos arriving to the detector as the main reason behind the low efficiencies. The tilted mode is primarily supposed to increase the exposure for extreme energy cosmic rays events, i.e. events having an energy higher than 10^{20} eV. Therefore, we evaluate how the reconstruction quality is affected, if we consider only EHE events (Fig. 6.2.7). Comparing Fig. 6.2.7 to Fig. 6.2.5 reveals a clear improvement of the reconstruction quality, once we restrict ourselves to the detection of EHE events exclusively. The mean separation angle for events near the centre of the FOV has improved by almost 2° for EHE events. It reaches the level of about 4° only after 300km displacement from the nadir position. Also in terms of efficiency, the 'EHE only scenario' shows a significant increase in the overall performance. Reaching 100 % efficiency in the centre region, the efficiency drops to 50 % is at 400 km distance from the detector's nadir point. In comparison, if we consider all energies, the efficiency drops down to 50% already at a radius of about 200 km. The maximum reachable efficiency at the centre is only 85 %.

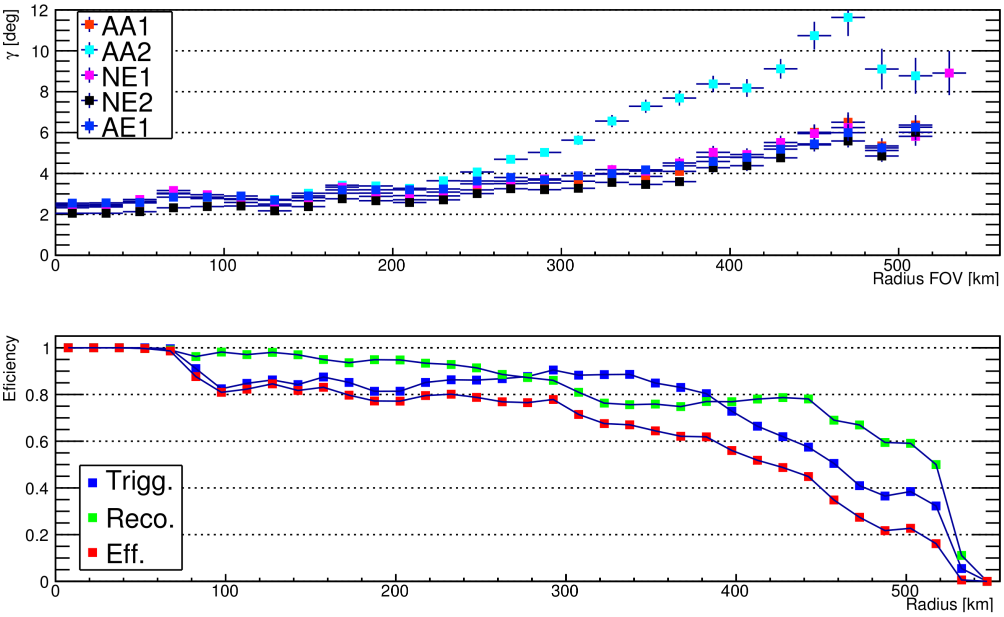

Figure 6.2.7: JEM-EUSO tilted mode, 20°, extremely high energies: γ vs FOV radius and efficiency.

We can clearly see that the sensitive area in which a meaningful reconstruction of the events is still possible is clearly larger when we use the detector for EHE events.

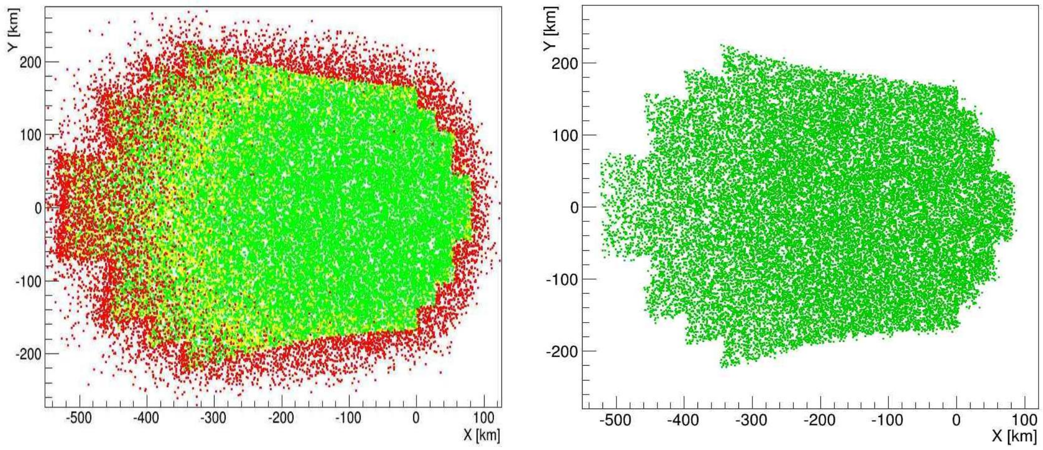

(a) FOV position of maxima, superimposed view

(b) Reconstructed events

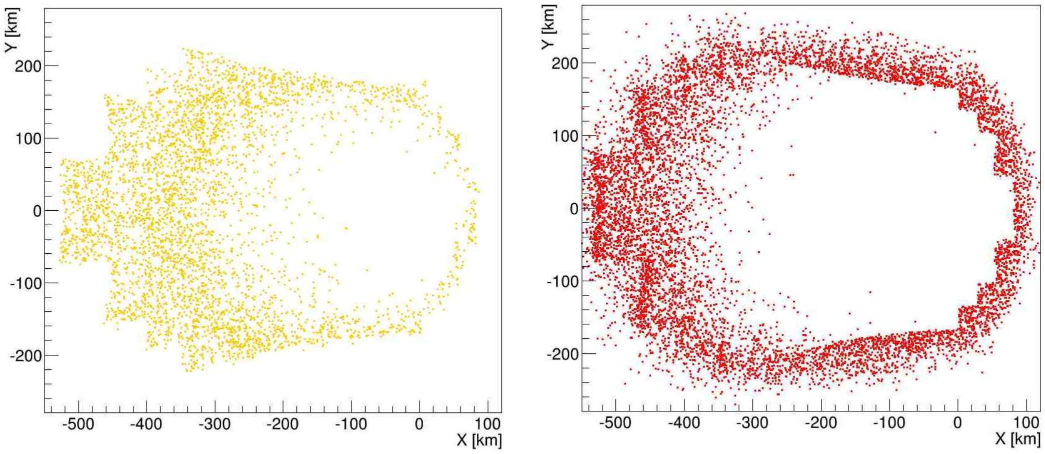

(c) Failed events

(d) Non-triggering events

Figure 6.2.8: JEM-EUSO tilted mode, 20°, extremely high energy: shower maxima positions within the telescope's FOV. Red: Population of non-triggering events. Yellow: Events, triggered but not reconstructed. Green: Events, triggered and successfully reconstructed.

This becomes even clearer when we check the distribution of the successfully reconstructed, the triggered and the non-triggering events within the FOV for EHE events (Fig. 6.2.8). The area in which events are not even triggering is by far smaller than in Fig. 6.2.6 and lies in the border region of the FOV. The same applies to the distribution of failed events. In the case of all energies, these events could be found on the entire focal surface, whereas for EHE events, almost every event within a radius of 250 km could be triggered and reconstructed.

6.3 PHOTON AND SIGNAL ANALYSIS 40°

From the previous tilting of the instrument by 20° it became evident that there is a substantial impact of the tilting on the signal behaviour. For the 40° tilting, we therefore expect a similar, but even more increased effect. Thus, we have conducted an additional study of the expected signal attenuation for the 40° case. Again, we have utilized air showers with an energy of 10^{20} eV and a zenith angle with Θ=60° as a standard candle. To account for the far larger field of view, we have deployed more than $2 \cdot 10^5$ events homogeneously distributed in the entire FOV. Again, we check how many photons per event reach the telescope, pass through the optics, produce a signal on the focal surface detector and give a trigger signal in the end. Obviously, for the 40° tilted telescope the proximity effect, i.e. the loss of photons due to the $1/d^2$ scaling effect plays a far more dominant role than for the 20° case. From Fig. 6.3.1 we learn that also for the 40° tilt, showers that develop right below the telescope yield the highest rate of photons reaching the instrument. However, the showers in the outer region of the FOV are much farther away from the detector than in the 20 ° tilted case. Now, the remote showers that are nevertheless still inside the field of view are up to 1300 km displaced from the detector's nadir point. To check the validity of the proximity effect, we plot the number of arriving photons per event as function of the event's distance d to the detector. Moreover, we compensate for the effect that the entrance pupil can only be seen under a certain angle α which depends on the horizontal distance to the detector by adding a cosine term (Fig. 6.3.2).

$$scalefactor = \frac{1}{d^2} \cdot \cos\left[\alpha + 40^\circ\right] \tag{6.1}$$

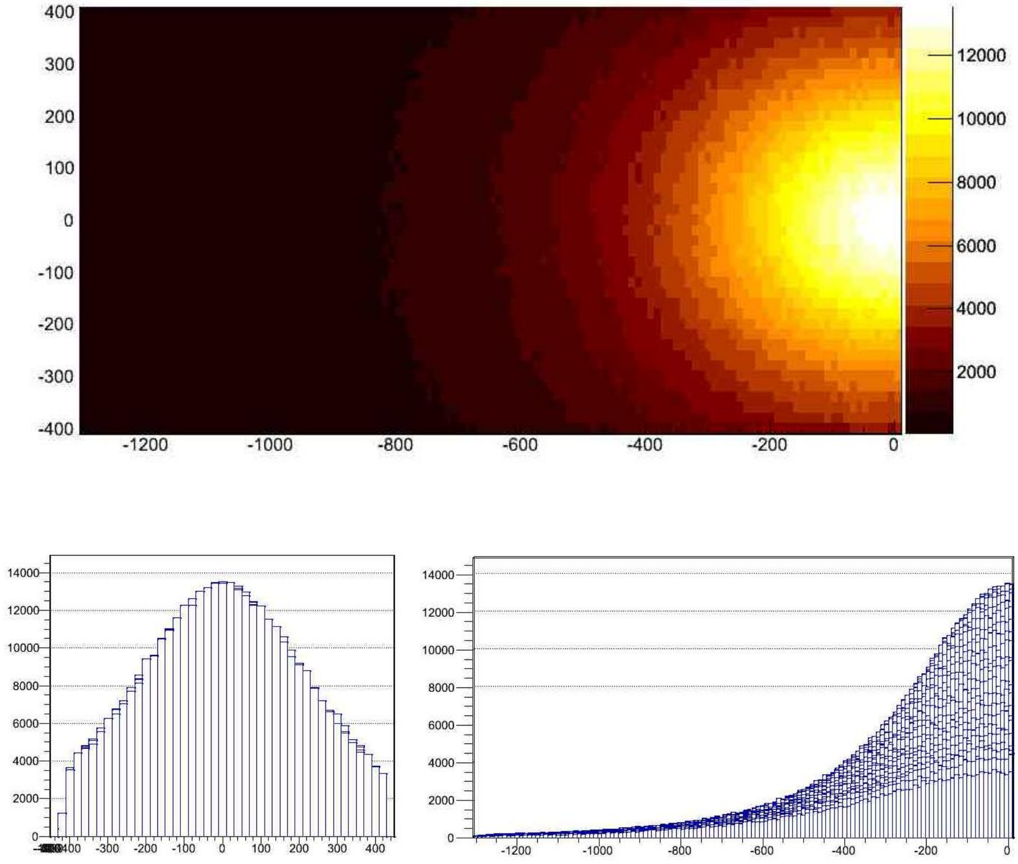

Figure 6.3.1: JEM-EUSO tilted mode, 40°: photons/event distribution arriving at the telescope. Top: FOV as seen from above, amount of photons per event is colour coded, bottom left: y-profile of the FOV, bottom right: x-profile of the FOV.

The 40° term appears due to the reason that the detector is tilted by actually -40. Thus, when an event appears 335 km horizontally displaced from the nadir point it points orthogonally to the lens. Now we assume that the showers have their maximum at approximately 6 km altitude and express the event's distance d by the radius from the detector's nadir point to the event r.

$$scalefactor = \frac{1}{(394\,km)^2 + r^2} \cdot \cos\left[\arctan\left(\frac{r}{400\,km}\right) + 40^\circ\right] \tag{6.2}$$

Due to the strong tilting of the telescope, the optimal optics performance is now situated within an area, in which the showers are already relatively far away from the telescope. Comparing the position of the brightest events to the distribution of the optics efficiency, we can see that these regions do not strongly overlap (Figs. 6.3.3 and

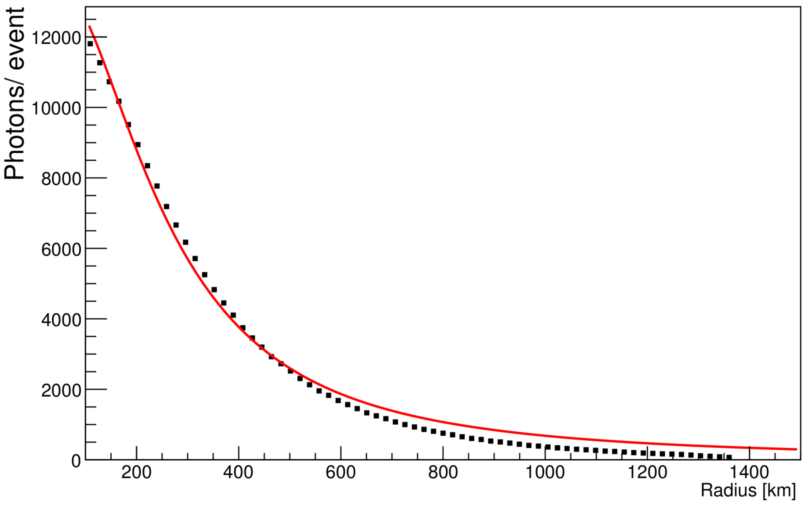

Figure 6.3.2: JEM-EUSO tilted mode, 40°: To verify the impact of the proximity effect, we superimpose the photons per event as function of the FOV radius with the graph of the analytical formula.

6.3.1). Thus, the proximity effect and the optical attenuation effect leads to a scenario, where the instrument never reaches its full performance. Hence, the photons arriving to the focal surface per event is reduced by 25%, from 4000 photons at maximum to 3000 photons (Fig. 6.3.4). The superposition of the two effects leads to a strongly attenuated photon flux on the focal surface and eventually to a strongly attenuated signal behaviour. (Fig. 6.3.5) The losses are in fact remarkable. From a maximum of about 850 signal counts per event at X=-150 km, the count curve drops to about 150 counts per event at X=-600 km — this is only about half the entire FOV (X-component). This is actually the threshold from which on the events cannot be triggered. Consequently, about 50% of the entire FOV is not sensitive to 10^{20} eV, 60° events (Fig. 6.3.6). However, in terms of total area within the theoretical field of view of the tilted telescope, the majority of events are situated in a part which is not sufficiently efficient to trigger them. It would require far brighter events with higher energies and higher zenith angles than 10^{20} eV, 60° events.

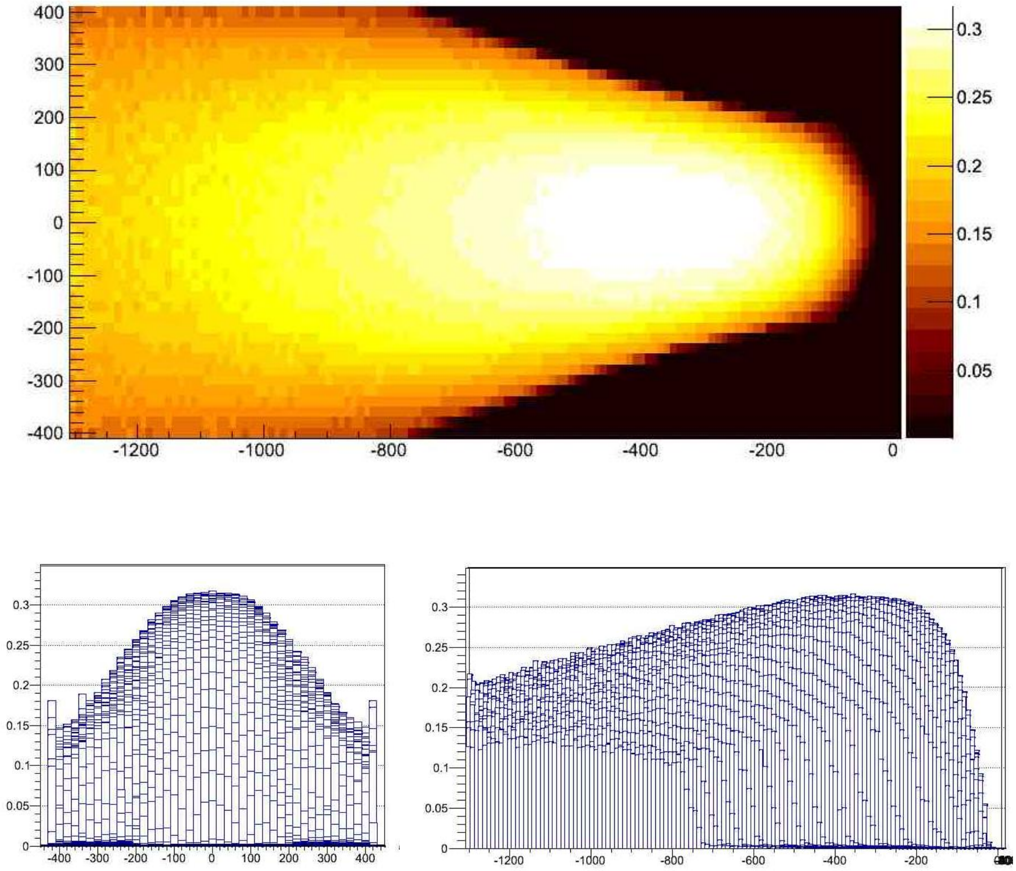

Figure 6.3.3: JEM-EUSO tilted mode, 40°: Optics throughput efficiency. Top: FOV as seen from above, efficiency is colour coded, bottom left: y-profile of the FOV, bottom right: x-profile of the FOV.

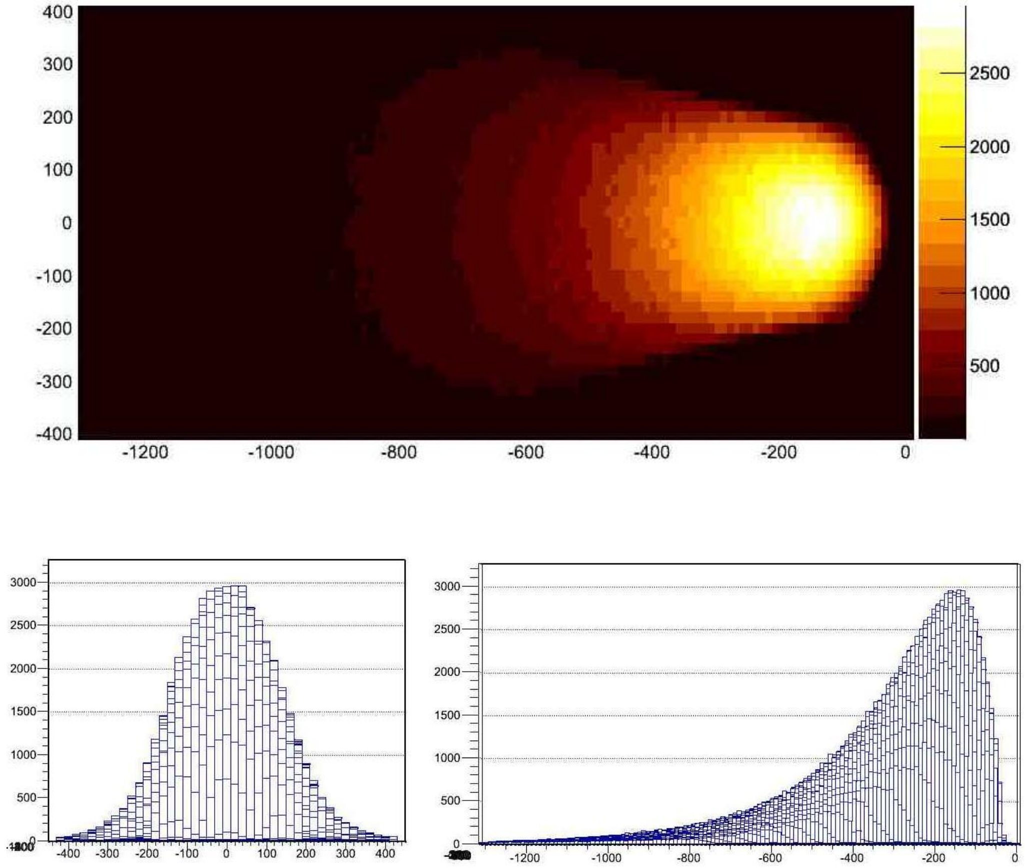

Figure 6.3.4: JEM-EUSO tilted mode, 40°: photons/event distribution on the focal surface after passing the optical system. Top: FOV as seen from above, amount of photons per event is colour coded, bottom left: y-profile of the FOV, bottom right: x-profile of the FOV.

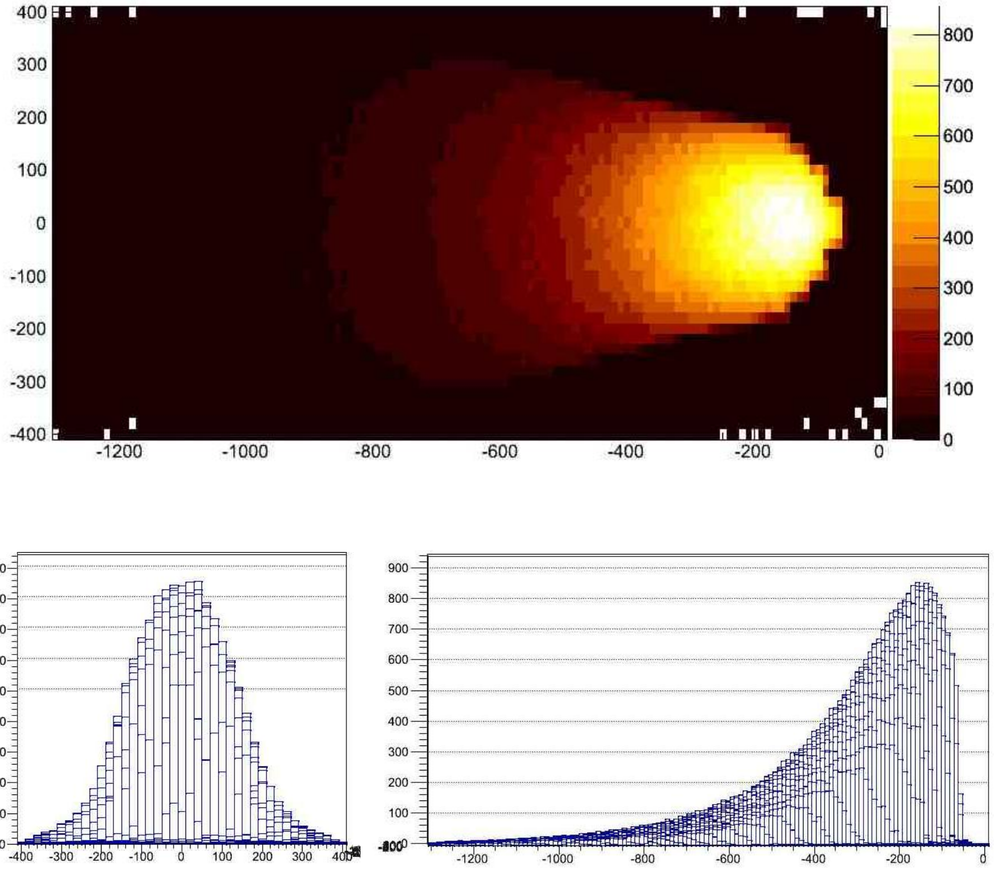

Figure 6.3.5: Tilted Mode 40: signals/event distribution on the focal surface. Top: FOV as seen from above, number of signals per event is colour coded, bottom left: y-profile of the FOV, bottom right: x-profile of the FOV.

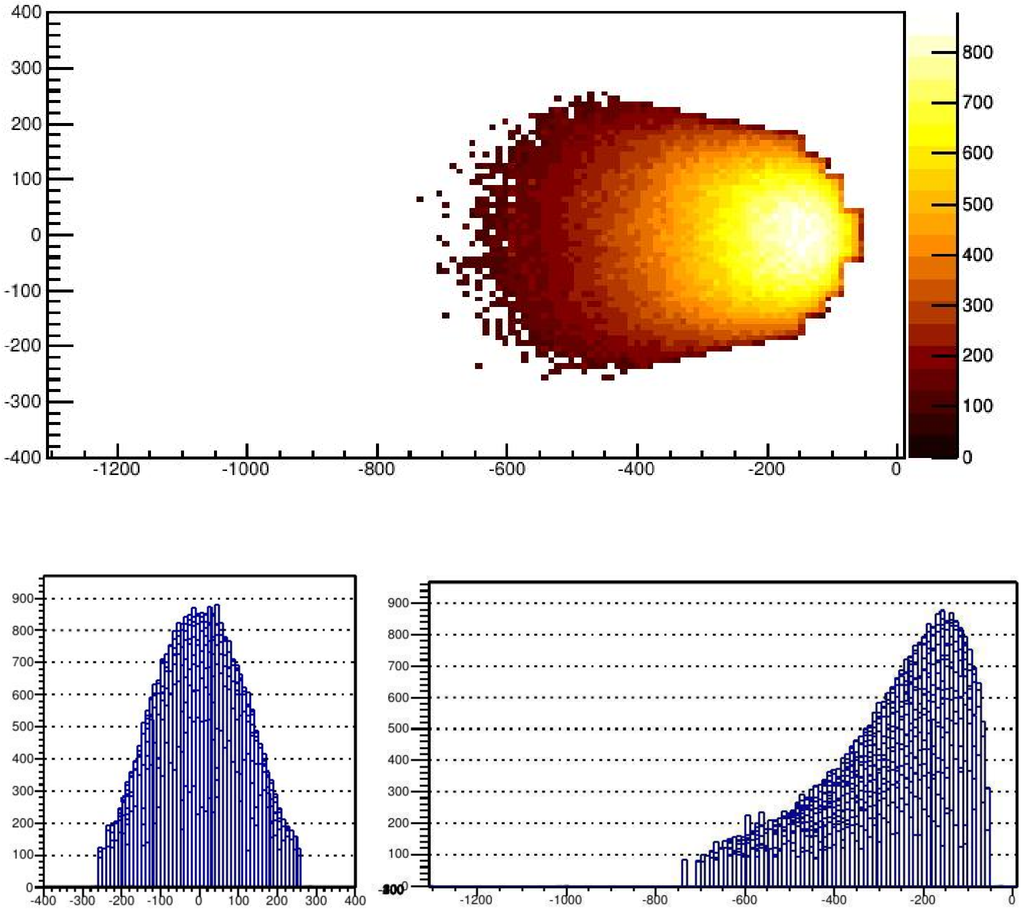

Figure 6.3.6: JEM-EUSO tilted mode, 40°: signals/triggering event distribution on the focal surface. Top: FOV as seen from above, number of signals per triggering event is colour coded, bottom left: y-profile of the FOV, bottom right: x-profile of the FOV.

6.4 ANGULAR RESOLUTION: 40° TILTING

As for the evaluation of the nadir and tilted mode (20°) we have generated a third individual database of showers. Again, the same energies and zenith angle configurations have been used. For the tilted mode (40°), the statistics have been increased again to an order of about 5000 triggering events for the lower energies and even exceeding 10000 triggering events for the higher energies. The impact points of the simulated showers have been placed in a rectangle with the dimensions of x: -1300 km – 0 km × y: -400 km – +400 km. This is again well larger than the actual FOV of the tilted instrument. The angular resolution of the tilted (40°) telescope decreases compared to the tilted (20°). Also here, the effect mainly depends on the zenith angle of the showers and to a smaller extent on the energy. The decline of the angular resolution is about 1.5° compared to the tilted (20°) case. Interestingly, there seems to be almost no en-

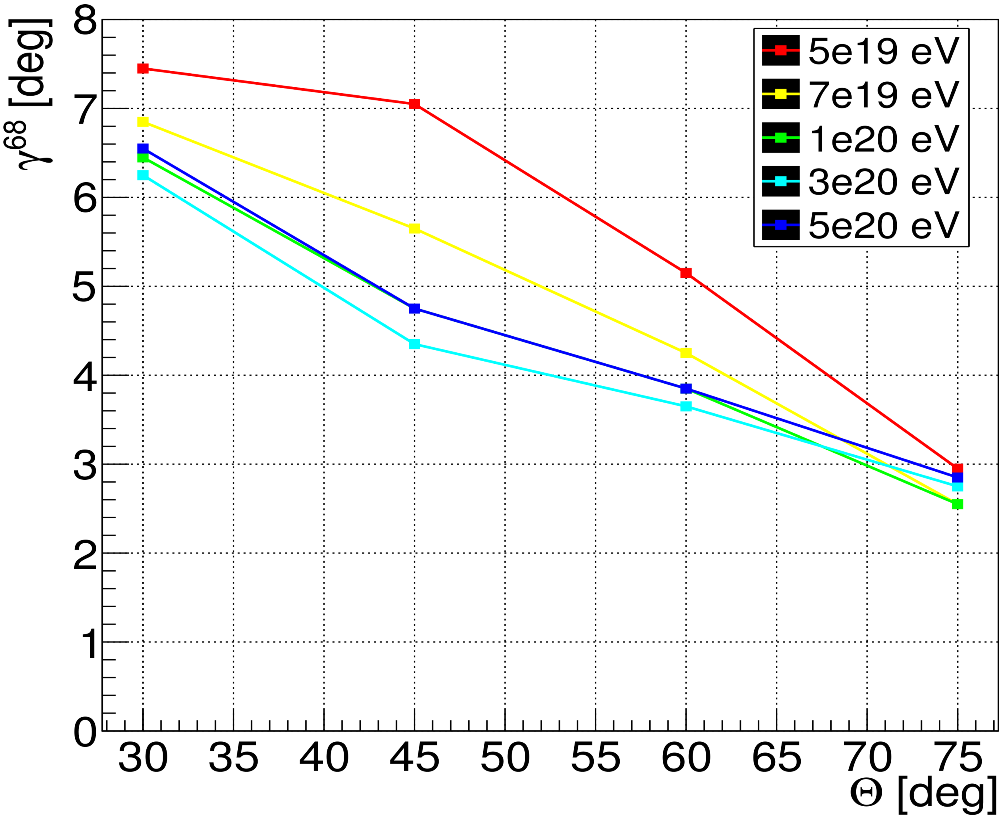

Figure 6.4.1: JEM-EUSO tilted mode, 40°: Angular resolution in terms of γ^{68} obtained by the NE2 algorithm for proton events plotted against the true zenith angle for different energies (colour coded).

ergy dependence for the highly inclined showers. The effective efficiencies decrease by about 50% compared to the tilted (20°) mode. This means a decrease of almost 80% for the 75° zenith angles and still almost 60% for the 30° zenith angles. Apparently, the reconstruction efficiency itself does not seem to suffer very much. The substantial loss of effective efficiency is clearly owed to the rapid decline of the trigger efficiency. Those events that survive the first selection are thus more likely to be reconstructed (Fig. 6.4.2). The analysis of the behaviour of the different reconstruction algorithms supports the assumption that the angular reconstruction module is already performing at an optimum. From Figs. 6.4.3 and 6.4.4 we can infer that the delivered results are relatively close to each other, with the exception of the AA2 algorithm (in cyan). Furthermore, the variance of the results of the individual algorithms is very low. The error bars indicating the standard deviation of the mean γ in Fig. 6.4.3 and the mean Θ in Fig. 6.4.4 are not even visible in the histogram plots. In plotting the separation angle distribution and the efficiencies as function of the radius inside the telescope's FOV, we can see the reason for the massive degradation in both angular resolution and efficiency. From Fig. 6.4.5 we can see that the overall angular reconstruction works relatively constant at $\gamma \approx 4°$ within the first 400 km of the FOV radius. From there

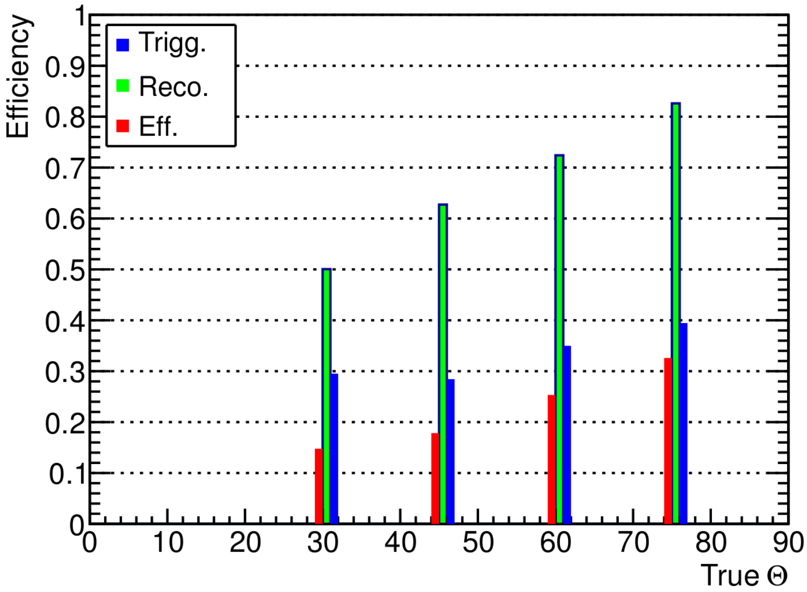

Figure 6.4.2: JEM-EUSO tilted mode, 40°: trigger efficiency (blue), reconstruction efficiency (green) and the effective efficiency (red) for the different zenith angles and cumulative energies.

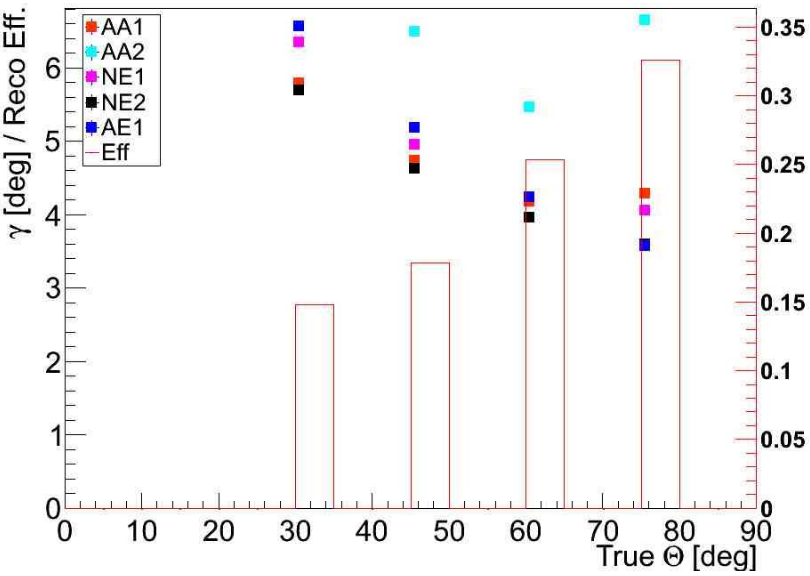

Figure 6.4.3: JEM-EUSO tilted mode, 40°: $\langle\gamma\rangle$ for the five algorithms (colour coded)and their standard deviation plotted as function of the true zenith angle together with the reconstruction efficiency (red bars).

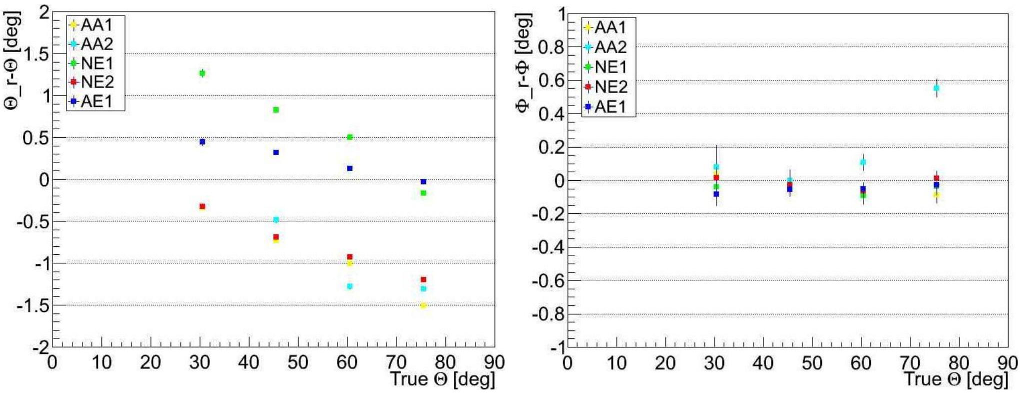

Figure 6.4.4: JEM-EUSO tilted mode, 40°: reconstructed $\langle\Delta\Theta\rangle$ (left) and $\langle\Delta\Phi\rangle$ distributions (right) for cumulative energies. The colours represent the five different algorithms to show their individual performance. The error bars indicate the standard deviations.

to the outer parts of the FOV, it continuously increases up to $\gamma \approx 8°$ at 800 km. Beyond that the behaviour becomes a little chaotic. This is due to the lack of sufficient statistics, since in this region of the FOV, the efficiency has already fallen below 5%. In the tilted (40°) setup, the detector never reaches a full trigger efficiency. As shown in Chap. 6.3, this arises from the circumstance that the showers in relatively close proximity to the detector appear within a part of the FOV, where the optics throughput is relatively low, compared to the centre. The centre part of the optics however, with its maximum throughput detects only those showers that are already 340 km displaced from the detectors nadir point. Hence, from its maximum effective efficiency of 60% at 200 km radius, we experience an almost linear decrease to about 800 km radius. Beyond a radius of about 900 km, the detector is essentially blind — even for the very bright events. To support this, we show the distributions of the shower maxima inside the tilted FOV for the three populations: non-triggering events, failed events and reconstructed events (Fig. 6.4.7).

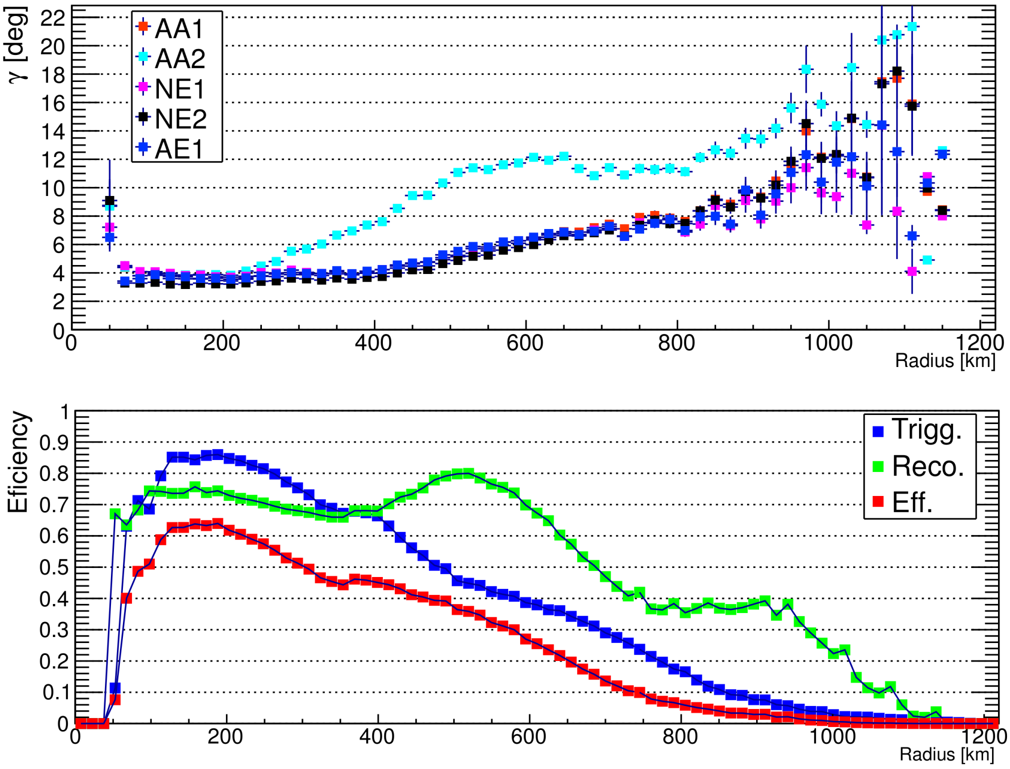

Figure 6.4.5: JEM-EUSO tilted mode, 40°: top: $\langle\gamma\rangle$ for the five algorithms (colour coded) and their standard deviation plotted as function of the FOV radius. bottom: trigger (blue), reconstruction (green) and effective efficiency (red) as function of the FOV radius.

Taking a closer look at the plots in Fig. 6.4.7, we note that the area in which the tilted detector allows for a meaningful trigger scenario is only a relatively small region at around x= -200 km, y=0 km. However, the same area seen in the plots of the failed and reconstructed population does not allow for any conclusion, since both plots are

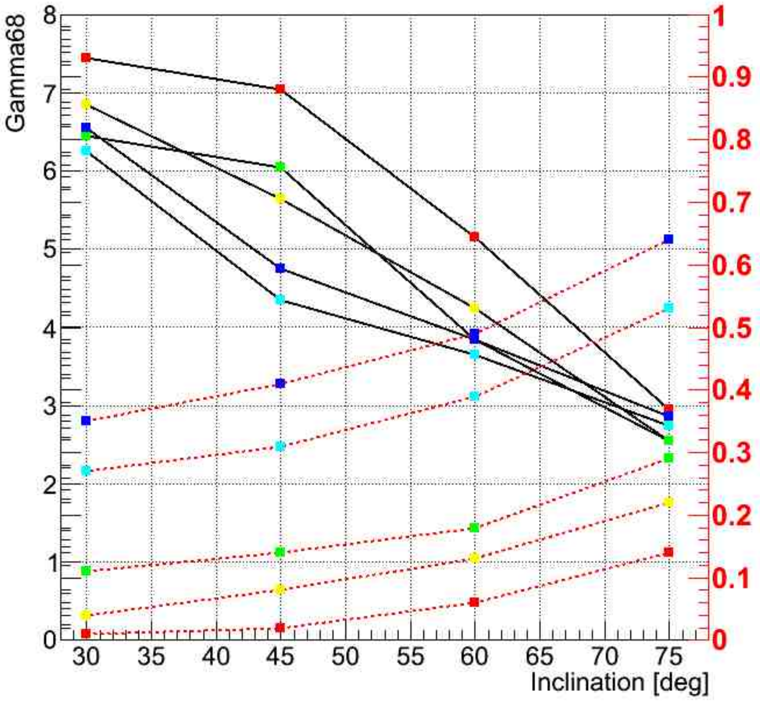

Figure 6.4.6: JEM-EUSO tilted mode, 40°: γ^{68} and efficiencies.

saturated here. This means that some classes of events cannot be reconstructed even in this most efficient part of the detector FOV, while others apparently can. Thus, we have to reconsider the same plots, this time neglecting all energies below 10^{20} eV. We assume that this kind of detector configuration might allow for observation of the extreme energies, only.

Indeed the picture changes when we limit the resolution study to extreme energy events above 10^{20} eV. The overall angular resolution performance increases and so does the efficiency. However, the improvement is not as clear as in the 20° tilting case. Also here, we can observe an improvement in angular resolution of about 1° (from 4° to 3°) for centre events (Fig. 6.4.8). But already at a radius of 400 km, both distribution become indistinguishable (Fig. 6.4.5). This means that restricting ourselves to EHE events only, does not improve the results for remote events, but compensates for optics inefficiencies in the centre region of the FOV.

In terms of efficiency, the 'EHE-only scenario' shows an improvement. However, even in the EHE case, it never reaches its full efficiency. In the centre region we see an increase from 60 % to 80 %. Also the 50 % efficiency radius increases from about 300

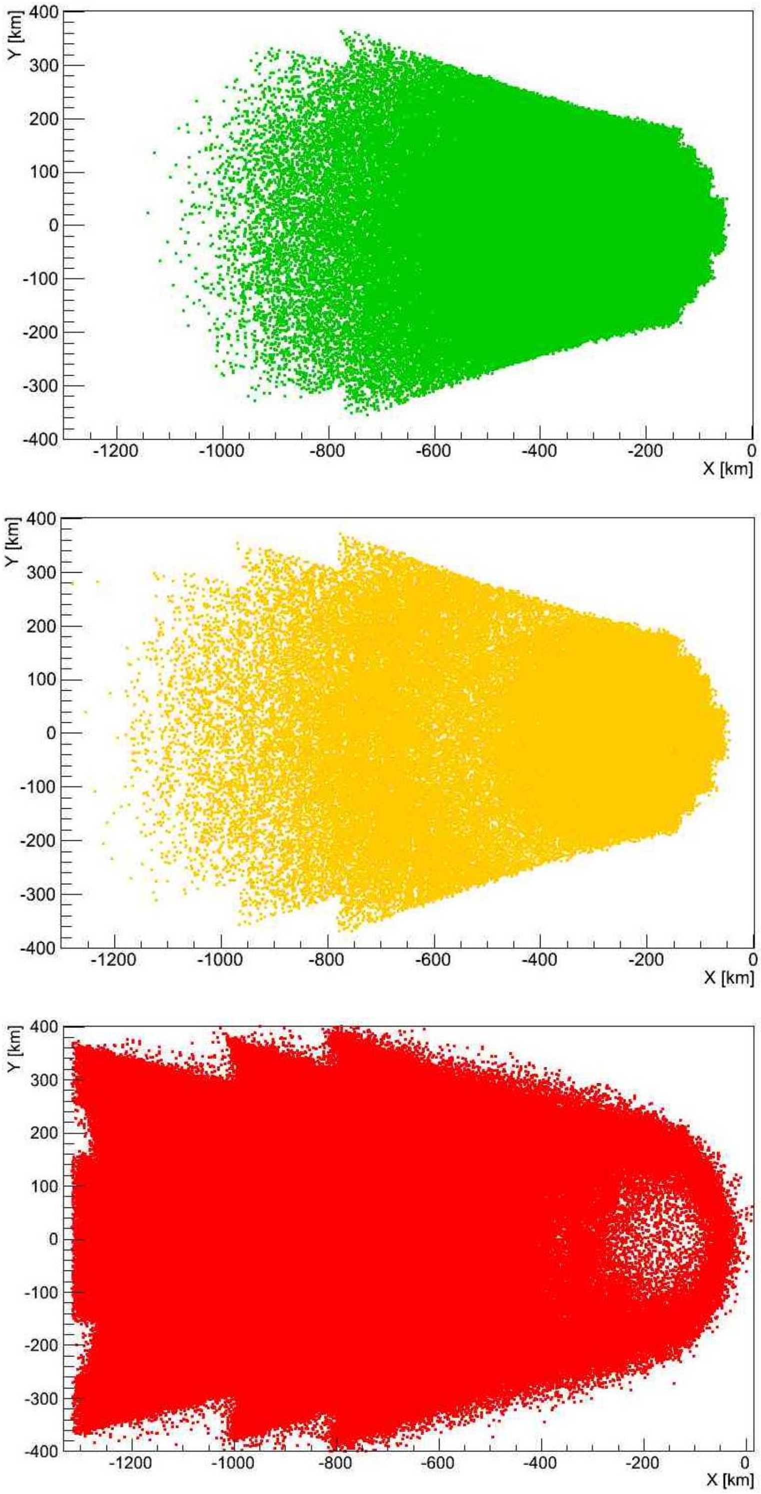

Figure 6.4.7: JEM-EUSO tilted mode, 40°: Shower fluorescence light maximum distribution in the FOV of the tilted instrument for the reconstructed events (green), the failed reconstruction events (orange) and the not-triggered events (red).

km to about 580 km (Fig. 6.4.8). Still major parts of the FOV remain at low efficiencies and a bad resolution. Plotting the maximum position of the non-triggered, the failed

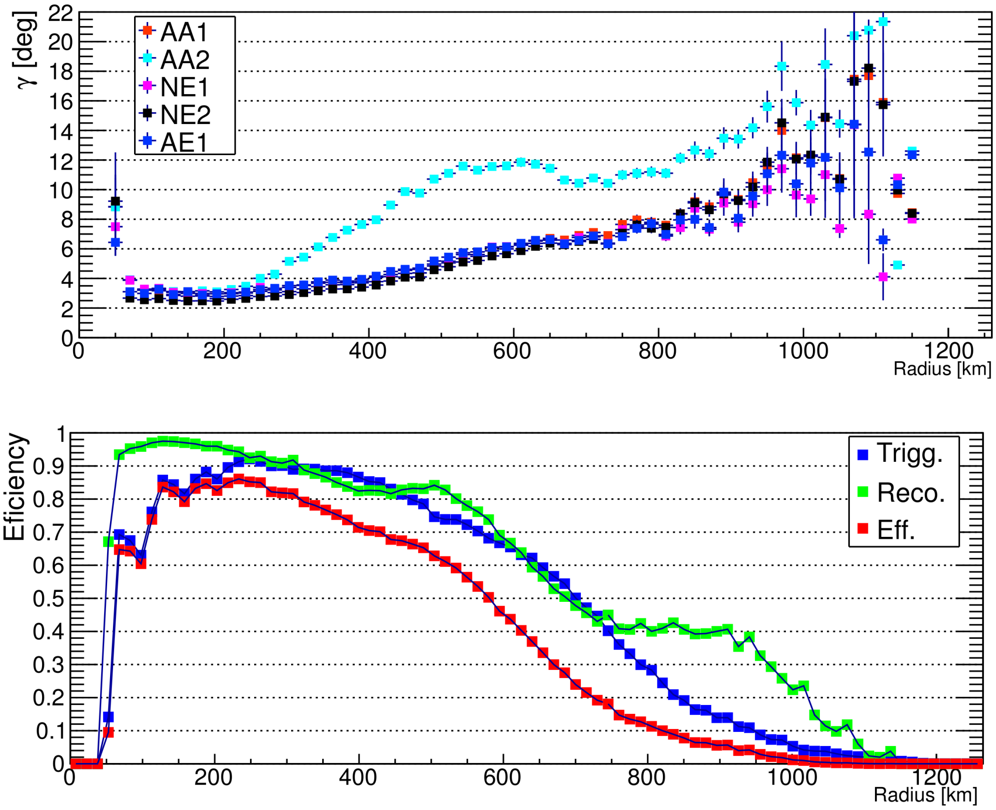

Figure 6.4.8: JEM-EUSO tilted mode, 40°, extremely high energies: γ vs FOV radius and efficiency.

and the reconstructed events, it becomes clear that the sensitive area inside the tilted FOV increases. However, it does not apply to the remote parts of the FOV. The results beyond a radius of 400 km remains largely unaffected by selecting only EHE events. The only major difference concerns the area between -100 to -3500 km. Here, we can clearly see an improvement. More events are triggered and also reconstructed (Fig. 6.4.9). But obviously this increase does not compensate for the losses we experience when we tilt the telescope by 40°. Between -600 and -800 km we have a strong accumulation of failed events. In this region of the FOV, the trigger still recognizes a number of extremely high energetic events. However, the amount of light reaching the detector is not sufficient in order to provide enough information to the track direction module. The angular determination becomes challenging, if not impossible. Beyond -800 km in the rest of the FOV we clearly see the population of events which is not even triggered. The detector cannot see them.

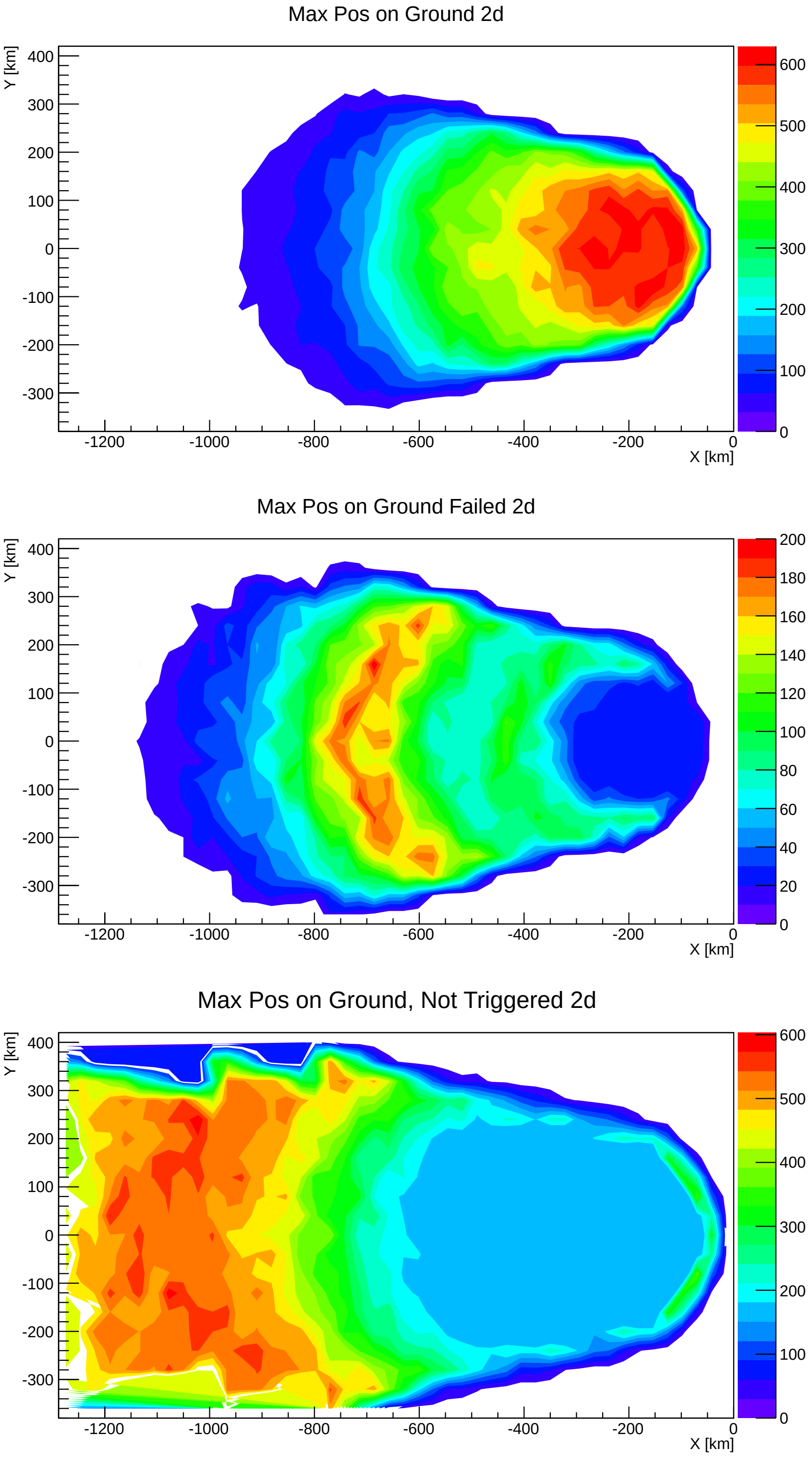

Figure 6.4.9: JEM-EUSO tilted mode, 40°, extremely high energies: Shower fluorescence light maximum distribution in the FOV of the tilted instrument for the reconstructed events (top), the failed reconstruction events (middle) and the non-triggering events (bottom).

The fact that we live at the bottom of a deep gravity well, on the surface of a gas covered planet going around a nuclear fireball 90 million miles away and think this to be normal is obviously some indication of how skewed our perspective tends to be.

Douglas Adams, The Salmon of Doubt

7

Conclusio

THE ANALYSIS of the angular resolution capabilities of the instruments within the context of the JEM-EUSO mission has been the objective of this dissertation. In the course of our studies the following topics have been successfully addressed:

- The evaluation and debugging of the angular reconstruction algorithms within the ESAF software, the verification of the performance of the pattern recognition and direction reconstruction modules under various conditions;

- The evaluation of the angular resolution of the JEM-EUSO baseline instrument in nadir mode. An emphasis is dedicated to quality cuts in order to achieve a better resolution for a subclass of UHECR events;

- The effect of Rayleigh scattering on the behaviour of the fluorescence light signal and its impact on the angular resolution of the telescope;

- The assessment of the angular resolution capabilities of SpaceX-EUSO, a modified version of the JEM-EUSO telescope, in nadir mode;

- A study of the angular resolution capabilities of a slim and lightweight version of the JEM-EUSO instrument — EUSO500;
- Simulations and a brief performance estimate of the EUSO Balloon pathfinder experiment;
- An extensive analysis how the behaviour of the fluorescence light signal changes, once the JEM-EUSO telescope is tilted from its nadir position by 20° and 40°. In a second step we have quantified, how this affects the angular resolution of the instrument and the efficiency of the reconstruction procedure.

In the assessment of the angular reconstruction performance of an UHECR observatory, our judgement is first of all guided by the resolution. This is expressed by the distribution of the separation angles or by $\Delta\Theta$ and $\Delta\Phi$. However, we should also consider the fact that in a number of measurements no high quality result can be obtained. Hence, a second indicator for the reconstruction quality is the rate of successfully reconstructed events — the efficiency. Of course, the notion of what can be considered as 'successfully reconstructed' depends on the *quality cuts* imposed which discriminate events considered as useful for the scientific objective under study from those that are not. In Chap. 5.1.3, we have introduced two possible quality cuts to show that under certain conditions and for a sub-range of all collected events, JEM-EUSO is able to deliver a resolution which is higher than the average. Nevertheless, also for the other results presented in this work without naming them *quality cuts*, certain selection criteria have been applied. The very existence of the efficiency curves reflects the fact that in all of the event distributions analysed, we have always identified a number of events as not qualifying and therefore excluded them from the resolution plots. This has been the case for events that

1. did not feature a sufficient amount of pixels hit (10 pixels at min.),
2. did not feature sufficiently bright pixels (7 counts at min.),
3. or exhibit a signal pattern which could not automatically be fitted.

Certainly, all three conditions formulated here are not fixed and can be adjusted to a certain extent. They have been selected in view of a quality of events that can allow source identification studies. Naturally, once one or more conditions are changed, both the resolution and the efficiency curves will be shifted in accordance. In that sense, these results must be regarded as a pair of scales. Considering only the resolution without taking into account the exact conditions under which the efficiencies have been obtained, is therefore not meaningful. This applies especially, when comparing the data to other UHECR experiments.

THE ASSESSMENT OF JEM-EUSO IN NADIR MODE has been one of the key objectives of this thesis. The scientific requirements as stated in [230], demand an angular resolution of 3° or better for energies above $8 \cdot 10^{19}$ eV (expressed in terms of γ^{68}). We can confirm that the angular resolution estimates obtained in Chap. 5.1.2 are meeting the scientific requirements of the mission. Therefore, the expected resolution can considered as appropriate to identify the sources of UHECR. Considering detector modifications and taking the changes in the evaluation methods into account, the results obtained are well in accordance with former studies [62, 181, 184, for comparison]. Comparing the results to the findings of an independent group, i.e. Berat et al. [38], is not a trivial task. Being part of the former (ESA-) EUSO collaboration, this group has simulated an instrument that is comparable in many regards (standard EUSO parameters). However, the details differ in some important aspects. For instance, the EUSO mission had been equipped with a circular optics and the Hamamatsu M36 photomultiplier instead of the M64 to name only two major discrepancies. Both studies have used the ESAF package for the end-to-end simulations. However, the techniques used for the event reconstruction are clearly different, since the PWISE module had not been available of the time of Berat et al.. Additionally, improvements of the angular reconstruction module change the reconstruction scenario. Finally, the authors of Berat et al. do not mention the reconstruction efficiency, making it virtually impossible to compare the results to one another. Interestingly, the performance estimates are still in the same range, at least for the high zenith angles. For the lower zenith angles JEM-EUSO shows a clearly improved performance.

MULTIPLE SCATTERING OF FLUORESCENCE PHOTONS in atmosphere has been considered in this dissertation for the first time in an angular resolution performance estimate for an UHECR space observatory, to this extent. As expected and despite of fine tuning of the reconstruction procedure, the resolution worsens by about one degree in such a scenario. This is not surprising, since the behaviour of the signal changes clearly with respect to the non-scattering scenario, as shown in Chap. 5.2.1. Nevertheless, it is remarkable how close the numbers are to those results obtained without taking scattering effects into account. Especially, when keeping in mind that the pattern identification and angular reconstruction algorithms have been developed for the *bunch* scenario. Therefore, we are confident that tuning the reconstruction techniques and tailoring the modules in accordance to the more complex multiple scattering scenario will enable us to reach the resolution obtained as for the non-scattering case. This claim is clearly supported, if we take a closer look at the fraction of events that have not successfully been reconstructed. Many of them appear to be able to be fitted by hand, at first glance. Thus, it is rather the automatic fitting procedure which appears to have problems adapting to the broadened shape of the signal tracks. All this will be subject of further studies.

TILTING AN UHECR DETECTOR IN SPACE has never been evaluated in an end-to-end simulation before. Hence, there is no data available to compare the results obtained with. From the analysis how the signal tracks behave and the from the experience gained in nadir mode studies the results can be regarded as coherent and self-consistent. A priori, we have decided to probe two tilting angles — 20° and 40°. From the results obtained, it appears that an intermediate choice would be interesting to investigate. The 40° tilting does not seem to yield an advantage from the angular resolution point of view. A large fraction of the detector becomes virtually blind, even to extremely energetic UHECR events. At the same time the overall resolution significantly worsens. The gain we receive in the FOV by tilting is neutralized to a large extent, due to the low light intensities when we try to observe the very remote showers. On the contrary, tilting the detector just moderately by 20° increases the FOV only slightly. At the same time, the losses are far less severe than for the 40° case. By restricting the observation to EHE events, the entire FOV remains sensitive. It will be the objective of future tilting studies to find the optimum tilting angle to meet the scientific objectives.

SPACEX EUSO yields an improved and satisfactory resolution compared to the baseline instrument. The expected angular resolution performance of SpaceX EUSO can approximately be compared to the performance of the baseline side-cut instrument when quality cuts are applied and we concentrate on those events within the centre part of the field of view of the baseline detector. However, the overall achievement of SpaceX EUSO even outperforms this sub-sample by an improvement of the angular resolution of about 1°. Evaluating the reasons why the alternative setup excels also explains why the tilted instrument faces difficulties and reconstruction of events in the outer FOV regions can be challenging. The main factor determining the angular resolution performance is identified as the distance of the air shower to the telescope. Due to the fact that the circular SpaceX EUSO observes events which on average occur closer to the detector compared to the side-cut JEM-EUSO, it benefits from a significantly higher reconstruction quality.

In the scope of the different analyses conducted, we have evaluated the expected angular resolution performances of the JEM-EUSO detector for nadir and tilted mode, furthermore we have estimated the expected impact of the scattering effects in atmosphere. Apart from characterising the JEM-EUSO instrument under different conditions and the other sister instruments of the EUSO family, a greater picture has emerged. We understand that the resolution is guided by four major determining factors which apply to all of the inspected scenarios. Three of them are related to the distance of the shower to the detector.

- The proximity effect: Events occurring in the vicinity of the detector appear brighter than those farther away. Since the amount of photons reaching the telescope is scaled by a factor of $1/d^2$ the signal attenuates remarkably for the showers that are displaced from the nadir point (Fig. 7.0.1).
- Projected pixel size on ground: the size of one pixel inside the FOV determines the minimum theoretically reachable air shower resolution of the telescope. The more remotely a pixel is projected on ground the higher, the minimum reachable resolution becomes. For instance, at the nadir point right below the telescope, one pixel has the size of $\sim$ 0,5 km by 0,5 km. In the most extreme scenario, i.e. the 40° tilted mode , a pixel which is displaced by 1 100 km has the size of 1.5 by 1.5 km (Fig. 7.0.2).
- Optics throughput: Events occurring in the outer parts of the FOV exceedingly suffer from optical losses, due to a lower transmittance of the optical system. Thus, having already fewer photons arriving to the telescope with respect to the centre events, the probability of being attenuated or defocussed by the telescopes's optics is clearly larger (Fig. 7.0.3).
- Skimming effect: The ratio of the lens surface area to outer borders is at an optimum for an instrument with a circular optical system in nadir mode operation. Here, the probability for shower events to skim the field of view and appear only

partially on the FS is at its lowest. When the circular FOV is deformed by either side cuts or tilting of the detector, the probability of skimming events increases.

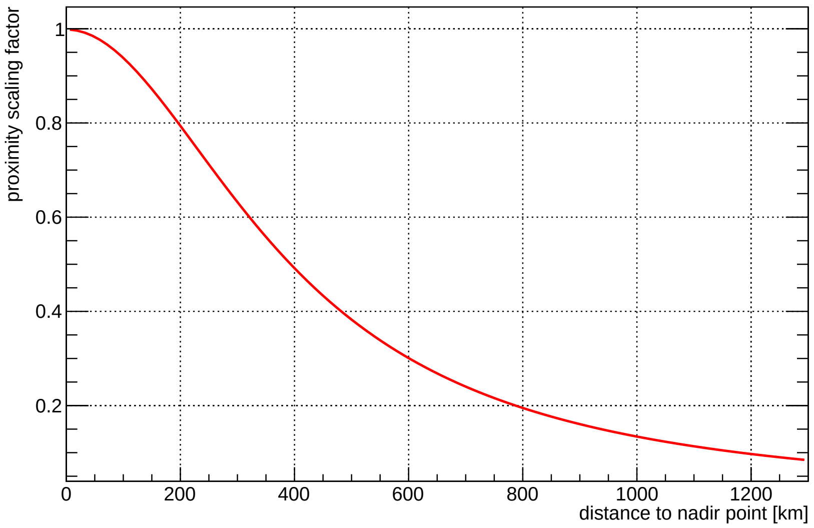

Figure 7.0.1: Proximity effect as function of the distance from the detector's nadir point. Normalized.

By their nature, all of the effects described above show an increased relevance with advancing radii within the FOV. Moreover, the negative impact is weighted even stronger, due to the fact that the air volume monitored in the outer regions is disproportionately high. This scenario suggests the best performance of the spatial resolution of the instrument for the nadir mode and a non-side-cut optics. If a high resolution space borne UHECR telescope with an exposure exceeding the one of a SpaceX EUSO type detector is desired, two possible strategies apply. Either the additional exposure would have to be accomplished by a longer mission duration or by deploying more than one detector into space. The latter solution would bear the advantage of a more sophisticated trigger scheme and the possibility of stereoscopic shower observation. This in turn would increase the angular resolution even more.

The studies presented in this dissertation can be improved in two aspects: the air shower simulation and the background treatment. All studies conducted made use of the SLAST event generator instead of a more sophisticated CONEX or even a full Montecarlo code such as CORSIKA. To meet constraints on computing time and en-

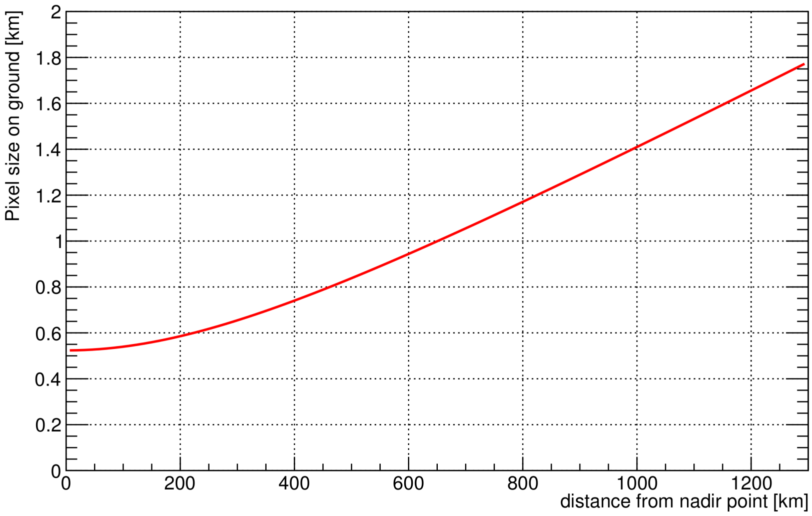

Figure 7.0.2: Pixel size projected on ground as function of the distance from the detector's nadir point.

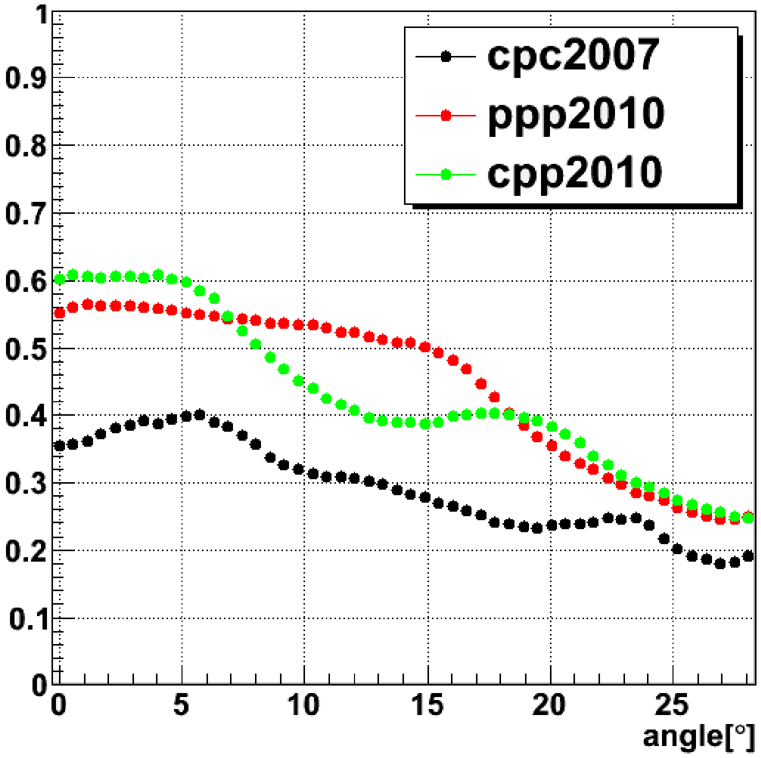

Figure 7.0.3: Optics throughput as function of the field angle. The plot additionally accounts for the focussing power by including only those photons that fall inside a bucket of 2.5 mm on the FS. 30° corresponds to the edge of the FOV. (~ 230 km from nadir point for JEM-EUSO, ~ 1200 km for the 40° tilted telescope.) The colours represent three different optics designs . Taken from [238].

able a high statistics of events, SLAST qualifies as the appropriate tool. Moreover, having limited ourselves to the exclusive simulation of proton events permitted this choice. At the same time, using a parametrized approach and solely protons as primaries, is certainly an immanent weakness of our studies. When we compare SLAST to CONEX generated showers, the most striking difference is the lack of random sampling of the first interaction. Thus, the SLAST showers develop always in the same atmospheric depth. The CONEX showers, on the contrary appear as randomly shifted in both directions. Another feature is the number of particles produced in the shower maximum. The CONEX showers show a maximum that is lower by about 10% compared to the SLAST events. Nevertheless, since the shape of the distribution is practically the same and the discrepancies are of the order of a few percent, we believe that the use of SLAST for this purpose is adequate. This is supported by Catalano et al. [82]. We expect the impact on the angular resolution to be minor. The current debate, whether the UHECR primaries detected so far are proton or heavier is not yet concluded. However, even for the case of heavier primaries, the angular resolution is not expected to be negatively affected.

The background treatment must still be regarded as preliminary. The value of 500 photons m^{-2} sr^{-1} ns^{-1} can be considered as a very reasonable approximation and in good agreement with results obtained by the Tatiana 2 satellite [109] and BABY[1] [160]. However, both setups have their own inadequacies. The BABY measurements for instance have been taken at altitudes of $\sim$ 30 to 40 km. The atmospheric night glow however originates from an altitude of about 100 km. Tatiana 2 is a real space based UV detector orbiting the earth. However, it is not equipped with any focussing optics and the position of the instrument has not always been clear due to an uncontrolled rolling of the instrument. Thus, at the moment our knowledge on the real UV atmospheric background to be expected from space is afflicted with uncertainties. The JEM-EUSO pathfinders will certainly contribute to our understanding of the background. The EUSO-Balloon, will perform a number of flight under different meteorological conditions and fly over different ground compositions. This will enable the JEM-EUSO collaboration to better determine the impact on the expected background from space. Mini-EUSO has the potential to measure the background, including the atmospheric night glow, exactly from the position of the future JEM-EUSO detector, using the same technology. It can therefore be regarded as a precious tool for a proper background es-

---

[1] BABY: BAckground BYpass, a balloon borne mission to measure the nocturnal UV background. Conducted by the AIRWATCH collaboration.

timation. The simulation studies of the future will definitely profit from these findings. The distribution of the background on the focal surface has been assumed as constant all over the focal surface. Due to the degrading optics efficiency towards the outer regions of the FOV, we can also expect the background to decrease here. Therefore the signal to noise ratio has been systematically overestimated and we expect the angular resolution to improve in the outer parts, once this effect has fully been taken into account. This also applies to the trigger efficiency. However, compared to the absolute number of signal photons, the impact of the signal to noise ratio can be considered as minor.

In general, the results presented in this work have to be regarded a conservative estimate. The main source of errors in the reconstruction process utilized in the studies presented here are the automatic fitting procedures. A total amount of $\sim 5 \cdot 10^5$ events have been generated and reconstructed. Once, real data from the JEM-EUSO mission will be available, the analysis will be conducted on an individual base — shower by shower. During the entire mission time, JEM-EUSO is expected to measure 1000 events. Thus, there are sufficient capacities to shift the emphasis from a fast and efficient event reconstruction to a careful analysis. This arguments applies even more to multiple scattering events.

7.1 PROSPECTS

The uncertainties of the current studies identified above demand for future studies addressing these issues. Prospective assessments of the expected angular reconstruction for an EUSO like detector will have to aim into two directions. First, to improve the details of the simulation and second, to upgrade the reconstruction algorithms further in order to enhance their precision.

A major step towards a more 'true-to-life' simulation will certainly include the transition from SLAST to CONEX showers to circumvent the justified critique, why an outdated and perhaps simplistic technique is used to simulate a future space mission. This can be accomplished in a rather straightforward manner, since all the necessary technical requirements have already been allocated. The designated interface to inject CONEX showers into the ESAF simulations is in a stable configuration. A database of CONEX showers has already been produced. Hence, this step can be regarded as a technical formality. However, it is not likely that this will have a significant impact on the overall picture. A second task will necessarily include a more sophisticated treatment of the background simulation. Being assumed as constant all over the FOV, as a first step, the background distribution needs to roughly feature a cosine distribution in order to reflect the optical transmittance of the lenses. Even if the implementation of the new background distribution itself is feasible in a relatively short period of time, the consequences will require further attention. For instance, the trigger algorithm will need to have an in-built focal surface map with a distribution of signal to noise ratios in dependence of the FS position. the same applies to the pattern recognition and in a wider sense also to the track reconstruction module. Implementing these proposed changes into the ESAF software will require an extensive approach and is not feasible in a short amount of time. However, the consequences might have a significant impact on the expected performance of the telescope. Especially the effect on the tilted mode is not trivial to approximate without dedicated simulations. Doubtlessly, the background related uncertainties of our estimates will severely decrease.

The multiple scattering of fluorescence light in the atmosphere has been neglected in many space based UHECR observatory studies in the past. Even though, in this work a multiple scattering approach has already been undertaken, this will have to be implemented for the tilted mode as well as for the SpaceX EUSO detector in future studies. The technical requirements are given and well understood. A limiting factor is certainly the computing time. Especially for the tilted mode which requires a far larger database of events, the use of dedicated computing resources is inevitable. However, this issue can be successfully addressed by an allocation of supercomputing facilities within the JEM-EUSO collaboration.

Apart from creating a more realistic setting for the virtual UHECR measurement, there is still room for improving the performance of the event reconstruction chain. This concerns the pattern recognition in order to cope with the multiple scattering scenario but also the angular reconstruction module itself. The extraction of the signal from background will have to account for the broadened tracks without loosing major fractions of the signal. This is necessarily a trade-off. On the one hand, the direction reconstruction in principle only needs the central axis of the signal track, neglecting its lateral expansion. Thus, the pattern recognition could be tuned in accordance, delivering only the very distinct and well-focussed centre part. On the other hand, this would be insufficient for the energy reconstruction which requires a precise light curve.

A second improvement concerns the angular reconstruction module itself. Currently, a starting point for the first angular reconstruction algorithm is the approximation of the altitude of the shower maximum H_{max}. This is achieved in a simplistic approach utilizing a parametrization of the atmosphere. The uncertainties in the H_{max} determination affect the reconstruction of the Θ direction to some extent, introducing systematic errors. H_{max} is determined to a higher precision at a later step — during the energy reconstruction procedure. A possible way to improve the Θ reconstruction is therefore a second iteration of the track direction module, this time after the energy reconstruction. It is even possible that the energy module, if applied for the second time after the repeated track direction module run, might profit from that.

7.2 PERSONAL ACHIEVEMENTS

In the course of the three year PhD-programme we have been involved in the assessment of different JEM-EUSO detector configurations and feasibility studies. The important milestones have been presented in this dissertation. All of them are the result of a collective effort in the context of the JEM-EUSO collaboration. Without the vital discussions during the frequent JEM-EUSO meetings and especially the designated JEM-EUSO simulation group meetings, these findings would have been unthinkable. The outcomes have also been presented at international conferences in form of poster presentations or oral contributions.

- International Cosmic Ray Conference, Beijing, 2011
- European Cosmic Ray Symposium, Moscow, 2012
- Annual Meeting of the Deutsche Physikalische Gesellschaft, Dresden, 2013
- International Cosmic Ray Conference, Rio de Janeiro, 2013

The participation to these conferences was made possible due to generous travel grants by the Deutsche Akademische Austauschdienst (DAAD), the Deutsche Physikalische Gesellschaft (DPG) and the Kepler Graduiertenkolleg of the University of Tübingen.

Being the first author or co-authoring, a number of articles has emerged from our research:

- "Performances of JEM-EUSO: angular reconstruction"; The JEM-EUSO collaboration, corresponding authors: S. Biktemerova, A. Guzman, T. Mernik. *Experimental Astronomy*, 2014 [62]
- "Performances and air-shower reconstruction techniques for the JEM-EUSO mission"; M. Bertaina, S. Biktemerova, K. Bittermann, P. Bobik, D. Campana,

F. Fenu, A. Gorgi, F. Guarino, A. Guzman, K. Higashide, G. Medina-Tanco, T. Mernik, D. Naumov, M. Putis, M. D. Rodriguez Frias, S. Toscano. *Journal for Advances in Space Research*, 2014 [56]

- "An evaluation of the exposure in nadir observation of the JEM-EUSO mission"; The JEM-EUSO collaboration. *Astroparticle Physics*, 2013 [7]
- "Performances of JEM-EUSO"; M. Bertaina, P. Bobik, F. Fenu, F. Garino, A. Guzman, K. Higashide, G. Medina Tanco, T. Mernik, G. Saez Cano, A. Santangelo and K. Shinozaki. *UHECR 2012 - International Symposium on Future Directions in UHECR Physics*, 2013 [55]
- "The Peak and Window Searching Technique for the EUSO Simulation and Analysis Framework: Impact on the angular reconstruction of EAS"; A. Guzman, T. Mernik, A. Santangelo, G. Medina-Tanco, M. Bertaina, K. Shinozaki, F. Fenu, A. Gorgi and the JEM-EUSO collaboration. *Journal of Physics*, 2013 [123]
- "ESAF-Simulation of the EUSO-Balloon"; T. Mernik, A. Guzman, A. Santangelo, K. Shinozaki, N. Sakaki, C. Moretto, D. Monnier-Ragaigne, H. Miyamoto, S. Dagoret-Campagne, C. Catalano, P. von Ballmooss for the JEM-EUSO Collaboration. *Proceedings of the International Cosmic Ray Conference*, 2013 [185]
- "Simulating the JEM-EUSO Mission: Expected Reconstruction Performance"; T. Mernik, A. Guzman, F. Fenu, K. Shinozaki, A. Santangelo, M. Bertaina for the JEM-EUSO collaboration. *Proceedings of the International Cosmic Ray Conference*, 2013 [184]
- "UV night background estimation in South Atlantic Anomaly"; P. Bobik, M. Putis, M. Bertaina, S. Biktemerova, D. Campana, F. Fenu, F. Guarino, K. Kudela, T. Mernik, B. Pastircak, K. Shinozaki for the JEM-EUSO collaboration. *Proceedings of the International Cosmic Ray Conference*, 2013 [69]
- "A study on JEM-EUSO's trigger probabillity for neutrino-initiated EAS"; A. Guzman, D. Supanitsky, E. Iwotschkin, T. Mernik, F. Fenu, G. Medina-Tanco, A. Santangelo for the JEM-EUSO collaboration. *Proceedings of the International Cosmic Ray Conference*, 2013 [248]
- "The JEM-EUSO Mission: Status and Prospects in 2011"; The JEM-EUSO collaboration. *Instrumentation and Methods for Astrophysics*, 2012 [261]

- “The ESAF-Reconstruction Framework of UHECR Events for the JEM-EUSO Mission”; T. Mernik, F. Fenu, D. D’Urso, A. Santangelo, K. Bittermann, K. Shinozaki, M. Bertaina, S. Biktemerova, D. Naumov, G. Medina-Tanco on behalf of the JEM-EUSO collaboration. *Proceedings of the International Cosmic Ray Conference*, 2011 [183]

- “The ESAF Simulation Framework for the JEM-EUSO Mission”; F. Fenu, T. Mernik, A. Santangelo, K. Shinozaki, M. Bertaina, L. Valore, S. Biktemerova, D. Naumov, G. Medina-Tanco on behalf of the JEM-EUSO collaboration. *Proceedings of the International Cosmic Ray Conference*, 2011 [101]

- “Estimation of aperture for extreme energy cosmic rays observation by JEM-EUSO Telescope”; K. Shinozaki, M. Bertaina, S. Biktemerova, P. Bobik, F. Fenu, A. Guzman, K. Higashide, G. Medina Tanco, T. Mernik, J. A. Morales de los Rios Pappa, D. Naumov. *Proceedings of the International Cosmic Ray Conference*, 2011 [239]

- “Requirement and expected performances of the JEM-EUSO mission”; M. Bertaina, A. Santangelo, K. Shinozaki, F. Fenu, T. Mernik, P. Bobik, F. Guarino, K. Higashide, G. Medina-Tanco, and G. Saez-Cano on behalf of the JEM-EUSO collaboration. *Proceedings of the International Cosmic Ray Conference*, 2011 [54]

Further co-authorships include: [67], [124], [102], [57], [247], [219], [265], [80], [118], [270], [87], [81], [58].

References

[1] M. G. Aartsen, R. Abbasi, Y. Abdou, M. Ackermann, J. Adams, J. A. Aguilar, M. Ahlers, D. Altmann, J. Auffenberg, X. Bai, et al. First Observation of PeV-Energy Neutrinos with IceCube. *Physical Review Letters*, 111(2):021103, July 2013. doi: 10.1103/PhysRevLett.111.021103.

[2] J. Abraham, M. Aglietta, I. C. Aguirre, M. Albrow, D. Allard, I. Allekotte, P. Allison, J. Alvarez Muñiz, M. G. Do Amaral, M. Ambrosio, et al. Properties and performance of the prototype instrument for the Pierre Auger Observatory. *Nuclear Instruments and Methods in Physics Research A*, 523:50–95, May 2004. doi: 10.1016/j.nima.2003.12.012.

[3] V. Abrashkin, V. Alexandrov, Y. Arakcheev, E. Bitkin, A. Cordero, S. Eremin, M. Finger, G. Garipov, V. Grebenyuk, N. Kalmykov, B. Khrenov, V. Koval, O. Martinez, A. Matyushkin, E. Moreno, D. Naumov, A. Olshevsky, M. Panasyuk, I. Park, C. Robledo, I. Rubinstein, S. Sharakin, A. Silaev, L. Tkatchev, V. Tulupov, R. Tyukaev, B. Sabirov, H. Salazar, O. Saprykin, V. Syromyatnikov, F. Urmantsev, L. Villasenor, I. Yashin, N. Zaikin, and A. Zepeda. The TUS space fluorescence detector for study of UHECR and other phenomena of variable fluorescence light in the atmosphere. *Advances in Space Research*, 37:1876–1883, 2006. doi: 10.1016/j.asr.2005.05.095.

[4] P. Abreu, M. Aglietta, E. J. Ahn, D. Allard, I. Allekotte, J. Allen, J. Alvarez Castillo, J. Alvarez-Muniz, M. Ambrosio, A. Aminaei, et al. Update on the correlation of the highest energy cosmic rays with nearby extragalactic matter. *Astroparticle Physics*, 34:314–326, 2010. doi: 10.1016/j.astropartphys.2010.08.010.

[5] T. Abu-Zayyad, R. Aida, M. Allen, R. Anderson, R. Azuma, E. Barcikowski, J. W. Belz, D. R. Bergman, S. A. Blake, R. Cady, B. G. Cheon, J. Chiba, M. Chikawa, E. J. Cho, W. R. Cho, H. Fujii, T. Fujii, T. Fukuda, M. Fukushima, W. Hanlon, K. Hayashi, Y. Hayashi, N. Hayashida, K. Hibino, K. Hiyama, K. Honda, T. Iguchi, D. Ikeda, K. Ikuta, N. Inoue, T. Ishii, R. Ishimori, D. Ivanov, S. Iwamoto, C. C. H. Jui, K. Kadota, F. Kakimoto, O. Kalashev, T. Kanbe, K. Kasahara, H. Kawai, S. Kawakami, S. Kawana, E. Kido, H. B. Kim, H. K. Kim, J. H. Kim, J. H. Kim, K. Kitamoto, S. Kitamura, Y. Kitamura, K. Kobayashi, Y. Kobayashi, Y. Kondo, K. Kuramoto, V. Kuzmin, Y. J. Kwon, S. I. Lim, S. Machida, K. Martens, J. Martineau, T. Matsuda, T. Matsuura, T. Matsuyama,

J. N. Matthews, M. Minamino, K. Miyata, Y. Murano, I. Myers, K. Nagasawa, S. Nagataki, T. Nakamura, S. W. Nam, T. Nonaka, S. Ogio, M. Ohnishi, H. Ohoka, K. Oki, D. Oku, T. Okuda, A. Oshima, S. Ozawa, I. H. Park, M. S. Pshirkov, D. C. Rodriguez, S. Y. Roh, G. Rubtsov, D. Ryu, H. Sagawa, N. Sakurai, A. L. Sampson, L. M. Scott, P. D. Shah, F. Shibata, T. Shibata, H. Shimodaira, B. K. Shin, J. I. Shin, T. Shirahama, J. D. Smith, P. Sokolsky, T. J. Sonley, R. W. Springer, B. T. Stokes, S. R. Stratton, T. Stroman, S. Suzuki, Y. Takahashi, M. Takeda, A. Taketa, M. Takita, Y. Tameda, H. Tanaka, K. Tanaka, M. Tanaka, S. B. Thomas, G. B. Thomson, P. Tinyakov, I. Tkachev, H. Tokuno, T. Tomida, S. Troitsky, Y. Tsunesada, K. Tsutsumi, Y. Tsuyuguchi, Y. Uchihori, S. Udo, H. Ukai, G. Vasiloff, Y. Wada, T. Wong, M. Wood, Y. Yamakawa, R. Yamane, H. Yamaoka, K. Yamazaki, J. Yang, Y. Yoneda, S. Yoshida, H. Yoshii, X. Zhou, R. Zollinger, and Z. Zundel. Search for Anisotropy of Ultrahigh Energy Cosmic Rays with the Telescope Array Experiment. *The Astrophysical Journal*, 757: 26, September 2012. doi: 10.1088/0004-637X/757/1/26.

[6] M. Ackermann, M. Ajello, A. Allafort, L. Baldini, J. Ballet, G. Barbiellini, M. G. Baring, D. Bastieri, K. Bechtol, R. Bellazzini, R. D. Blandford, E. D. Bloom, E. Bonamente, A. W. Borgland, E. Bottacini, T. J. Brandt, J. Bregeon, M. Brigida, P. Bruel, R. Buehler, G. Busetto, S. Buson, G. A. Caliandro, R. A. Cameron, P. A. Caraveo, J. M. Casandjian, C. Cecchi, Ö. Çelik, E. Charles, S. Chaty, R. C. G. Chaves, A. Chekhtman, C. C. Cheung, J. Chiang, G. Chiaro, A. N. Cillis, S. Ciprini, R. Claus, J. Cohen-Tanugi, L. R. Cominsky, J. Conrad, S. Corbel, S. Cutini, F. D'Ammando, A. de Angelis, F. de Palma, C. D. Dermer, E. do Couto e Silva, P. S. Drell, A. Drlica-Wagner, L. Falletti, C. Favuzzi, E. C. Ferrara, A. Franckowiak, Y. Fukazawa, S. Funk, P. Fusco, F. Gargano, S. Germani, N. Giglietto, P. Giommi, F. Giordano, M. Giroletti, T. Glanzman, G. Godfrey, I. A. Grenier, M.-H. Grondin, J. E. Grove, S. Guiriec, D. Hadasch, Y. Hanabata, A. K. Harding, M. Hayashida, K. Hayashi, E. Hays, J. W. Hewitt, A. B. Hill, R. E. Hughes, M. S. Jackson, T. Jogler, G. Jóhannesson, A. S. Johnson, T. Kamae, J. Kataoka, J. Katsuta, J. Knödlseder, M. Kuss, J. Lande, S. Larsson, L. Latronico, M. Lemoine-Goumard, F. Longo, F. Loparco, M. N. Lovellette, P. Lubrano, G. M. Madejski, F. Massaro, M. Mayer, M. N. Mazziotta, J. E. McEnery, J. Mehault, P. F. Michelson, R. P. Mignani, W. Mitthumsiri, T. Mizuno, A. A. Moiseev, M. E. Monzani, A. Morselli, I. V. Moskalenko, S. Murgia, T. Nakamori, R. Nemmen, E. Nuss, M. Ohno, T. Ohsugi, N. Omodei, M. Orienti, E. Orlando, J. F. Ormes, D. Paneque, J. S. Perkins, M. Pesce-Rollins, F. Piron, G. Pivato, S. Rainò, R. Rando, M. Razzano, S. Razzaque, A. Reimer, O. Reimer, S. Ritz, C. Romoli, M. Sánchez-Conde, A. Schulz, C. Sgrò, P. E. Simeon, E. J. Siskind, D. A. Smith, G. Spandre, P. Spinelli, F. W. Stecker, A. W. Strong, D. J. Suson, H. Tajima, H. Takahashi, T. Takahashi, T. Tanaka, J. G. Thayer, J. B. Thayer, D. J. Thompson, S. E. Thorsett, L. Tibaldo, O. Tibolla, M. Tinivella, E. Troja, Y. Uchiyama, T. L. Usher, J. Vandenbroucke,

V. Vasileiou, G. Vianello, V. Vitale, A. P. Waite, M. Werner, B. L. Winer, K. S. Wood, M. Wood, R. Yamazaki, Z. Yang, and S. Zimmer. Detection of the Characteristic Pion-Decay Signature in Supernova Remnants. *Science*, 339:807–811, February 2013. doi: 10.1126/science.1231160.

[7] J. H. Adams, S. Ahmad, J.-N. Albert, D. Allard, M. Ambrosio, L. Anchordoqui, A. Anzalone, Y. Arai, C. Aramo, K. Asano, et al. An evaluation of the exposure in nadir observation of the JEM-EUSO mission. *Astroparticle Physics*, 44:76–90, April 2013. doi: 10.1016/j.astropartphys.2013.01.008.

[8] J. H. Adams, Jr, M. J. Christl, S. E. Csorna, F. Sarazin, and L. R. Wiencke. Ground Truth calibration for the JEM-EUSO Mission. *ArXiv e-prints*, February 2013.

[9] J.H. Adams Jr., R.M. Young, A. Olinto, et al. JEM-EUSO Design for Accomodation on the SpaceX Dragon Spacecraft. In *Proceedings of the International Cosmic Ray Conference*, International Cosmic Ray Conference Rio de Janeiro, Brazil, 2013.

[10] M. Aguilar, G. Alberti, B. Alpat, A. Alvino, G. Ambrosi, K. Andeen, H. Anderhub, L. Arruda, P. Azzarello, A. Bachlechner, et al. First Result from the Alpha Magnetic Spectrometer on the International Space Station: Precision Measurement of the Positron Fraction in Primary Cosmic Rays of 0.5-350 GeV. *Physical Review Letters*, 110(14):141102, April 2013. doi: 10.1103/PhysRevLett.110.141102.

[11] E.-J. Ahn, R. Engel, T. K. Gaisser, P. Lipari, and T. Stanev. Cosmic ray interaction event generator SIBYLL 2.1. *Physical Review D*, 80(9):094003, November 2009. doi: 10.1103/PhysRevD.80.094003.

[12] M. Alekseeva, T. Bergmann, V. Chernatkin, R. Engel, D. Heck, N. Kalmykov, S. Ostapchenko, T. Pierog, and K. Werner. Extensive Air Shower Simulation Program CONEX: Matching Monte Carlo and Numerical Methods. *Proceedings of the International Cosmic Ray Conference*, 7:139, 2005.

[13] D. Allard, E. Parizot, A. V. Olinto, E. Khan, and S. Goriely. UHE nuclei propagation and the interpretation of the ankle in the cosmic-ray spectrum. *Astronomy and Astrophysics*, 443:L29–L32, December 2005. doi: 10.1051/0004-6361:200500199.

[14] D. Allard, A. V. Olinto, and E. Parizot. Signatures of the extragalactic cosmic-ray source composition from spectrum and shower depth measurements. *Astronomy and Astrophysics*, 473:59–66, October 2007. doi: 10.1051/0004-6361:20077478.

[15] D. Allard, E. Parizot, and A. V. Olinto. On the transition from galactic to extragalactic cosmic-rays: Spectral and composition features from two opposite scenarios. *Astroparticle Physics*, 27:61–75, February 2007. doi: 10.1016/j.astropartphys.2006.09.006.

[16] J. Allen, A. Castellina, R. Engel, K. Kasahara, S. Knurenko, T. Pierog, A. Sabourov, B. T. Stokes, R. Ulrich, T. Sako, and S. Ostapchenko. Air shower simulation and hadronic interactions. *EPJ Web of Conferences*, 53:01007, 2013. doi: 10.1051/epjconf/20135301007. URL `http://dx.doi.org/10.1051/epjconf/20135301007`.

[17] R. Aloisio. The DIP model in Ultra High Energy Cosmic Ray Physics. *Searching for the Origins of Cosmic Rays, Trondheim Norway*, June 2009. Online; accessed 21-February-2014.

[18] R. Aloisio. Ultra high energy particles propagation and the transition from galactic to extra-galactic cosmic rays. *EPJ Web of Conferences*, 53:06001, 2013. doi: 10.1051/epjconf/20135306001. URL `http://dx.doi.org/10.1051/epjconf/20135306001`.

[19] R. Aloisio, V. Berezinsky, P. Blasi, A. Gazizov, S. Grigorieva, and B. Hnatyk. A dip in the UHECR spectrum and the transition from galactic to extragalactic cosmic rays. *Astroparticle Physics*, 27:76–91, February 2007. doi: 10.1016/j.astropartphys.2006.09.004.

[20] R. Aloisio, V. Berezinsky, and A. Gazizov. Ultra high energy cosmic rays: The disappointing model. *Astroparticle Physics*, 34:620–626, March 2011. doi: 10.1016/j.astropartphys.2010.12.008.

[21] R. Aloisio, V. Berezinsky, and A. Gazizov. Disappointing model for ultrahigh-energy cosmic rays. *Journal of Physics Conference Series*, 337(1):012042, February 2012. doi: 10.1088/1742-6596/337/1/012042.

[22] R. Aloisio, V. Berezinsky, and S. Grigorieva. Analytic calculations of the spectra of ultra-high energy cosmic ray nuclei. I. The case of CMB radiation. *Astroparticle Physics*, 41:73–93, January 2013. doi: 10.1016/j.astropartphys.2012.07.010.

[23] J. Alvarez-Muñiz, M. Risse, G.I. Rubtsov, and B.T. Stokes. Review of the multimessenger working group at uhecr-2012. *EPJ Web of Conferences*, 53:01009, 2013. doi: 10.1051/epjconf/20135301009. URL `http://dx.doi.org/10.1051/epjconf/20135301009`.

[24] G. P. Anderson, J. Wang, M. L. Hoke, F. X. Kneizys, J. H. Chetwynd, L. S. Rothman, L. M. Kimball, R. A. McClatchey, E. P. Shettle, S. A. Clough, W. O. Gallery, L. W. Abreu, and J. E. Selby. History of one family of atmospheric radiative transfer codes. In D. K. Lynch, editor, *Passive Infrared Remote Sensing*

of Clouds and the Atmosphere II, volume 2309 of *Society of Photo-Optical Instrumentation Engineers (SPIE) Conference Series*, pages 170–183, December 1994.

[25] M. Arcani, C. Guaita, and A. Paganoni. VHANESSA expedition. *Astroparticle Physics*, 2013. ISSN 0927-6505. doi: 10.1016/j.astropartphys.2013.03.005. URL http://www.sciencedirect.com/science/article/pii/S0927650513000583.

[26] P. Auger, P. Ehrenfest, R. Maze, J. Daudin, and R. A. Fréon. Extensive Cosmic-Ray Showers. *Reviews of Modern Physics*, 11:288–291, July 1939. doi: 10.1103/RevModPhys.11.288.

[27] Unknown Author. Cosmic String. *Memory Alpha - The Star Trek Wiki*, January 2014. URL http://en.memory-alpha.org/wiki/Cosmic_string. Online; accessed 28-January-2013.

[28] R. M. Baltrusaitis, R. Cady, G. L. Cassiday, R. Cooperv, J. W. Elbert, P. R. Gerhardy, S. Ko, E. C. Loh, M. Salamon, D. Steck, and P. Sokolsky. The Utah Fly's Eye detector. *Nuclear Instruments and Methods in Physics Research A*, 240:410–428, October 1985. doi: 10.1016/0168-9002(85)90658-8.

[29] R. M. Baltrusaitis, G. L. Cassiday, R. Cooper, B. R. Dawson, J. W. Elbert, B. Fick, P. R. Gerhardy, S. Ko, D. F. Liebing, E. C. Loh, Y. Mizumoto, D. Steck, P. Sokolsky, and M. Ye. Measurement of the angular distribution of Cerenkov light in ultra-high-energy extensive air showers. *Journal of Physics G Nuclear Physics*, 13:115–119, January 1987. doi: 10.1088/0305-4616/13/1/013.

[30] E. Barcikowski, J. Bellido, J. Belz, Y. Egorov, S. Knurenko, V. de Souza, Y. Tameda, Y. Tsunesada, and M. Unger. Mass composition working group report. *EPJ Web of Conferences*, 53:01006, 2013. doi: 10.1051/epjconf/20135301006. URL http://dx.doi.org/10.1051/epjconf/20135301006.

[31] S. A. Bass, M. Belkacem, M. Bleicher, M. Brandstetter, L. Bravina, C. Ernst, L. Gerland, M. Hofmann, S. Hofmann, J. Konopka, G. Mao, L. Neise, S. Soff, C. Spieles, H. Weber, L. A. Winckelmann, H. Stöcker, W. Greiner, C. Hartnack, J. Aichelin, and N. Amelin. Microscopic models for ultrarelativistic heavy ion collisions. *Progress in Particle and Nuclear Physics*, 41:255–369, 1998. doi: 10.1016/S0146-6410(98)00058-1.

[32] J. Bayer, M. Bertaina, G. Distratis, F. Fenu, A. Santangelo, T. Schanz, C. Tenzer, and the JEM-EUSO Collaboration. The Cluster Control Board of the JEM-EUSO mission. *Proceedings of the International Cosmic Ray Conference*, 3:168, 2011.

[33] J. Bayer, G. Distratis, D. Gottschall, A. Santangelo, C. Tenzer, M. Bertaina, M. Casolino, G. Osteria, and the JEM-EUSO Collaboration. Second level trigger and Cluster Control Board for the JEM-EUSO mission. In *Proceedings of*

the International Cosmic Ray Conference, International Cosmic Ray Conference Rio de Janeiro, Brazil, 2013.

[34] A.R. Bell. The acceleration of cosmic rays in shock fronts. I. *Monthly Notices of the RAS*, 182:147–156, January 1978.

[35] A.R. Bell. The acceleration of cosmic rays in shock fronts. II. *Monthly Notices of the RAS*, 182:443–455, February 1978.

[36] R. Benson and J. Linsley. Satellite Observation of Cosmic-Ray Air Showers. In *Bulletin of the American Astronomical Society*, volume 12 of *Bulletin of the American Astronomical Society*, page 818, September 1980.

[37] R. Benson and J. Linsley. Satellite observation of cosmic ray air showers. *Proceedings of the International Cosmic Ray Conference*, 8:145–148, 1981.

[38] C. Berat, S. Bottai, D. De Marco, S. Moreggia, D. Naumov, M. Pallavicini, R. Pesce, A. Petrolini, A. Stutz, E. Taddei, and A. Thea. Full simulation of space-based extensive air showers detectors with ESAF. *Astroparticle Physics*, 33:221–247, May 2010. doi: 10.1016/j.astropartphys.2010.02.005.

[39] V. S. Beresinsky and G. T. Zatsepin. Cosmic rays at ultra high energies (neutrino?). *Physics Letters B*, 28:423–424, January 1969. doi: 10.1016/0370-2693(69)90341-4.

[40] V. Berezinsky. Ultra high energy cosmic rays. *Nuclear Physics B Proceedings Supplements*, 70:419–430, January 1999. doi: 10.1016/S0920-5632(98)00463-0.

[41] V. Berezinsky. Origin of ultra high energy cosmic rays. In *36th COSPAR Scientific Assembly*, volume 36 of *COSPAR Meeting*, page 1002, 2006.

[42] V. Berezinsky. UHE neutrinos: From conventional to new physics. *Nuclear Instruments and Methods in Physics Research A*, 604:92, June 2009. doi: 10.1016/j.nima.2009.03.038.

[43] V. Berezinsky. Uhecr: Signatures and models. *EPJ Web of Conferences*, 53:01003, 2013. doi: 10.1051/epjconf/20135301003. URL `http://dx.doi.org/10.1051/epjconf/20135301003`.

[44] V. Berezinsky and A. Vilenkin. Cosmic Necklaces and Ultrahigh Energy Cosmic Rays. *Physical Review Letters*, 79:5202–5205, December 1997. doi: 10.1103/PhysRevLett.79.5202.

[45] V. Berezinsky, M. Kachelriess, and A. Vilenkin. Ultra-high energy cosmic rays from decaying relic particles. *Nuclear Physics B Proceedings Supplements*, 70:500–502, January 1999. doi: 10.1016/S0920-5632(98)00482-4.

[46] V. Berezinsky, A. Gazizov, and S. Grigorieva. On astrophysical solution to ultrahigh energy cosmic rays. *Physical Review D*, 74(4):043005, August 2006. doi: 10.1103/PhysRevD.74.043005.

[47] D. R. Bergman. UHECR Composition Measurements Using the HiRes-II Detector. *Proceedings of the International Cosmic Ray Conference*, 7:311, 2005.

[48] D. R. Bergman. Hires and ta spectrum measurements. *EPJ Web of Conferences*, 53:04001, 2013. doi: 10.1051/epjconf/20135304001. URL `http://dx.doi.org/10.1051/epjconf/20135304001`.

[49] L. Bergmann and C. Schaefer. *Lehrbuch der Experimentalphysik — Elektromagnetismus*, volume 2. Walter de Gruyter, Berlin New York, eightth edition, 2002.

[50] T. Bergmann, R. Engel, D. Heck, N. N. Kalmykov, S. Ostapchenko, T. Pierog, T. Thouw, and K. Werner. One-dimensional hybrid approach to extensive air shower simulation. *Astroparticle Physics*, 26:420–432, January 2007. doi: 10.1016/j.astropartphys.2006.08.005.

[51] L. Bergström and A. Goobar. *Cosmology and Particle Astrophysics*. Springer Berlin Heidelberg, Jointly published with Praxis Publishing, UK, second edition, 2004. doi: 10.1007/3-540-37719-0.

[52] M. Bertaina. Some facts about Mini-EUSO. *Private Communication*, January 2014.

[53] M. Bertaina and the JEM-EUSO Collaboration. The JEM-EUSO Mission. *Nuclear Physics B Proceedings Supplements*, 190:300–307, May 2009. doi: 10.1016/j.nuclphysbps.2009.03.103.

[54] M. Bertaina, A. Santangelo, K. Shinozaki, F. Fenu, T. Mernik, P. Bobik, F. Guarino, K. Higashide, G. Medina-Tanco, G. Saez-Cano, and the JEM-EUSO Collaboration. Requirement and expected performances of the JEM-EUSO mission. *Proceedings of the International Cosmic Ray Conference*, 3:219, 2011.

[55] M. Bertaina, P. Bobik, F. Fenu, F. Garino, A. Guzman, K. Higashide, G. Medina-Tanco, T. Mernik, G. Saez Cano, A. Santangelo, and K. Shinozaki. Performances of jem-euso. *EPJ Web of Conferences*, 53:09002, 2013. doi: 10.1051/epjconf/20135309002. URL `http://dx.doi.org/10.1051/epjconf/20135309002`.

[56] M. Bertaina, S. Biktemerova, K. Bittermann, P. Bobik, D. Campana, F. Fenu, A. Gorgi, F. Guarino, A. Guzmán, K. Higashide, G. Medina-Tanco, T. Mernik, D. Naumov, M. Putis, M. D. Rodríguez Frías, G. Sáez Cano, A. Santangelo, K. Shinozaki, and S. Toscano. Performance and air-shower reconstruction techniques for the JEM-EUSO mission. *Advances in Space Research*, 53:1515–1535, May 2014. doi: 10.1016/j.asr.2014.02.018.

[57] M. Bertaina, P. Bobik, F. Fenu, K. Shinozaki, and the JEM-EUSO Collaboration. JEM-EUSO observational technique and exposure. *Experimental Astronomy*, March 2014. doi: 10.1007/s10686-014-9376-3.

[58] M. Bertaina, A. Cellino, and F. Ronga. JEM-EUSO: Meteor and nuclearite observations. *Experimental Astronomy*, April 2014. doi: 10.1007/s10686-014-9375-4.

[59] H. Bethe and W. Heitler. On the Stopping of Fast Particles and on the Creation of Positive Electrons. *Royal Society of London Proceedings Series A*, 146:83–112, August 1934. doi: 10.1098/rspa.1934.0140.

[60] P. L. Biermann and G. Sigl. Introduction to Cosmic Rays. In M. Lemoine and G. Sigl, editors, *Physics and Astrophysics of Ultra-High-Energy Cosmic Rays*, volume 576 of *Lecture Notes in Physics, Berlin Springer Verlag*, page 1, 2001.

[61] S. Biktemerova, M. Gonchar, S. Sharakin, and the JEM-EUSO-Collaboration. Pattern Recognition and direction reconstruction for the JEM-EUSO experiment. In *Proceedings of the International Cosmic Ray Conference*, International Cosmic Ray Conference Rio de Janeiro, Brazil, 2013.

[62] S. Biktemerova, A. Guzman, T. Mernik, and the JEM-EUSO Collaboration. Performances of JEM-EUSO: angular reconstruction - The JEM-EUSO Collaboration. *Experimental Astronomy*, February 2014. doi: 10.1007/s10686-013-9371-0.

[63] P. Billoir. Phenomenology of Ultra-High-Energy Atmospheric Showers. In M. Lemoine and G. Sigl, editors, *Physics and Astrophysics of Ultra-High-Energy Cosmic Rays*, volume 576 of *Lecture Notes in Physics, Berlin Springer Verlag*, page 27, 2001.

[64] K. Bittermann. Studies on detection of neutrinos from space, the capabilities of jem-euso. Diploma thesis, Eberhard Karls Universität Tübingen, Institut für Astronomie und Astrophysik, Germany, June 2010.

[65] R. D. Blandford and J. P. Ostriker. Particle acceleration by astrophysical shocks. *Astrophysical Journal, Letters*, 221:L29–L32, April 1978. doi: 10.1086/182658.

[66] R. D. Blandford and R. L. Znajek. Electromagnetic extraction of energy from Kerr black holes. *Monthly Notices of the RAS*, 179:433–456, May 1977.

[67] J. Blecki, G. K. Garipov, P. Klimov, and the JEM-EUSO Collaboration. Science of atmospheric phenomena with JEM-EUSO. *Submitted to Experimental Astronomy*, December 2014.

[68] M. Bleicher, E. Zabrodin, C. Spieles, S. A. Bass, C. Ernst, S. Soff, L. Bravina, M. Belkacem, H. Weber, H. Stöcker, and W. Greiner. Relativistic hadron-hadron collisions in the ultra-relativistic quantum molecular dynamics model. *Journal of Physics G Nuclear Physics*, 25:1859–1896, September 1999. doi: 10.1088/0954-3899/25/9/308.

[69] P. Bobik, M. Putis, M. Bertaina, S. Biktemerova, D. Campana, F. Fenu, F. Guarino, K. Kudela, T. Mernik, B. Pastircak, K. Shinozaki, and the JEM-EUSO Collaboration. UV night background estimation in South Atlantic Anomaly. In *Proceedings of the International Cosmic Ray Conference*, International Cosmic Ray Conference Rio de Janeiro, Brazil, 2013.

[70] S. Bottai. Some algorithms for the direction reconstruction in euso and optimization of pixel size. *EUSO Technical Report*, 2003.

[71] S. Bottai and M. Tognetti. Proton and neutrino simulation with unisim. *EUSO Technical Report*, 2001.

[72] S. Bottai, G. D'Alì Staiti, M. C. Maccarone, and T. Mineo. Simulation and Data Analysis for EUSO. In *Proceedings of the International Cosmic Ray Conference*, volume 2 of *International Cosmic Ray Conference*, pages 943–946, July 2003.

[73] B. Breisky. On Its Centenary, Celebrating a Ride That Advanced Physics. *New York Times Online*, August 2012. URL http://www.nytimes.com/2012/08/07/science/space/when-victor-hess-discovered-cosmic-rays-in-a-hydrogen-\balloon.html?_r=0. Online; accessed 20-July-2014.

[74] B. Breisky. Quick Facts about SpaceX. *SpaceX Homepage*, March 2014. URL http://www.spacex.com/about. Online; accessed 6-March-2014.

[75] R. Brun and F. Rademakers. ROOT - An object oriented data analysis framework. *Nuclear Instruments and Methods in Physics Research A*, 389:81–86, February 1997. doi: 10.1016/S0168-9002(97)00048-X.

[76] J. N. Capdevielle, F. Cohen, C. Le Gall, J. Gawin, I. Kurp, B. Szabelska, J. Szabelski, and T. Wibig. Primary energy determination of UHE events from published Volcano Ranch, Yakutsk and AGASA data. *Proceedings of the International Cosmic Ray Conference*, 2:479, 2001.

[77] J. N. Capdevielle, F. Cohen, C. Le Gall, J. Gawin, I. Kurp, B. Szabelska, J. Szabelski, and T. Wibig. The hypergeometric formalism for the lateral distributions of charged particles in EAS. *Proceedings of the International Cosmic Ray Conference*, 2:503, 2001.

[78] M. Casolino. Revised configuration of jem-euso instrument. Presentation, June 2013.

[79] M. Casolino, T. Fujii, D. Ikeda, Y. Tameda, T. Shibata, H. Sagawa, M. Fukushima, J.N. Matthews, G.B. Thomson, M. Takeda, S. Ogio, Y. Tsunesada, T. Tomida, J. Belz, and P. Sokolsky. Calibration and testing of a prototype of the jem-euso telescope on telescope array site. *EPJ Web of Conferences*, 53:09005, 2013. doi: 10.1051/epjconf/20135309005. URL http://dx.doi.org/10.1051/epjconf/20135309005.

[80] M. Casolino, T. Ebisuzaki, M. Fukushima, F. Kajino, Y. Kawasaki, S. Ogio, L. W.. Piotrowski, H. Sagawa, M. Takeda, Y. Takizawa, T. Tomida, and the JEM-EUSO Collaboration. The Ground-based Test of JEM-EUSO at Telescope Array Site — TA-EUSO. *Submitted to Experimental Astronomy*, May 2014.

[81] M. Casolino, F. Kajino, and the JEM-EUSO Collaboration. An Overview of the JEM-EUSO Instrument. *Submitted to Experimental Astronomy*, May 2014.

[82] O. Catalano, G. D'Ali Staiti, M. Gabriele, and L. La Fata. The longitudinal EAS profile at $E > 10^{19}$eV: A comparison between GIL analytical formula and the predictions of detailed Montecarlo simulations. In *Proceedings of the International Cosmic Ray Conference*, volume 2 of *International Cosmic Ray Conference*, page 498, 2001.

[83] A. Cellino, A. Dell'Oro, and M. Bertaina. The planned JEM-EUSO mission and applications to meteor observation.. *Memorie della Societa Astronomica Italiana Supplementi*, 20:35, 2012.

[84] R. Chadysiene and A. Girgzdys. Ultraviolet Radiation Albedo of Natural Surfaces. *Journal of Environmental Engineering and Landscape Management*, 16:83–88, February 2008. URL http://dspace.vgtu.lt/jspui/bitstream/1/327/1/JEELM_ISSN_1648-6897_Vol16_No2_2008_83-88_Chadysiene.pdf.

[85] N. Chiba, K. Hashimoto, N. Hayashida, K. Honda, M. Honda, N. Inoue, F. Kakimoto, K. Kamata, S. Kawaguchi, N. Kawasumi, Y. Matsubara, K. Murakami, M. Nagano, S. Ogio, H. Ohoka, T. Saito, Y. Sakuma, I. Tsushima, M. Teshima, T. Umezawa, S. Yoshida, and H. Yoshii. Akeno Giant Air Shower Array (AGASA) covering 100 km ^{2} area. *Nuclear Instruments and Methods in Physics Research A*, 311:338–349, January 1992. doi: 10.1016/0168-9002(92)90882-5.

[86] The Pierre Auger Collaboration. Pierre Auger Observatory — Southern Site Technical Information. *Website of the Pierre Auger Collaboration*, April 2014. URL http://www.auger.org.ar/survey/surveyindex.shtml. Online; accessed 26-April-2014.

[87] S. Dagoret, P. Barillon, A. Jung, A. Ebersoldt, and the JEM-EUSO Collaboration. The Photodetector Module of the JEM-EUSO Mission. *Submitted to Experimental Astronomy*, June 2014.

[88] A. De Angelis. Domenico Pacini, uncredited pioneer of the discovery of cosmic rays. *ArXiv e-prints*, March 2011.

[89] C. De Donato and G. A. Medina-Tanco. Experimental constraints on the astrophysical interpretation of the cosmic ray Galactic-extragalactic transition region. *Astroparticle Physics*, 32:253–268, December 2009. doi: 10.1016/j.astropartphys.2009.09.004.

[90] o. Deligny, J. de Mello Neto, P. Sommers, H. Sagawa, P. Tinyakov, I. Tkachev, A. lvanov, L. T. f. t. P. Auger, T. Array, and Yakutsk Collaborations. Review of the anisotropy working group at UHECR-2012. *ArXiv e-prints*, June 2013.

[91] C. D. Dermer and S. Razzaque. Acceleration of Ultra-high-energy Cosmic Rays in the Colliding Shells of Blazars and Gamma-ray Bursts: Constraints from the Fermi Gamma-ray Space Telescope. *The Astrophysical Journal*, 724:1366–1372, December 2010. doi: 10.1088/0004-637X/724/2/1366.

[92] C. D. Dermer, S. Razzaque, J. D. Finke, and A. Atoyan. Ultra-high-energy cosmic rays from black hole jets of radio galaxies. *New Journal of Physics*, 11(6): 065016, June 2009. doi: 10.1088/1367-2630/11/6/065016.

[93] T. Ebisuzaki. Space-based observation of the extensive airshowers. *EPJ Web of Conferences*, 53:01014, 2013. doi: 10.1051/epjconf/20135301014. URL http://dx.doi.org/10.1051/epjconf/20135301014.

[94] T. Ebisuzaki, Y. Uehara, H. Ohmori, K. Kawai, Y. Kawasaki, M. Sato, Y. Takizawa, M. E. Bertaina, F. Kajino, T. Sawabe, K. Inoue, A. Sasaki, M. Sakata, Y. Yamamoto, M. Nagano, N. Inoue, T. Shibata, N. Sakaki, Y. Uchihori, Y. Takahashi, H. Shimizu, Y. Arai, Y. Kurihara, H. Fujimoto, S. Yoshida, Y. Mizumoto, S. Inoue, K. Asano, T. Sugiyama, J. Watanabe, H. Ikeda, M. Suzuki, T. Imamura, H. Yano, T. Murakami, D. Yonetoku, Y. Itow, M. Taguchi, M. Nagata, S. Nagataki, S. Abe, T. Tajima, J. H. Adams, S. Mitchell, M. J. Christl, J. Watts, A. English, Y. Takahashi, K. Pitalo, J. Hadaway, J. Geary, P. Readon, H. Crawford, C. Pennypacker, K. Arisaka, D. Cline, P. Gorodetsky, P. Salin, T. Patzark, A. Maurissen, and M. Valentin. The JEM-EUSO Project: Observing Extremely High Energy Cosmic Rays and Neutrinos from the International Space Station. *Nuclear Physics B Proceedings Supplements*, 175:237–240, January 2008. doi: 10.1016/j.nuclphysbps.2007.11.005.

[95] J. W. Elbert and P. Sommers. In search of a source for the 320 EeV Fly's Eye cosmic ray. *The Astrophysical Journal*, 441:151–161, March 1995. doi: 10.1086/175345.

[96] J. W. Elbert, T. Stanev, and S. Torii. Geomagnetic effects in electromagnetic cascades. *Proceedings of the International Cosmic Ray Conference*, 6:227–230, August 1983.

[97] F. Fenu. A simulation study of space based missions for ultra high energy cosmic ray search. Diploma thesis, Eberhard Karls Universität Tübingen, Institut für Astronomie und Astrophysik, Germany, October 2008.

[98] F. Fenu. Pmttoshowerreco software module, 2013. URL `svn+ssh://svn.in2p3.fr/esaf/trunk/esaf/packages/reconstruction/modules/shower/energy/src/PmtToShowerReco.cc`.

[99] F. Fenu. *A Simulation Study of the JEM–EUSO Mission for the Detection of Ultra–High Energy Cosmic Rays*. PhD thesis, Eberhard Karls Universität Tübingen, Institut für Astronomie und Astrophysik, 2013.

[100] F. Fenu, A. Santangelo, T. Mernik, K. Shinozaki, D. Naumov, S. Dagoret-Campagne, G. Medina-Tanco, D. Supanitsky, H. Miyamoto, J. Szabelski, and the JEM-EUSO Collaboration. The ESAF Simulation Framework for the JEM-EUSO Mission. In *Proceedings of the International Cosmic Ray Conference*, International Cosmic Ray Conference, 2009.

[101] F. Fenu, T. Mernik, A. Santangelo, K. Shinozaki, M. Bertaina, L. Valore, S. Biktemerova, D. Naumov, G. Medina-Tanco, and the JEM-EUSO Collaboration. The ESAF Simulation Framework for the JEM-EUSO Mission. In *Proceedings of the International Cosmic Ray Conference*, International Cosmic Ray Conference, 2011.

[102] F. Fenu, D. Naumov, M. Unger, and the JEM-EUSO Collaboration. Performances of JEM-EUSO: Energy Resolution. *submitted to Experimental Astronomy*, June 2014.

[103] H. Fesefeldt. The Simulation of Hadronic Showers: Physics and Applications. *Technical Report PITHA 85-02*, 1985.

[104] S. E. Forbush. Three Unusual Cosmic-Ray Increases Possibly due to Charged Particles from the Sun. *Physical Review*, 70:771–772, November 1946. doi: 10.1103/PhysRev.70.771.

[105] D. Fuhrmann, W. D. Apel, J. C. Arteaga-Velazquez, K. Bekk, M. Bertaina, J. Bluemer, H. Bozdog, I. M. Brancus, E. Cantoni, A. Chiavassa, F. Cossavella, C. Curcio, K. Daumiller, V. de Souza, F. Di Pierro, P. Doll, R. Engel, J. Engler, B. Fuchs, H. J. Gils, R. Glasstetter, C. Grupen, A. Haungs, D. Heck, J. R. Hoerandel, D. Huber, T. Huege, K.-H. Kampert, D. Kang, H. O. Klages, K. Link, P. Luczak, M. Ludwig, H. J. Mathes, H. J. Mayer, M. Melissas, J. Milke, B. Mitrica, C. Morello, J. Oehlschlaeger, S. Ostapchenko, N. Palmieri, M. Petcu, T. Pierog, H. Rebel, M. Roth, H. Schieler, S. Schoo, F. G. Schroeder, O. Sima, G. Toma, G. C. Trinchero, H. Ulrich, A. Weindl, D. Wochele, J. Wochele, and J. Zabierowski-KASCADE-Grande Collaboration. KASCADE-Grande measurements of energy spectra for elemental groups of cosmic rays. *ArXiv e-prints*, August 2013.

[106] M. Fukushima. Measurement of ultra-high energy cosmic rays: An experimental summary and prospects. *EPJ Web of Conferences*, 53:02002, 2013. doi: 10.1051/epjconf/20135302002. URL `http://dx.doi.org/10.1051/epjconf/20135302002`.

[107] T. K. Gaisser and A. M. Hillas. Reliability of the method of constant intensity cuts for reconstructing the average development of vertical showers. *Proceedings of the International Cosmic Ray Conference*, 8:353–357, 1977.

[108] G. K. Garipov, B. A. Khrenov, M. I. Panasyuk, V. I. Tulupov, A. V. Shirokov, I. V. Yashin, and H. Salazar. UV radiation from the atmosphere: Results of the MSU Tatiana satellite measurements. *Astroparticle Physics*, 24:400–408, December 2005. doi: 10.1016/j.astropartphys.2005.09.001.

[109] G. K. Garipov, B. A. Khrenov, P. A. Klimov, V. S. Morozenko, M. I. Panasyuk, S. N. Petrova, V. I. Tulupov, V. M. Shahparonov, S. I. Svertilov, N. N. Vedenkin, I. V. Yashin, J. A. Jeon, S. M. Jeong, A. R. Jung, J. E. Kim, J. Lee, H. Y. Lee, G. W. Na, J. W. Nam, S. Nam, I. H. Park, J. E. Suh, J. Y. Jin, M. Kim, Y. K. Kim, B. W. Yoo, Y.-S. Park, H. J. Yu, C.-H. Lee, J. H. Park, H. I. Salazar, O. B. Martinez, E. L. Ponce, and J. P. Cotsomi. Program of transient UV event research at Tatiana-2 satellite. *Journal of Geophysical Research (Space Physics)*, 115:A00E24, May 2010. doi: 10.1029/2009JA014765.

[110] G. K. Garipov, B. A. Khrenov, P. A. Klimov, V. V. Klimenko, E. A. Mareev, O. Martines, E. Mendoza, V. S. Morozenko, M. I. Panasyuk, I. H. Park, E. Ponce, L. Rivera, H. Salazar, V. I. Tulupov, N. N. Vedenkin, and I. V. Yashin. Global transients in ultraviolet and red-infrared ranges from data of Universitetsky-Tatiana-2 satellite. *Journal of Geophysical Research (Atmospheres)*, 118:370–379, January 2013. doi: 10.1029/2012JD017501.

[111] H. Gemmeke, W. D. Apel, F. A. Badea, L. Bähren, K. Bekk, A. Bercuci, M. Bertaina, P. L. Biermann, J. Blümer, H. Bozdog, I. M. Brancus, M. Brüggemann, P. Buchholz, S. Buitink, H. Butcher, A. Chiavassa, K. Daumiller, A. G. de Bruyn, C. M. de Vos, F. di Pierro, P. Doll, R. Engel, H. Falcke, P. L. Ghia, R. Glasstetter, C. Grupen, A. Haungs, D. Heck, J. R. Hörandel, A. Horneffer, T. Huege, K.-H. Kampert, G. W. Kant, U. Klein, Y. Kolotaev, Y. Koopman, O. Krömer, J. Kuijpers, S. Lafebre, G. Maier, H. J. Mathes, H. J. Mayer, J. Milke, B. Mitrica, C. Morello, G. Navarra, S. Nehls, A. Nigl, R. Obenland, J. Oehlschläger, S. Ostapchenko, S. Over, H. J. Pepping, M. Petcu, J. Petrovic, T. Pierog, S. Plewnia, H. Rebel, A. Risse, M. Roth, H. Schieler, G. Schoonderbeek, O. Sima, M. Stümpert, G. Toma, G. C. Trinchero, H. Ulrich, J. van Buren, W. van Capellen, W. Walkowiak, A. Weindl, S. Wijnholds, J. Wochele, J. Zabierowski, J. A. Zensus, and D. Zimmermann. Advanced Detection Methods of Radio Signals from Cosmic Rays for KASCADE Grande and Auger.

International Journal of Modern Physics A, 21:242–246, 2006. doi: 10.1142/S0217751X06033702.

[112] G. Giacinti, M. Kachelrieß, D. Semikoz, and G. Sigl. Transition from galactic to extragalactic cosmic rays and cosmic ray anisotropy. *EPJ Web of Conferences*, 53:06002, 2013. doi: 10.1051/epjconf/20135306002. URL `http://dx.doi.org/10.1051/epjconf/20135306002`.

[113] G. Giacinti, M. Kachelrieß, D. Semikoz, and G. Sigl. Deflection of ultra-high energy heavy nuclei in the galactic magnetic field. *EPJ Web of Conferences*, 53:06004, 2013. doi: 10.1051/epjconf/20135306004. URL `http://dx.doi.org/10.1051/epjconf/20135306004`.

[114] N. Giglietto. The contribution by Domenico Pacini to the Cosmic Ray Physics. *Nuclear Physics B Proceedings Supplements*, 212:3–12, March 2011. doi: 10.1016/j.nuclphysbps.2011.03.002.

[115] M. Giller, G. Wieczorek, A. Kacperczyk, H. Stojek, and W. Tkaczyk. Energy spectra of electrons in the extensive air showers of ultra-high energy. *Journal of Physics G Nuclear Physics*, 30:97–105, February 2004. doi: 10.1088/0954-3899/30/2/009.

[116] D. Góra, R. Engel, D. Heck, P. Homola, H. Klages, J. PeĶala, M. Risse, B. Wilczyńska, and H. Wilczyński. Universal lateral distribution of energy deposit in air showers and its application to shower reconstruction. *Astroparticle Physics*, 24:484–494, January 2006. doi: 10.1016/j.astropartphys.2005.09.007.

[117] A. Gorgi. Ltt-preclustering software module, 2011. URL `svn+ssh://svn.in2p3.fr/esaf/trunk/esaf/packages/reconstruction/modules/shower/fitting/src/LTTPreClusteringModule.cc`.

[118] P. Gorodetzky, L. Wiencke, N. Sakaki, A. Haungs, and the JEM-EUSO Collaboration. The Calibration Aspects of the JEM-EUSO Mission. *Submitttted to Experimental Astronomy*, May 2014.

[119] K. Greisen. Cosmic Ray Showers. *Annual Review of Nuclear and Particle Science*, 10:63–108, 1960. doi: 10.1146/annurev.ns.10.120160.000431.

[120] K. Greisen. End to the Cosmic-Ray Spectrum? *Physical Review Letters*, 16:748–750, April 1966. doi: 10.1103/PhysRevLett.16.748.

[121] B. Grossan, S. Brandt, C. Budtz-Jørgensen, A. Castro-Tirado, I. Kuvvetli, H. Lim, J. Nam, K. Nam, M. I. Panasyuk, I. Park, V. Reglero, and N. Vedenkin. Update on The Ultra-Fast Flash Observatory (UFFO) Pathfinder. In J. E. McEnery, J. L. Racusin, and N. Gehrels, editors, *American Institute of Physics Conference Series*, volume 1358 of *American Institute of Physics Conference Series*, pages 419–422, August 2011. doi: 10.1063/1.3621818.

[122] A. Guzman. Pwise software module, 2011. URL svn+ssh://svn.in2p3.fr/esaf/trunk/esaf/packages/reconstruction/modules/base/clustering/src/PWISEModule.cc.

[123] A. Guzman, T. Mernik, A. Santangelo, G. Medina-Tanco, M. Bertaina, K. Shinozaki, F. Fenu, A. Gorgi, and theJEM-EUSO Collaboration. The Peak and Window Searching Technique for the EUSO Simulation and Analysis Framework: Impact on the Angular Reconstruction of EAS. *Journal of Physics Conference Series*, 409(1):012104, February 2013. doi: 10.1088/1742-6596/409/1/012104.

[124] A. Guzman, G. Saez-Cano, K. Shinozaki, and the JEM-EUSO Collaboration. JEM-EUSO observation in cloudy conditions. *Submitted to Experimental Astronomy*, May 2014.

[125] A. Guzman et al. JEM-EUSO's angular reconstruction within the EUSO simulation and analysis framework. In *Tours Symposium on Nuclear Physics and Astrophysics*, Tours Symposium on Nuclear Physics and Astrophysics, 2012. Talk.

[126] A. Haungs. Status of JEM-EUSO and its test experiments EUSO-Balloon and TA-EUSO. In *European Physical Journal Web of Conferences*, volume 52 of *European Physical Journal Web of Conferences*, page 6005, June 2013. doi: 10.1051/epjconf/20125206005.

[127] A. Haungs and the AugerNext Consortium. Augernext: innovative research studies for the next generation ground-based ultra-high energy cosmic ray experiment. *EPJ Web of Conferences*, 53:08019, 2013. doi: 10.1051/epjconf/20135308019. URL http://dx.doi.org/10.1051/epjconf/20135308019.

[128] A. Haungs, W. D. Apel, J. C. Arteaga-Velazquez, K. Bekk, M. Bertaina, J. Blümer, H. Bozdog, I. M. Brancus, E. Cantoni, A. Chiavassa, F. Cossavella, K. Daumiller, V. de Souza, F. Di Pierro, P. Doll, R. Engel, J. Engler, M. Finger, B. Fuchs, D. Fuhrmann, H. J. Gils, R. Glasstetter, C. Grupen, D. Heck, J. R. Hörandel, D. Huber, T. Huege, K.-H. Kampert, D. Kang, H. O. Klages, K. Link, P. Łuczak, M. Ludwig, H. J. Mathes, H. J. Mayer, M. Melissas, J. Milke, C. Morello, J. Oehlschläger, S. Ostapchenko, N. Palmieri, M. Petcu, T. Pierog, H. Rebel, M. Roth, H. Schieler, S. Schoo, F. Schroder, O. Sima, G. Toma, G. C. Trinchero, H. Ulrich, A. Weindl, J. Wochele, M. Wommer, and J. Zabierowski. KASCADE-Grande observation of features in the cosmic ray spectrum between knee and ankle. *Journal of Physics Conference Series*, 409(1):012005, February 2013. doi: 10.1088/1742-6596/409/1/012005.

[129] D. Heck, J. Knapp, J. N. Capdevielle, G. Schatz, and T. Thouw. *CORSIKA: a Monte Carlo code to simulate extensive air showers.* TIB, Hannover, February 1998.

[130] A.E. Hedin. Extension of the MSIS thermosphere model into the middle and lower atmosphere. *Journal of Geophysics Research*, 96:1159–1172, February 1991. doi: 10.1029/90JA02125.

[131] V. Higgins. John Linsley Papers. *Fermilab History and Archives Project, Fermi National Accelerator Laboratory, Batavia, IL*, 2012. URL http://history.fnal.gov/findingaids/Linsley_ibatf2012001.html. Online; accessed 23-October-2013.

[132] High Resolution Fly'S Eye Collaboration, R. U. Abbasi, T. Abu-Zayyad, M. Allen, J. F. Amman, G. Archbold, K. Belov, J. W. Belz, S. Y. Benzvi, D. R. Bergman, S. A. Blake, J. H. Boyer, O. A. Brusova, G. W. Burt, C. Cannon, Z. Cao, W. Deng, Y. Fedorova, J. Findlay, C. B. Finley, R. C. Gray, W. F. Hanlon, C. M. Hoffman, M. H. Holzscheiter, G. Hughes, P. Hüntemeyer, D. Ivanov, B. F. Jones, C. C. H. Jui, K. Kim, M. A. Kirn, B. C. Knapp, E. C. Loh, M. M. Maestas, N. Manago, E. J. Mannel, L. J. Marek, K. Martens, J. N. Matthews, S. A. Moore, A. O'Neill, C. A. Painter, L. Perera, K. Reil, R. Riehle, M. D. Roberts, D. Rodriguez, N. Sasaki, S. R. Schnetzer, L. M. Scott, M. Seman, G. Sinnis, J. D. Smith, R. Snow, P. Sokolsky, C. Song, R. W. Springer, B. T. Stokes, S. R. Stratton, J. R. Thomas, S. B. Thomas, G. B. Thomson, D. Tupa, L. R. Wiencke, A. Zech, X. Zhang, and the High Resolution Fly's Eye Collaboration. Search for correlations between HiRes stereo events and active galactic nuclei. *Astroparticle Physics*, 30:175–179, November 2008. doi: 10.1016/j.astropartphys.2008.08.004.

[133] A. M. Hillas. Angular and energy distributions of charged particles in electron-photon cascades in air. *Journal of Physics G Nuclear Physics*, 8:1461–1473, October 1982. doi: 10.1088/0305-4616/8/10/016.

[134] A. M. Hillas. The Origin of Ultra-High-Energy Cosmic Rays. *Annual review of astronomy and astrophysics*, 22:425–444, 1984. doi: 10.1146/annurev.aa.22.090184.002233.

[135] J. R. Hörandel. Early cosmic-ray work published in German. In J. F. Ormes, editor, *American Institute of Physics Conference Series*, volume 1516 of *American Institute of Physics Conference Series*, pages 52–60, February 2013. doi: 10.1063/1.4792540.

[136] P. V. C. Hough. A Method for Faster Analysis of Bubble Chamber Photographs (Hough and Powell). In *Instrumentation for High-Energy Physics*, pages 242–+, 1961.

[137] D. Ikeda, T. Abu-Zayyad, M. Allen, E. Barcikowski, H. Sagawa, B.T. Stokes, and G.B. Thomson. Hybrid analysis for the telescope array. *EPJ Web of Conferences*, 53:04006, 2013. doi: 10.1051/epjconf/20135304006. URL http://dx.doi.org/10.1051/epjconf/20135304006.

[138] N. P. Ilina, N. N. Kalmykov, and V. V. Prosin. Cherenkov radiation and parameters of extensive air showers. *Sov. J. Nucl. Phys.*, 55:1540–1547, 1992.

[139] E. Iwotschkin. A preliminary assessment of trigger efficiency for neutrinos observed with jem-euso. Bachelor's thesis, Eberhard Karls Universität Tübingen, Institut für Astronomie und Astrophysik, Germany, September 2013.

[140] M. Kachelriess. The rise and fall of top-down models as main UHECR sources. *ArXiv e-prints*, October 2008.

[141] F. Kajino, T. Ebisuzaki, H. Mase, K. Tsuno, Y. Takizawa, Y. Kawasaki, K. Shinozaki, H. Ohmori, S. Wada, N. Inoue, N. Sakaki, J. Adams, M. Christl, R. Young, C. Ferguson, M. Bonamente, A. Santangelo, M. Teshima, E. Parizot, P. Gorodetzky, O. Catalano, P. Picozza, M. Casolino, M. Bertaina, M. Panasyuk, B. A. Khrenov, I. H. Park, A. Neronov, G. Medina-Tanco, D. Rodriguez-Frias, J. Szabelski, P. Bobik, and R. Tsenov. Overall View of the JEM-EUSO Instruments. In H. Sagawa, Y. Kawasaki, T. Sako, M. Takeda, and Y. Tsunesada, editors, *American Institute of Physics Conference Series*, volume 1367 of *American Institute of Physics Conference Series*, pages 197–200, September 2011. doi: 10.1063/1.3628744.

[142] F. Kakimoto, E. C. Loh, M. Nagano, H. Okuno, M. Teshima, and S. Ueno. A measurement of the air fluorescence yield. *Nuclear Instruments and Methods in Physics Research A*, 372:527–533, February 1996. doi: 10.1016/0168-9002(95)01423-3.

[143] O. Kalashev, K. Ptitsyna, and S. Troitsky. Constraints on direct acceleration of uhecrs in astrophysical sources. *EPJ Web of Conferences*, 53:06003, 2013. doi: 10.1051/epjconf/20135306003. URL `http://dx.doi.org/10.1051/epjconf/20135306003`.

[144] N. N. Kalmykov and S. S. Ostapchenko. The nucleus-nucleus interaction, nuclear fragmentation, and fluctuations of extensive air showers. *Physics of Atomic Nuclei*, 56:346–353, March 1993.

[145] N. N. Kalmykov, B. A. Khrenov, G. V. Kulikov, and M. Y. Zotov. Sources of UHECRs in view of the TUS and JEM-EUSO experiments. *Journal of Physics Conference Series*, 409(1):012100, February 2013. doi: 10.1088/1742-6596/409/1/012100.

[146] K. Kamata and J. Nishimura. The Lateral and the Angular Structure Functions of Electron Showers. *Progress of Theoretical Physics Supplement*, 6:93–155, 1958. doi: 10.1143/PTPS.6.93.

[147] Y. Kawasaki, M. Casolino, P. Gorodetzky, A. Santangelo, M. Ricci, F. Kajino, T. Ebisuzaki, and the JEM-EUSO Collaboration. The focal surface of the JEM-EUSO instrument. *Astrophysics and Space Sciences Transactions*, 7:167–169, May 2011. doi: 10.5194/astra-7-167-2011.

[148] B. Keilhauer, M. Bohacova, M. Fraga, J. Matthews, N. Sakaki, et al. Nitrogen fluorescence in air for observing extensive air showers. *EPJ Web Conf.*, 53:01010, 2013. doi: 10.1051/epjconf/20135301010.

[149] B. A. Khrenov, M. I. Panasyuk, V. V. Alexandrov, D. I. Bugrov, A. Cordero, G. K. Garipov, J. Linsley, O. Martinez, H. Salazar, O. A. Saprykin, A. A. Silaev, D. V. Surogatov, V. S. Syromyatnikov, L. Villaseñor, and A. Zepeda. Space Program KOSMOTEPETL (project KLYPVE and TUS) for the study of extremely high energy cosmic rays. In H. Salazar, L. Villasenor, and A. Zepeda, editors, *Observing Ultrahigh Energy Cosmic Rays from Space and Earth*, volume 566 of *American Institute of Physics Conference Series*, pages 57–75, May 2001. doi: 10.1063/1.1378622.

[150] B. A. Khrenov, V. V. Alexandrov, D. I. Bugrov, G. K. Garipov, N. N. Kalmykov, M. I. Panasyuk, S. A. Sharakin, A. A. Silaev, I. V. Yashin, V. M. Grebenyuk, D. V. Naumov, A. G. Olshevsky, B. M. Sabirov, R. N. Semenov, M. Slunechka, I. I. Skryl, L. G. Tkatchev, O. A. Saprykin, V. S. Syromyatnikov, V. E. Bitkin, S. A. Eremin, A. I. Matyushkin, F. F. Urmantsev, V. Abrashin, V. Koval, Y. Arakcheev, A. Cordero, O. Martinez, E. Morena, C. Robledo, H. Salazar, L. Villasenor, A. Zepeda, I. Park, M. Shonsky, and J. Zicha. KLYPVE/TUS space experiments for study of ultrahigh-energy cosmic rays. *Physics of Atomic Nuclei*, 67:2058–2061, November 2004. doi: 10.1134/1.1825529.

[151] B.A. Khrenov, M.I. Panasyuk, G.K. Garipov, N.N. Kalmykov, P.A. Klimov, V.S. Morozenko, S.A. Sharakin, A.V. Shirokov, I.V. Yashin, S.V. Biktemerova, A.A. Grinyuk, D.V. Naumov, L.G. Tkachev, A.V. Tkachenko, O.A. Saprykin, A.A. Botvinko, I. Park, J. Lee, G. Na, O. Martinez, H. Salazar, and E. Ponce. Pioneering space based detector for study of cosmic rays beyond gzk limit. *EPJ Web of Conferences*, 53:09006, 2013. doi: 10.1051/epjconf/20135309006. URL `http://dx.doi.org/10.1051/epjconf/20135309006`.

[152] H. B. Kim. A Study on Anisotropy in the Arrival Directions of Ultra-High Cosmic Rays Observed by Pierre Auger Observatory. *Modern Physics Letters A*, 28: 1350075, June 2013. doi: 10.1142/S0217732313500752.

[153] S. Klein. Suppression of bremsstrahlung and pair production due to environmental factors. *Reviews of Modern Physics*, 71:1501–1538, October 1999. doi: 10.1103/RevModPhys.71.1501.

[154] P. Klimov, Garipov G., Khrenov B. Kalmykov N., Morozenko V., Panasyuk M., Sharakin S., and Shirokov A. Yashin I. Status of the UHE CR Orbital Fluorescence Detector TUS. In S. Giani, Leroy C., and Rancoita P. G., editors, *Cosmic Rays for Particle and Astroparticle Physics*, volume 6 of *Proceedings of the 12th ICATPP Conference (Astroparticle, Particle, Space Physics, Radiation Interaction, Detectors and Medical Physics Applications)*, pages 196–206, June 2011.

[155] S.P. Knurenko and A. Sabourov. Spectrum and mass composition of cosmic rays in the energy range 10^{15} - 10^{18} ev derived from the yakutsk array data. *EPJ Web of Conferences*, 53:04004, 2013. doi: 10.1051/epjconf/20135304004. URL http://dx.doi.org/10.1051/epjconf/20135304004.

[156] K. Kotera and A. V. Olinto. The Astrophysics of Ultrahigh-Energy Cosmic Rays. *Annu. Rev. Astron. Astrophys.*, 49:119–153, September 2011. doi: 10.1146/annurev-astro-081710-102620.

[157] J. F. Krizmanic, J. W. Mitchell, and R. E. Streitmatter. Optimization of the Orbiting Wide-angle Light Collectors (OWL) Mission for Charged-Particle and Neutrino Astronomy. *ArXiv e-prints*, July 2013.

[158] G. F. Krymskyj. A regular mechanism for the acceleration of charged particles on the front of a shock wave. *Akademiia Nauk SSSR Doklady*, 234:1306–1308, June 1977.

[159] A. Kusenko. Extragalactic and galactic sources: New evidence, new challenges, new opportunities. *EPJ Web of Conferences*, 53:06006, 2013. doi: 10.1051/epjconf/20135306006. URL http://dx.doi.org/10.1051/epjconf/20135306006.

[160] G. La Rosa, G. Agnetta, B. Biondo, O. Catalano, F. Celi, R. Di Raffaele, S. Giarrusso, A. Mangano, F. Russo, J. Linsley, and A. Lo Bue. Atmospheric Background Measurement in the 300-400 nm Band with a Balloon Borne Experiment During a Nocturnal Flight. *Astrophysics and Space Science*, 276:219–226, March 2001.

[161] L.D. Landau and I. Pomeranchuk. Electron cascade process at very high-energies. *Dokl.Akad.Nauk Ser.Fiz.*, 92:735–738, 1953.

[162] L.D. Landau and I. Pomeranchuk. Limits of applicability of the theory of bremsstrahlung electrons and pair production at high-energies. *Dokl.Akad.Nauk Ser.Fiz.*, 92:535–536, 1953.

[163] M. A. Leigui di Oliveira et al. The ionization energy deposit in the atmosphere and the fluorescence light generation at shower axis. In *Proceedings of the International Cosmic Ray Conference*, International Cosmic Ray Conference, 2009.

[164] M. Lemoine and G. Sigl, editors. *Physics and astrophysics of ultra-high-energy cosmic rays*, volume 576 of *Lecture Notes in Physics, Berlin Springer Verlag*, 2001. Springer Berlin Heidelberg, New York, Barcelona, Hong Kong, London, Milan, Paris, Tokyo.

[165] A. Letessier-Selvon and T. Stanev. Ultrahigh energy cosmic rays. *Reviews of Modern Physics*, 83:907–942, July 2011. doi: 10.1103/RevModPhys.83.907.

[166] A. Letessier-Selvon, for the Pierre Auger Collaboration, :, A. Aab, P. Abreu, M. Aglietta, M. Ahlers, E. J. Ahn, I. F. M. Albuquerque, I. Allekotte, et al. Highlights from the Pierre Auger Observatory. *ArXiv e-prints*, October 2013.

[167] Letessier-Selvon, Antoine. The need for a multicomponent uhecr observatory. *EPJ Web of Conferences*, 53:08018, 2013. doi: 10.1051/epjconf/20135308018. URL `http://dx.doi.org/10.1051/epjconf/20135308018`.

[168] Z. Levay, NASA, and ESA. Astronomy Picture of the Day, July 4, 2008: SN 1006 Supernova Remnant. *Astronomy Picture of the Day*, July 2008. URL `http://apod.nasa.gov/apod/ap080704.html`. Online; accessed 22-January-2014.

[169] J. Linsley. Evidence for a Primary Cosmic-Ray Particle with Energy 10^{20} eV. *Physical Review Letters*, 10:146–148, February 1963. doi: 10.1103/PhysRevLett.10.146.

[170] J. Linsley. GIL: a formula for EAS longitudinal profiles. In *Proceedings of the International Cosmic Ray Conference*, volume 2 of *International Cosmic Ray Conference*, page 502, 2001.

[171] E. C. Loh and Fly's Eye Group. High Resolution Fly's Eye detector. *Nuclear Physics B Proceedings Supplements*, 14:256–264, March 1990. doi: 10.1016/0920-5632(90)90430-3.

[172] M. S. Longair. *High Energy Astrophysics*. Cambridge University Press, February 2011.

[173] P. Łuczak, W. D. Apel, J. C. Arteaga-Velázquez, K. Bekk, M. Bertaina, J. Blümer, H. Bozdog, I. M. Brancus, E. Cantoni, A. Chiavassa, F. Cossavella, C. Curcio, K. Daumiller, V. de Souza, F. Di Pierro, P. Doll, R. Engel, J. Engler, B. Fuchs, D. Fuhrmann, H. J. Gils, R. Glasstetter, C. Grupen, A. Haungs, D. Heck, J. R. Hörandel, D. Huber, T. Huege, K.-H. Kampert, D. Kang, H. O. Klages, K. Link, M. Ludwig, H. J. Mathes, H. J. Mayer, M. Melissas, J. Milke, B. Mitrica, C. Morello, J. Oehlschläger, S. Ostapchenko, N. Palmieri, M. Petcu, T. Pierog, H. Rebel, M. Roth, H. Schieler, S. Schoo, F. G. Schröder, O. Sima, G. Toma, G. C. Trinchero, H. Ulrich, A. Weindl, J. Wochele, and J. Zabierowski. The <lnA> study in the primary energy range 10^{16} - 10^{17} eV with the Muon Tracking Detector in the KASCADE-Grande experiment. *ArXiv e-prints*, August 2013.

[174] M.C. Maccarone. Cluster analysis and line fits to reconstruct euso tracks. *The EUSO Collaboration*, Apr 2002.

[175] M.C. Maccarone. Hough transform to reconstruct euso tracks: Preliminary notes. *The EUSO Collaboration*, Apr 2002.

[176] K. Mannheim, R. J. Protheroe, and J. P. Rachen. Cosmic ray bound for models of extragalactic neutrino production. *Physical Review D*, 63(2):023003, January 2001. doi: 10.1103/PhysRevD.63.023003.

[177] Maris, Ioana C. Measurement of the energy spectrum of cosmic rays at the highest energies using data from pierre auger observatory. *EPJ Web of Conferences*, 53:04002, 2013. doi: 10.1051/epjconf/20135304002. URL http://dx.doi.org/10.1051/epjconf/20135304002.

[178] G. Medina-Tanco. Ultra-High Energy Cosmic Rays: Are They Isotropic? *The Astrophysical Journal*, 549:711–715, March 2001. doi: 10.1086/319467.

[179] G. Medina-Tanco, K. Asano, D. Cline, T. Ebisuzaki, S. Inoue, P. Lipari, E. Parizot, A. Santangelo, G. Sigl, Y. Takahashi, H. Takami, M. Teshima, T. J. Weiler, and for the JEM-EUSO Collaboration. JEM-EUSO Science Objectives. *ArXiv e-prints*, September 2009.

[180] D. L. Meier. *Black Hole Astrophysics: The Engine Paradigm*. Springer Berlin Heidelberg, New York, Jointly published with Praxis Publishing, UK, 2012.

[181] T. Mernik. It came from outer space - reconstruction of uhecr events for the jem-euso mission. Diploma thesis, Eberhard Karls Universität Tübingen, Institut für Astronomie und Astrophysik, Germany, December 2009.

[182] T. Mernik, A. Santangelo, F. Fenu, K. Shinozaki, D. Naumov, S. Dagoret-Campagne, G. Medina-Tanco, D. Supanitsky, H. Miyamoto, J. Szabelski, and the JEM-EUSO Collaboration. ESAF-Reconstruction of Extreme Energy Cosmic Ray Events Observed by JEM-EUSO. In *Proceedings of the International Cosmic Ray Conference*, International Cosmic Ray Conference, 2009.

[183] T. Mernik, F. Fenu, D. D'Urso, A. Santangelo, K. Bittermann, K. Shinozaki, M. Bertaina, S. Biktemerova, D. Naumov, G. Medina-Tanco, and the JEM-EUSO Collaboration. The ESAF Reconstruction Framework of UHECR Events for the JEM-EUSO Mission. In *Proceedings of the International Cosmic Ray Conference*, volume 3 of *International Cosmic Ray Conference*, page 116, 2011.

[184] T. Mernik, A. Guzman, F. Fenu, K. Shinozaki, A. Santangelo, M. Bertaina, and the JEM-EUSO Collaboration. Simulating the JEM-EUSO Mission: Expected Reconstruction Performance. In *Proceedings of the International Cosmic Ray Conference*, International Cosmic Ray Conference Rio de Janeiro, Brazil, 2013.

[185] T. Mernik, A. Guzman, A. Santangelo, K. Shinozaki, N. Sakaki, C. Moretto, D. Monnier-Ragaigne, H. Miyamoto, S. Dagoret-Campagne, C. Catalano, P. von Balloos, and the JEM-EUSO Collaboration. ESAF-Simulation of the EUSO-Balloon. In *Proceedings of the International Cosmic Ray Conference*, International Cosmic Ray Conference Rio de Janeiro, Brazil, 2013.

[186] P. Mészáros. *The High Energy Universe: Ultra-High Energy Events in Astrophysics and Cosmology*. Cambridge University Press, September 2010.

[187] A. B. Migdal. Bremsstrahlung and Pair Production in Condensed Media at High Energies. *Physical Review*, 103:1811–1820, September 1956. doi: 10.1103/PhysRev.103.1811.

[188] M. Mönchmeyer. Anisotropy studies with the pierre auger observatory. *EPJ Web of Conferences*, 53:04011, 2013. doi: 10.1051/epjconf/20135304011. URL `http://dx.doi.org/10.1051/epjconf/20135304011`.

[189] S. Moreggia. Bunch radiative transfer software module, 2004. URL `svn+ssh://svn.in2p3.fr/esaf/trunk/esaf/packages/simulation/radiativetransfer/src/BunchRadiativeTransfer.cc`.

[190] S. Moreggia. Mc radiative transfer software module, 2005. URL `svn+ssh://svn.in2p3.fr/esaf/trunk/esaf/packages/simulation/radiativetransfer/src/MCRadiativeTransfer.cc`.

[191] M. Nagano, K. Kobayakawa, N. Sakaki, and K. Ando. Photon yields from nitrogen gas and dry air excited by electrons. *Astroparticle Physics*, 20:293–309, December 2003. doi: 10.1016/S0927-6505(03)00192-0.

[192] M. Nagano, K. Kobayakawa, N. Sakaki, and K. Ando. New measurement on photon yields from air and the application to the energy estimation of primary cosmic rays. *Astroparticle Physics*, 22:235–248, November 2004. doi: 10.1016/j.astropartphys.2004.08.002.

[193] Navas, S. Search for ultra-high energy neutrinos at the pierre auger observatory. *EPJ Web of Conferences*, 53:05003, 2013. doi: 10.1051/epjconf/20135305003. URL `http://dx.doi.org/10.1051/epjconf/20135305003`.

[194] F. Nerling, J. Bluemer, R. Engel, and M. Risse. Universality of electron distributions in high-energy air showers - Description of Cherenkov light production. *Astroparticle Physics*, 24:421–437, January 2006. doi: 10.1016/j.astropartphys.2005.09.002.

[195] Z. Norman. Positioning of ground-based Global Light System stations around the World for the JEM-EUSO mission. In *APS April Meeting Abstracts*, page 8002, April 2013.

[196] S. Ogio. Future plans for the telescope array experiment. *EPJ Web of Conferences*, 53:08020, 2013. doi: 10.1051/epjconf/20135308020. URL http://dx.doi.org/10.1051/epjconf/20135308020.

[197] A. V. Olinto. UHECR theory and phenomenology: Summary and outlook. In *European Physical Journal Web of Conferences*, volume 53 of *European Physical Journal Web of Conferences*, page 2001, June 2013. doi: 10.1051/epjconf/20135302001. URL http://dx.doi.org/10.1051/epjconf/20135302001.

[198] U.S. Committee on Extension to the Standard Atmosphere. U.S. Standard Atmosphere 1976. Technical report, U.S. Government Printing Office, Oct 1976.

[199] S. Ostapchenko. Monte Carlo treatment of hadronic interactions in enhanced Pomeron scheme: QGSJET-II model. *Physical Review D*, 83(1):014018, January 2011. doi: 10.1103/PhysRevD.83.014018.

[200] G. Osteria and V. Scotti. Euso-Balloon: A pathfinder mission for the JEM-EUSO experiment. *Nuclear Instruments and Methods in Physics Research A*, 732:320–324, December 2013. doi: 10.1016/j.nima.2013.05.124.

[201] G. Osteria, V. Scotti, and the JEM EUSO Collaboration. The JEM-EUSO time synchronization system and EUSO BALLOON Data Processor. *Journal of Physics Conference Series*, 409(1):012106, February 2013. doi: 10.1088/1742-6596/409/1/012106.

[202] D. Pacini. La radiazione penetrante sul mare. *Ann. Uff. Centr. Meteor*, 32, 1910.

[203] M. I. Panasyuk, V. V. Bogomolov, G. K. Garipov, O. R. Grigoryan, Y. I. Denisov, B. A. Khrenov, P. A. Klimov, L. L. Lazutin, S. I. Svertilov, N. N. Vedenkin, I. V. Yashin, S. I. Klimov, L. M. Zeleny, V. S. Makhmutov, Y. I. Stozkov, N. S. Svirzhevsky, V. V. Klimenko, E. A. Mareev, Y. V. Shlyugaev, V. E. Korepanov, I. H. Park, H. I. Salazar, and H. Rothkaehl. Transient luminous event phenomena and energetic particles impacting the upper atmosphere: Russian space experiment programs. *Journal of Geophysical Research (Space Physics)*, 115:A00E33, June 2010. doi: 10.1029/2009JA014763.

[204] R. Penrose. Gravitational Collapse: the Role of General Relativity. *Nuovo Cimento Rivista Serie*, 1:252, 1969.

[205] A. A. Penzias and R. W. Wilson. A Measurement of Excess Antenna Temperature at 4080 Mc/s. *Astrophysical Journal*, 142:419–421, July 1965. doi: 10.1086/148307.

[206] R. Pesce. Studio ed ottimizzazione delle prestazioni di un apparato per la rilevazione di raggi cosmici di altissima energia dallo spazio. Master's thesis, Universita Degli Studi Di Genova, 2004.

[207] A. Petrolini. The extreme universe space observatory (EUSO) instrument. *Nuclear Physics B Proceedings Supplements*, 113:329–336, 2002. doi: 10.1016/S0920-5632(02)01860-1.

[208] A. Petrolini. Ultra-High Energy Cosmic Particles studies from space: Super-EUSO, a possible next-generation experiment. *Nuclear Instruments and Methods in Physics Research A*, 630:131–135, February 2011. doi: 10.1016/j.nima.2010.06.044.

[209] J. M. Picone, A. E. Hedin, D. P. Drob, and A. C. Aikin. NRLMSISE-00 empirical model of the atmosphere: Statistical comparisons and scientific issues. *Journal of Geophysical Research (Space Physics)*, 107:1468–+, December 2002. doi: 10.1029/2002JA009430.

[210] T. Pierog, M. K. Alekseeva, T. Bergmann, V. Chernatkin, R. Engel, D. Heck, N. N. Kalmykov, J. Moyon, S. Ostapchenko, T. Thouw, and K. Werner. First results of fast one-dimensional hybrid simulation of EAS using CONEX. *Nuclear Physics B Proceedings Supplements*, 151:159–162, January 2006. doi: 10.1016/j.nuclphysbps.2005.07.029.

[211] T. Pierog, R. Engel, D. Heck, et al. Latest Results of Air Shower Simulation Programs CORSIKA and CONEX. In *Proceedings of the International Cosmic Ray Conference*, volume 4 of *International Cosmic Ray Conference*, pages 625–628, 2008.

[212] T. Pierog, I. Karpenko, J. M. Katzy, E. Yatsenko, and K. Werner. EPOS LHC : test of collective hadronization with LHC data. *ArXiv e-prints*, June 2013.

[213] Pierre Auger Collaboration, J. Abraham, P. Abreu, M. Aglietta, C. Aguirre, D. Allard, I. Allekotte, J. Allen, P. Allison, C. Alvarez, et al. Correlation of the Highest-Energy Cosmic Rays with Nearby Extragalactic Objects. *Science*, 318:938–, November 2007. doi: 10.1126/science.1151124.

[214] S. B. Popov and M. E. Prokhorov. Progenitors with enhanced rotation and the origin of magnetars. *Monthly Notices of the RAS*, 367:732–736, April 2006. doi: 10.1111/j.1365-2966.2005.09983.x.

[215] P. Privitera. The Pierre Auger Observatory. *Nuclear Physics B Proceedings Supplements*, 110:487–490, July 2002. doi: 10.1016/S0920-5632(02)80187-6.

[216] S. Razzaque, C. D. Dermer, and J. D. Finke. Lower Limits on Ultrahigh-energy Cosmic Ray and Jet powers of TeV Blazars. *The Astrophysical Journal*, 745:196, February 2012. doi: 10.1088/0004-637X/745/2/196.

[217] M. Ricci and JEM-EUSO Collaboration. The JEM-EUSO mission. *Journal of Physics Conference Series*, 375(5):052009, July 2012. doi: 10.1088/1742-6596/375/1/052009.

[218] M.D. Rodríguez Frías, J.A. Morales de losRíos, L. del Peral, G. Sáez-Cano, K. Shinozaki, H. Prieto, J. H-Carretero, M.D. Sabau, T. Belenguer, C. González Alvarado, M. Sanz Palomino, S. Briz, A.J. de Castro, I. Fernández, F. Cortés, F. López, J. Licandro, M. Reyes, E. Joven, K. Tsuno, T. Ogawa, O. Catalano, A. Anzalone, F. Isgró, L. Valore, F. Guarino, M. Casolino, A. Cellino, M. Di Martino, M. Bertaina, R. Cremonini, F. Gola, F. Garino, B. Keilhauer, A. Neronov, and S. Wada. The atmospheric monitoring system of the jem-euso space mission. *EPJ Web of Conferences*, 53:10005, 2013. doi: 10.1051/epjconf/20135310005. URL `http://dx.doi.org/10.1051/epjconf/20135310005`.

[219] M.D. Rodriguez-Frias, J. A. Morales de los Rios, and the JEM-EUSO Collaboration. The Infrared Camera onboard JEM-EUSO. *Submitted to Experimental Astronomy*, May 2014.

[220] B. Rossi and K. Greisen. Cosmic-Ray Theory. *Reviews of Modern Physics*, 13: 240–309, October 1941. doi: 10.1103/RevModPhys.13.240.

[221] S. Rosswog and M. Brüggen. *Introduction to High-Energy Astrophysics*. Cambridge University Press, August 2007.

[222] B. Rouillé d'Orfeuil, D. Allard, C. Lachaud, E. Parizot, C. Blaksley, and S. Nagataki. Anisotropy expectations for ultra-high-energy cosmic rays with future high statistics experiments. *ArXiv e-prints*, January 2014.

[223] Rubtsov, G.I., Fukushima, M., Ivanov, D., Stokes, B.T., Thomson, G.B., and Troitsky, S.V. Search for ultra-high energy photons and neutrinos using telescope array surface detector. *EPJ Web of Conferences*, 53:05001, 2013. doi: 10.1051/epjconf/20135305001. URL `http://dx.doi.org/10.1051/epjconf/20135305001`.

[224] G. Saez-Cano. Observation of extensive air showers in cloudy conditions by the JEM-EUSO Space Mission. *Advances in Space Research*, 111:111–111, March 2014. doi: 10.1016/j.asr.2013.07.015.

[225] H. Sagawa. Cosmic-ray composition. *Website of Hiroyuki Sagawa, University of Tokyo*, January 2014. URL `http://www-ta.icrr.u-tokyo.ac.jp/hsagawa/index.php?id=9`. Online; accessed 17-January-2014.

[226] N. Sakaki, J. Adams, M. Christl, P. Gorodetzky, and L. Wiencke. Calibration of the jem-euso detector. *EPJ Web of Conferences*, 53:09004, 2013. doi: 10.1051/epjconf/20135309004. URL `http://dx.doi.org/10.1051/epjconf/20135309004`.

[227] A. Santangelo. The JEM-EUSO mission: Context and Status. *EPJ Web of Conferences*, 53:09001, 2013. doi: 10.1051/epjconf/20135309001. URL `http://dx.doi.org/10.1051/epjconf/20135309001`.

[228] A. Santangelo and the S-EUSO Collaboration. S-EUSO: A Proposal for a Space-Based Observatory of Ultra High-Energy Cosmic Particles. *S-EUSO Proposal to ESA*, Jun 2007. URL `http://astro.uni-tuebingen.de/groups/uhe/cv-proposals/S-EUSO-proposal-29.06.2007.pdf`. Online; accessed 25-February-2014.

[229] A. Santangelo, K. Bittermann, T. Mernik, and F. Fenu. Space based studies of UHE neutrinos. *Progress in Particle and Nuclear Physics*, 64:366–370, April 2010. doi: 10.1016/j.ppnp.2009.12.050.

[230] A. Santangelo, P. Picozza, T. Ebisuzaki, and the JEM-EUSO-Collaboration. Status of the JEM-EUSO Mission. In *Proceedings of the International Cosmic Ray Conference*, International Cosmic Ray Conference Rio de Janeiro, Brazil, 2013.

[231] L. Scarsi, O. Catalano, M. C. Maccarone, and B. Sacco. EUSO - Extreme Universe Space Observatory:. In *Proceedings of the International Cosmic Ray Conference*, volume 2 of *International Cosmic Ray Conference*, pages 839–842, 2001.

[232] V. Scherini. Search for ultra-high energy photons at the pierre auger observatory. *EPJ Web of Conferences*, 53:05002, 2013. doi: 10.1051/epjconf/20135305002. URL `http://dx.doi.org/10.1051/epjconf/20135305002`.

[233] P. Schneider. *Extragalactic Astronomy and Cosmology*. Springer Berlin Heidelberg, New York, 2006.

[234] F. Schüssler. Searches for the sources of cosmic rays with the antares neutrino telescope. *EPJ Web of Conferences*, 53:05004, 2013. doi: 10.1051/epjconf/20135305004. URL `http://dx.doi.org/10.1051/epjconf/20135305004`.

[235] S. M. Seltzer and M. J. Berger. Improved procedure for calculating the collision stopping power of elements and compounds for electrons and positrons. *The International Journal of Applied Radiation and Isotopes*, 35:665–676, July 1984. doi: 10.1016/0020-708X(84)90113-3.

[236] D. Semikoz. Constraints on top-down models for the origin of UHECRs from the Pierre Auger Observatory data. *Proceedings of the International Cosmic Ray Conference*, 4:433–436, 2008.

[237] T. Shibata, M. Beitollahi, M. Fukushima, D. Ikeda, K. Langely, J.N. Matthews, H. Sagawa, B.K. Shin, S.B. Thomas, and G.B. Thomson. Absolute energy calibration of the telescope array fluorescence detector with an electron linear accelerator. *EPJ Web of Conferences*, 53:10004, 2013. doi: 10.1051/epjconf/20135310004. URL `http://dx.doi.org/10.1051/epjconf/20135310004`.

[238] K. Shinozaki. Optics Throughput Efficiency of JEM-EUSO. *Private Communication*, October 2014.

[239] K. Shinozaki, M. Bertaina, S. Biktemerova, P. Bobik, F. Fenu, A. Guzman, K. Higashide, G. Medina-Tanco, T. Mernik, J.A. Morales De Los Rios Pappa, D. Naumov, M.D. Rodriguez-Frias, G. Saez-Cano, A. Santangelo, and the JEM-EUSO Collaboration. Estimation of aperture for extreme energy cosmic rays observation by JEM-EUSO Telescope. In *Proceedings of the International Cosmic Ray Conference*, International Cosmic Ray Conference Beijing, China, 2011.

[240] P. Sokolsky. Ultra-high energy cosmic rays: Setting the stage. *EPJ Web of Conferences*, 53:01001, 2013. doi: 10.1051/epjconf/20135301001. URL `http://dx.doi.org/10.1051/epjconf/20135301001`.

[241] T. Stanev. *High Energy Cosmic Rays*. Springer, Berlin, Heidelberg, New York, second edition, 2010.

[242] T. Stanev, K. Vankov, S. Petrov, and J. W. Elbert. Some energy and angular characteristics of electrons in electromagnetic cascades in air. *Proceedings of the International Cosmic Ray Conference*, 6:256–259, 1981.

[243] F. W. Stecker. Ice Cube Observed PeV Neutrinos from AGN Cores. *ArXiv e-prints*, May 2013.

[244] F. W. Stecker and M. H. Salamon. Photodisintegration of Ultra-High-Energy Cosmic Rays: A New Determination. *The Astrophysical Journal*, 512:521–526, February 1999. doi: 10.1086/306816.

[245] R. E. Streitmatter. Orbiting Wide-angle Light-collectors (OWL): Observing cosmic rays from space. In J. F. Krizmanic, J. F. Ormes, and R. E. Streitmatter, editors, *Workshop on Observing Giant Cosmic Ray Air Showers From >10(20) eV Particles From Space*, volume 433 of *American Institute of Physics Conference Series*, pages 95–107, June 1998. doi: 10.1063/1.56149.

[246] A. D. Supanitsky and G. Medina-Tanco. Neutrino initiated cascades at mid and high altitudes in the atmosphere. *Astroparticle Physics*, 35:8–16, August 2011. doi: 10.1016/j.astropartphys.2011.03.007.

[247] A. D. Supanitsky, G. Medina-Tanco, A. Guzmán, and the JEM-EUSO Collaboration. Ultra high energy photons and neutrinos with JEM-EUSO. *Experimental Astronomy*, October 2013. doi: 10.1007/s10686-013-9353-2.

[248] A. D. Supanitsky et al. A study on JEM-EUSO's trigger probabillity for neutrino-initiated EAS. In *Proceedings of the International Cosmic Ray Conference*, International Cosmic Ray Conference Rio de Janeiro, Brazil, 2013.

[249] E. Taddei. Trackdirection2 software module, 2004. URL `svn+ssh://svn.in2p3.fr/esaf/trunk/esaf/packages/reconstruction/modules/shower/fitting/src/TrackDirection2Module.cc`.

[250] E. Taddei. Studio di algoritmi per la riconstruzione della direzione degli sciami atmosferici in euso. Master's thesis, Universita Degli Studi Di Firenze, 2004.

[251] Y. Takahashi and JEM-EUSO Collaboration. The JEM-EUSO mission. *New Journal of Physics*, 11(6):065009, June 2009. doi: 10.1088/1367-2630/11/6/065009.

[252] M. Takeda, N. Hayashida, K. Honda, N. Inoue, K. Kadota, F. Kakimoto, K. Kamata, S. Kawaguchi, Y. Kawasaki, N. Kawasumi, E. Kusano, Y. Matsubara, K. Murakami, M. Nagano, D. Nishikawa, H. Ohoka, S. Osone, N. Sakaki, M. Sasaki, K. Shinozaki, N. Souma, M. Teshima, R. Torii, I. Tsushima, Y. Uchihori, T. Yamamoto, S. Yoshida, and H. Yoshii. Small-Scale Anisotropy of Cosmic Rays above 10^19 eV Observed with the Akeno Giant Air Shower Array. *The Astrophysical Journal*, 522:225–237, September 1999. doi: 10.1086/307646.

[253] Y. Tameda. HiRes and TA Composition Measurements. *EPJ Web of Conferences*, 53:04005, 2013. doi: 10.1051/epjconf/20135304005. URL http://dx.doi.org/10.1051/epjconf/20135304005.

[254] G. M. Tanco. Cosmic Magnetic Fields from the Perspective of Ultra-High-Energy Cosmic Rays Propagation. In M. Lemoine and G. Sigl, editors, *Physics and Astrophysics of Ultra-High-Energy Cosmic Rays*, volume 576 of *Lecture Notes in Physics, Berlin Springer Verlag*, page 155, 2001.

[255] The CERN Press Office. The first LHC protons run ends with new milestone. *CERN press release*, December 2012. URL http://press.web.cern.ch/press-releases/2012/12/first-lhc-protons-run-ends-new-milestone. Online; accessed 15-February-2014.

[256] The EUSO Consortium. The EUSO Mission. *Nuclear Physics B Proceedings Supplements*, 134:15–22, September 2004. doi: 10.1016/j.nuclphysbps.2004.08.002.

[257] The JEM-EUSO Collaboration. *Report on the Phase-A Study 2010 (Purple Book)*. The JEM-EUSO Collaboration, 2011.

[258] The JEM-EUSO Collaboration. The JEM-EUSO Mission: Contributions to the ICRC 2013. *ArXiv e-prints*, July 2013.

[259] The JEM-EUSO Collaboration. EUSO-Balloon — A pathfinder mission for JEM-EUSO. *The EUSO-Balloon Website*, March 2014. URL http://euso-balloon.lal.in2p3.fr/. Online; accessed 12-March-2014.

[260] The JEM-EUSO Collaboration. Mini EUSO. *Italian Collaboration Website*, March 2014. URL http://jem-euso.roma2.infn.it/?page_id=818. Online; accessed 7-March-2014.

[261] The JEM-EUSO Collaboration, :, J. H. Adams, Jr, S. Ahmad, J.-N. Albert, D. Allard, M. Ambrosio, L. Anchordoqui, A. Anzalone, Y. Arai, et al. The JEM-EUSO Mission: Status and Prospects in 2011. *ArXiv e-prints*, April 2012.

[262] A. Thea. *Osservazione di radiazione cosmica di altissima energia dallo spazio*. PhD thesis, Universita Degli Studi Di Genova, 2003.

[263] A. Thea, C. Berat, S. Bottai, O. Catalano, G. D'Alì Staiti, J. Dolbeau, M. C. Maccarone, S. Moreggia, D. Naumov, M. Pallavicini, R. Pesce, A. Petrolini, E. Plagnol, A. Stutz, and E. Taddei. The EUSO Simulation and Analysis Framework. In *Proceedings of the International Cosmic Ray Conference*, volume 9 of *International Cosmic Ray Conference*, pages 133–136, 2005.

[264] Tomida, T., Chikawa, M., Fukushima, M., Honda, K., Ikeda, D., Matthews, J., Ogio, S., Oku, D., Shibata, H., Tokuno, H., Tsunesada, Y., and Udo, S. Atmospheric monitor for telescope array experiment. *EPJ Web of Conferences*, 53: 10003, 2013. doi: 10.1051/epjconf/20135310003. URL http://dx.doi.org/10.1051/epjconf/20135310003.

[265] S. Toscano, J. A. Morales de los Rios, A. Neronov, M. Rodriguez-Frias, S. Wada, and the JEM-EUSO Collaboration. The Atmospheric Monitoring System of the JEM-EUSO Instrument. *Accepted by Experimental Astronomy*, May 2014.

[266] S. Toscano, A. Neronov, M. D. Rodríguez Frías, and S. Wada for the JEM-EUSO Collaboration. The Atmospheric Monitoring system of the JEM-EUSO telescope. *ArXiv e-prints*, February 2014.

[267] M. D. Trigo, J. C. A. Miller-Jones, S. Migliari, J. W. Broderick, and T. Tzioumis. Baryons in the relativistic jets of the stellar-mass black-hole candidate 4U1630-47. *Nature*, 504:260–262, December 2013. doi: 10.1038/nature12672.

[268] Unknown Author. Seven days: 18-24 May 2012. *Nature*, 485:420–421, May 2012. doi: 10.1038/485420a.

[269] A. Unsoeld and B. Baschek. *Der neue Kosmos*. Springer, Berlin Heidelberg, seventh edition, 2002.

[270] P. von Ballmoos and the JEM-EUSO Collaboration. The EUSO-Balloon Pathfinder. *Submittted to Experimental Astronomy*, May 2014.

[271] P. von Ballmoos, S. Dagoret, A. Santangelo, J.H. Adams, P. Barrillon, J. Bayer, M. Bertaina, F. Cafagna, M. Casolino, G. Distratis, M. Dupieux, A. Ebersoldt, T. Ebisuzaki, Ph. Gorodetzky, A. Haungs, A. Jung, Y. Kawasaki, G. Medina-Tanco, B. Mot, G. Osteria, E. Parizot, I.H. Park, P. Picozza, G. Prévôt, H. Prieto, M. Ricci, M.D. Rodríguez Frías, G. Roudil, V. Scotti, J. Szabelski, Y. Takizawa, and K. Tsuno. Euso-balloon a pathfinder for detecting uhecr's from the

edge of space. *EPJ Web of Conferences*, 53:09003, 2013. doi: 10.1051/epjconf/20135309003. URL http://dx.doi.org/10.1051/epjconf/20135309003.

[272] E. Waxman and J. Bahcall. High energy neutrinos from astrophysical sources: An upper bound. *Physical Review D*, 59(2):023002, January 1999. doi: 10.1103/PhysRevD.59.023002.

[273] E. Waxman and J. Miralda-Escude. Images of Bursting Sources of High-Energy Cosmic Rays: Effects of Magnetic Fields. *Astrophysical Journal Letters*, 472:L89, December 1996. doi: 10.1086/310367.

[274] G. J. Wieczorek, M. Giller, A. Kacperczyk, J. Malinowski, H. Stojek, W. Tkaczyk, and Wieczorek. On the Cherenkov Light Contribution to the Fluorescence of the Highest Energy Air Showers. In *Proceedings of the International Cosmic Ray Conference*, volume 2 of *International Cosmic Ray Conference*, pages 619–+, July 2003.

[275] L. Wiencke. The JEM-EUSO Mission. In *APS Meeting Abstracts*, page 14001, April 2013.

[276] L. Wiencke. Interdisciplinary science with large aperture detectors. *EPJ Web of Conferences*, 53:11001, 2013. doi: 10.1051/epjconf/20135311001. URL http://dx.doi.org/10.1051/epjconf/20135311001.

[277] Q. Xu and L. M. Brown. The early history of cosmic ray research. *American Journal of Physics*, 55:23–33, January 1987. doi: 10.1119/1.14967.

[278] S. Yoshida. The Air Fluorescence Method for Measuring Extremely-High-Energy Cosmic Rays. In M. Lemoine and G. Sigl, editors, *Physics and Astrophysics of Ultra-High-Energy Cosmic Rays*, volume 576 of *Lecture Notes in Physics, Berlin Springer Verlag*, page 45, 2001.

[279] G. T. Zatsepin and V. A. Kuz'min. Upper Limit of the Spectrum of Cosmic Rays. *Soviet Journal of Experimental and Theoretical Physics Letters*, 4:78, August 1966.

Appendix

Appendix A

A detailed view and the dimensions of the 'Trunk' of the SpaceX Dragon.

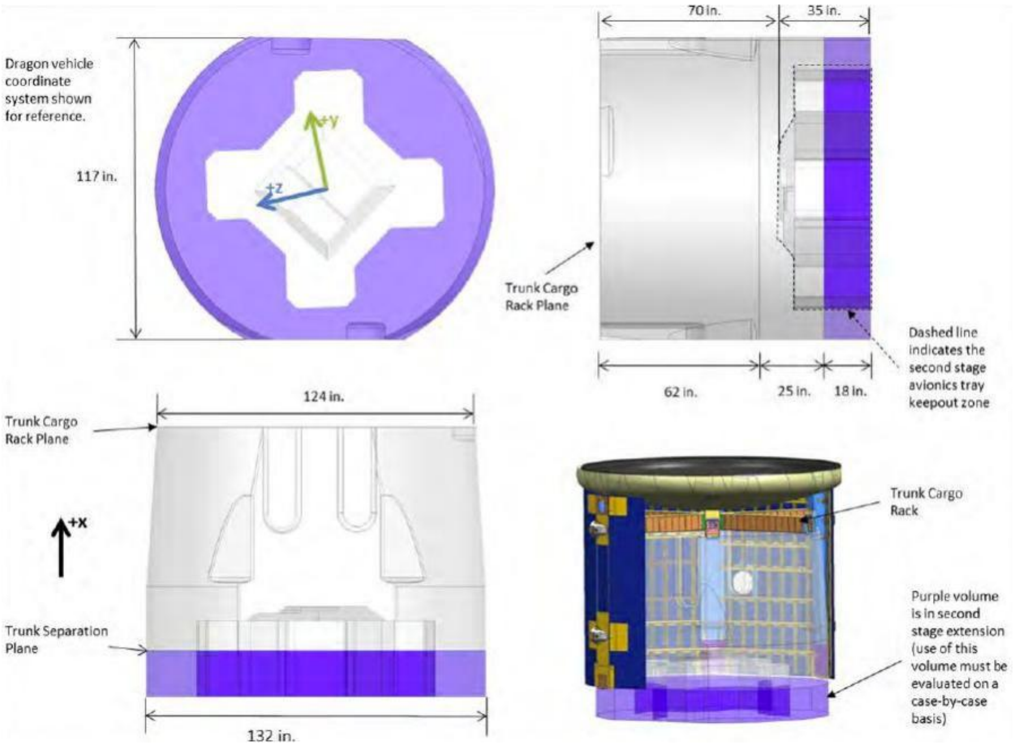

Figure 7.2.1: Space available for payload in the SpaceX Dragon Trunk. Taken from [9].

APPENDIX B: THE JEM-EUSO COLLABORATION. FULL MEMBER LIST

The Collaboration:
J.H. Adams Jr.[md], S. Ahmad[bb], J.-N. Albert[ba], D. Allard[bc], L. Anchordoqui[mf], V. Andreev[me], A. Anzalone[dh,dn], Y. Arai[ev], K. Asano[et], M. Ave Pernas[kc], P. Barrillon[ba], T. Batsch[hc], J. Bayer[cd], T. Belenguer[kb], R. Bellotti[da,db], K. Belov[me], A.A. Berlind[mh], M. Bertaina[dk,dl], P.L. Biermann[cb], S. Biktemerova[ia], C. Blaksley[bc], N. Blanc[la], J. Błęcki[hd], S. Blin-Bondil[bb], J. Blümer[cb], P. Bobik[ja], M. Bogomilov[aa], M. Bonamente[md], M.S. Briggs[md], S. Briz[kd], A. Bruno[da], F. Cafagna[da], D. Campana[df], J-N. Capdevielle[bc], R. Caruso[dc,dn], M. Casolino[ew,di], C. Cassardo[dk,dl], G. Castellini[dd], C. Catalano[bd], O. Catalano[dh,dn], A. Cellino[dk,dm], M. Chikawa[ed], M.J. Christl[mg], D. Cline[me], V. Connaughton[md], L. Conti[do], G. Cordero[ga], H.J. Crawford[ma], R. Cremonini[dl], S. Csorna[mh], S. Dagoret-Campagne[ba], A.J. de Castro[kd], C. De Donato[di], C. de la Taille[bb], C. De Santis[di,dj], L. del Peral[kc], A. Dell'Oro[dk,dm] N. De Simone[di], M. Di Martino[dk,dm], G. Distratis[cd], F. Dulucq[bb], M. Dupieux[bd], A. Ebersoldt[cb], T. Ebisuzaki[ew], R. Engel[cb], S. Falk[cb], K. Fang[mb], F. Fenu[cd], I. Fernández-Gómez[kd], S. Ferrarese[dk,dl], D. Finco[do], M. Flamini[do], C. Fornaro[do], A. Franceschi[de], J. Fujimoto[ev], M. Fukushima[eg], P. Galeotti[dk,dl], G. Garipov[ic], J. Geary[md], G. Gelmini[me], G. Giraudo[dk], M. Gonchar[ia], C. González Alvarado[kb], P. Gorodetzky[bc], F. Guarino[df,dg], A. Guzmán[cd], Y. Hachisu[ew], B. Harlov[ib], A. Haungs[cb], J. Hernández Carretero[kc], K. Higashide[er,ew], D. Ikeda[eg], H. Ikeda[ep], N. Inoue[er], S. Inoue[eg], A. Insolia[dc,dn], F. Isgrò[df,dp], Y. Itow[en], E. Joven[ke], E.G. Judd[ma], A. Jung[fb], F. Kajino[ei], T. Kajino[el], I. Kaneko[ew], Y. Karadzhov[aa], J. Karczmarczyk[hc], M. Karus[cb], K. Katahira[ew], K. Kawai[ew], Y. Kawasaki[ew], B. Keilhauer[cb], B.A. Khrenov[ic], Jeong-Sook Kim[fa], Soon-Wook Kim[fa], Sug-Whan Kim[fd], M. Kleifges[cb], P.A. Klimov[ic], D. Kolev[aa], I. Kreykenbohm[ca], K. Kudela[ja], Y. Kurihara[ev], A. Kusenko[me], E. Kuznetsov[md], M. Lacombe[bd], C. Lachaud[bc], J. Lee[fc], J. Licandro[ke], H. Lim[fc], F. López[kd], M.C. Maccarone[dh,dn], K. Mannheim[ce], D. Maravilla[ga], L. Marcelli[dj], A. Marini[de], O. Martinez[gc], G. Masciantonio[di,dj], K. Mase[ea], R. Matev[aa], G. Medina-Tanco[ga], T. Mernik[cd], H. Miyamoto[ba], Y. Miyazaki[ec], Y. Mizumoto[el], G. Modestino[de], A. Monaco[da,db], D. Monnier-Ragaigne[ba], J.A. Morales de los Ríos[ka,kc], C. Moretto[ba], V.S. Morozenko[ic], B. Mot[bd], T. Murakami[ef], M. Nagano[ec], M. Nagata[eh], S. Nagataki[ek], T. Nakamura[ej], T. Napolitano[de], D. Naumov[ia], R. Nava[ga], A. Neronov[lb], K. Nomoto[eu], T. Nonaka[eg], T. Ogawa[ew], S. Ogio[eo], H. Ohmori[ew], A.V. Olinto[mb], P. Orleański[hd], G. Osteria[df], M.I. Panasyuk[ic], E. Parizot[bc], I.H. Park[fc], H.W. Park[fc], B. Pastircak[ja], T. Patzak[bc], T. Paul[mf], C. Pennypacker[ma], S. Perez Cano[kc], T. Peter[lc], P. Picozza[di,dj,ew], T. Pierog[cb], L.W. Piotrowski[ew], S. Piraino[cd,dh], Z. Plebaniak[hc], A. Pollini[la], P. Prat[bc], G. Prévôt[bc], H. Prieto[kc], M. Putis[ja], P. Reardon[md], M. Reyes[ke], M. Ricci[de], I. Rodríguez[kd], M.D. Rodríguez Frías[kc], F. Ronga[de], M. Roth[cb], H. Rothkaehl[hd], G. Roudil[bd], I. Rusinov[aa], M. Rybczyński[ha], M.D. Sabau[kb], G. Sáez Cano[kc], H. Sagawa[eg], A. Saito[ej], N. Sakaki[cb], M. Sakata[ei], H. Salazar[gc], S. Sánchez[kd], A. Santangelo[cd], L. Santiago Crúz[ga], M. Sanz Palomino[kb], O. Saprykin[ib], F. Sarazin[mc], H. Sato[ei], M. Sato[es], T. Schanz[cd], H. Schieler[cb], V. Scotti[df,dg], A. Segreto[dh,dn], S. Selmane[bc], D. Semikoz[bc], M. Serra[ke], S. Sharakin[ic], T. Shibata[eq], H.M. Shimizu[em], K. Shinozaki[ew], T. Shirahama[er], G. Siemieniec-Oziębło[hb], H.H. Silva López[ga], J. Sledd[mg], K. Słomińska[hd], A. Sobey[mg], T. Sugiyama[em], D. Supanitsky[ga], M. Suzuki[ep], B. Szabelska[hc], J. Szabelski[hc], F. Tajima[ee], N. Tajima[ew], T. Tajima[cc], Y. Takahashi[es], H. Takami[ev], M. Takeda[eg], Y. Takizawa[ew], C. Tenzer[cd], O. Tibolla[ce], L. Tkachev[ia], H. Tokuno[et], T. Tomida[ew], N. Tone[ew], S. Toscano[lb], F. Trillaud[ga], R. Tsenov[aa], Y. Tsunesada[et], K. Tsuno[ew], T. Tymieniecka[hc], Y. Uchihori[eb], M. Unger[cb], O. Vaduvescu[ke], J.F. Valdés-Galicia[ga], P. Vallania[dk,dm], L. Valore[df,dg], G. Vankova[aa], C. Vigorito[dk,dl], L. Villaseñor[gb], P. von Ballmoos[bd], S. Wada[ew], J. Watanabe[el], S. Watanabe[es], J. Watts Jr.[md], M. Weber[cb], T.J. Weiler[mh], T. Wibig[hc], L. Wiencke[mc], M. Wille[ca], J. Wilms[ca], Z. Włodarczyk[ha], T. Yamamoto[ei], Y. Yamamoto[ei], J. Yang[fb], H. Yano[ep], I.V. Yashin[ic], D. Yonetoku[ef], K. Yoshida[ei], S. Yoshida[ea], R. Young[mg], M.Yu. Zotov[ic], A. Zuccaro Marchi[ew]

[aa] St. Kliment Ohridski University of Sofia, Bulgaria
[ba] LAL, Univ Paris-Sud, CNRS/IN2P3, Orsay, France
[bb] Omega, Ecole Polytechnique, CNRS/IN2P3, Palaiseau, France
[bc] APC, Univ Paris Diderot, CNRS/IN2P3, CEA/Irfu, Obs de Paris, Sorbonne Paris Cité, France
[bd] IRAP, Université de Toulouse, CNRS, Toulouse, France
[ca] ECAP, University of Erlangen-Nuremberg, Germany
[cb] Karlsruhe Institute of Technology (KIT), Germany
[cc] Ludwig Maximilian University, Munich, Germany
[cd] Institute for Astronomy and Astrophysics, Kepler Center, University of Tübingen, Germany
[ce] Institut für Theoretische Physik und Astrophysik, University of Würzburg, Germany
[da] Istituto Nazionale di Fisica Nucleare - Sezione di Bari, Italy
[db] Universita'degli Studi di Bari Aldo Moro and INFN - Sezione di Bari, Italy
[dc] Dipartimento di Fisica e Astronomia - Universita' di Catania, Italy
[dd] Cons. Nazionale delle Ricerche - Ist. di Fisica Applicata Nello Carrara, Firenze, Italy
[de] Istituto Nazionale di Fisica Nucleare - Laboratori Nazionali di Frascati, Italy
[df] Istituto Nazionale di Fisica Nucleare - Sezione di Napoli, Italy
[dg] Universita' di Napoli Federico II - Dipartimento di Scienze Fisiche, Italy
[dh] INAF - Istituto di Astrofisica Spaziale e Fisica Cosmica di Palermo, Italy
[di] Istituto Nazionale di Fisica Nucleare - Sezione di Roma Tor Vergata, Italy
[dj] Universita' di Roma Tor Vergata - Dipartimento di Fisica, Roma, Italy
[dk] Istituto Nazionale di Fisica Nucleare - Sezione di Torino, Italy
[dl] Dipartimento di Fisica, Universita' di Torino, Italy
[dm] Osservatorio Astrofisico di Torino, Istituto Nazionale di Astrofisica, Italy
[dn] Istituto Nazionale di Fisica Nucleare - Sezione di Catania, Italy
[do] UTIU, Dipartimento di Ingegneria, Rome, Italy

[dp] DIETI, Universita' degli Studi di Napoli Federico II, Napoli, Italy
[ea] Chiba University, Chiba, Japan
[eb] National Institute of Radiological Sciences, Chiba, Japan
[ec] Fukui University of Technology, Fukui, Japan
[ed] Kinki University, Higashi-Osaka, Japan
[ee] Hiroshima University, Hiroshima, Japan
[ef] Kanazawa University, Kanazawa, Japan
[eg] Institute for Cosmic Ray Research, University of Tokyo, Kashiwa, Japan
[eh] Kobe University, Kobe, Japan
[ei] Konan University, Kobe, Japan
[ej] Kyoto University, Kyoto, Japan
[ek] Yukawa Institute, Kyoto University, Kyoto, Japan
[el] National Astronomical Observatory, Mitaka, Japan
[em] Nagoya University, Nagoya, Japan
[en] Solar-Terrestrial Environment Laboratory, Nagoya University, Nagoya, Japan
[eo] Graduate School of Science, Osaka City University, Japan
[ep] Institute of Space and Astronautical Science/JAXA, Sagamihara, Japan
[eq] Aoyama Gakuin University, Sagamihara, Japan
[er] Saitama University, Saitama, Japan
[es] Hokkaido University, Sapporo, Japan
[et] Interactive Research Center of Science, Tokyo Institute of Technology, Tokyo, Japan
[eu] University of Tokyo, Tokyo, Japan
[ev] High Energy Accelerator Research Organization (KEK), Tsukuba, Japan
[ew] RIKEN Advanced Science Institute, Wako, Japan
[fa] Korea Astronomy and Space Science Institute (KASI), Daejeon, Republic of Korea
[fb] Ewha Womans University, Seoul, Republic of Korea
[fc] Sungkyunkwan University, Seoul, Republic of Korea
[fd] Center for Galaxy Evolution Research, Yonsei University, Seoul, Republic of Korea
[ga] Universidad Nacional Autónoma de México (UNAM), Mexico
[gb] Universidad Michoacana de San Nicolas de Hidalgo (UMSNH), Morelia, Mexico
[gc] Benemérita Universidad Autónoma de Puebla (BUAP), Mexico
[ha] Jan Kochanowski University, Institute of Physics, Kielce, Poland
[hb] Jagiellonian University, Astronomical Observatory, Krakow, Poland
[hc] National Centre for Nuclear Research, Lodz, Poland
[hd] Space Research Centre of the Polish Academy of Sciences (CBK), Warsaw, Poland
[ia] Joint Institute for Nuclear Research, Dubna, Russia
[ib] Central Research Institute of Machine Building, TsNIIMash, Korolev, Russia
[ic] Skobeltsyn Institute of Nuclear Physics, Lomonosov Moscow State University, Russia
[ja] Institute of Experimental Physics, Kosice, Slovakia
[ka] Consejo Superior de Investigaciones Científicas (CSIC), Madrid, Spain
[kb] Instituto Nacional de Técnica Aeroespacial (INTA), Madrid, Spain
[kc] Universidad de Alcalá (UAH), Madrid, Spain
[kd] Universidad Carlos III de Madrid, Spain
[ke] Instituto de Astrofísica de Canarias (IAC), Tenerife, Spain
[la] Swiss Center for Electronics and Microtechnology (CSEM), Neuchâtel, Switzerland
[lb] ISDC Data Centre for Astrophysics, Versoix, Switzerland
[lc] Institute for Atmospheric and Climate Science, ETH Zürich, Switzerland
[ma] Space Science Laboratory, University of California, Berkeley, USA
[mb] University of Chicago, USA
[mc] Colorado School of Mines, Golden, USA
[md] University of Alabama in Huntsville, Huntsville, USA
[me] University of California (UCLA), Los Angeles, USA
[mf] University of Wisconsin-Milwaukee, Milwaukee, USA
[mg] NASA - Marshall Space Flight Center, USA
[mh] Vanderbilt University, Nashville, USA

Appendix C: Simulation Parameters JEM-EUSO, Nadir Mode

```
## config file dump generated by ESAF
   ## Dump for class name BunchRadiativeTransfer
BunchRadiativeTransfer.DepthStep = 10
BunchRadiativeTransfer.fStep-along-track = 0.5
BunchRadiativeTransfer.fCloudStatus = yes
BunchRadiativeTransfer.fDecoupled = optimized
## End of dump for class name BunchRadiativeTransfer

## Dump for class name CCB-LTTTrigger
CCB-LTTTrigger.EC-PDM = 0
CCB-LTTTrigger.fDebug = 0
CCB-LTTTrigger.fGtu-light = 0.74981
CCB-LTTTrigger.fPixel-size = 0.55 # AVE. OVER FS (PPP2010)
CCB-LTTTrigger.fInputTrigger = 1
CCB-LTTTrigger.fIntegrateSum = 97 # FOR AVE. BG LEVEL (0.42)
CCB-LTTTrigger.fNum-Dir = 324
CCB-LTTTrigger.fNum-Steps = 7
CCB-LTTTrigger.fYellowThreshold = 3 # 2
CCB-LTTTrigger.fDataDirectory = DirectionFiles
CCB-LTTTrigger.fDirectionFileName = angles-liv3.dat
## End of dump for class name CCB-LTTTrigger

## Dump for class name ConicBaffle
ConicBaffle.fTopRadius = 1325. # baffle radius
ConicBaffle.fPos.Z = 132.894280 # the base of the bottom lens
ConicBaffle.DZdown = 134 # height of the baffle
ConicBaffle.fAlpha = 36 # TO SECURE FOV # baffle's field of view
## End of dump for class name ConicBaffle

## Dump for class name DetectorTransportManager
DetectorTransportManager.fInnerRadius = 1325
DetectorTransportManager.fMaxIterations = 10
## End of dump for class name DetectorTransportManager

## Dump for class name ElectronicsFactory
ElectronicsFactory.AfeeType = Full
ElectronicsFactory.Detector = Euso
ElectronicsFactory.ElementaryCellType = Standard
ElectronicsFactory.FrontEndType = Standard
ElectronicsFactory.MacroCellType = Standard
ElectronicsFactory.PmtType = R8900M64Photomultiplier
```

```
ElectronicsFactory.TelemetryType = Standard
## End of dump for class name ElectronicsFactory

## Dump for class name Euso
Euso.fAltitude = 400 # ALTITUDE 400KM
Euso.fRadius = 1325
Euso.fLightToEuso = standard
## End of dump for class name Euso

## Dump for class name EusoDetector
EusoDetector.fFieldOfView = 36
EusoDetector.fMaxRadius = 1325
EusoDetector.fScaleFactor = 1
EusoDetector.fFixMaxRadius = yes
## End of dump for class name EusoDetector

## Dump for class name EusoElectronics
EusoElectronics.fFrontEndSize = 256 # (M64)
EusoElectronics.fLowSignalMacrocellThreshold = 3
EusoElectronics.fNightGlowCode = -2
EusoElectronics.fNightGlowEnd = -1
EusoElectronics.fNightGlowRadiance = 500
EusoElectronics.fNightGlowRateOnAxis = 0.42
EusoElectronics.fNightGlowStart = -1
EusoElectronics.fPmtSide = 8
EusoElectronics.fAddRandomGtuPhase = yes
EusoElectronics.fEnable = yes
EusoElectronics.fFocalSurfaceFile = @cfg/Electronics/layout-137-PPP2010-08c-m64-pmt27mm.fsr
EusoElectronics.fNightGlow = byRate
EusoElectronics.fNightGlowShape = Flat
EusoElectronics.fSimulateLowSignalMacroCells = absolute
## End of dump for class name EusoElectronics

## Dump for class name EusoMapping
EusoMapping.fMapFile = @cfg/Optics/mapKenji-NEW.gz
EusoMapping.fUseCache = no
## End of dump for class name EusoMapping

################ ## Dump for class name IdealOpticalAdaptor
IdealOpticalAdaptor.fCathode.reflectivity = 0
IdealOpticalAdaptor.fFilterThickness = 2
IdealOpticalAdaptor.fHeight = 20
```

```
IdealOpticalAdaptor.fSide = 27
IdealOpticalAdaptor.fSmallSide = 23.6616
IdealOpticalAdaptor.fFilter = BG3
## End of dump for class name IdealOpticalAdaptor

## Dump for class name LowtranManager
LowtranAtmosphere.Gndalt = 0
LowtranAtmosphere.Icld = 0
LowtranAtmosphere.Icstl = 0
LowtranAtmosphere.Ihaze = 0
LowtranAtmosphere.Im = 1
LowtranAtmosphere.Iseasn = 0
LowtranAtmosphere.Ivsa = 0
LowtranAtmosphere.Ivulcn = 0
LowtranAtmosphere.Linf = 250
LowtranAtmosphere.Lsup = 485
LowtranAtmosphere.Noprt = 0
LowtranAtmosphere.Rainrt = 0
LowtranAtmosphere.Salb = 0
LowtranAtmosphere.Vis = 0
LowtranAtmosphere.Whh = 0
LowtranAtmosphere.Wss = 0
LowtranAtmosphere.model = 6
## End of dump for class name LowtranAtmosphere

## Dump for class name LowtranRadiativeProcessesCalculator
LowtranRadiativeProcessesCalculator.fStep-detector = 0.5
## End of dump for class name LowtranRadiativeProcessesCalculator

## Dump for class name MacroCell
MacroCell.fGtuTimeLength = 2500
MacroCell.fSize = 200
MacroCell.fTriggerThreshold = 5
MacroCell.fTriggerType = 10240 # PTT+CCB-LTT TRIGGER
MacroCell.fLogicEnabled = no
MacroCell.fSaveAllChipGtuData = yes
## End of dump for class name MacroCell

## Dump for class name NOpticalSystem
NOpticalSystem.EsafRandom = 0
NOpticalSystem.fPos.Z = 0
NOpticalSystem.lens-dir = config/Optics/NOpticalSystem/
NOpticalSystem.tel-par = telparm-PPP-2010-08a-NOptics
```

```
## End of dump for class name NOpticalSystem

## Dump for class name OpticsFactory
OpticsFactory.fBaffle = ConicBaffle
OpticsFactory.fFocalPlane = PolarFocalPlane
OpticsFactory.fIdealFocalSurface = NIdealFocalSurface
OpticsFactory.fOpticalAdaptor = IdealOpticalAdaptor #FakeOpticalAdapator
OpticsFactory.fOpticalSystem = NOpticalSystem
OpticsFactory.fTransportManager = Standard
OpticsFactory.fWalls = WallInteraction
## End of dump for class name OpticsFactory

## Dump for class name PTTTrigger
PTTTrigger.Integration = 32 # FOR AVE. BG LEVEL (0.42)
PTTTrigger.Persistency = 5
PTTTrigger.PixelThr = 3 # 2 # FOR AVE. BG LEVEL (0.42)
PTTTrigger.fDebug = 0
## End of dump for class name PTTTrigger

## Dump for class name PolarFocalPlane
PolarFocalPlane.fDZdown = 500
PolarFocalPlane.fPos.Z = 3593.141 # FOR PPP2010 OPTICS
PolarFocalPlane.fRadius = 1325
## End of dump for class name PolarFocalPlane

## Dump for class name R8900M64Photomultiplier
Photomultiplier.PmtDeadInner = 0.001
Photomultiplier.PmtDeadLateral = 1.6692
Photomultiplier.PmtGain = 4.8e+06
Photomultiplier.PmtGainSigma = 910000
Photomultiplier.PmtQuantum = 0.2695
Photomultiplier.PmtSide = 8
Photomultiplier.PmtSize = 27
Photomultiplier.PmtTimeWidth = 1
Photomultiplier.fDarkNoiseRate = 0
R8900M64Photomultiplier.fAngularDependence.FileName = AngularDependence.dat
R8900M64Photomultiplier.fCollectionEfficiency.FileName = AverageCollectionEfficiency-m64-0.80.dat
R8900M64Photomultiplier.fCrossTalk.FileName = AverageCrossTalk-m64-nocrosstalk.dat
R8900M64Photomultiplier.fQuantumEfficiency.FileName = AverageQuantumEfficiency20070827.dat
R8900M64Photomultiplier.fgUsePmtAdd = no
## End of dump for class name R8900M64Photomultiplier
```

```
## Dump for class name RadiativeFactory
RadiativeFactory.ClearSkyPropagator = alongtrack
RadiativeFactory.Ground = test
RadiativeFactory.RadiativeProcessesCalculator = lowtran
## End of dump for class name RadiativeFactory

## Dump for class name ShowerLightSource
ShowerLightSource.fLambdaMax = 485
ShowerLightSource.fLambdaMin = 250
ShowerLightSource.AngularDistributionName = baltru
ShowerLightSource.CrkCalculator = simple
ShowerLightSource.EnergyDistributionName = giller
ShowerLightSource.EnergyDistributionType = parametrized
ShowerLightSource.FluoCalculator = nagano
ShowerLightSource.LateralDistributionName = NKGhadron
ShowerLightSource.fUseAngDev = no
## End of dump for class name ShowerLightSource

## Dump for class name SimuRootFileManager
SimuRootFileManager.fMaxFileSize = 1000
SimuRootFileManager.fDetector.fNightGlowFillable = yes
SimuRootFileManager.fDetector.fPhotonFillable = yes
SimuRootFileManager.fDetector.fPhotonFillingMode = All
SimuRootFileManager.fRootOutputFile = output/euso
SimuRootFileManager.fSaveAtmosphere = yes
SimuRootFileManager.fSaveCCB-LTTTrigger = yes
SimuRootFileManager.fSaveChipTrackTrigger = no # yes
SimuRootFileManager.fSaveDetector = yes
SimuRootFileManager.fSaveLTTTrigger = no # noyes
SimuRootFileManager.fSaveLblTrackTrigger = yes
SimuRootFileManager.fSavePTTTrigger = yes
SimuRootFileManager.fSaveRunTree = yes
SimuRootFileManager.fSaveShower = yes
SimuRootFileManager.fSaveSimpleDetector = yes
## End of dump for class name SimuRootFileManager

## Dump for class name StandardLightToEuso
StandardLightToEuso.fGenerator = slast++
StandardLightToEuso.fLightSource = shower
StandardLightToEuso.fRadiativeTransfer = bunch
## End of dump for class name StandardLightToEuso

SlastLightToEuso.Albedo = 0.05
```

```
SlastLightToEuso.AtmTemperature = 288
SlastLightToEuso.GTU = 0.8
SlastLightToEuso.WaveRangeMax = 485
SlastLightToEuso.WaveRangeMin = 250
SlastLightToEuso.AtmCurvature = Curved
SlastLightToEuso.AtmosphericType = USStandard
SlastLightToEuso.DoCherenkov = yes
SlastLightToEuso.DoFluorescence = yes
SlastLightToEuso.EnergyDistributionParametrization = Hillas
SlastLightToEuso.ShowerParametrization = GIL
## End of dump for class name SlastLightToEuso

## Dump for class name TestGround
TestGround.fAlbedo = 0.05
TestGround.fAltitude = 0
TestGround.fSigma = -1
TestGround.fSpec = 0.75
TestGround.fWindSpeed = 11
TestGround.fType = lambertian
## End of dump for class name TestGround

## Dump for class name WallInteraction
WallInteraction.fSpecularReflectivity = 0
## End of dump for class name WallInteraction

#PhPRootFileLightToEuso.fAltitude = 400


    GeneratorLightToEuso.DepthStep = 10 # Step for the shower development [g/cm2] 10
GeneratorLightToEuso.InteractionType = none # random X1=none, fixed position=POS, fixed X1=X1
GeneratorLightToEuso.InteractionVectorX = 140 # Interaction X Point [km]
GeneratorLightToEuso.InteractionVectorY = 140 # Interaction Y Point [km]
GeneratorLightToEuso.InteractionVectorZ = 70 # Interaction Z Point [km]
GeneratorLightToEuso.InteractionX1 = 35 # grammage of the first interaction (if fixed X1)
GeneratorLightToEuso.ImpactMode = ASL # TOA or ASL(in a square)
GeneratorLightToEuso.altitude = 400 #
GeneratorLightToEuso.FoV = 35 # Euso Field of View [deg]
GeneratorLightToEuso.RejectFakeEvents = no # reject cosmic rays that (did not interact in atmosphere || not in FoV)
GeneratorLightToEuso.RejectNoXmax = no # reject showers without Xmax in the FoV
GeneratorLightToEuso.ImpactXmin = -270 # impact X Point [km]
```

```
GeneratorLightToEuso.ImpactXmax = 270 # impact X Point [km]
GeneratorLightToEuso.ImpactYmin = -190 # impact Y Point [km]
GeneratorLightToEuso.ImpactYmax = 190 # impact Y Point [km]
```

Acronyms

AGASA: Akeno Giant Air Shower Array
AGN: Active Galactic Nuclei
AMS: Alpha Magnetic Spectrometer
ASIC: Application Specific Integrated Circuit
a.s.l.: above sea level
BABY: BAckground BYpass
BR: Baryonic resonances
CCB: Cluster Control Board
CERN: Conseil Européen pour la Recherche Nucléaire
CORSIKA: COsmic Ray SImulation for KAscade
CR: Cosmic Ray
CMB: Cosmic Microwave Background
CPU: Central Processing Unit
DLR: Deutsches Zentrum für Luft und Raumfahrt
DOF: Degrees Of Freedom
EAS: Extended Air Showers
EBL: Extragalactic Background Light
EC: Elementary Cell
ECMWF: European Centre for Medium-Range Weather Forecasts
EE: Extreme Energy
EEU: Equipment Exchange Unit
EF: Exposed Facility
ESA: European Space Agency
ESAF: Euso Simulation and Analysis Framework
EUSO: Extreme Universe Space Observatory
FEE: Front End Electronics
FOV: Field Of View
FPGA: Field Programmable Gate Array
FRAM: Flight Releasable Attachment Mechanism
FS: Focal Surface
GDR: Giant Dipol Resonance
GIL: Gaisser Ilina Linsley
GMAO: Global Modeling and Assimilation Office
GMF: Galactic Magnetic Filed

GRB: Gamma Ray Burst
GTR: General Theory of Relativity
GTU: Gate Time Unit
GZK: Greisen Zatsepin Kuzmin
HiRes: High Resolution Fly's Eye
HTV: H-II Transfer Vehicle
HST: Hubble Space Telescope
IAAT: Institut für Astronomy und Astrophysik Tübingen
IGM: InterGalactic Medium
IGMF: InterGalactic Magnetic Field
IR: InfraRed
ISM: InterStellar Medium
ISS: International Space Station
JAXA: Japan Aerospace eXploration Agency
JEM: Japanese Experimental Module
JEM-EUSO: Extreme Universe Space Observatory onboard the Japanese Experiment Module
JEMRMS: JEM Remote Manipulator System
LHC: Large Hadron Collider
LIDAR: Light Detection And Ranging
LOWTRAN: LOW-resolution TRANsmittance
LTT: Linear Tracking Trigger
MA-PMT: Multi Anode PhotoMulTiplier
MC: MonteCarlo
MDP: Mission Data Processor
NASA: North American Space Agency
NCEP: National Centers for Environmental Predictions
NS: Neutron Star
OWL: Orbiting Wide angle Light collectors
PAO: Pierre Auger Observatory
PDM: Photo Detection Module
PF: Photo-Fragmentation
PI: Principal Investigator
PMMA: PolyMethyl MethAcrylate
PMT: PhotoMulTiplier
PPP: Pair Production by Protons
PSF: Point Spread Function
Pulsar: PULSating stAR
QDP: Quasi-deuteron processes
Quasar: Quasi-Stellar Radio source
rad-hard: rad(iation)-hardened
ROC: ReadOut and Control
SCU: Storage and Control Unit

SDP: Shower Detector Plane
SHDM: Super-Heavy Dark Matter
S-EUSO: Super- Extreme Universe Space Observatory
SLAST: Shower Light Attenuated to the Space Telescope
SM: Standard Model
SNR: Supernova Remnant
SOCRAS: Satellite Observation of Cosmic Air Showers
TA: Telescope Array
TD: Topological Defect
TDP: Track Detector Plane
TLE: Transient Luminous Events
UFFO: Ultra-Fast Flash Observatory
UHE: Ultra High Energy
UHECR: Ultra High Energy Cosmic Ray
UV: Ultraviolet
VLT: Very Large Telescope

Curriculum Vitæ

PERSONAL DETAILS

Name	Thomas Mernik
Birth	1980
Address	Tübingen
Phone	(+49) 7071-2975279
Mail	`mernik(at)astro.uni-tuebingen.de`

EDUCATION

Diploma in Physics 2002-2010

Eberhard Karls Universität Tübingen, Germany

Physics studies with an emphasis on astrophysics and astronomy. Diploma thesis with the title *IT CAME FROM OUTER SPACE - Reconstruction of UHECR Events for the JEM-EUSO Mission*

Exchange Student 2006

Victoria University of Wellington, New Zealand

Physics and Maori Science Studies, Scientific writing.

Egyptian Studies 2001-2002

Universität Hamburg, Germany

Introduction to ancient Egyptian culture and religion. Middle Egyptian language.

Abitur 1997-2000

Gesamtschule Harburg, Hamburg, Germany

Advanced courses: Physics and English

WORK EXPERIENCE

Scientific Employee 2011-now

Institute for Astronomy and Astrophysics, Universität Tübingen, Germany, Full-time

Simulation and reconstruction studies for the JEM-EUSO Collaboration

Visiting Technician Jan. - Apr. 2010

RIKEN, Tokyo, Japan, Full-time

Simulation and reconstruction studies for the JEM-EUSO Collaboration

Research Assistant 2008-2010

Institute for Astronomy and Astrophysics, Universität Tübingen, Germany, Part-time

Quality assessment of the H.E.S.S. telescope mirrors for the HESS Collaboration. Simulation and reconstruction studies for the JEM-EUSO Collaboration

Alternative Civilian Service 2000-2001

Arbeiter Samariter Bund and Vereinigung Hamburger Kindertagestätten e.V., Hamburg, Germany, Full-time

Transportation of handicapped persons. School Bus Driver. Individual care for a handicapped child.

Trainee Oct. 1995

DESY – Deutsches Elektronen-Synchrotron, Hamburg, Germany, Full-time

Introduction to vacuum components, Electronics design.

SKILLS

Languages	English (fluent) German (mother tongue) French (basic)
Software	ROOT, LaTeX, Linux, C++

PUBLICATIONS

1. "Space based studies of UHE neutrinos"; A. Santangelo, K. Bittermann, T. Mernik, F. Fenu *Progress in Particle and Nuclear Physics*, 2010

2. "A simulation study on the JEM-EUSO performances with ESAF"; F. Fenu , M. Bertaina , A. Santangelo , T. Mernik , K. Shinozaki , K. Bitterman *Abstracts of the 22nd European Cosmic Ray Symposium*, 2010

3. "A simulation study on the JEM-EUSO performances with ESAF"; F. Fenu , A. Santangelo , M. Bertaina , T. Mernik , K. Shinozaki , K. Bittermann, O. Catalano, P. Bobik , S. Dagoret , G. Medina Tanco , D. Naumov , M.D. Rodriguez Frias , J. Szabelski and the JEM-EUSO collaboration *38th COSPAR Scientific Assembly*, 2010

4. “An evaluation of the exposure in nadir observation of the JEM-EUSO mission”; The JEM-EUSO collaboration *Astroparticle Physics*, 2013

5. “The ESAF-Reconstruction Framework of UHECR Events for the JEM-EUSO Mission”; T. Mernik, F. Fenu, D. D’Urso, A. Santangelo, K. Bittermann, K. Shinozaki, M. Bertaina, S. Biktemerova, D. Naumov, G. Medina-Tanco on behalf of the JEM-EUSO collaboration. *Proceedings of the International Cosmic Ray Conference*, 2011

6. “The ESAF Simulation Framework for the JEM-EUSO Mission”; F. Fenu, T. Mernik, A. Santangelo, K. Shinozaki, M. Bertaina, L. Valore, S. Biktemerova, D. Naumov, G. Medina-Tanco on behalf of the JEM-EUSO collaboration. *Proceedings of the International Cosmic Ray Conference*, 2011

7. “Estimation of aperture for extreme energy cosmic rays observation by JEM-EUSO Telescope”; K. Shinozaki, M. Bertaina, S. Biktemerova, P. Bobik, F. Fenu, A. Guzman, K. Higashide, G. Medina Tanco, T. Mernik, J. A. Morales de los Rios Pappa, D. Naumov. *Proceedings of the International Cosmic Ray Conference*, 2011

8. “Requirement and expected performances of the JEM-EUSO mission”; M. Bertaina, A. Santangelo, K. Shinozaki, F. Fenu, T. Mernik, P. Bobik, F. Guarino, K. Higashide, G. Medina-Tanco, and G. Saez-Cano on behalf of the JEM-EUSO collaboration. *Proceedings of the International Cosmic Ray Conference*, 2011

9. “The JEM-EUSO Mission: Status and Prospects in 2011”; The JEM-EUSO collaboration. *Instrumentation and Methods for Astrophysics*, 2012

10. “The Peak and Window Searching Technique for the EUSO Simulation and Analysis Framework: Impact on the angular reconstruction of EAS”; A. Guzman, T. Mernik, A. Santangelo, G. Medina-Tanco, M. Bertaina, K. Shinozaki, F. Fenu, A. Gorgi and the JEM-EUSO collaboration. *Journal of Physics*, 2013

11. “Performances of JEM-EUSO”; M. Bertaina, P. Bobik, F. Fenu, F. Garino, A. Guzman, K. Higashide, G. Medina Tanco, T. Mernik, G. Saez Cano, A. Santangelo and K. Shinozaki. *UHECR 2012 - International Symposium on Future Directions in UHECR Physics*, 2013

12. “ESAF-Simulation of the EUSO-Balloon”; T. Mernik, A. Guzman, A. Santangelo, K. Shinozaki, N. Sakaki, C. Moretto, D. Monnier-Ragaigne, H. Miyamoto, S. Dagoret-Campagne, C. Catalano, P. von Ballmooss for the JEM-EUSO Collaboration. *Proceedings of the International Cosmic Ray Conference*, 2013

13. “Simulating the JEM-EUSO Mission: Expected Reconstruction Performance”; T. Mernik, A. Guzman, F. Fenu, K. Shinozaki, A. Santangelo, M. Bertaina for the JEM-EUSO collaboration. *Proceedings of the International Cosmic Ray Conference*, 2013

14. "UV night background estimation in South Atlantic Anomaly"; P. Bobik, M. Putis, M. Bertaina, S. Biktemerova, D. Campana, F. Fenu, F. Guarino, K. Kudela, T. Mernik, B. Pastircak, K. Shinozaki for the JEM-EUSO collaboration. *Proceedings of the International Cosmic Ray Conference*, 2013

15. "A study on JEM-EUSO's trigger probabillity for neutrino-initiated EAS"; A. Guzman, D. Supanitsky, E. Iwotschkin, T. Mernik, F. Fenu, G. Medina-Tanco, A. Santangelo for the JEM-EUSO collaboration. *Proceedings of the International Cosmic Ray Conference*, 2013

16. "Performances and air-shower reconstruction techniques for the JEM-EUSO mission"; M. Bertaina, S. Biktemerova, K. Bittermann, P. Bobik, D. Campana, F. Fenu, A. Gorgi, F. Guarino, A. Guzman, K. Higashide, G. Medina-Tanco, T. Mernik, D. Naumov, M. Putis, M. D. Rodriguez Frias, S. Toscano. *Journal for Advances in Space Research*, 2014

17. "Performances of JEM-EUSO: angular reconstruction"; The JEM-EUSO collaboration, corresponding authors: S. Biktemerova, A. Guzman, T. Mernik. *Experimental Astronomy*, 2014

WORKSHOPS

ISPA, International Symposium on Parallel and Distributed Processing with Applications Jul. 2012

Madrid, Spain

Scientific Advisory Board member

Neutrinos in Cosmology, in Astro, Particle and Nuclear Physics Sept. 2009

Erice, Sicily, Italy

International Workshop on Nuclear Physics, 31st course

SCHOLARSHIPS

Scholarship of the Kepler Graduiertenkolleg 2012 - 2014

Tübingen, Germany

Monthly support during the research phase of the PhD.

Travel Grant of the Deutscher Akademische Auslandsdienst — DAAD Jul. 2013

Tübingen, Germany

Travel grant for attending the ICRC 2013, Rio de Janeiro, Brazil

REFERENCES

Available upon request

Colophon

THIS THESIS WAS TYPESET using LaTeX, originally developed by Leslie Lamport and based on Donald Knuth's TeX. The body text is set in 11 point Arno Pro, designed by Robert Slimbach in the style of book types from the Aldine Press in Venice, and issued by Adobe in 2007. The style of this dissertation is based on a template, which has been released under the permissive MIT (X11) license, and can be found online at github.com/suchow/ or from the author at suchow@post.harvard.edu.